ONE-DIMENSIONAL INTERACTING FERMIONIC SYSTEMS

A study of geometry, topology and symmetry in synthetic quantum matter

JOHANNES JÜNEMANN

geb. in Lüdinghausen

Mainz, Oktober 2017

Freude heißt die starke Feder
in der ewigen Natur.
Freude, Freude treibt die Räder
in der großen Weltenuhr.
Blumen lockt sie aus den Keimen,
Sonnen aus dem Firmament,
Sphären rollt sie in den Räumen,
die des Sehers Rohr nicht kennt!

— Friedrich von Schiller, An die Freude —

ZUSAMMENFASSUNG

In den vergangenen Jahren hat es einen gewaltigen Fortschritt in der Handhabung ultrakalter Gase gegeben. Laser-Kühlmethoden erlauben Zugang zum Quantenregime und Experimente haben eine Präzision erreicht, die die Kontrolle und Messung einzelner Atome zulässt. Durch ausgefeilte Lasertechniken können optische Gitter mit verschiedenen Geometrien erzeugt, Wechselwirkungen präzise eingestellt und neue Konzepte wie z.B. künstliche Eichfelder umgesetzt werden. Einerseits erlauben kalte Atome als Quantensimulatoren die Studie kondensierter Materie - die relevanten Freiheitsgrade des Ursprungssystems werden dafür auf das experimentell besser zugängliche Setup abgebildet. Andererseits ermöglicht die Kombination verschiedener experimenteller Komponenten das Design neuer Materialien, sogenannter synthetischer Quantenmaterie, die nicht zwangsläufig außerhalb der Versuchsumgebung existiert.

Gleichzeitig erweitern Konzepte aus der Quanteninformation unser Verständnis von Quantenphasen insgesamt. Das Konzept der Quantenverschränkung revolutioniert die Beschreibung von Vielteilchensystemen, indem es (Hilbertraum-)Wellenfunktionen durch intuitive Tensornetzwerke ersetzt. Das Verständnis dieser Tensoren als elementare Bausteine ermöglicht die Erklärung von Phänomenen wie topologischen Zuständen in einem Bottom-up-Ansatz. Zudem erlauben Tensornetzwerke eine effiziente Beschreibung von Vielteilchen-Zuständen und können deshalb für numerische Simulationen genutzt werden.

In dieser Arbeit konzentrieren wir uns auf eindimensionale fermionische Systeme und untersuchen den Einfluss von verschiedenen Faktoren wie z.B. Wechselwirkungen, inneren Freiheitsgraden, künstlichen Eichfeldern, Symmetrien und verschiedenförmigen Potentialen. Während die Wirkung der Einzelkomponenten wohlbekannt sein mag, bietet die Kombination verschiedener solcher Faktoren spannende neue Physik. Die theoretische Untersuchung wird durch die Möglichkeit der Realisierung in den oben genannten Experimenten ermutigt. Wir nutzen dazu - neben analytischen und störungstheoretischen Ansätzen - Tensornetzwerk-Methoden als numerische Technik. Insbesondere untersuchen wir drei Beispiele exotischer eindimensionaler fermionischer Systeme: (i) eine Creutz-Hubbard-Leiter, in der Wechselwirkungen und topologische Eigenschaften im Wettstreit stehen; wir erforschen das gesamte Phasendiagramm und erklären die (topologischen) Übergänge durch effektive Theorien; (ii) ein ringförmiges System mit einer ähnlichen mikroskopischen Leiterarchitektur, die als effektive Theorie relativistischer, masseloser Fermionen verstanden werden kann; für diese sogenannten Weyl-Fermionen erforschen wir die Gleichstrom-Antwort auf externe Felder; wir finden, dass Wechselwirkungen in bestimmten Parameterbereichen den diamagnetischen Strom entlang des Rings verstärken; (iii) ein fermionisches Multikomponentengas mit $SU(N)$-Wechselwirkungen in einer harmonischen Falle; wir bieten ein pädagogisches Verständnis der Symmetrie und stellen eine Verbindung zur Magnetisierung und zur experimentell messbaren Impulsverteilung der Energiezustände her.

ABSTRACT

Recent years have seen a tremendous step forward in the manipulation of ultra-cold atomic gases. Laser cooling techniques give access to the quantum regime and experiments have reached a level, at which control and measurement of individual atoms is possible. Sophisticated laser schemes provide optical lattices with different geometries, and allow the precise tuning of interactions and the realization of new concepts such as artificial gauge fields. On the one hand, cold atoms can be used as quantum simulators to study condensed matter systems by mapping the relevant degrees of freedom of the original system to the experimentally better accessible setup. On the other hand, combining different experimental features permits the design of new phases of matter, so-called synthetic quantum matter, which may or may not exist outside the experimental environment.

At the same time, concepts from quantum information are pushing the frontier of our understanding of quantum phases as a whole. The concept of entanglement revolutionizes the description of quantum many-body states by replacing (Hilbert space) wave functions with intuition-charged tensor networks. Taking these tensors as elementary building blocks makes it possible to explain phenomena like topology in a bottom-up approach. Moreover, tensor networks permit an efficient description of quantum many-body states and are therefore exploited for numerical simulations.

In this thesis, we focus on one-dimensional fermionic systems and explore the influence of different ingredients such as interactions, internal degrees of freedom, artificial gauge fields, symmetries and differently-shaped trapping potentials. While the individual effects might be well understood, the combination of these factors offers new exciting physics. Theoretical research on such systems is encouraged by the forthcoming realizability in the above-mentioned experiments. For our investigation, we employ - besides analytical and perturbative approaches - tensor network methods as a numerical means. In particular, we study three instances of exotic one-dimensional fermionic systems: (i) a Creutz-Hubbard ladder model with a competition between interactions and topological features; we lay out the complete phase diagram and explain the (topological) phase transitions through effective theories; (ii) a ring-shaped system with a similar microscopic ladder architecture, which can be understood as an effective theory of relativistic massless fermions; for these Weyl fermions, we explore the current response to external fields; we find that in certain regimes, the interactions enhance the diamagnetic current flowing along the ring; (iii) a fermionic multi-component gas in a harmonic trap interacting through $SU(N)$-symmetric contact potentials; we offer a pedagogic understanding of the symmetry and establish a link to the magnetization and to the experimentally accessible momentum distribution of the energy eigenstates.

CONTENTS

INTRODUCTION

A man grows stale if he works all the time on insoluble problems, and a trip to the beautiful world of one dimension will refresh his imagination better than a dose of LSD.

— Freeman Dyson

To understand the physical world we live in on a fundamental level, a microscopical approach on the atomic scale is required. The phenomena occurring in this regime are necessarily quantum-mechanical. While the equations of motion for single particles in external fields can in principle be solved, the more interesting physical characteristics of many-body systems often emerge from the interplay of the individual components. Describing such interacting systems fully requires a number of coefficients that scales exponentially in the number of constituents. This makes exact calculations of their behavior impossible as the information to store quickly exceeds the resources available in classical computers.

Richard Feynman proposed a new approach to access the properties of condensed matter systems [1]. His idea was to use more controllable setups of quantum particles to encode the relevant degrees of freedom of complex real materials, for which the isolated control of single ingredients is usually complicated. When Feynman put forward this revolutionary idea of *quantum simulations*, he did not specify a particular setup. Nevertheless, since then a whole zoo of such purpose-built analog quantum computers has emerged and comprises such diverse setups as ultracold atoms [2], trapped ions [3], superconducting circuits with Josephson junctions [4] and photonic technologies [5]: Quantum simulators have become reality and the control and understanding they offer might pave the way towards universal quantum computation.

In cold atomic setups, particles are cooled to extremely low temperatures to access the quantum regime. Due to the ultra-low coupling to the environment, the setup allows the measurement of ground state properties and therefore offers a particularly apt platform for the study of quantum phenomena [2, 6–8]. Optical manipulation of the constituents gives control over the effective dimensionality, lattice geometry and the internal state dependence of kinetic terms, thereby allowing for the realization of such exotic effects as synthetic gauge fields [9–11] and spin-orbit coupling [12]. Interactions can be tailored in strength and range by tuning external parameters [13] or by selecting constituents which are, e.g., strongly dipolar. The fact that these different contributions can be to a great extent individually controlled and combined accounts for the great success of ultracold atoms. Another reason for the popularity of the setup might be the fact that it offers the most intuitive access to the simulation of quantum effects in solid state systems: Apart from interactions with phonons, the hopping of atoms in the optical lattice imitates very intuitively the electron dynamics in an atomic lattice.

The extreme control and tunability of physical phenomena in quantum simulators has instilled the imagination of the scientific community beyond the mere imitation and understanding of existing physical phenomena. The development goes towards the creative combination of the available ingredients such as to discover or engineer new exotic phases of matter, which might not even exist in condensed matter systems, and which form a category of their own: synthetic quantum matter.

Spurred by the same ideas about a quantum computer, a whole new research branch about quantum information theory has flourished in the last three decades. Advances thereof have, among other milestones, significantly altered our understanding of what a quantum phase is by identifying entanglement as a fundamental concept [14–16]. The description of quantum many-body states in terms of tensor networks (instead of full Hilbert space wave functions) exploits the favorable scaling of this entanglement in the low energy spectrum of local Hamiltonians [17–20]. Numerical methods based on tensor networks allow us to access the strongly correlated regime of many-body systems where other techniques fail [21, 22]. Complementary to quantum simulations, they therefore advance our understanding of quantum many-body systems.

In the light of synthetic quantum matter, analytical and numerical approaches (such as tensor networks) assist the experimental progress: theoretical calculations allow us to predict physical behavior and can therefore guide the experimental efforts into promising directions. In this respect, one-dimensional systems serve a two-fold purpose: On the one hand, they can be appreciated as physical systems of their own right, which due to strong quantum fluctuations display physics significantly different from higher dimensions. On the other hand, in the form of *quasi*-one-dimensional systems, they can be used as a test-bed to explore the minimum requirements to construct higher-dimensional theories.

In this thesis, we consider one-dimensional fermionic setups and investigate the influence of different features that can be implemented in cold atom experiments. These components can be described as *geometrical* (i.e. concerning the graph-structure of a lattice), *topological* (i.e. being connected to non-local properties of the system) and *symmetrical* (i.e. related to some invariant property of the system). In fact, these categories are not exclusive and their effects are tightly interwoven. While the individual factors might be well understood, our ambition is to combine them in a way that allows for interesting new physics. A guiding principle for all systems is the presence of interactions that correlate the behavior of the individual particles. To access the strongly correlated physics and to account for the different microscopic ingredients, we employ tensor network methods as a versatile and powerful technique.

The thesis is organized as follows:

- In Chapter 2, we present general concepts that play a role in the study of one-dimensional synthetic quantum matter. We introduce these components pedagogically and contextualize them with respect to each other and to current research. The ideas shown here represent the building blocks that we combine in the following chapters.

- In Chapter 3, we study the imbalanced Creutz-Hubbard ladder. This fermionic lattice model combines aspects of lattice geometry and artificial gauge fields to display flat-band physics with topological features. We study the stability of the topological phase with respect to interactions and lay out the full phase diagram using matrix product state methods. We then describe limiting parameter regimes through effective models, shining a new light on the mechanisms at work in topological phase transitions. The results of this project were published in Ref. [23].

- Chapter 4 addresses the current response to an external field of a ring of interacting fermions with linear dispersion. These Weyl fermions have a relevance both in field theories and in topological insulators. The setup chosen here to model the dispersion is similar to the Creutz-Hubbard ladder in the previous chapter. We show that unlike conventional Hubbard interactions, nearest-neighbor interactions can have an enhancing effect on currents in the ring. The output of this work can also be found in Ref. [24].

- In Chapter 5, we investigate a continuum model of fermions with different internal states in a harmonic trap. Scattering of these particles gives rise to $SU(N)$-symmetric interactions. The symmetry is closely related to magnetic ordering and we therefore study the role of interactions in the formation of magnetic structures. Our research refines earlier results in the limit of strong interactions and extends these to the (only numerically accessible) regime of intermediate interactions. A particular focus is put on the identification of symmetry features in experimentally accessible properties. The results obtained here were published in Refs. [25, 26].

- Finally, we present some conclusions and discuss possible directions of future research in Chapter 6.

The focus of the main body of this thesis is on one-dimensional fermionic models and the physics arising in these models. Nevertheless, the numerical techniques involved in our studies and the possible experimental implementation of the models are highly relevant aspects that also deserve their place in this work:

- Most of our numerical results in interacting systems were obtained using tensor networks. In Appendix A, we explain how these tensor networks efficiently represent many-body ground states and explain their importance both as a quantum-informational concept and as a numerical technique. We give details on the specific tensor networks used in our projects.

- In Appendix B, we present a more in-depth introduction to cold atomic experiments and thereby detail the implementation of the concepts addressed in Chapter 2. Moreover, we present technical specifications for the experimental realization of the models presented in Chapters 3-5.

- Finally, in Appendix C, we show details of calculations and proofs that were too long for the main text, but can be of interest for researchers working on related questions.

RECURRING CONCEPTS

The target of this thesis is to explore the interplay of different effects on one-dimensional fermionic systems. Our investigation is focused on such features which are unattainable or hard to tune in traditional condensed matter systems, but within reach in the context of cold atom experiments. In this chapter, we specify the phenomena that we are interested in and lay out their fundamental concepts. We discuss and contextualize the ideas with respect to previous research and give pedagogical examples. The combination of two or more of these basic ingredients and the new physics arising therefrom is then studied in depth at the hand of several instances in Secs. 3-5.

In Sec. 2.1, we address the overall framework of quantum simulators and cold atoms; in Sec. 2.2, we specify on one-dimensional fermionic systems. Sec. 2.3 introduces interactions; in particular, we discuss how they are special in one dimension and how they can be technically treated. We then add internal degrees of freedom or a finite second spatial dimension to enter the regime of quasi-one-dimensional systems (Sec. 2.4). If the so-obtained systems allow for hopping-processes that correspond to closed loops in the lattice graph, artificial gauge fields can be realized. These are studied next (Sec. 2.5). Artificial gauge fields can have two significant influences: On the one hand, they can drive currents in the system (Sec. 2.6). On the other hand, combined with specific system geometries, they can alter the dispersion relation of free fermions such as to display topological features. Sec. 2.7 discusses the occurrence of such topological effects and their characteristics. The last ingredient relevant for our studies are symmetries. In Sec. 2.8, we motivate their relevance for both physical phenomena and for efficient numerical methods. Finally, in Sec. 2.9, we introduce Jordan-Wigner transformations as an often-used tool in our research. While not a physical ingredient itself, the technique allows the mapping between fermionic and spin systems and therefore adds an additional perspective to our understanding.

2.1 QUANTUM SIMULATORS AND COLD ATOMS

Purpose-built quantum simulators that address particular questions about a physical system are important as they allow us to understand processes in other, more complicated systems. In particular, such simulations can avoid nuisances like defects and decoherence that can obscure the study of fundamental processes in condensed matter systems. Moreover, quantum simulators might allow the engineering of other interesting quantum matter phases, which do not necessarily occur naturally, from scratch. In the last decade, experimentalists have reached unprecedented levels of control in the preparation and measurement of all kinds of quantum particles and systems [27–29]. This giant leap towards scalable purpose-built quantum simulators can be most vividly followed in ultracold

atoms with or without optical lattices [2, 6]. While earlier experiments focused on benchmarking and the individual addressing of single particles, since then a lot of inherent many-body features have been tested. Some milestones in this respect were the creation of Bose-Einstein condensates (BECs) [30] and the proof of their interference in a double-well setup [31], the demonstration of superfluid-Mott [32] and BEC-BCS transitions [33], the measurement of the equation of state of universal fermion gases [34], and the observation of Anderson [35, 36] and many-body localization [37]. An abundance of even further reaching features can today be implemented in cold atom systems: different lattice geometries [38], long-range interactions [13] and synthetic gauge fields [10] to name just a few. At the same time also the possibilities to perform measurements have advanced, and now allow control with single site precision [39] and the determination of e.g. nearest-neighbor correlations [40].

In the following, we focus on those features that play a role in one-dimensional systems and discuss their physical consequences. Details on the technical implementation with ultracold atoms can be found in App. B.

2.2   ONE-DIMENSIONAL FERMIONIC SYSTEMS

For a long time, one-dimensional systems have only been relevant as an intellectual gedankenexperiment or as a sandbox model in a first step towards more complex higher-dimensional systems. More recently, the setup has gained relevance in the study of chemical compounds such as polymers and organic compounds or of bulk materials with one-dimensional structures (like organic superconductors [41]). It was further pushed by progress in nanotechnology now allowing the realization of quantum wires such as carbon nanotubes [42, 43] and Josephson junction arrays [4].

Today, however, the most accessible and tunable environments for the investigation of one-dimensional physics are certainly cold atom experiments. Here, the one-dimensional confinement is obtained through counter-propagating laser-pairs at wavelengths $\lambda_i = 2\pi/k_i$ which, using the ac-Stark shift, form an optical potential

$$V_{\text{ext}}(\mathbf{r}) = \sum_{i \in \{x,y,z\}} V_{0,i} \sin^2 (k_i r_i). \tag{1}$$

The amplitudes of the potential can be tuned such that the confinement is much stronger in two directions than in the third, $V_{0,y}, V_{0,z} \gg V_{0,x}$. For deep optical lattices, the confinement on each lattice site is approximately harmonic with frequencies ω_i. For sufficiently low temperatures $kT \lesssim \hbar\omega_i$, particles can only occupy the lowest radial mode and the system is truly one-dimensional. The periodic potential in x-direction then gives rise to an effective *lattice* model. Alternatively, if the potential along the axial direction is turned off, the gas remains weakly confined in this direction due to the residual harmonic potential caused by the Gaussian profiles of the remaining lasers [2]; in this case, a one-dimensional *continuum* model is realized. The setups outlined here lay the foundation for all further manipulations of one-dimensional systems.

Up to this point, we have described a system of free fermions (considering only kinetic energy and external potentials). For such free models, the methods used for the study of one-dimensional physics do not differ conceptually from their higher-dimensional counterparts. We discuss next how interactions alter the picture.

2.3 EFFECTS OF INTERACTIONS

For non-interacting systems as considered so far, there is no significant difference to higher-dimensional systems: dispersion relations are calculated in the same fashion, etc. However, interactions in one-dimensional systems are special as the *Fermi liquid* picture which is valid for higher dimensions does not apply. Without interactions, particles at $T = 0$ occupy the lowest possible energy levels - up to the *Fermi level* or *surface* where the momentum distribution has a discontinuity. For dimensions higher than one, this does not change much when (weak) interactions are switched on. The only difference is that the elementary particles are no longer individual electrons, but instead electrons dressed with density fluctuations (particle-hole excitations) which behave like free fermions and are therefore called *quasi-particles* [44]. In one dimension, such perturbative approaches fail, as electrons that want to move along the one-dimensional system affect neighboring particles and an individual motion is impossible; particle dynamics become collective and the system becomes strongly correlated. The Fermi liquid picture then gets replaced by the *Luttinger liquid* picture. A particular feature of this model consists in a so-called spin-charge separation: for spinful fermions, the charges and spin of an excitation decouple and move independently.

Thanks to powerful analytical techniques like the Bethe ansatz [45] or bosonization [44], many aspects of interacting one-dimensional systems are well understood. With respect to numerical methods, we note that in particular, interactions do not pose a problem to tensor network methods that we use as the primary tool for our study of interacting systems in all interaction regimes where perturbative approaches fail.

In cold atomic systems, interactions are due to scattering events between particles, which correlate the physics of the individual atoms. In the simplest case of s-wave scattering, particles can be modeled as interacting through contact pseudo-potentials, which in lattice models translate into on-site interactions. For fermions, however, this is only possible if the particles have some label distinguishing them. For fully identical fermions, the Pauli-principle forbids the spatial concurrence, but the particles might then scatter through higher channels (e.g. p-wave). In a lattice, this yields *nearest-neighbor interactions*. While (electron-electron) interactions in condensed matter systems are limited by charge and distance and therefore hard to manipulate, in cold atom experiments so-called *Feshbach resonances* can be tuned to change the interaction strength and sign, and enable us (together with the control of lattice depth which tunes the hopping parameter) to explore the competition between kinetic terms and interactions

in a wide range. Laying out the full phase diagram in terms of interactions is therefore not only a theoretical exercise.

In particular for spin-carrying, interacting particles moving in a periodic potential like the one introduced in Eq. (1), the *tight-binding approximation* offers an economical theoretical description of the physics. It arises naturally when expanding the field operators in a discretized basis of maximally localized single-particle (Wannier) wave functions centered around the minima of the potential. The (partial) overlap of these Wannier functions gives rise to a kinetic term describing the hopping between neighboring sites and a second on-site term due to the two-body interactions. The resulting Hamiltonian represents the so-called *Hubbard model* and reads [46]

$$H = -t \sum_{j,\sigma} c_{j+1,\sigma}^\dagger c_{j,\sigma} + \frac{U}{2} \sum_j n_{j,\uparrow} n_{j,\downarrow} + \text{h.c.}, \qquad (2)$$

where the index j labels the minima of the periodic potential (dubbed lattice sites) and $\sigma \in \{\uparrow, \downarrow\}$ identifies the internal state of the particles. The operator $c_{j,\sigma}^\dagger$ ($c_{j,\sigma}$) has the effect of creating (annihilating) a particle and $n_{j,\sigma}$ measures the presence of a particle with spin σ on lattice site j. In typical applications, terms that emerge due to higher than s-wave scattering processes and lead to e.g. nearest-neighbor interaction terms are often dominated by the on-site term and therefore neglected in this model.

The effective second-quantized model (2) can describe cold atom setups [47, 48] (details in App. B.1), but is historically motivated through the study of electrons in atomic crystals [49] and in particular can explain metal-insulator transitions: For strong repulsive interactions, $U \gg t$ and half-filling (i.e. one particle per lattice site j), the ground state of the Hubbard model realizes a so-called *Mott insulator*, in which particles are localized on the individual sites of the lattice; without interactions, the system is metallic. In the following sections, we show how the Hubbard model can be "upgraded" to describe even more exciting physics.

2.4   GEOMETRY IN ONE-DIMENSIONAL SYSTEMS

We define a *quasi-one-dimensional* system as a system where in addition to the first spatial direction (which can be of infinite extent in the sense that we extrapolate the finite number of lattice sites $L \to \infty$), particles can tunnel along a second dimension with a finite number of states. In a lattice system, the second dimension can indeed correspond to physical sites along a spatial direction, i.e. to minima of the lattice potential. Alternatively - and experimentally more feasible in cold atomic experiments - the second direction can correspond to an internal degree of freedom, e.g. hyperfine levels. The latter alternative is dubbed *synthetic dimension* [50]. Hopping along such a synthetic dimension corresponds to the change of an internal state of the particle. In the example of fermionic particles with spin, this could correspond to a spin flip of the kind $c_{i,\uparrow}^\dagger c_{i,\downarrow}$, or a spin-orbit coupling $c_{i+1,\uparrow}^\dagger c_{i,\downarrow}$. The condition of hopping along the second dimension

makes quasi-one-dimensional systems different from traditional systems like the Hubbard model (2) which also consider internal states.

Experimentally, the tunneling along a *synthetic* dimension can be obtained through two-photon Raman transitions (more about this in App. B). Compared to a physical second dimension, the implementation with internal states has the advantage of sharp boundaries [11]. Interactions along a synthetic dimension are often (if not always) long-range. This is at a difference with respect to most setups with two spatial dimensions.

An important feature of quasi-one-dimensional systems is the fact that particles can take different paths to reach another site in the system. Similar to periodic boundary conditions, this feature allows particles to move around closed lines and motivates the following sections on artificial gauge fields and currents.

2.5   ARTIFICIAL GAUGE FIELDS AND FLAT BAND PHYSICS

Charged particles moving along alternative paths through a magnetic field pick up a relative phase dependent on the magnetic flux enclosed by the paths. This phenomenon is called *Aharonov-Bohm effect*. Although ultracold atoms usually do not carry a charge, the same physics can be obtained in this setup using *artificial gauge fields*. We will introduce these two notions first.

Artificial gauge fields can lead to energy dispersions with flat bands. These can lead to interesting physical features such as flat-band ferromagnetism [51] or pair superfluidity [52, 53]. Our interest in flat bands arises from their occurrence in systems with topological features such as the *integer quantum Hall effect* (see also Sec. 2.7). For partial fillings of flat energy bands, particles can choose their ground state from a highly degenerate manifold. In an interacting system, the resulting lack of a relevant comparative energy scale renders a perturbative approach invalid and the many-body ground state emerges from the manifold non-trivially. This is relevant for another, even more intricate, topological phase, the *fractional quantum Hall state*. Investigating *one-dimensional* flat band systems with topological properties in the presence of interactions is therefore interesting: It may shed new light on known facts in higher dimensions and possibly lead to discover new phases. We therefore shortly explain how such flat-band systems can be constructed.

ARTIFICIAL GAUGE FIELDS.   Consider some contour $\mathcal{C}$ that is limiting a two-dimensional region $\mathcal{S}$. For simplicity, let us assume that $\mathcal{S}$ is lying in the *xy*-plane and has a surface A. If the *xy*-plane is pierced by a homogeneous magnetic field $\mathbf{B} = B\mathbf{e}_z$, we can write the electromagnetic potential in Coulomb gauge (with $\nabla \times \mathbf{A} = \mathbf{B}$ and $\nabla \cdot \mathbf{A} = 0$) as $\mathbf{A} = \frac{Br}{2}\mathbf{e}_\varphi$. A charged particle surrounding $\mathcal{S}$ on the contour picks up a phase

$$\varphi = \frac{e}{\hbar} \oint_{\mathcal{C}} \mathbf{A} \cdot d\mathbf{r} = \frac{eB}{2\hbar} \oint_{\mathcal{C}} r \, dr = \frac{\Phi}{\Phi_0}, \tag{3}$$

which is proportional to the flux $\Phi = BA$ piercing the region $\mathcal{S}$. $\Phi_0 = \frac{e}{\hbar}$ is called a *flux quantum*.
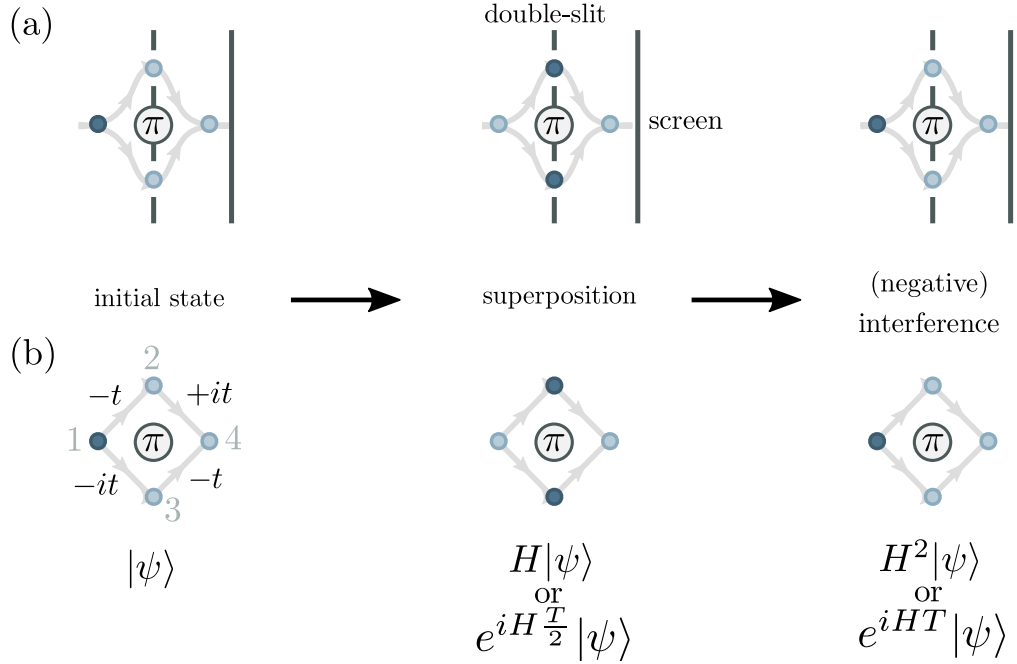
Figure 1: **Analogy between the Aharonov-Bohm effect and localized states due to magnetic or artificial gauge fields.** (a) A particle can travel along two paths in a double-slit experiment before interfering on a screen. The area enclosed by the paths is pierced by a magnetic flux Φ. In addition to the effect of different path lengths, the wave-functions corresponding to the two paths are therefore shifted by a phase $\varphi \sim \Phi/\Phi_0$. This is independent of whether the magnetic field actually extends to the region of the paths and shows the physical importance of gauge fields. For equal path lengths and $\varphi = \pi$, negative interference is observed on the screen. (b) In a cold atom lattice, the same effect can be simulated using artificial gauge fields. When hopping around a closed path in the lattice, the particle picks up a phase φ. In the given example, this leads to a negative interference on the right-most site after two hoppings - or alternatively, in a time evolution after $T = \pi/t$. The particle is can therefore never travel to this site and oscillates between the left and the center sites.

If alternatively, we pierce the system with a flux-tube $\tilde{\mathbf{B}} = \Phi\delta(\mathbf{r})\mathbf{e}_z$, we observe the same effect. This is curious as in the second case, the magnetic field does not extend to the path taken by the particle. We can rewrite the phase as

$$\varphi = \frac{e}{\hbar} \oint_{\mathcal{C}} \mathbf{A} \cdot \mathrm{d}\mathbf{r} = \frac{e}{\hbar} \int_{\mathcal{S}} (\nabla \times \mathbf{A}) \cdot \mathrm{d}\mathbf{S} = \frac{e}{\hbar} \int_{S} \mathbf{B} \cdot \mathrm{d}\mathbf{S}, \tag{4}$$

where in the second step, we apply Stokes' theorem. This shows that only the flux piercing the enclosed region is relevant, not the specifics of the magnetic field at the contour. We could also split the contour into two segments and compare the phase taken up by a particle traveling along the two paths. The resulting interference is called *Aharonov-Bohm effect* and has been experimentally demonstrated [54]. It shows the physical relevance of gauge potentials beyond a mere mathematical convenience to describe electric and magnetic fields.

According to the *Peierls substitution*, the effect of a slowly varying vector potential along some path (here in x-direction) can be absorbed in a tight-binding Hamiltonian as [55]

$$c^\dagger_{m+1,n}c_{m,n}e^{i\varphi_{m,n}} \quad \text{with} \quad \varphi_{m,n} = \frac{e}{\hbar} \int_{ma}^{(m+1)a} \mathbf{A}(x,na) \cdot \mathbf{e}_x \mathrm{d}x. \tag{5}$$

Unlike electrons in a condensed matter system, particles in a cold atomic setup are neutral and therefore a priori cannot couple to gauge fields and mimic the effect of charged particles. However, *artificial* or *synthetic gauge fields* can be created by dressing either the hopping along the physical direction through laser-assisted tunneling [9, 56] or by equipping the internal transitions (along the synthetic direction) with a phase. In particular, the phases imprinted on the hopping terms are then no longer limited by the constraints that apply to the original Peierls substitution. Alternative schemes rely on shaking or modulation of the lattice (for details see App. B).

The analogy between the Aharonov-Bohm effect in a double-slit experiment and artificial gauge fields on a lattice fragment is demonstrated in Fig. 1. In cold atoms, a generalization of the latter setup from a single plaquette to two-dimensional lattices allows the realization of the *Harper-Hofstadter Hamiltonian* [57, 58]. In quasi-one-dimensional systems, gauge fields were used to demonstrate the existence of chiral edge currents [59, 60], which are connected to topological edge states. We discuss such topological phenomena and their link to the introduced setup in the following section.

FLAT BAND PHYSICS.   Particles in a flat energy band cannot move due to the vanishing slope in their dispersion, $v = \partial\varepsilon_k/\partial k = 0$ (even if the band is not completely filled). This leads to localization and makes flat-band insulators yet another type of insulator than band-, Anderson or Mott insulators. In lattice models, depending on the geometry, flat-band physics can arise either without or with (artificial) gauge fields. Examples are given in Fig. 2.

While a priori, a system can have both curved and flat dispersion bands, models can be designed such that all the bands are flat. The approach relies on a combination of lattice geometry and artificial gauge fields: If the flux enclosed by a minimal hopping circle in the lattice-graph (i.e. around a so-called *plaquette*) corresponds to a π-phase ($\varphi = \pi$) and if for any path of a given length one can find a second path of the same length to interfere with, the hopping along these two paths leads to negative interference (compare Fig. 1).

To illustrate the localization in a simple example, let us take a microscopical perspective at a single particle on a four-site plaquette, where the hoppings have phases as indicated in Fig. 1b. The action of the Hamiltonian on a particle on the leftmost site is then

$$H(c_1^\dagger |0\rangle) = t(-c_2^\dagger - ic_3^\dagger)|0\rangle \tag{6}$$

$$H^2(c_1^\dagger |0\rangle) = t^2(-c_1^\dagger c_2 + ic_1^\dagger c_3 + ic_4^\dagger c_2 - c_4^\dagger c_3)(-c_2^\dagger - ic_3^\dagger)|0\rangle$$

$$= t^2 \underbrace{(-1(-1) + i(-i))}_{=2}(c_1^\dagger |0\rangle) + t^2 \underbrace{(i(-1) - 1(-i))}_{=0}(c_4^\dagger |0\rangle) \tag{7}$$
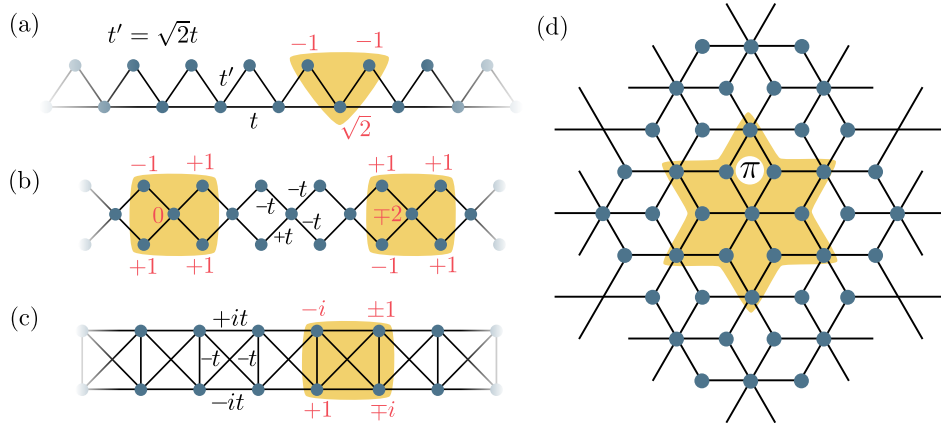
Figure 2: **Different lattice geometries allowing for flat dispersion bands and localized states.** (a) On a sawtooth lattice, the hopping amplitudes (black labels) can be chosen such that certain states (with the amplitudes for eigenstates indicated in red) are completely localized (yellow shaded). In this setup, a flat dispersion band occurs without artificial gauge fields. Not all eigenstates of the model are localized. (b) The diamond chain and (c) the Creutz ladder offer examples where a similar affect is obtained through an artificial gauge field reflected by the complex hopping amplitudes. Here, however, all energy bands are flat and the localized states are given by plaquettes consisting of five and four sites, respectively. (d) A two-dimensional flat-band system can be realized on the dice-lattice [52, 64]. The latter three examples are instances of Aharonov-Bohm cages, in which negative interference forces all states of the system to be localized. As a consequence, all bands are flat. The negative interference is obtained through a π-flux through any closed loop in the lattice geometry.

and therefore, under time-evolution (with time τ)

$$e^{-iH\tau}c_{i,\ell}^\dagger \left|0\right\rangle = \cos(t\tau)c_1^\dagger\left|0\right\rangle - \frac{iH}{t}\sin(t\tau)(-c_2^\dagger - ic_3^\dagger)\left|0\right\rangle, \qquad (8)$$

the particle oscillates between the leftmost and the center-site without ever reaching the right site. If we take a large numbers of such plaquettes, we can, e.g., construct Josephson diamond chains [61] or Creutz ladders [62, 63] (see Fig. 2). On these lattices, we can build superpositions of oscillating states on neighboring sites, for which oscillations are completely suppressed. Due to the origin of the localization effect, these completely localized eigenstates of the Hamiltonian are called *Aharonov-Bohm cages* [52]. We will encounter such Aharonov-Bohm cages in Chapters 3 and 4.

2.6 CURRENTS

Transport phenomena yield a very direct access to the phase properties in a system: Currents flowing through the bulk of a system distinguish conductors from insulators, *edge currents* are indicative of topological properties and closely related to *persistent currents* in non-simply connected geometries. In cold atomic

setups, currents can be induced and controlled through the earlier introduced artificial gauge fields [65, 66].

In general, the current density $\mathbf{j}$ in some point in space is related to the charge density ρ at the same point through the continuity equation

$$\nabla \cdot \mathbf{j} = -\frac{\partial \rho}{\partial t}. \tag{9}$$

For a one-dimensional system in x-direction, the current I and the current density $\mathbf{j} = j_x \mathbf{e}_x$ are equivalent, simplifying the above to:

$$\frac{\partial I}{\partial x} = -\frac{\partial \rho_x}{\partial t}, \tag{10}$$

where ρ_x describes the one-dimensional density. Assume that we consider a region of our one-dimensional system V and study the currents entering and leaving this subsystem. In integral notation, this yields

$$I_R - I_L = -\frac{\partial}{\partial t} \int_V \rho_x \mathrm{d}V, \tag{11}$$

where L labels the current entering the volume from the left and R identifies the current leaving it to the right. If we consider the energy eigenstate of a system, the density distribution of particles will be time-independent, necessitating $I_R = I_L$ (Kirchhoff law): The inflow of particles equals the outflow.

We now assume a general tight-binding setup

$$H = \sum_{j,l} \sum_{\sigma_j, \sigma_l} c^\dagger_{j,\sigma_j} T_{j,\sigma_j,l,\sigma_l} c_{l,\sigma_l}, \tag{12}$$

with annihilation (creation) operators $c^{(\dagger)}$, where j and l label physical sites, and the indices σ_j and σ_l indicate internal degrees of freedom. The tensor T contains the hopping coefficients. If the number of particles in the system $\hat{N} = \sum_{j,\sigma_j} c^\dagger_{j,\sigma_j} c_{j,\sigma_j}$ is conserved, $[H, \hat{N}] = 0$, this requires a zero net-current. In particular, if we split our system into two subsystems, the net-current of particles between these two subsystems should be zero for any solution. The above considerations allow us to find a generic definition for the currents. Assume, we have a region in our lattice containing sites p through q. The total current ("outflow from the region") then is

$$\hat{I}_R - \hat{I}_L = -e\frac{\partial}{\partial t} \left(\sum_{j=p}^q \sum_\sigma n_{j,\sigma} \right) = -\frac{ie}{\hbar} \left[H, \sum_{j=p}^q \sum_\sigma n_{j,\sigma} \right] \tag{13}$$

and it is easy to identify the current over a particular link as

$$\hat{I}_{(x,\sigma) \to (x',\sigma')} = -\frac{ie}{\hbar} \left(T_{x',\sigma',x,\sigma} c^\dagger_{x',\sigma'} c_{x,\sigma} - \mathrm{h.c.} \right). \tag{14}$$

The expectation value of the current can then be written as

$$I_{(x,\sigma) \to (x',\sigma')} = \frac{2e}{\hbar} \mathrm{Im} \left[T_{x',\sigma',x,\sigma} \langle c^\dagger_{x',\sigma'} c_{x,\sigma} \rangle \right]. \tag{15}$$

Note that this notation also allows us to understand hoppings along a second (possibly synthetic) dimension $\sigma \to \sigma'$ as currents.

If a system is now described by a real Hamiltonian, also the correlations are real and no currents flow. If, on the contrary, the Hamiltonian is complex, and in particular $T_{x'\sigma',x,\sigma} = e^{i\varphi}\left|T_{x'\sigma',x,\sigma}\right|$,

$$
\begin{aligned}
I_{(x,\sigma)\to(x',\sigma')} &= -\frac{e}{\hbar}\left\langle c_{x',\sigma'}^\dagger \left|\frac{\partial T}{\partial\varphi}\right|c_{x,\sigma}\right\rangle \\
&= -\frac{e}{\hbar}\frac{\partial}{\partial\varphi}\left\langle H_{x',\sigma',x,\sigma}\right\rangle = -\frac{e}{\hbar}\frac{\partial E_{x',\sigma',x,\sigma}}{\partial\varphi},
\end{aligned}
\tag{16}
$$

i.e. the current can be understood in terms of the phase-dependence of the kinetic energy of a state.

CURRENTS IN QUASI-ONE-DIMENSIONAL SYSTEMS.   For the eigenstate of a one-dimensional system with open boundary conditions, no current is expected to flow between any two subsystems. Otherwise, the state would be unstable. However, a *quasi*-one-dimensional setup does allow flows. With two sites (species) in the second (synthetic) dimension, transport can manifest in the form of opposing currents along the legs (*Meissner phase*) or as currents around individual plaquettes (*vortex phases*) [67–69]. Note that the nomenclature hints at the relevance of quasi-one-dimensional system for higher-dimensional superconducting setups. With higher numbers of species, even more intricate current patterns are possible [70].

CURRENTS IN RINGS.   In a system with periodic boundary conditions, contrary to the above, a current through a cut of the system can occur. This is the case if the system encircles a magnetic flux Φ. Following the Peierls prescription, on a periodic lattice with L sites such a phase can be distributed along the ring such that the phase acquired by a particle jumping from one site to the next enters the Hamiltonian as

$$
T_{x+1,\sigma_{x+1},x,\sigma_x} \propto \exp\left(i\varphi\right) \quad \text{with} \quad \varphi = \frac{2\pi}{L}\frac{\Phi}{\Phi_0}.
\tag{17}
$$

In analogy to Eq. (16), a current through a link of the ring can be written

$$
\hat{I}_{x\to x+1} = -\frac{e}{\hbar}\frac{\partial H_{x,x+1}}{\partial\varphi},
\tag{18}
$$

where $H_{x,x+1}$ collects all the possible hoppings through the cut. Equivalently, we can consider the total Hamiltonian H and write

$$
\hat{I} = -\frac{e}{\hbar L}\frac{\partial H}{\partial\varphi},
\tag{19}
$$

which, due to the Kirchhoff law and the one-directedness of the graph, is equivalent to the above. In terms of the total flux piercing the ring, this is

$$
\hat{I} = -\frac{e\Phi_0}{2\pi\hbar}\frac{\partial H}{\partial\Phi} = -\frac{\partial H}{\partial\Phi},
\tag{20}
$$

where we used $\varphi = \frac{2\pi}{L} \frac{\Phi}{\Phi_0}$ and $\Phi_0 = \frac{h}{e}$. The Hellmann-Feynman theorem then allows us to determine the current from the flux-dependence of the energy E of a state $|\phi\rangle$:

$$I = \langle\phi|\hat{I}|\phi\rangle \overset{H.F.}{=} -\frac{\partial \langle\phi|H|\phi\rangle}{\partial\Phi} = -\frac{\partial E}{\partial\Phi} \quad \text{with} \quad E = \langle\phi|H|\phi\rangle. \tag{21}$$

Currents originating from an enclosed magnetic flux are called *persistent currents* due to the fact that they are not driven by a force (as in the case of a (static) electric or alternating magnetic field) and therefore do not dissipate energy. We investigate such currents in more detail in Chapter 4.

2.7 TOPOLOGICAL EFFECTS

CLASSIFICATION.   Traditionally, classical and quantum phases were understood in Landau's theory of *spontaneous symmetry-breaking*: The energy landscape of a system is described as a function of external parameters (e.g. the temperature) and local observables, the *order parameters*. If the system displays a symmetry, the free energy is symmetric with respect to the corresponding order parameter for any value of the external parameter. When the external parameter is tuned, a phase transition can occur in which the system changes from a *disordered* phase, where the free energy is minimal for a vanishing order parameter (and the ground state therefore displays the symmetry), to an ordered phase. In the later, the minima of the (still symmetric) free energy lie at finite values of the order parameter (*"Mexican hat potential"*). To minimize the energy, the symmetry of the state is then spontaneously broken.

More recently, it was found that phase transitions exist which cannot be treated with the above formalism [71–75]. In *topological* phase transitions, the ground state does not break any symmetry of the Hamiltonian. Today, topological properties in quantum many-body systems offers a new paradigm for understanding phases of matter. This categorization focuses on the states themselves, and less on the underlying Hamiltonian. The categorization distinguishes two classes of states: long-ranged entangled (LRE) states and short-range entangled (SRE) states. A state is called a *long-range entangled* if it cannot be transformed under a local-unitary transformation [14, 76]

$$U = \mathcal{T}\left[e^{-i\int_0^1 dg\ \tilde{H}(g)}\right], \tag{22}$$

where $\tilde{H}$ contains only local Hermitian terms, to a fully unentangled (i.e. product) state. States that are no product state but neither connectible through such a time evolution have different topologies and are also called *(intrinsic) topological states*. All other states are called *short-range entangled*. They can be further distinguished by asking whether they are still connectible through a transformation like the above if $\tilde{H}$ displays some symmetry. States which under this constraint are unconnectible are considered different *symmetry-protected topological* states (SPT). Symmetry-breaking states also fall into the SRE-category. Note that the above classification and terminology is not unanimously used by all authors.

OCCURRENCE.   In a cold two-dimensional gas of electrons which is exposed to a strong magnetic field, the Hall (i.e. transverse) conductance is quantized [77]. This effect is known as the *integer quantum Hall* (IQH) effect, and the (very precise) quantization of the conductance σ_H can be connected to a topological invariant ν, i.e. a quantity that does not change under continuous deformation of the setup, via

$$\sigma_H = \nu \frac{e^2}{h}, \tag{23}$$

where e is the electron charge, and h the Planck constant. The topological quantum number, the so-called *Chern number*, is determined as [78]

$$\nu = \frac{i}{2\pi} \sum \int d^2k \int d^2r \; \left(\frac{\partial \psi^*}{\partial k_1} \frac{\partial \psi}{\partial k_2} - \frac{\partial \psi^*}{\partial k_2} \frac{\partial \psi}{\partial k_1} \right) \tag{24}$$

$$= \frac{i}{4\pi} \sum \oint dk_j \int d^2r \; \left(\psi^* \frac{\partial \psi}{\partial k_j} - \frac{\partial \psi^*}{\partial k_j} \psi \right), \tag{25}$$

and can only take integer values. Here, ψ denotes the wave function, the sum runs over the occupied subbands and the integrals over the unit cells in position and momentum space, respectively. The quantity below the integral is the so-called *Berry connection* that we will use in Chapter 3; the full expression is related to the Kubo formula that we will encounter in Chapter 4.

The above system has the property of being insulating (i.e. gapped) in the bulk and the observed conductivity is exclusively due to quantized currents flowing on the edge of the material. No deformation can alter this quantization and only if the bulk gap closes, the edge current can change. The IQH state was the first physical system to be found to display intrinsic topological order. In quantum spin Hall (QSH) states occurring in semi-conductors with spin-orbit coupling [79, 80], a chiral spin current flows (instead of a charge current). This system has a time-reversal symmetry that protects the phase, which categorizes the QSH state as an SPT phase.

If the interaction of particles is taken into account in the quantum Hall effect [81, 82], this gives rise to *fractional quantum Hall* (FQH) states that lead to a new variety of topological phenomena such as fractional statistics (for which a wave function acquires a phase different from the bosonic/fermionic ± 1 under the exchange of particles), fractional charges of quasi-particles, composite fermions (bound states of an electron and quantized vortices), etc. While hard to pinpoint unambiguously in real materials, technical advances have brought the topological phenomena closer to realization with cold atom systems using the earlier introduced ingredients [83]. In particular, the realization of FQH physics has stirred a remarkable number of suggestions for experimental implementation [84–91]. In addition, experimentalists also advance techniques for the measurement of indicators of topological states, e.g. of topological invariants [92] or of entanglement signatures [93].

QUANTUM PHASES IN ONE DIMENSION.   In one dimension, all phases which are possible according to the above categorization have been completely

identified [14–16, 94, 95] (see also Sec. 2.8). Long-range entangled states cannot exist in one dimension, and without symmetries all states would belong to the same phase. With symmetry, all non-trivial gapped phases are then either symmetry-breaking or SPT phases [76]. Let us discuss the two possibilities at the hand of simple paradigmatic models.

Take as a first example the one-dimensional transverse-field Ising model

$$H = -J \sum_{j=1}^{N-1} \sigma_j^x \sigma_{j+1}^x - h_z \sum_{j=1}^{N} \sigma_j^z, \tag{26}$$

which is invariant with respect to the parity $P = \prod_j \sigma_j^z$: $[H, P] = 0$. In the thermodynamic limit $N \to \infty$, the ground state is unique for $h_z > J$ and for $h_z \gg J$ given by $|\psi\rangle = |\uparrow \ldots \uparrow\rangle$, where $|\uparrow\rangle$ is the eigenstate to the eigenvalue 1 of the operator σ^z. For $h_z < J$, the ground state is doubly degenerate and in the limit $h_z = 0$, the manifold is spanned by $|\psi_\leftarrow\rangle = |\leftarrow \ldots \leftarrow\rangle$ and $|\psi_\rightarrow\rangle = |\rightarrow \ldots \rightarrow\rangle$, where $|\leftarrow\rangle$ and $|\rightarrow\rangle$ are the eigenstates of σ^x. The two given states break the symmetry, i.e. the parity does not have a defined value ± 1: $\langle \psi_\rightarrow | P | \psi_\rightarrow \rangle = \langle \psi_\leftarrow | P | \psi_\leftarrow \rangle = 0$.

On the contrary, in the fermionic model of a one-dimensional p-wave superconductor, the so-called *Kitaev chain* [96]

$$H = - \sum_{j=1}^{N-1} \left(-w(c_j^\dagger c_{j+1} + c_{j+1}^\dagger c_j) + \Delta c_j c_{j+1} + \Delta^* c_j^\dagger c_{j+1}^\dagger \right) - \mu \sum_{j=1}^{N} \left(c_j^\dagger c_j - \frac{1}{2} \right), \tag{27}$$

where for simplicity $\Delta = \Delta^* = \omega$, the fermionic parity $P = e^{i\pi \sum n_i}$ is always conserved. For $2\omega < \mu$, the ground state is unique and can be adiabatically connected to a product state. For $2\omega > \mu$, the ground state is degenerate with two states $|\psi_0\rangle$ (with even parity) and $|\psi_1\rangle$ (with odd parity) and cannot be connected through a symmetry-preserving transformation (22) to the large-ω phase: it is an SPT phase.

EDGE STATES.   Continuing with the above example, the degeneracy of the SPT phase can be understood in terms of so-called *Majorana modes*. A conventional fermion splits into two Majoranas, $a_{2j-1} = -i(c_j - c_j^\dagger)$ and $a_{2j} = c_j + c_j^\dagger$, which are their own anti-particles in the sense $a_j^\dagger = a_j$. In this notation, the Hamiltonian (27) reads

$$H = \frac{i}{2} \left(-\mu \sum_{j=1}^{N} a_{2j-1} a_{2j} + 2\omega \sum_{j=1}^{N-1} a_{2j} a_{2j+1} \right). \tag{28}$$

For $\mu = 0$, the edge Majoranas a_1 and a_{2N} do not appear in this Hamiltonian and are unpaired. Recombining these Majoranas to a physical mode with zero energy $d^\dagger d = (i a_{2N} a_1 + 1)/2$ allows us to give an intuitive picture to the SPT-character of the phase: The operator $i a_{2N} a_1$ measures the parity of the ground states and is equivalent to the presence $(d^\dagger d |\psi_0\rangle = 1 |\psi_0\rangle$, odd) or absence $(d^\dagger d |\psi_1\rangle = 0 |\psi_1\rangle$, even) of the edge mode. Only this very non-local measure can

distinguish the two phases. For finite $\mu < 2\omega$, the edge Majorana modes are no longer exactly localized on the outmost sides, but decay exponentially into the bulk. As a consequence, in the thermodynamic limit, the two Majoranas stay well separated.

The above is a minimal working example of topological edge effects, but we can understand it in close analogy with more complex examples such as the AKLT state in spin-1 chains [97] or the earlier mentioned edge currents in quantum Hall or quantum spin Hall states. In particular, the Majorana edge modes share with the latter the feature of being localized, of carrying zero energy and of needing a closing of the bulk energy gap to change the topological nature of the system. We will re-encounter topological states with edge modes in Chapter 3.

2.8 SYMMETRIES

Symmetry is a fundamental concept for all physical systems. We say that a Hamiltonian has a certain symmetry $\mathcal{G}$ if it is invariant under a unitary (or anti-unitary) representation $U(g)$ for all elements g of this group, i.e.

$$[H, U(g)] = 0 \quad \forall\, g \in \mathcal{G}. \tag{29}$$

For *continuous* symmetries, the generators of the unitary operation also commute with the Hamiltonian (e.g. the momentum operator for a translation symmetry) and the corresponding observable is a conserved quantity. The action of an operator associated with a *discrete* symmetry (such as parity) is a non-infinitesimal change of the system. If such a symmetry is present, the wave function is invariant under the effect of the (anti-)unitary operator apart from a multiplicative factor that identifies the symmetry sector. In both cases, the invariant quantity allows to label different sectors of the Hamiltonian. In our research, symmetries fulfill different purposes:

In condensed matter systems, the presence of symmetries categorizes the possible phases (symmetry-breaking and symmetry-protected topological phases, see above). In particular for one-dimensional systems, beyond the fermionic parity (compare Sec. 2.7) all physical phases can be fully categorized by three discrete symmetries: time-reversal $\mathcal{T}$, charge conjugation (or particle-hole symmetry) $\mathcal{C}$ and the combination (chiral symmetry) $\mathcal{S} = \mathcal{T}\mathcal{C}$ [98]. The time-reversal symmetry is anti-unitary and represented by an operator $T = U_T K$, where U_T is unitary and K is the complex conjugation. A time-reversal symmetric system fulfills $U_T H^* U_T^\dagger = H$. The (anti-unitary) charge conjugation symmetry $C = U_C K$ similarly has the property $U_C H^* U_C^\dagger = -H$. The combination of the two yields the chiral symmetry with $U_S H U_S^\dagger = -H$. The presence of these symmetries and their eigenvalues define the SPT-character according to the *Altland-Zirnbauer* classification [98, 99]. In this work, we will investigate a topological insulator protected by a chiral symmetry in Chapter 3.

In our models, we often consider systems in which the particle number is conserved and which therefore display a U(1)-symmetry. Cold atom experiments, however, offer the possibility to engineer systems with much higher continuous symmetries such as the SU(N) group [100]. In condensed matter systems, the

SU(2)-group appears naturally in systems which are invariant under spin rotations. Here, higher symmetries with $N > 2$, however, are usually not guaranteed by fundamental principles and emerge only in rather exotic materials [101]. In particle physics, on the contrary, such symmetries are highly relevant. The cold atomic setup can therefore serve as a test-bed for high-energy theories, and in addition, might lead to new exotic quantum matter phases. The achievement of high symmetries in cold atoms is based on the use of alkaline-earth or Ytterbium atoms, for which the nuclear spin decouples from the electronic spin. Scattering between such particles is then usually independent of the internal state and leads to interactions that preserve the symmetry. We discuss systems with SU(N)-symmetry and their properties in more detail in Chapter 5.

In numerical simulations, the presence of symmetries permits to greatly reduce the necessary computational effort. In an exact diagonalization, projections to the subspaces with the different quantum numbers of the symmetry operator make the original problem block-diagonal, and the diagonalization can be performed for each of these lower-dimensional blocks individually. In tensor networks, both Abelian and non-Abelian symmetries can be implemented [102, 103]. In our programs we only make use of the former, but we note that for non-Abelian symmetries, we can exploit the respective largest Abelian subgroups. The earlier introduced SU(N) symmetry, e.g., can be treated in terms of $N - 1$ U(1)-symmetries which can be implemented with our methods. Technical details of how such an implementation is achieved in tensor networks can be found in App. A.

2.9   FERMION-SPIN CORRESPONDENCE

It turns out that one-dimensional systems of spins, fermions or hard-core bosons (i.e. bosons that cannot occupy the same state due to infinite repulsive interactions) can all be mapped into each other [104, 105] and therefore, they can technically be treated in the same fashion. Here, we will discuss the *Jordan-Wigner transformation* [105] as a means to map a spin chain to a fermionic chain and vice-versa. Despite the mathematical equivalence, spin and fermionic systems describe physically distinct systems. We will reconcile these two facts by picking up the example of the Ising model and the Kitaev chain introduced earlier. We show that the two are mathematically equivalent and retrace why anyway, they are topologically different.

Just as a spin-1/2 particle can be in two different states, any site of a fermionic (or hard-core bosonic) lattice can be characterized by the absence or presence of a particle. Naively, one could therefore suggest a mapping between a spin lattice and a fermionic lattice by associating the raising and lowering operators of the spins ($\sigma_j^+ = (\sigma_j^x + i\sigma_j^y)/2$ and $\sigma_j^- = (\sigma_j^x - i\sigma_j^y)/2$) with the creation- and the annihilation operators of the fermions ($c_j^\dagger$ and c_j). However, spin and fermionic

operators do not display the same commutation relations: While on-site indeed both operator sets are anti-commutative,

$$\{\sigma_j^+, \sigma_j^-\} = 1 \quad \text{and} \quad \{\sigma_j^+, \sigma_j^+\} = \{\sigma_j^-, \sigma_j^-\} = 0, \tag{30}$$

$$\{c_j^\dagger, c_j\} = 1 \quad \text{and} \quad \{c_j^\dagger, c_j^\dagger\} = \{c_j, c_j\} = 0, \tag{31}$$

the exchange of operators on different sites i and j is commutative for spins, but anti-commutative for fermions:

$$[\sigma_i^+, \sigma_j^-] = 0 \quad \text{and} \quad [\sigma_i^+, \sigma_j^+] = [\sigma_i^-, \sigma_j^-] = 0, \tag{32}$$

$$\{c_i^\dagger, c_j\} = 0 \quad \text{and} \quad \{c_i^\dagger, c_j^\dagger\} = \{c_i, c_j\} = 0. \tag{33}$$

Luckily it turns out that for finite systems a method exists to map between a spin and a fermionic lattice, the so-called *Jordan-Wigner transformation*. By introducing an ordering of all sites in the lattice, the transformation can be written as

$$c_j^\dagger = \prod_{i<j} e^{i\pi \sum \sigma_i^+ \sigma_i^-} \sigma_j^+ = \prod_{i<j} (-\sigma_i^z)\sigma_j^+ \tag{34}$$

or

$$\sigma_j^+ = \left(e^{i\pi \sum_{i<j} n_i} \right) c_j^\dagger = \prod_{i<j}(1 - 2n_i)c_j^\dagger, \tag{35}$$

where $n_j = c_j^\dagger c_j$. It can easily be checked that the commutation relations for the two systems are correctly reproduced under this transformation. If we visualize the two operators, we see that the fermionic creation and annihilation operators in spin notation have a *Jordan-Wigner string* of σ^z-matrices on all sites that occur prior in the ordering. The terms therefore give a sign to the respective observables that depends on the parity (even/odd number of up-spins). Similarly, when writing the spin operators, we see that a sign gets attributed to the operator depending on the parity of the particle number on the previous sites. Number operators, on the contrary, are strictly local in the spin basis, $n_j = \frac{1}{2}(\sigma_j^z + 1)$, as the Jordan-Wigner strings of the involved operators $c_j^\dagger$ and c_j cancel each other. Correlators between sites i and j display a Jordan-Wigner string on all sites in the ordering between i and j: $c_i^\dagger c_j = \sigma_i^+(-\sigma_{i+1}^z)\ldots(-\sigma_{j-1}^z)\sigma_j^-$.

Now, spin models with nearest-neighbor coupling are mapped by the transformation to a nearest-neighbor fermionic model and vice versa. In particular, the transformation relates the quantum Ising model (26) to the Kitaev chain (27) if one sets $J = 2\omega$ and $h_z = \mu$. In Sec. 2.7, we discussed that the earlier system displays a transition between a disordered and a symmetry-broken (or ordered) phase, while the latter displays a symmetry-protected topological phase. This is interesting because both Hamiltonians (26) and (27) possess a $\mathbb{Z}_2$-symmetry.

The symmetry of the fermionic system is protected because the fermionic parity cannot be broken [98]. If, in the fermionic model for simplicity we consider the case $h = 0$, we find two degenerate ground states with opposite parity which consist of an equally weighted mixture of all the basis states of the operator n_j. For any finite region in the bulk, the number of particles in both states can be

either even or odd and no local measurement can distinguish between them. The two states (and their parity) can only be distinguished by measuring the parity of the full system or by looking at the edges and determining the occupation of the (Majorana) edge mode $c_N^\dagger c_1 + c_N^\dagger c_1^\dagger + $ h.c. [95]. This is clearly a very non-local feature. Similarly, for the Ising model, $h_z = 0$ yields any superposition of $|\leftarrow \ldots \leftarrow\rangle$ and $|\rightarrow \ldots \rightarrow\rangle$ as the ground state, including the parity-conserving state $|\psi^+\rangle = |\leftarrow \ldots \leftarrow\rangle + |\rightarrow \ldots \rightarrow\rangle$. For perturbations that preserve the parity (in particular the transverse field), the ground state is always symmetric under simultaneous spin flip of the whole chain along the x-direction (i.e. application of the parity operator). Why then do we call the spin phase with $h_z < J$ symmetry-breaking? While not all the questions on symmetry-breaking in (finite) quantum systems have been answered [106, 107], an intuition can be built on the fact that, while formally the same, the states of the Ising chain and of the Kitaev chain have different properties due to the non-local basis of the fermionic system. In particular, the fermionic correlations $c_i^\dagger c_j = \sigma_i^+(-\sigma_{i+1}^z) \ldots (-\sigma_{j-1}^z)\sigma_j^-$ are obviously different from spin correlations $\sigma_i^+\sigma_j^-$ which do not contain a Jordan-Wigner string. Therefore the particles in the two systems display inherently different physics.

The above ideas are intended to give a rough idea of how the different aspects of symmetry, topology and the Jordan-Wigner transformation are inter-connected. For more formal approaches, see Refs. [15, 108].

Jordan-Wigner transformations are also an important method to take care of the non-locality of the fermionic exchange relations when treating fermionic systems (even when quasi-one-dimensional) using tensor network methods. We present some further considerations on this issue in App. A.3.

THE IMBALANCED CREUTZ-HUBBARD MODEL:
A PARADIGMATIC 1D TOPOLOGICAL INSULATOR

In the previous chapter, we have introduced different specifications of one-dimensional fermionic systems. Here, we present a first instance of a setup in which several of these features are combined to explore new physics: We take a system of fermions on the so-called *Creutz ladder* as an instance of a one-dimensional topological insulator and explore the effects of imbalance and repulsive Hubbard interactions on this setup.

As discussed in Sec. 2.7, the advances in quantum simulations, and in particular in ultracold atomic gases in optical lattices, have enabled experimentalists to realize topological insulators. The role of interactions on topological phases, however, is less explored. This is true both experimentally and theoretically. Theoretical investigation is rendered particularly difficult by the fact that many of the standard tools used for the identification of a topological phase rely on analytical methods. For example, winding and Chern numbers are usually determined through the non-interacting band structure and the topological classification stems from the Hamiltonian matrix [109, 110]. For strongly correlated systems, attempts of generalization are being made [111–113], but general numerically cheap and quantitatively reliable methods barely exist [114]. Nonetheless, developing an understanding of the interplay between topological phases and interactions is a highly relevant issue. The paradigmatic example in this context is the integer quantum Hall effect of a two-dimensional fermionic gas exposed to a magnetic field [82, 115]. With interactions, the phenomenon "upgrades" to the fractional quantum Hall effect [116] and allows for excitations with fractional statistics which could e.g. play a role in the development of quantum computers [117, 118].

It is interesting to explore the interplay between topology and interactions in a one-dimensional setup in a sandbox like fashion. We therefore take up the quasi-one-dimensional, so-called *Creutz model* which is known to have topological properties and study the effect of repulsive Hubbard interactions. This allows us to probe the stability of the topological phase when exposed to strong correlations. The Creutz ladder, a model originally developed in the field of high energy physics [62] and later transported to condensed matter by the same author [63], has been studied previously with bosons [119, 120]. Recently, it was shown that the Creutz ladder when charged with spinful fermions and exposed to attractive interactions gives rise to a BCS description [121]. For spinless fermions, we are aware of only a single study, however with a different focus on an additional superconductor s-wave pairing [122].

Due to slight differences in the model, the *imbalanced* Creutz ladder studied by us belongs to a different symmetry class than the original model and therefore realizes a different SPT phase. The effect of Hubbard interactions on this kind of topological insulator is widely unexplored. We show that, unlike in

the bosonic case, a projection onto a single flat band is insufficient: All bands and edge modes have to be retained to fully account for the effects of correlations and topological effects. To be more precise, we investigate the influence of both an energy imbalance (between the two fermionic species appearing in the model) and of Hubbard interactions. We show that the two adjustments to the original flat-band model evoke a competition between the topological phase and two types of (orbital) quantum magnetism. At large imbalance, the system is driven through a phase transition of Ising universality towards a paramagnetic phase. For large interactions, on the contrary, long-range ferromagnetic order arises as in the symmetry-broken phase of the quantum Ising model. Away from these limiting scenarios, we introduce effective theories by mapping the original system to models of quantum magnetism. This allows us to predict the critical lines for weak, intermediate and strong interactions and to identify the different underlying conformal field theories (CFT).

The procedure is as follows: In Sec. 3.1, we introduce the Creutz model and our alterations to it. We then make a detailed analysis of the different regimes (Sec. 3.2): In the non-interacting model, we focus on the toplogical insulator phase and analyze and explain the topological properties. For weak interactions, we predict the critical line through a self-consistent mean-field approach. For the opposite case of strong interactions, we write an effective super-exchange model. We then evaluate the intermediate regime. In Sec. 3.3, the analytical prediction is backed by a numerical study, allowing us to lay out the full phase diagram. We complete the study by presenting an interpretation of the topological phase transitions in terms of impurity physics and effective edge theories (Sec. 3.4). Details of the implementation of the model with cold atoms in optical lattices are given in App. B.2.1.

The results presented in this chapter have been published in Ref. [23].

3.1   SETUP

The model of interest is given by

$$H_{\pi\mathrm{CH}} = H_{\pi\mathrm{C}} + V_{\mathrm{Hubb}}, \quad H_{\pi\mathrm{C}} = H_{\mathrm{FB}} + V_{\mathrm{imb}}, \tag{36}$$

where we collect the kinetic terms H_{FB} and the imbalance term V_{imb} in the free-fermionic model $H_{\pi\mathrm{C}}$. V_{Hubb} is a repulsive Hubbard on-site interaction. We will henceforth refer to the full model as the *imbalanced Creutz-Hubbard model*.

To detail the Hamiltonian, we introduce a one-dimensional ladder lattice where the sites (rungs) have a distance a and are labeled $j \in \{1, \ldots, N\}$ and the legs (labeling an internal degree of freedom) are denoted $\ell \in \{u, d\}$. The fermionic operator $c_{j,\ell}^\dagger$ ($c_{j,\ell}$) creates (annihilates) a particle at a given site. The kinetic term reads

$$H_{\mathrm{FB}} = \sum_{j,\ell} \left(-\tilde{t} c_{j+1,\ell}^\dagger c_{j,\bar{\ell}} + i s_\ell \tilde{t} c_{j+1,\ell}^\dagger c_{j,\ell} + \mathrm{h.c.} \right), \tag{37}$$

where $s_{u/d} = \pm 1$ and $\bar{\ell}$ labels the opposite rung to ℓ, namely $\bar{u} = d$ and $\bar{d} = u$. H_{FB} contains all kinetic terms of the full model: The first term describes *diagonal*
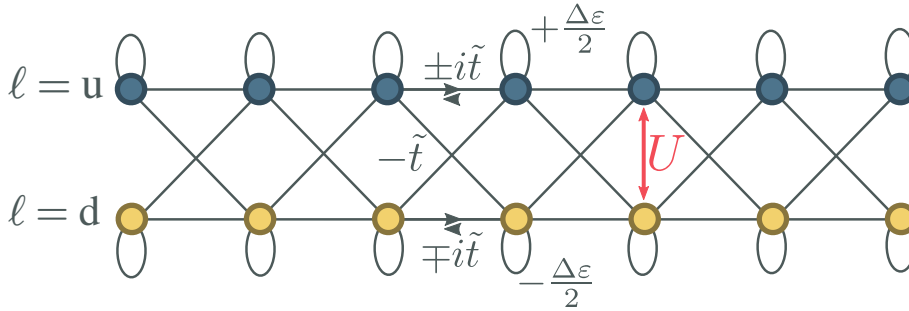
Figure 3: **Hopping and interaction processes in the imbalanced Creutz-Hubbard model.** The sites of the two-legged ladder are represented by blue ($\ell = \mathrm{u}$) and yellow ($\ell = \mathrm{d}$) dots. Particles can hop from one site to another along the grey lines. For the complex hopping amplitudes, we indicate the direction by arrows. The imbalance terms are expressed as on-site hoppings. Moreover, particles on the same lattice site j interact through a repulsive Hubbard interaction U.

tunneling, the second term *horizontal* tunneling along the legs of the ladder (see Fig. 3).

Depending on the implementation of the model, a hopping term of the type $c^{\dagger}_{j(+1),\ell}c_{j,\bar{\ell}}$ can refer to two physically different processes. On the one hand, it can correspond to an actual (i.e. physical) hopping in the direction orthogonal or diagonal with respect to the underlying one-dimensional system. This justifies the expression *quasi-one-dimensional* system as the system physically extends (finitely) into a second dimension. On the other hand, u and d can also be understood as labels for the two states of an internal two-level system. In this image, a half-filled chain, in which every site i is singly-occupied, can be understood as an *orbital magnet*: Depending on the pattern of occupation, we can label a state e.g. as an orbital (anti-)ferro- or paramagnet. An important difference between the fermionic ladder model and a simple spin-1/2 chain is the possibility to double-occupy a physical site.

One particularity of the Creutz-model are the imaginary hopping coefficients $\pm i\tilde{t}$. For neutral atoms, these can originate from artificial gauge fields (compare Sec. 2.5). As a consequence, the particles acquire a phase factor $e^{\pm i\varphi}$ when moving from one site to the next. In the setup at hand, we have $\varphi = \pm\frac{\pi}{2} \rightarrow e^{\pm i\varphi} = \pm i$ and a particle following a triangular or lozenge-shaped unit-cell path on the lattice encircles a π-flux (see Fig. 6).

The imbalance term

$$V_{\mathrm{imb}} = \sum_{j,\ell} \frac{\Delta\varepsilon}{2} s_\ell n_{j,\ell} \tag{38}$$

favors the occupation of one particle species energetically (u for $\Delta\varepsilon < 0$, d for $\Delta\varepsilon > 0$). The imbalanced Creutz ladder $H_{\pi\mathrm{C}}$ differs from the original Creutz model [62], in which a vertical hopping $t_\mathrm{v}c^{\dagger}_{j,\ell}c_{j,\bar{\ell}}$ is considered instead of an imbalance.
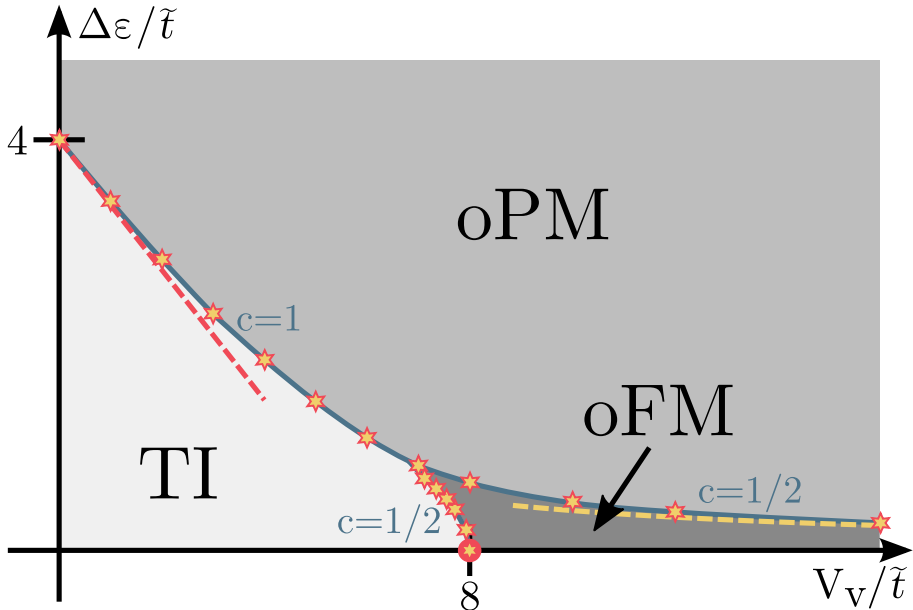
Figure 4: **Complete phase diagram of the imbalanced Creutz-Hubbard model.**
The model has three gapped phases: a topological insulator phase (TI), an
orbital paramagnet (oPM) and an orbital ferromagnet phase (oFM). Stars
denote critical points as determined numerically, the dashed lines are results
of a perturbative approach (yellow) and a self-consistent mean-field analysis
(red). In addition, we determine the transition between topological insulator
and orbital ferromagnet analytically (red dot). The blue lines are guides to
the eye for the critical lines, their label shows the central charge describing
the corresponding conformal field theory.

The second term in Eq. (36) describes a repulsive ($V_v > 0$) interaction between
particles occupying the same lattice site,

$$V_{\text{Hubb}} = \sum_{j,\ell} \frac{V_v}{2} n_{j,\ell} n_{j,\ell}. \tag{39}$$

3.2   REGIMES AND TRANSITIONS

In this section, we explore the different parameter regimes of the Hamiltonian in
Eq. (36). Fig. 4 shows the phase diagram containing the various results as a visual
aid for the following discussion. Starting from the pure flat-band model (37), we
discuss features and properties in the topological insulator regime (Sec. 3.2.1).
We then turn to the two additional terms.

First, we consider the influence of the imbalance (38) which still can be treated
in the formalism of free fermions. We explain how the introduction of the energy
imbalance between the two fermionic species induces a phase transition to a
physically trivial phase. We then give an alternative explanation to the transition
by rewriting the system as a double-copy of the one-dimensional quantum Ising
model.

For the interacting model, we distinguish three parameter regimes:

Weak interactions can be understood as a ferromagnetic coupling between the two chains in the Ising model description. We can explore the influence of this coupling on the individual chains through a self-consistent mean-field approach that allows us to analytically predict the critical line (Sec. 3.2.2).

We then turn to the opposite limit of *strong* interactions (Sec. 3.2.3). We derive an effective spin model in an analog fashion to the Heisenberg model arising in the strong-coupling limit of the Hubbard model. This effective model explains the observed orbital paramagnetic and ferromagnetic phases and yields a prediction of the critical line separating them.

Eventually, we study the *intermediate* regime, in which neither the kinetic term nor the interaction can be treated in a perturbative manner (Sec. 3.2.4). However, it turns out that indeed an effective model arises that correctly predicts the phase transition for the balanced model.

3.2.1   *Non-interacting regime*

For free fermions, we can solve the model analytically. This allows us to identify two phases in this regime. We first diagonalize the Hamiltonian and discuss its features and then characterize the two occurring phases.

For periodic boundary conditions, the kinetic part of the Hamiltonian (36) can be Fourier-transformed, $c_\ell(q) = \sum_j e^{iqaj} c_{j,\ell}/\sqrt{N}$, and re-written in spinor-basis $\Psi(q) = (c_\mathrm{u}(q), c_\mathrm{d}(q))^T$ as

$$H_{\pi C} = \sum_{q \in \mathrm{BZ}} \Psi^\dagger(q) \left[\mathbf{B}(q) \cdot \boldsymbol{\sigma} \right] \Psi(q) \tag{40}$$

with $\mathbf{B}(q) = 2\tilde{t}(\Delta\varepsilon - \cos(qa), 0, \sin(qa))^T$ and the vector of Pauli matrices $\boldsymbol{\sigma} = (\sigma_x, \sigma_y, \sigma_z)^T$. We denote $q \in \mathrm{BZ} = (-\pi/a, \pi/a]$ the permitted quasi-momenta and set $a = 1$ in the following. The dispersion relation is easily obtained through diagonalization as

$$\epsilon_\pm(q) = \pm\epsilon(q) = \pm 2\tilde{t}\sqrt{1 + \left(\frac{4\tilde{t}}{\Delta\varepsilon}\right)^2 + 2\left(\frac{4\tilde{t}}{\Delta\varepsilon}\right)\sin q}. \tag{41}$$

For $\Delta\varepsilon/\tilde{t} = 4$, the single-particle gap closes indicating a phase transition (see Fig. 5a).

To identify the topological nature of the system, we study the symmetry of the Hamiltonian. The Altland-Zirnbauer classification allows a categorization of topological phases in one dimension according to their time-reversal, their parity and their chiral symmetry [98, 99] (compare Sec. 2.8). For the Hamiltonian at hand, we can find a chiral symmetry operator $U_\mathrm{chiral} = \sigma_y$ fulfilling $U_\mathrm{chiral} H(-q) U_\mathrm{chiral}^\dagger = -H(q)$. However, the component $B_z(q) = \Delta\varepsilon/2 + 2\tilde{t}\sin(q)$ does not have a defined parity under $q \leftrightarrow -q$. As a consequence, neither a time-reversal operator with $U_T H(-q)^* U_T^\dagger = +H(q)$ nor a particle-hole operator with $U_C H(-q)^* U_C^\dagger = -H(q)$ can be found. Therefore possible topological phases in the imbalanced Creutz ladder fall into the AIII-class of the Altland-Zirnbauer classification. This is different from the conventional Creutz ladder, which belongs to the BDI-class due the presence of time-reversal and particle-hole symmetry.
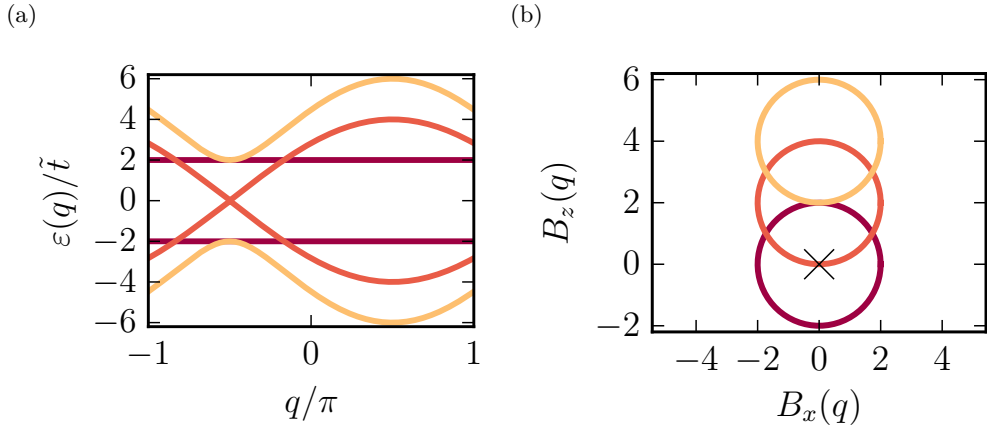
(a)

(b)

Figure 5: **Dispersion relation and winding of the imbalanced Creutz ladder.**
(a) Dispersion bands of the imbalanced Creutz ladder in different regimes:
in the TI-phase with flat bands ($\Delta\varepsilon/\tilde{t} = 0.0$, purple), at the critical point
($\Delta\varepsilon/\tilde{t} = 4.0$, red) and in the oPM-phase ($\Delta\varepsilon/\tilde{t} = 8.0$, orange). (b) Winding
of the spinor $(B_x(q), B_y(q))$ for the same parameters: Within the topological
phase the spinor encircles the origin (black cross), while in the non-topological
phase it does not.

To determine whether the two phases separated by the above-found critical
point are SPT or trivial, it is instructive to revisit the Hamiltonian in Eq. (40).
As a Bloch-vector, $\mathbf{B}(q)/\mathcal{N}$ identifies the direction on the Bloch-sphere in which
the Hamiltonian is diagonalized. Due to the symmetry properties of the system,
the Bloch sphere is constrained to the xz-plain. For $\Delta\varepsilon/\tilde{t} < 4$, the Bloch vector
describes a circle around the origin when running the wave vector through the
Brillouin zone $q \in (-\pi/a, \pi/a]$. This property identifies a quantized winding
number $\mathcal{W} = 1$ in this parameter regime. For $\Delta\varepsilon/\tilde{t} > 4$, on the contrary, the
origin is not enclosed by the path, i.e. $\mathcal{W} = 0$. Fig. 5b illustrates this finding. We
therefore dub the first phase with $\Delta\varepsilon/\tilde{t} < 4$ an AIII-topological insulator and
the second phase a trivial phase.

More formally (but equivalently), the topological property can also be iden-
tified by integrating the Berry connection $\mathcal{A}_{\pm}(q) = i \langle \varepsilon_{\pm}(q)|\partial_q|\varepsilon_{\pm}(q)\rangle$ over the
Brillouin zone, where $|\varepsilon_{\pm}(q)\rangle$ are the spin eigenstates of the Hamiltonian (40).
This yields the so-called Zak phase $\varphi_{\text{Zak},\pm} = \int_{\text{BZ}} dq\, \mathcal{A}_{\pm}(q)$ [123]. If we define
the flatness parameter $\mathfrak{f} = 4\tilde{t}/\varepsilon$, we obtain

$$\varphi_{\text{Zak},\pm} = \int_{\text{BZ}} dq\, \frac{1 + \mathfrak{f}^{-1}\sin q}{2(1 + \mathfrak{f}^{-2} + 2\mathfrak{f}^{-1}\sin q)} = \pi\theta(\mathfrak{f} - 1), \qquad (42)$$

i.e. the Zak phase takes the value $\varphi_{\text{Zak},\pm} = \pi$ for the upper and lower band in
the topological phase and $\varphi_{\text{Zak},\pm} = 0$ in the non-topological region. We discuss
properties of the former in the following section.
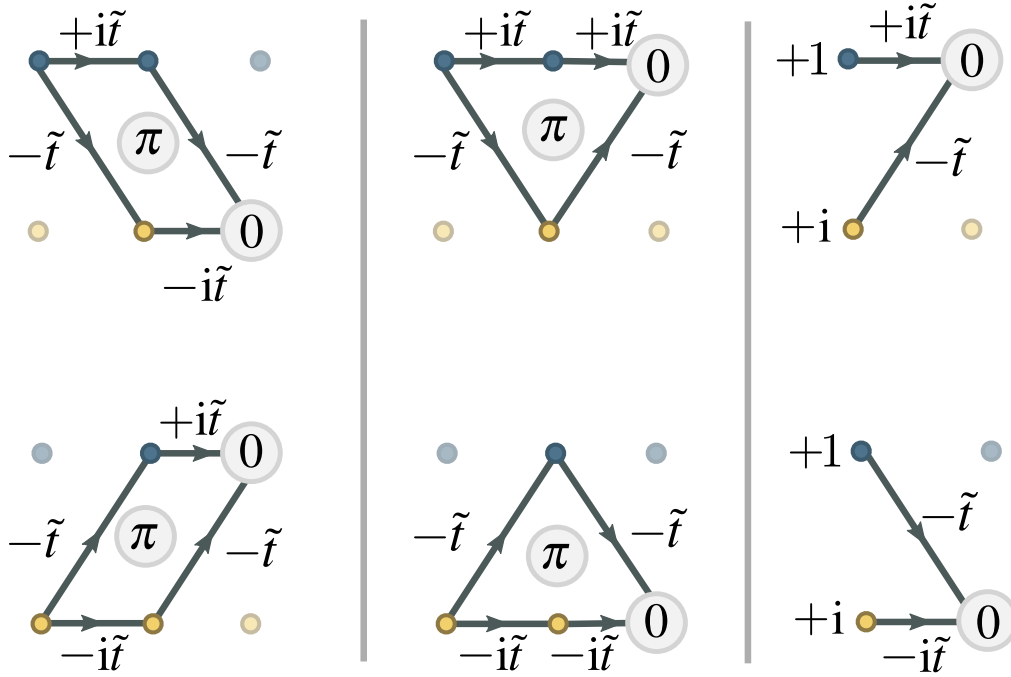
Figure 6: **Interference patterns in the Creutz ladder.** The blue and yellow dots indicate sites on the upper and on the lower leg, respectively. The arrows correspond to hopping processes on the lattice. Left and middle: Due to the π-flux encountered for any double-hopping not returning to the original site, destructive interference occurs constraining the dynamics of a particle to a site and its nearest neighbors. Right: By choosing superpositions with the appropriate phase difference, negative interference can be obtained for single-hopping processes. This is used for the definitions of Aharonov-Bohm cages in Eqs. (43) and (45).
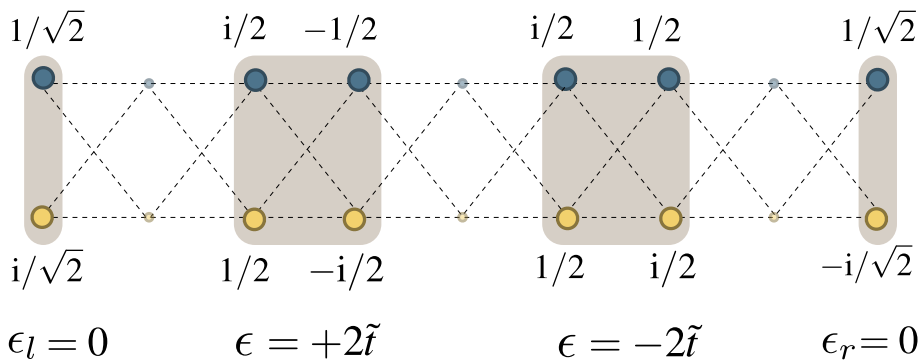
Figure 7: **Eigenstates of the balanced Creutz ladder.** The bulk solutions (43) to the Creutz ladder without imbalance ($\Delta\varepsilon = 0$) can be expressed in terms of localized Aharonov-Bohm cages. Destructive interference prevents these states from delocalizing (compare Fig. 6). Edge states of the systems (45) involve single physical sites only and have zero energy.

3.2.1.1 *Topological insulator phase*

In the particular case of perfect balance ($\Delta\varepsilon = 0$), we observe that $\partial_k \epsilon_\pm(k) = 0$: The model displays completely flat bands in the dispersion. As a consequence, the particles' velocity is zero and they cannot propagate along the lattice. Microscopically, the effect can be understood through the particular artificial gauge field (see also Sec. 2.5). The phase acquisition of a particle after two hoppings leads to a destructive interference of the particle's wave function at next-to-nearest neighbor sites. This is shown in Fig. 6. The resulting flat-band insulator is neither a band insulator nor a Mott insulator. In fact, it shares aspects of both: As for a band-insulator, the insulating property is not due to correlations; however, like in a Mott-insulator, the particles are localized.

While a particle placed on some site (j, ℓ) would start to oscillate between the original site and the neighboring sites, we can find a basis of the Hamiltonian in terms of Aharonov-Bohm cages (compare Sec. 2.5) for which any movement is suppressed:

$$
\begin{aligned}
|{+}2\tilde{t}\rangle_j &= w^\dagger_{j,+} |0\rangle\,, \quad w^\dagger_{j,+} = \frac{1}{2}\left(ic^\dagger_{j,u} + c^\dagger_{j,d} - c^\dagger_{j+1,u} - ic^\dagger_{j+1,d}\right),\\
|{-}2\tilde{t}\rangle_j &= w^\dagger_{j,-} |0\rangle\,, \quad w^\dagger_{j,-} = \frac{1}{2}\left(ic^\dagger_{j,u} + c^\dagger_{j,d} + c^\dagger_{j+1,u} + ic^\dagger_{j+1,d}\right).
\end{aligned}
\tag{43}
$$

The eigenstates are superpositions of particles living on the four possible sites of neighboring rungs of the ladder (see Fig. 7).

The flat-band Hamiltonian can be equivalently described in this *plaquette basis* as

$$
H_{\text{FB}} = \sum_j \sum_{\alpha=\pm} \epsilon_\alpha w^\dagger_{j,\alpha} w_{j,\alpha},
\tag{44}
$$

where every plaquette has the same energy $\epsilon_\pm = \pm 2\tilde{t}$. For periodic boundary conditions, we find $2N$ of these plaquette states. For open boundary conditions, however, we can only form $2(N-1)$ "bulk" states, and we require $2N - (2N - 2) = 2$ more states to fully determine a basis. These missing states reside on the left- and right-most sites,

$$
\begin{aligned}
|0\rangle_{\text{L}} &= l^\dagger |0\rangle\,, \quad l^\dagger = \frac{1}{\sqrt{2}}\left(c^\dagger_{1,u} + ic^\dagger_{1,d}\right),\\
|0\rangle_{\text{R}} &= r^\dagger |0\rangle\,, \quad r^\dagger = \frac{1}{\sqrt{2}}\left(c^\dagger_{N,u} - ic^\dagger_{N,d}\right),
\end{aligned}
\tag{45}
$$

and yield an additional contribution $\sum_{\eta=l,r} \epsilon_\eta \eta^\dagger \eta$ to the above Hamiltonian with $\epsilon_l = \epsilon_r = 0$: a pair of zero-energy topological edge states (see again Fig. 7).

Turning on the imbalance $\Delta\varepsilon$ then leads to an effective hopping between these plaquettes

$$
\begin{aligned}
V_{\text{imb}} = \frac{\Delta\varepsilon}{4} \sum_{j=2}^{N-1} &\left(w^\dagger_{j-1,+} - w^\dagger_{j-1,-}\right)\left(w_{j,+} + w_{j,-}\right)\\
&+ \frac{\Delta\varepsilon}{4} \sum_{\alpha=\pm} \sqrt{2}\left(-l^\dagger w_{1,\alpha} - i\alpha r^\dagger w_{N-1,\alpha}\right) + \text{h.c.},
\end{aligned}
\tag{46}
$$

and results in a deforming of the flat energy bands up to $\Delta\varepsilon = 4\tilde{t}$, where the gap closes and reopens (see Fig. 5a). An important observation in this context is that the edge modes maintain zero energy throughout the TI-region (if we restrict ourselves to the thermodynamic limit, $L \to \infty$). While no longer exclusively localized on sites 1 and L, the zero-energy modes anyway preserve their edge character as the probability of finding the modes decays exponentially with distance from the boundary, i.e. $p_j \propto e^{-j/\xi(\Delta\varepsilon,\tilde{t})}$ with some characteristic length $\xi(\Delta\varepsilon, \tilde{t})$. As a consequence, in the thermodynamic limit, the two modes reside in distinct regions of the chain. For $\Delta\varepsilon/\tilde{t} \to 4$, the characteristic length ξ increases and diverges at the critical point, "merging" the two edge modes and destroying the topological character.

3.2.1.2   *Orbital paramagnetic phase*

As the leg imbalance $\Delta\varepsilon$ is increased above the critical point, the system changes into an orbital paramagnet, in which all the particles tend to occupy the lower leg. In the limit of $\Delta\varepsilon \gg \tilde{t}$, writing the Hamiltonian in real-space spinor notation yields

$$H_{\pi\text{C}} = \sum_{q\in\text{BZ}} \Psi_j^\dagger (\boldsymbol{B}_i \cdot \boldsymbol{\sigma}) \Psi_j \tag{47}$$

with $\boldsymbol{B}_j \approx (0, 0, \Delta\varepsilon)$, demonstrating the paramagnetic property. To make the classification even more evident, we explore an analogy of the imbalanced Creutz ladder to a pair of Ising chains in the next section.

3.2.1.3   *Ising chain correspondence*

A first similarity of the Creutz ladder model to the Ising model is its duality under the transformation

$$\Psi_j = (c_{j,\text{u}}, c_{j,\text{d}})^\text{t} \to W_j = e^{-i\frac{\pi}{4}\sigma_j^z} (w_{j,+}, w_{j,-})^\text{t}. \tag{48}$$

Upon exchange $\Delta\varepsilon/4 \leftrightarrow \tilde{t}$, the original model $H_{\pi\text{C}}$ in Eq. (37) takes the form of the latter model (44), i.e.

$$H_{\pi\text{C}}(\tilde{t}, \Delta\varepsilon) \to \frac{\Delta\varepsilon}{4\tilde{t}} H_{\pi\text{C}}\left(\tilde{t}, \frac{16\tilde{t}^2}{\Delta\varepsilon}\right). \tag{49}$$

The self-similar point $\Delta\varepsilon = (4\tilde{t})^2/\Delta\varepsilon$ corresponds to the earlier discussed critical point $\Delta\varepsilon/\tilde{t} = 4$. Due to this correspondence, we expect the same results for the observables $\langle c_j^\dagger \sigma_3 c_j \rangle$ at some point in phase space $(\tilde{t}, \Delta\varepsilon)$ and for $\langle w_j^\dagger \sigma_3 w_j \rangle = \langle c_j^\dagger (-\sigma_1 - i\sigma_3) c_{j+1} + \text{h.c.} \rangle$ in $(\Delta\varepsilon/4, 4\tilde{t})$. This means that the two terms in the original Hamiltonian can be treated on the same footing. The observation is reminiscent of the self-duality of the quantum Ising model [124] and motivates a closer look. Indeed, we find that the canonical transformation

$$\begin{aligned} r_{j,1} &= \frac{i^j}{\sqrt{2}} \left(ic_{j,\text{u}} + (-1)^j c_{j,\text{d}}^\dagger\right), \\ r_{j,2} &= \frac{i^j}{\sqrt{2}} \left(c_{j,\text{u}} + i(-1)^j c_{j,\text{d}}^\dagger\right) \end{aligned} \tag{50}$$

converts the description to

$$
\begin{aligned}
H_{\pi C} = &- \tilde{t} \sum_j \sum_{n=1,2} \left(r_{j,n}^\dagger r_{j+1,n} + r_{j,n}^\dagger r_{j+1,n}^\dagger + \text{h.c.} \right) \\
&+ \frac{\Delta \varepsilon}{4} \sum_j \sum_{n=1,2} \left(2 r_{j,n}^\dagger r_{j,n} - 1 \right).
\end{aligned}
\tag{51}
$$

While the correctness of the transformation (50) can be easily checked *a posteriori*, the transformation rules are not evident *a priori*. A step-by-step derivation (using Majorana fermions) can therefore be found in App. C.1.

In the new notation, we can identify two fully independent subsystems, which do not display particle number conservation. Both terms can be identified as Ising models [125]. Under the Jordan-Wigner transformation

$$
r_{j,n}^\dagger = \prod_{l<j} \left(-\sigma_{l,n}^z \right) \sigma_{j,n}^+,
\tag{52}
$$

the Hamiltonian takes the form

$$
H_{\pi C} = \sum_j \sum_{n=1,2} \left(-\tilde{t} \sigma_{j,n}^x \sigma_{j+1,n}^x + \frac{\Delta \varepsilon}{4} \sigma_{j,n}^z \right).
\tag{53}
$$

As the Creutz ladder model and the two-copy Ising model are equivalent, they are described by the same mathematics. Nonetheless, it is instructive to compare some physical features from the two very different perspectives. If we take into account all possible fillings for our model, we can make the following observations for systems with open boundary conditions:

- In the thermodynamic limit, the ground state in the TI-phase of the Creutz ladder model is quadruple-degenerate. The ferromagnetic ground state of each Ising model is doubly degenerate (the two possible polarizations), yielding a total degeneracy of four, in agreement with the above.

- In the same limit, the ground state in the orbital paramagnetic phase of the Creutz ladder is unique. This is in agreement with the disordered phase in the Ising model, where both copies have a unique ground state.

- If the Creutz ladder with open boundary conditions becomes finite, the ground state loses its degeneracy. The localized and exponentially decaying left and right edge modes can then couple and obtain an energy (exponentially small in the system length). The earlier quadruple degeneracy resolves to a 1-2-1-degeneracy. When interpreting a finite Ising model as a Kitaev-Majorana chain (compare Sec. 2.9), likewise, the edge Majoranas couple and lead to a splitting between the formerly degenerate even and odd-parity state. As this happens in two copies of the model, we observe the said degeneracy of 1, 2 and 1 for the lowest states.

It should be stressed that while the two edge modes in the Creutz ladder correspond to the absence/presence of a fermion on the left or right boundary, the edges in the Kitaev model are single Majoranas [126], and populating the (single)

edge mode in this model means recombining the two (possibly far away) edges to form a single fermion. This is a highly non-local process. The presence of the second Ising chain, however, permits a recombination of the two left-boundary modes or of the two right-boundary modes, respectively, to build a localized fermion. Differently stated: In the thermodynamic limit, the left- and right-edge modes of the Creutz ladder do not communicate. They can be populated independently and both have zero energy. Two instances of the Ising model are therefore necessary to construct these localized modes.

Having discussed the two models from an energy perspective, let us now identify equivalent observables. The particle number $\sum_{j,\ell} n_{j,\ell}$ of the Creutz ladder translates into

$$\sum_{j,\ell} n_{j,\ell} = \sum_{j,\ell} c^\dagger_{j,\ell} c_{j,\ell} = \sum_i (i(r^\dagger_{j,1} r_{ij,2} - r^\dagger_{j,2} r_{j,1}) + 1). \tag{54}$$

Note that this term resembles the one found in current descriptions (compare Sec. 2.6).

In particular, in the limiting case $\Delta\varepsilon/\tilde{t} \gg 4$, both the Creutz ladder and the Ising model are particle number-conserving. Depending on the prefactor of the imbalance, this corresponds then to completely filled or completely vacant models. In the opposite limit of total balance ($\Delta\varepsilon = 0$), we only know that $\sum_j \langle r^\dagger_{j,1} r_{j,1} + r^\dagger_{j,2} r_{j,2} \rangle = N$, but all possible particle distributions between the two legs contribute equally to the state.

The imbalance of the Creutz ladder (with $\Delta n_j \equiv c^\dagger_{j,\mathrm{u}} c_{j,\mathrm{u}} - c^\dagger_{j,\mathrm{d}} c_{j,\mathrm{d}}$) translates to

$$\sum_j \Delta n_j = \sum_j r^\dagger_{j,1} r_{j,1} + r^\dagger_{j,2} r_{j,2} - 1 = \frac{1}{2} \sum_{j,n} \sigma^z_{j,n}, \tag{55}$$

i.e. to the sum of the transverse (paramagnetic) magnetizations of the two Ising models.

3.2.2 *Weakly-interacting regime*

We now consider the model with Hubbard-like interactions for the first time. In particular, we take a look at the regime of small interactions $V_\mathrm{v} \ll \tilde{t}, \Delta\varepsilon$ and study how these interactions alter the results of the non-interacting model. To this end, we further explore the analogy of the Creutz ladder to the quantum Ising model made in the section above.

Applying the canonical transformation (50) to the interaction term (39) yields

$$H_{\mathrm{Hubb}} = \frac{V_\mathrm{v}}{2} \sum_j \left[r^\dagger_{j,1} r_{j,1} + r^\dagger_{j,2} r_{j,2} + i r^\dagger_{j,1} r_{j,2} - i r^\dagger_{j,2} r_{j,1} - 2 r^\dagger_{j,1} r_{j,1} r^\dagger_{j,2} r_{j,2} \right]. \tag{56}$$

For half-filling, the relation (54) entails $\langle r^\dagger_{i,1} r_{i,2} - r^\dagger_{i,2} r_{i,1} \rangle = 0$, simplifying the Hamiltonian to

$$H_{\mathrm{Hubb,hf}} = \frac{V_\mathrm{v}}{2} \sum_j \left[r^\dagger_{j,1} r_{j,1} + r^\dagger_{j,2} r_{j,2} - 2 r^\dagger_{j,1} r_{j,1} r^\dagger_{j,2} r_{j,2} \right]. \tag{57}$$

The Jordan-Wigner transformation (52) translates this expression to a ferromagnetic coupling between the two Ising models (53):

$$H_{\text{Hubb,hf}} = \frac{V_{\text{v}}}{4} \sum_j \left[1 - (\sigma_j^z)_1 (\sigma_j^z)_2 \right]. \tag{58}$$

Up to this point, the derivation has been exact: In all parameter regimes, the imbalanced Creutz-Hubbard model can be understood as two coupled quantum Ising chains. In the following, we will study the transverse ground state magnetization of the individual Ising chains for different model parameters, $m(\Delta\varepsilon, V_{\text{v}}, \tilde{t}) = \langle \sigma_{j,n}^z \rangle$, in a mean-field approach. We therefore first note the analytical result for a simple Ising chain [127]:

$$M(\alpha) = - \begin{cases} 2\frac{1-\alpha^2}{\pi\alpha} \left(\Pi(\alpha^2, \alpha) - K(\alpha) \right) & \text{for} \quad \alpha < 1 \\ 2\frac{\alpha^2-1}{\pi\alpha^2} \Pi(1/\alpha^2, 1/\alpha) & \text{for} \quad \alpha > 1. \end{cases} \tag{59}$$

Here, we define $M(\alpha) \equiv m(\Delta\varepsilon, V_{\text{v}} = 0, \tilde{t})$ and $\alpha = \Delta\varepsilon/4\tilde{t}$. Π and K are full elliptical integrals of the first and of the third kind, respectively.

For weak interactions, $V_{\text{v}} \ll \tilde{t}$, we can treat the mutual effect of the chains on each other through a mean-field decoupling which renormalizes the original transverse magnetization term:

$$H_{\pi\text{CH}} \approx \sum_{j,n} \left(-\tilde{t}\sigma_{j,n}^x \sigma_{j+1,n}^x + \frac{\Delta\varepsilon - V_{\text{v}} m_{\bar{n}}(\Delta\varepsilon, V_{\text{v}}, \tilde{t})}{4} \sigma_{j,n}^z \right). \tag{60}$$

In the effective field of the respective other subsystem, the critical point is therefore shifted. Using the solution for the magnetization of the non-interacting system (59) and the symmetry between the two chains, we can determine a stable solution for the self-consistent mean-field approach by iteratively solving

$$m_n(\Delta\varepsilon, V_{\text{v}}, \tilde{t}) = M\left(\frac{\Delta\varepsilon - V_{\text{v}} m_{\bar{n}}(\Delta\varepsilon, V_{\text{v}}, \tilde{t})}{4\tilde{t}} \right). \tag{61}$$

Fig. 8 compares the numerically found magnetizations for different interaction strengths with this self-consistent mean-field prediction: The approximation describes the magnetization very accurately for considerably large interactions ($V_{\text{v}} \approx \tilde{t}$).

We can even go beyond the numerical approach, and solve the self-consistency equation (61) for small V_{v}. We therefore assume for the critical magnetization $M_{\text{c}} = \frac{2}{\pi} + \mathcal{O}(V_{\text{v}})$ and obtain to lowest order in V_{v}:

$$\frac{\Delta\varepsilon}{\tilde{t}} = 4 - \frac{2}{\pi}\frac{V_{\text{v}}}{\tilde{t}} + \mathcal{O}\left(\frac{V_{\text{v}}^2}{\tilde{t}^2} \right). \tag{62}$$

The equation predicts a critical line separating the topological and the non-topological phase in the weak-coupling limit. The red dashed line in Fig. 8 shows its agreement with the numerical results (presented in Sec. 3.3).
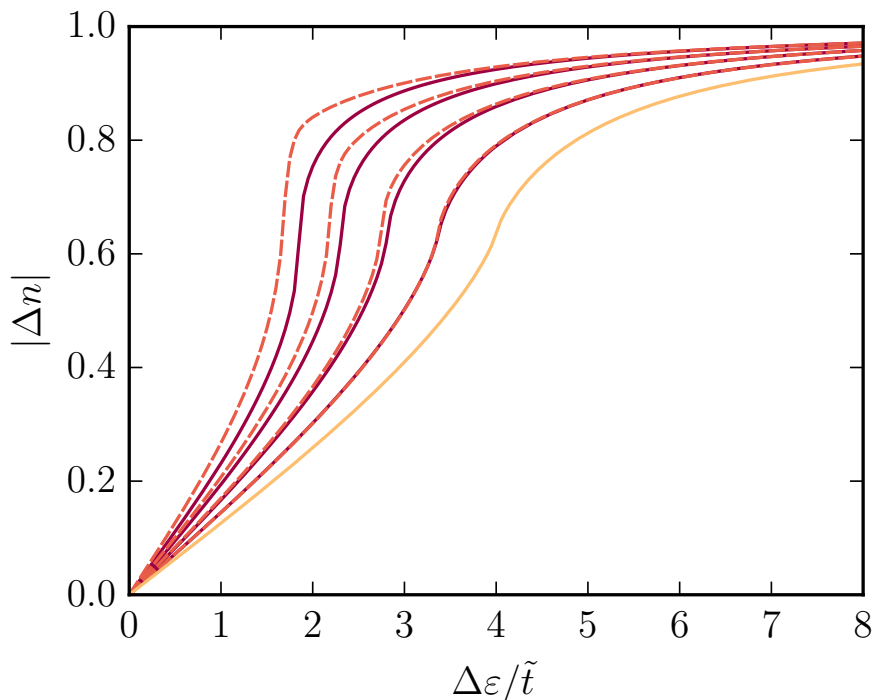
Figure 8: **Exact density imbalances and mean-field magnetizations.** For different interaction strengths (from bottom to top: $V_{\mathrm{v}}/\tilde{t} = 1, 2, 3, 4$), the continuous lines (purple) show the ground state imbalance (or equivalently, the mean-field magnetization) $\langle \Delta n_j \rangle = \langle \sigma_j^z \rangle$ as obtained through MPS calculations on a lattice with $N = 256$ sites. The dashed lines (red) are the analytical results from a self-consistent mean-field approach. The approximative result remains admissibly precise for rather large interactions. In orange, for comparison the exact analytical result for the density imbalance (magnetization) at $V_{\mathrm{v}} = 0$.

3.2.3 *Strongly-interacting regime*

In the limit $V_{\mathrm{v}} \gg \tilde{t}$, the ground state of the system is described by a Mott insulator phase in which double-occupancy of a rung is fully suppressed due to the strong on-site repulsion. The effective model can then be understood in analogy to the Heisenberg model which emerges in the strong-coupling limit of the Hubbard model. The ground state is obtained through a second-order process during which a rung of the ladder is occupied by two fermions. Introducing

$$T_j^y = \frac{1}{2}\left(-ic_{j,\mathrm{u}}^\dagger c_{j,\mathrm{d}} + ic_{j,\mathrm{d}}^\dagger c_{j,\mathrm{u}}\right), \ T_i^z = \frac{1}{2}\left(c_{j,\mathrm{u}}^\dagger c_{j,\mathrm{u}} - c_{j,\mathrm{d}}^\dagger c_{j,\mathrm{d}}\right), \quad (63)$$

and using second-order degenerate perturbation theory [128], the effective model can be written as

$$\frac{\mathcal{P}_{\mathrm{r}}^\dagger H_{\pi\mathrm{CH}}^2 \mathcal{P}_{\mathrm{r}}}{E_1 - E_0} = \tfrac{1}{4}JN + J\sum_j T_j^y T_{j+1}^y + \Delta\varepsilon \sum_j T_j^z. \quad (64)$$

Here, $E_1 - E_0$ is the energy difference between the ground state and the first excited manifold, $J = -8\tilde{t}^2/V_{\mathrm{v}}$, and the Gutzwiller operator $\mathcal{P}_{\mathrm{r}} = \Pi_i(1 - n_{i,u}n_{i,d})$

projects the kinetic part of the Hamiltonian onto the ground state manifold of the Mott insulator. This orbital quantum Ising model predicts the existence of two phases: for large imbalances a disordered *orbital paramagnetic phase*, which we already encountered in Sec. 3.2.1, and for small imbalances a long-range *orbital ferromagnetic phase*. In addition, we expect a phase transition to occur for

$$\frac{\Delta \varepsilon}{\tilde{t}} = \frac{4\tilde{t}}{V_{\mathrm{v}}}, \tag{65}$$

as indicated by the yellow dashed line in Fig. 4.

For strong interactions, the effective Ising model (64) predicts two phases: a symmetry-broken phase with long-range order [129]

$$\lim_{r \to \infty} \langle T_j^y T_{j+r}^y \rangle = \frac{1}{4} \left(1 - h^2 \right)^{\frac{1}{4}}, \tag{66}$$

where $h = 2\Delta\varepsilon/|J| < 1$, and a disordered phase ($h > 1$) with $\langle T_j^y T_{j+r}^y \rangle = 0$. For the non-interacting model, we find

$$\langle T_j^y T_{j+r}^y \rangle = 0, \tag{67}$$

i.e. absence of long-range order. This demonstrates that the topological phase for small interactions and the orbital ferromagnetic phase for strong interactions cannot be connected adiabatically. Therefore we expect a interaction-induced topological quantum phase transition for intermediate interactions. This is studied in the next section.

3.2.4 *Intermediate regime*

In the regime of intermediate interactions, the earlier approaches do not work as neither the interaction term nor the hopping can be treated in a perturbative fashion. In the following, we consider the model without imbalance and derive an effective description that allows us to identify the critical point between the topological and the orbital ferromagnetic phase, based on some simple assumptions.

As a first step, we rewrite the interaction Hamiltonian (39) in terms of the Aharonov-Bohm cages (43):

$$\begin{aligned} V_{\mathrm{Hubb}} = \sum_{j=2}^{N-1} t_{\mathrm{imb}} \left(w_{j-1,+}^\dagger - w_{j-1,-}^\dagger \right) \left(w_{j,+} + w_{j,-} \right) \\ + \sum_{\alpha=\pm} \sqrt{2} t_{\mathrm{imb}} \left(-l^\dagger w_{1,\alpha} - i\alpha r^\dagger w_{N-1,\alpha} \right) + \mathrm{h.c.} \end{aligned} \tag{68}$$

The notation is motivated by the fact that the we want to understand the influence of interactions on the eigenstates of the balanced Creutz ladder. We find that three distinct physical processes contribute in the plaquette picture,

$$V_{\mathrm{Hubb}} = V_{\mathrm{nn}} + V_{\mathrm{pt}} + V_{\mathrm{dt}}, \tag{69}$$

which we will analyze individually in the following.

The first contribution is a *nearest-neighbor interaction*

$$V_{\text{nn}} = \frac{V_{\text{v}}}{2} \sum_{\alpha=\pm} (n_l n_{1,\alpha} + n_r n_{N-1,\alpha}) + \frac{V_{\text{v}}}{4} \sum_{j=2}^{N-1} \sum_{\alpha,\beta=\pm} n_{j-1,\alpha} n_{j,\beta}, \tag{70}$$

where $n_{j,\alpha} = w_{j,\alpha}^{\dagger} w_{j,\alpha}$ with $\alpha \in \{+, -\}$ are the number operators in the plaquette basis, and $n_{\eta} = \eta^{\dagger} \eta$ with $\eta \in \{l, r\}$ are the corresponding edge terms.

The effective repulsion between the fermions can be understood in a new ladder scheme in which the two legs are given by the two flat energy bands with positive/negative energy. In addition, we find a *pair-tunneling* term

$$V_{\text{pt}} = \tilde{J} \sum_{j=2}^{N-1} \left(w_{j-1,+}^{\dagger} w_{j-1,-} \left(w_{j,-}^{\dagger} w_{j,+} + w_{j,+}^{\dagger} w_{j,-} \right) \right) + \text{h.c.} \tag{71}$$

where $\tilde{J} = -V_{\text{v}}/4$. This term corresponds to an anti-correlated pair tunneling along the rungs of neighboring sites. Finally, there is a *density-assisted tunneling* term

$$V_{\text{dt}} = T_{\text{d}} \sum_{j=2}^{N-1} (n_{j-1,+} + n_{j-1,-} - n_{j+1,+} - n_{j+1,-}) \, w_{j,+}^{\dagger} w_{j,-}$$
$$+ 2T_{\text{d}} \left(n_l w_{1,+}^{\dagger} w_{1,-} - n_r w_{N-1,+}^{\dagger} w_{N-1,-} \right) + \text{h.c.} \tag{72}$$

with $T_{\text{d}} = V_{\text{v}}/4$. The first term describes an on-site tunneling under the condition that there is a particle number imbalance between the nearest-neighbor sites. Apart from this bulk term, there is also a contribution, which couples the hopping on the outmost plaquettes to the edge modes.

Let us discuss the effect of these different contributions: While the correlated hopping terms in Eqs. (71) and (72) modify the distribution of particles on the rungs of the ladder, they will not change the distribution between neighboring sites as all terms conserve the on-site occupation. Therefore, the nearest-neighbor interaction term in Eq. (70) will only contribute a constant energy. Following the same argumentation, the bulk contribution of the density-assisted tunneling in Eq. (72) will be negligible due to the homogeneity following from the translational invariance of the bulk. The edge coupling, however, cannot be neglected and will play a role in the explanation of the topological transition.

We can reshuffle the Hamiltonian and write $H_{\pi\text{CH}} = H_{\text{bulk}} + H_{\text{edge}} + H_{\text{b}-\text{e}}$, where we collect the bulk and edge contribution in H_{bulk} and H_{edge}, respectively, and the coupling between edge and bulk in $H_{\text{b}-\text{e}}$. Defining an effective spinor-basis

$$\tilde{T}_j^x = \frac{1}{2} \left(w_{j,+}^{\dagger} w_{j,-} + w_{j,-}^{\dagger} w_{j,+} \right), \;\; \tilde{T}_i^z = \frac{1}{2} \left(w_{j,+}^{\dagger} w_{j,+} - w_{j,-}^{\dagger} w_{j,-} \right) \tag{73}$$

allows us to identify the bulk part of the Hamiltonian as yet another effective quantum Ising model

$$H_{\text{bulk}} = \frac{V_{\text{v}}}{4} N + \sum_{j=1}^{N-1} 4\tilde{t} \tilde{T}_j^z + \sum_{j=2}^{N-1} 4\tilde{J} \tilde{T}_{j-1}^x \tilde{T}_j^x. \tag{74}$$

Conceptually, this mapping is similar to the one performed in the strong coupling limit (see Eq. (63)). We can go backwards and re-express the spin operators in terms of a new set of spinless fermionic operators f_i and $f_i^\dagger$:

$$\tilde{T}_j^z = f_j^\dagger f_j - \tfrac{1}{2}, \quad \tilde{T}_j^x = \tfrac{1}{2} f_j^\dagger e^{i\pi \sum_{l<j} f_l^\dagger f_l} + \text{h.c.} \tag{75}$$

For periodic boundary conditions ($f_N = f_1$), we then obtain energy bands for single-particle excitations

$$\tilde{\epsilon}_\pm(q) = \pm \tilde{\epsilon}(q) = \pm 2|\tilde{J}|\sqrt{1 + \tilde{f}^2 - 2\tilde{f}\cos q} \tag{76}$$

with $\tilde{f} = 8\tilde{t}/V_\mathrm{v}$. It is easy to see that $\tilde{\epsilon}_\pm(q = 0) = 0$ for $\tilde{f} = 1$ identifies the critical point as $V_\mathrm{v}/\tilde{t} = 8$.

3.3   PHASE DIAGRAM AND NUMERICAL STUDY

In the previous section, we studied phases and transitions in the model with analytical means. To complete the phase diagram evoked in Fig. 4, we now present results of a numerical study with matrix product states (MPS). This allows us to access also the strongly correlated regimes which are not accessible to an analytical or perturbative investigation. Details of the numerical technique can be found in App. A.4.

3.3.1   *TI-oPM transition*

As shown in Sec. 3.2.2, the mapping of the Creutz ladder to a pair of quantum Ising models allows us to predict a critical line separating the topological insulator from the orbital paramagnetic phase for weak interactions (see Eq. (62)). We can use the density imbalance or equivalently the transverse magnetization of the corresponding Ising models as an indicator for the phase transition. In particular, we determine the critical points for cuts through the parameter space with fixed $V_\mathrm{v}/\tilde{t}$ by studying the divergence of the susceptibility of the magnetization $\chi_{\Delta n} = \partial \langle \Delta n \rangle / \partial(\Delta\varepsilon/\tilde{t})$ in Fig. 9.

Alternatively, we can study the behavior of the degeneracy of the ground state for different fillings. To be precise, we define the one- and two-particle energy gaps as

$$E_\Delta = \lim_{N\to\infty} \tfrac{1}{2} \left[E(N+2) + E(N-2) - 2E(N) \right], \tag{77}$$

$$E_\delta = \lim_{N\to\infty} \left[E(N+1) + E(N-1) - 2E(N) \right], \tag{78}$$

where $E(x)$ is the ground state energy of the system with x particles. We observe that a single particle which is added to (subtracted from) the half-filled model will occupy (evacuate) a zero-energy edge mode in the topological phase. In the non-topological phase, on the other hand, a particle added to the system will occupy a mode in the upper energy band. Lifting it therefore costs a non-zero energy $E(N+1) - E(N)$. This is reflected by the behavior of E_δ. The energy gap E_Δ, on the contrary, is non-zero in any gapped phase, as in both the topological

(a)

(b)
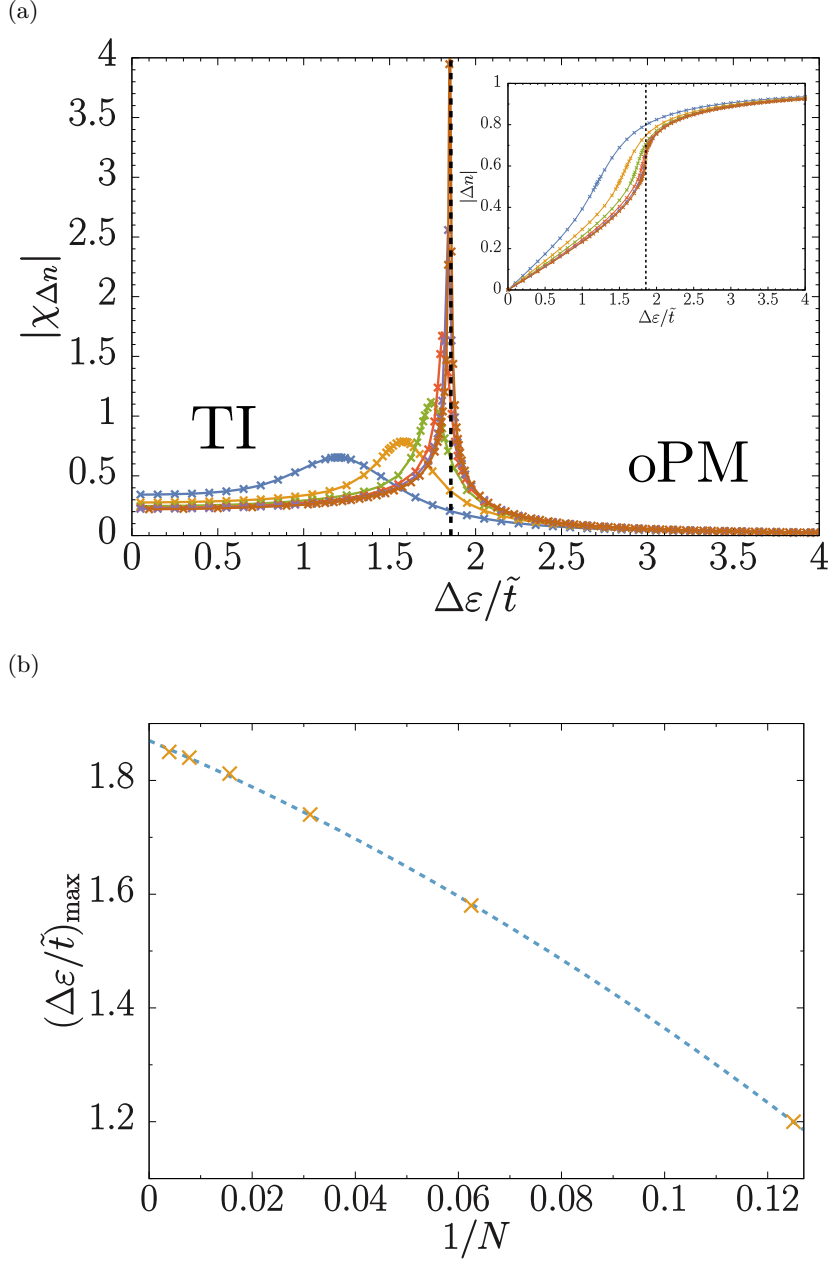
Figure 9: **Paramagnetic susceptibility along the TI-oPM transition.** We study the divergence of the paramagnetic susceptibility $\chi_{\Delta n}$ as an indicator of the phase transition. (a) The susceptibility is shown for $V_{\mathrm{v}}/\tilde{t} = 4$ in finite chains of length $N = 8$ (blue), $N = 16$ (yellow), $N = 32$ (green), $N = 64$ (red), $N = 128$ (violet) and $N = 256$ (brown). The inset presents the underlying measured paramagnetic magnetization $|\Delta n|$. (b) Finite-size scaling of the susceptibility peak parameters (yellow dots) to identify the critical point in the thermodynamic limit. The blue dashed line is a fit of the form $\Delta\varepsilon_{\mathrm{c}}(N) = \Delta\varepsilon_{\mathrm{c}}(1 + aN^{-1} + bN^{-2})$, yielding $\Delta\varepsilon = 1.857$.
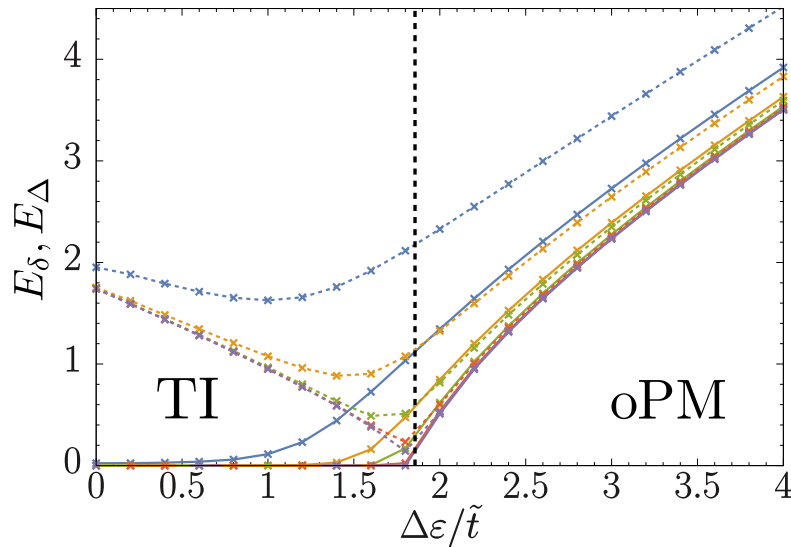
Figure 10: **Energy gaps along the TI-oPM transition.** For finite chains, we determine the single-particle gap E_δ (dashed lines) and the two-particle gap E_Δ (continued lines). E_δ converges to zero in the topological phase due to the presence of a zero-energy edge mode, and to a non-zero value in the paramagnetic phase. E_Δ is non-zero in the two phases; its gap-closing indicates the critical point. Blue: $N = 8$, yellow: $N = 16$, green: $N = 32$, red: $N = 64$, violet: $N = 128$.

and the non-topological system, at least one of the particles has to overcome the energy gap. At the critical point, the gap closes. We can use these definitions to identify a conventional insulator by $E_\Delta = E_\delta = 0$ and the topological insulator by $E_\Delta \neq E_\delta = 0$. Indeed, Fig. 10 shows that the predicted behavior is observed.

The two approaches yield the critical points indicated by yellow stars in Fig. 4. We observe that the mean-field approach (62) predicts the phase boundary well for small interaction strength. Towards larger interactions, the actual critical line deviates from the linear prediction towards larger imbalances.

3.3.2 *oFM-oPM transition*

For the transition between the orbital ferromagnetic and the paramagnetic phase, we have developed an effective quantum Ising model description in Sec. 3.2.3 predicting a critical line $\frac{\Delta\varepsilon}{\tilde{t}} = \frac{4\tilde{t}}{V_{\mathrm{v}}}$. To test this prediction, we calculate observables of the effective Ising model, namely the paramagnetic magnetization $\langle T_j^z \rangle$ and the ferromagnetic magnetization $\langle T_j^y \rangle$ (63). As the determination of the latter can suffer from incomplete symmetry breaking (superpositions of the two possible symmetry-broken states, we instead measure the zero-momentum orbital magnetic structure factor [130]

$$S_{T_y T_y}(k) = \frac{1}{N^2} \sum_{l,j} \mathrm{e}^{ik(l-j)} \left\langle T_l^y T_j^y \right\rangle. \tag{79}$$

(a)

(b)
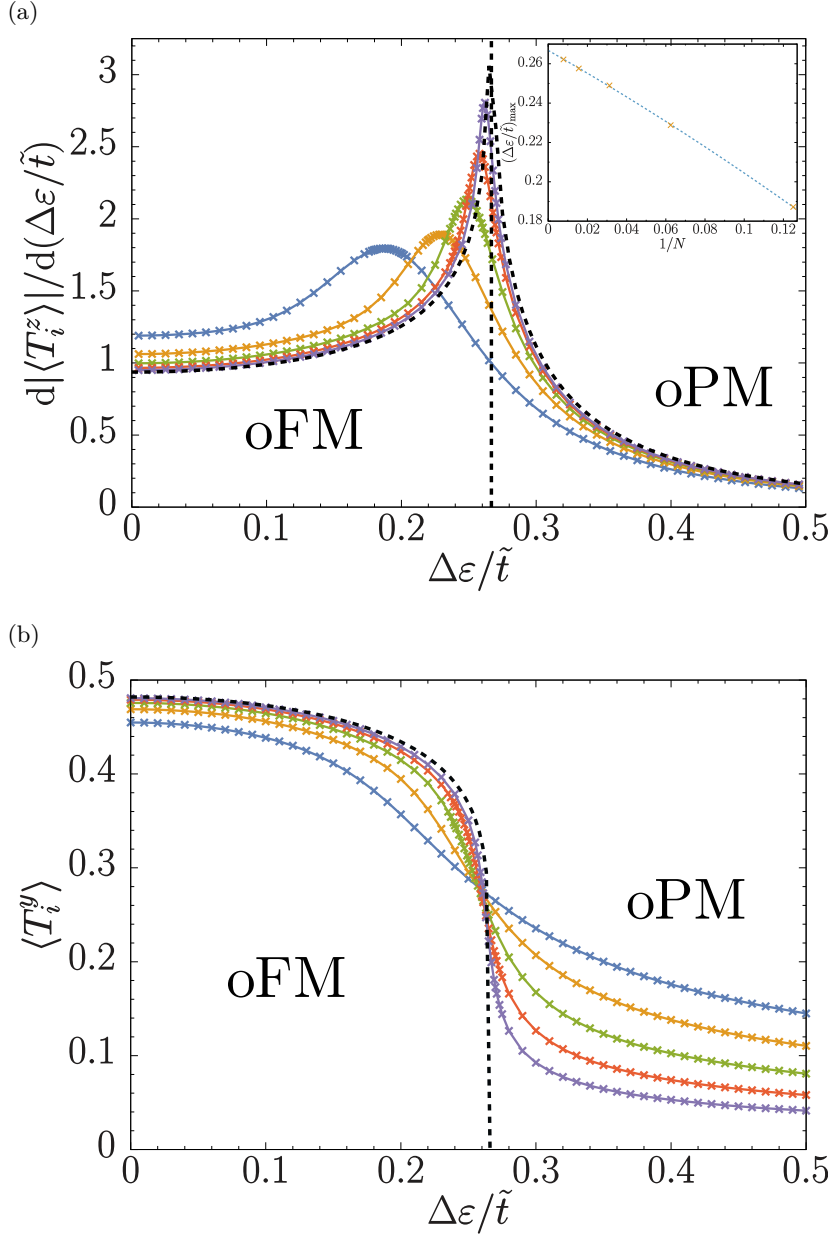
Figure 11: **Paramagnetic susceptibility and ferromagnetic magnetization along the oFM-oPM transition.** (a) Paramagnetic susceptibility for a cut through the phase diagram at $V_{\mathrm{v}} = 16.0$ and different system lengths. The inset shows a fitted finite-size scaling of the susceptibility maxima to identify the critical imbalance: $\Delta\varepsilon_{\mathrm{c}}(N) = \Delta\varepsilon_{\mathrm{c}}(1 + aN^{-1} + bN^{-2})$ and yields $\Delta\varepsilon_{\mathrm{c}}/\tilde{t} = 0.266$. (b) Ferromagnetic magnetization along the same line. Blue: $N = 8$, yellow: $N = 16$, green: $N = 32$, red: $N = 64$, violet: $N = 128$. The dashed black lines show the analytical TD-limit prediction for a quantum Ising model, where we fixed the critical point at $\Delta\varepsilon_{\mathrm{c}}/\tilde{t}$ and the maximal magnetization $\langle T_i^y \rangle_{\mathrm{max}} = 0.48$. For comparison, the effective Ising model (66) predicted $\Delta\varepsilon_{\mathrm{c}}/\tilde{t} = 0.25$ and $\langle T_i^y \rangle_{\mathrm{max}} = 0.5$.
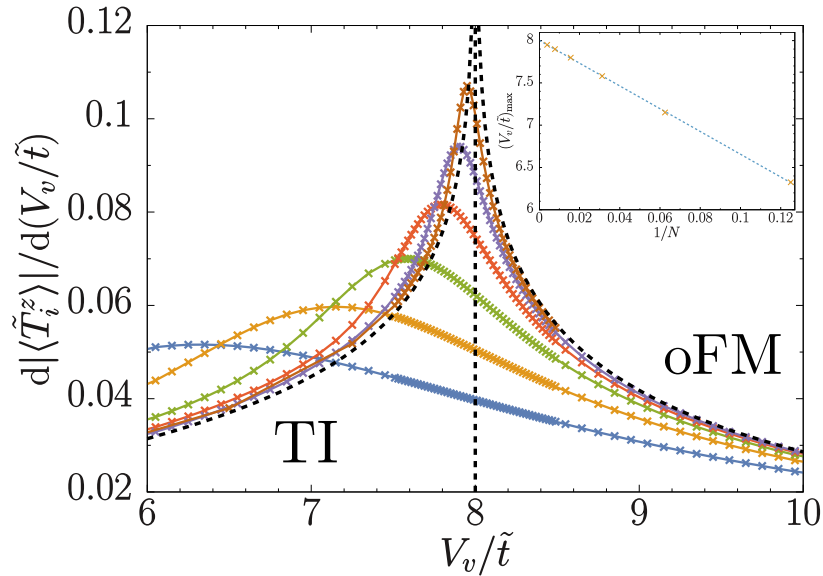
Figure 12: **Susceptibility of the paramagnetic magnetization along the TI-oFM transition.** The measured susceptibility $\partial|\langle\tilde{T}_i^z\rangle|/\partial(V_v/\tilde{t})$ is shown for chains of different length in the balanced Creutz-Hubbard ladder ($\Delta\varepsilon/\tilde{t} = 0$). The inset shows the scaling of the maxima position with system size. An extrapolation of the data using $V_{v,c,\mathrm{num}}(N) = V_{v,c,\mathrm{num}}(1 + aN^{-1})$ yields $(V_v/\tilde{t})_{c,\mathrm{num}} = 8.003$. This agrees well with the theoretical TD-limit result of a quantum Ising model $(V_v/\tilde{t})_{c,\mathrm{num}} = 8$ (black dashed line in main plot). Blue: $N = 8$, yellow: $N = 16$, green: $N = 32$, red: $N = 64$, violet: $N = 128$, brown: $N = 256$.

We find that the two quantities show the expected behavior of a quantum Ising transition, with a renormalization of the critical point and the maximal ferromagnetic magnetization as the only differences (see Fig. 11). The prediction of the effective model and the numerical results (yellow stars in Fig. 4) agree well even for moderate interaction strengths.

3.3.3 *TI-oFM transition*

For the transition between the topological insulator and the orbital ferromagnet, we determined a critical point at $V_v/\tilde{t} = 8$ in the balanced model ($\Delta\varepsilon/\tilde{t} = 0$) in Sec. 3.2.4. The effective model (74) identifies the paramagnetic susceptibility as a valid indicator of the transition (Fig. 12). Indeed, we observe that the divergence of this quantity continues to indicate a transition in the model with imbalance. This allows us to determine the critical line between topological insulator and orbital paramagnet, shown by stars in Fig. 4.

3.3.4 *Conformal field theories of the critical lines*

An alternative approach to understand the nature of quantum phase transition (in addition to the conventional study of critical scaling of observables)

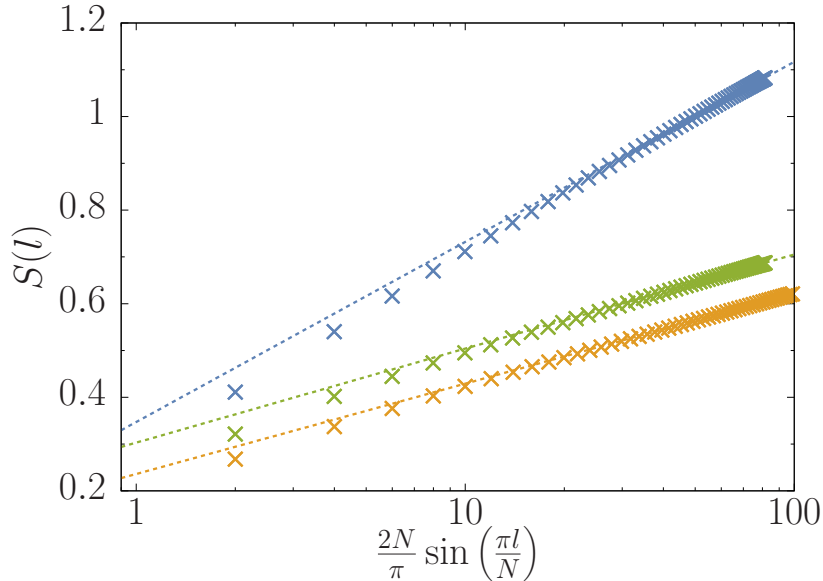Figure 13: **Entanglement entropy scaling and central charges of the various transition lines.** The scaling of the entanglement entropy with respect to size of the bi-partitions is studied for the three transitions in the model: TI-oFM transition (blue, $\Delta\varepsilon/\tilde{t} = 4.0$, $V_\text{v}/\tilde{t} = 1.857$, $N = 128$), oFM-oPM transition (green, $\Delta\varepsilon/\tilde{t} = 16.0$, $V_\text{v}/\tilde{t} = 0.266$, $N = 128$) and TI-oPM transition (yellow, $\Delta\varepsilon/\tilde{t} = 0.0$, $V_\text{v}/\tilde{t} = 8.0$, $N = 128$). The dashed lines present fits in the range $N/4 < l < N/2$ to identify the central charge c in Eq. (80). The numeric results $c_\text{TI−oFM} = 1.003$, $c_\text{oFM−oPM} = 0.524$ and $c_\text{TI−oPM} = 0.503$ agree well with the expected values of 1, 1/2, 1/2.

is the study of quantum-informational features. A quantity of particular interest in this context is the so-called *entanglement entropy* $S(l) = -\text{Tr}\{\rho_l \log \rho_l\}$, which can be extracted in a bi-partition after site l from the density matrix $\rho_l = \text{Tr}_{L-l}\{|\epsilon_\text{gs}\rangle \langle\epsilon_\text{gs}|\}$ where $|\epsilon_\text{gs}\rangle$ is the ground state. For a critical system with open boundary conditions, the entanglement entropy links directly to the central charge c of the conformal field theory underlying the critical phase [17, 18]

$$S(l) = \frac{c}{6}\ln\left(\frac{2L}{\pi}\sin\frac{\pi l}{L}\right) + \text{const.} \tag{80}$$

As the entanglement entropy is a conceptual building block of tensor networks, it is easily accessible in the numerical simulation (compare App. A.1.1).

For the weak-coupling limit, we argued that the phase transition can be described by two instances of the Ising model. Due to the fact that the critical point in a single quantum Ising model has a conformal charge $c = \frac{1}{2}$ [131], we therefore expect a central charge $c = \frac{1}{2} + \frac{1}{2} = 1$ for the transition in the free imbalanced Creutz ladder. An alternative perspective is the following: In the non-interacting limit, the model at the critical point can be understood as a massless Dirac fermion with central charge $c = 1$ (compare also Sec. 4.1.1).

In the strong-coupling limit, we found an effective description through another quantum Ising model, predicting a central charge $c = \frac{1}{2}$. Finally, for the intermediate regime, we understood the relevant physics explaining the transi-

tion between topological insulator and ferromagnetic phase by yet another Ising model, hence again we expect $c = \frac{1}{2}$. An analysis of the entanglement entropy scaling on the critical lines confirms all three predictions (see Fig. 13).

A curious observation is the following: The central charge $c = 1$ reigning at weak interactions seems to split into two massless Majorana fermions $c = 1/2$ at the tri-critical point (compare Fig. 4). The Majorana fermions then control the critical properties of the other two critical lines. As the charge is conserved in the tri-critical point, $c = 1/2 + 1/2 = 1$, the two Majoranas that paired to form the Dirac fermion become unpaired.

3.4   OUTLOOK: EDGE BEHAVIOR AND QUANTUM IMPURITY PICTURES

The understanding of the transition from the topological to the trivial phases can be further advanced by studying how the bulk mediates between the localized edge modes and leads to their disappearance at the critical point. The following argumentation was brought forward by a co-author of Ref. [23], A. Bermudez. We outline it here to complete the picture of the Creutz-Hubbard model.

NON-INTERACTING SYSTEM AND FANO-ANDERSON PHYSICS.   The free part of the Hamiltonian in plaquette notation (44)+(46) can be rewritten as

$$H = H_{\text{bulk}} + H_{\text{edge}} + H_{\text{b}-\text{e}}, \tag{81}$$

where H_{bulk} contains all the bulk terms of type $\omega_{i,\sigma}^{\dagger}\omega_{j,\tau}$, H_{edge} contains the zero-energy edge modes $l^{\dagger}l$ and $r^{\dagger}r$, and $H_{\text{b}-\text{e}}$ contains the coupling terms between bulk and edges of type $l^{\dagger}\omega_{1,\sigma}$, $r^{\dagger}\omega_{N-1,\sigma}$, etc.

Diagonalizing the bulk part of the Hamiltonian leads to the energy bands in Eq. (41) and propagating wave solutions for periodic boundary conditions. These propagating modes can be superposed to form standing-wave solutions $\gamma_{\pm}(q_n)$ of the problem with open boundary conditions (compare App. C.2). In the diagonal basis of the bulk, the bulk-edge coupling reads

$$H_{\text{b}-\text{e}} = \sum_{n,\alpha}(g_{n,\alpha}^{l}l^{\dagger} + g_{n,\alpha}^{r}r^{\dagger})\gamma_{\alpha}(q_n) \ + \text{h.c.} \tag{82}$$

with (here unspecified) coupling constants $g_{n,\alpha}^{l/r}$.

In this notation the system can be interpreted as a type of *Fano-Anderson model* [132, 133]. The original model describes the coupling of a localized state of fixed energy ϵ_c (an impurity) to a continuum of states, i.e. some energy band $\omega_1 \leq \epsilon_k \leq \omega_2$. The solution then depends on whether the energy of the impurity is within the band. However, not the original impurity energy ϵ_c has to be considered, but the (a-priori unknown) energy of the hybridized particle $\tilde{\epsilon}_c$. If $\omega_1 \leq \tilde{\epsilon}_c \leq \omega_2$, the renormalized state lies within the energy band and no localized state exists in the system as the continuum particles might hop on and off the impurity site. On the other hand, if the energy is outside the band, a true

localized state does exist. The energy of the dressed impurity then fulfills the self-consistency condition [134]

$$\tilde{\epsilon}_c = \epsilon_c + \sum_k \frac{A_k^2}{\tilde{\varepsilon}_c - \varepsilon_k}, \tag{83}$$

where A_k is the coupling amplitude between the continuum and the impurity state.

The analogy to our model is straight-forward. A slight difference is the presence of two bands and two impurities in the present setup. The hybridization can alter the modes l and r through shifting $\Delta\varepsilon_\eta$ and broadening Γ_η, such that $\varepsilon_\eta = 0 \to \Delta\varepsilon_\eta - i\Gamma_\eta/2$. However, the first effect is prevented by the particle-hole symmetry of the problem, and the broadening, which is dependent of the spectral density of the bulk bands, evaluates to zero as the bulk bands remain gapped for $\Delta\varepsilon < 4\tilde{t}$. Regardless, another effect, a bulk-mediated tunneling between the edges can be derived which is described by the effective Hamiltonian

$$H_{\text{e}-\text{e}} = t_{\text{ee}} r^\dagger l + \text{h.c.} \qquad \text{with} \qquad t_{\text{ee}} = \sum_{n,\alpha} \frac{g_{n,\alpha}^r (g_{n,\alpha}^l)^*}{\alpha\varepsilon(q_n)}. \tag{84}$$

For gapped bulk bands, this edge-edge tunneling decreases exponentially with the distance of the edges, such that it is fully suppressed in the thermodynamic limit for $\Delta\varepsilon < 4\tilde{t}$. At the critical point, however, the band gap vanishes and the former topological edge modes are no longer exponentially localized.

INTERACTING SYSTEM AND BULK-MEDIATED EDGE-EDGE INTERACTIONS.   In Secs. 3.2.4 and 3.3.3, we have studied the interaction-induced transition between a topological and a trivial phase. The derivation of the critical point was done by analyzing the gap-closing in the dispersion relation and the behavior of local order parameters. However, the previous analysis did not reveal the topological character of the transition. For the free model, we saw above that the on-set of the topological phase can be understood by looking at the effective theory of the edges. In the following, we qualitatively argue that a similar interpretation can be applied to understand the interaction-induced transition.

In particular, due to the symmetry $\tilde{\varepsilon}_\alpha(+q) = \tilde{\varepsilon}_\alpha(-q)$ the dispersion relation (76) allows the construction of standing wave solutions $\tilde{\gamma}_\pm(q_n)$ which respect the boundary condition $f_N = f_0 = 0$ and are constructed here as Bogoliubov modes from the earlier operators $f(q_n)$ and $f^\dagger(-q_n)$ (see again App. C.2).

In close analogy to Eq. (82), the bulk-edge coupling in the interaction Hamiltonian (68)

$$H_{\text{b}-\text{e}} = V_v(n_l \tilde{T}_1^x - n_r \tilde{T}_{N-1}^x), \tag{85}$$

takes the form

$$H_{\text{b}-\text{e}} = \sum_{n,\alpha} (\tilde{g}_{n,\alpha}^l l^\dagger l \ - \tilde{g}_{n,\alpha}^r r^\dagger r \ )\tilde{\gamma}_\alpha(q_n) + \text{h.c.} \tag{86}$$

Again, this coupling to the dispersive bulk bands can in principal have the effect of shifting and dephasing the zero-energy edge modes, $\varepsilon_\eta = 0 \to \tilde{\varepsilon}_\eta = \Delta\varepsilon_\eta +$

$i\tilde{\Gamma}_\eta/2$, and mediate an edge-edge interaction through spin-wave excitations of the bulk. For $V_{\rm v} < 8\tilde{t}$, the dephasing is made impossible due to the vanishing spectral density at the energy of the edge modes. The effect of level-shifts and edge-edge interactions can be summed up as

$$H_{\rm e-e} = \Delta\varepsilon_l n_l + \Delta\varepsilon_r n_r + U_{\rm ee} n_l n_r \tag{87}$$

with

$$\Delta\varepsilon_\eta = -\sum_{n,\alpha} \frac{\left|\tilde{g}_{n,\alpha}^\eta\right|^2}{\varepsilon(q_n)}, \qquad U_{\rm ee} = \sum_{n,\alpha} \frac{\tilde{g}_{n,\alpha}^l \tilde{g}_{n,\alpha}^r}{\varepsilon(q_n)} + {\rm h.c.} \tag{88}$$

Unlike for the free model, there is no particle-hole symmetry preventing a level-shift here, which then depends on the filling of the Bogoliubov-levels for the bulk ground state.

The effective model allows the following explanation for the phase transition: The effective interaction in Eq. (87) cannot have an effect as for half-filling the two edge-modes are not populated simultaneously. The energy shift $\Delta\varepsilon_\eta$ cannot destroy the topological degeneracy as $\Delta\varepsilon_l = \Delta\varepsilon_r$ and a dephasing does not take place as long as the Bogoliubov excitations are gapped. This is no longer the case at $V_{\rm v} = 8\tilde{t}$: The edge modes are then not localized excitations anymore and the topological nature is destroyed.

4

CURRENT BEHAVIOR OF
INTERACTING WEYL FERMIONS ON A RING

In this chapter, we explore the current response of interacting Weyl fermions (i.e. massless relativistic fermions) in one-dimensional ring traps. We use a geometry similar to the Creutz ladder presented in the previous chapter to mimic the linear dispersion of such particles in a lattice-discretized setup. Different to the earlier study, here we consider a periodic lattice to model a one-dimensional ring and allow for different kinds of interactions. We study the response of the currents flowing in the ring with respect to these interactions.

Similar to the dissipation-less currents observed in superconducting rings [135–137], it was shown that normal metal rings at extremely low temperatures display a *persistent current* when threaded by a magnetic flux [138]. Although very small, the signal was observed experimentally in stacks of mesoscopic copper rings [139], in single GaAs loops [140], in gold [141] and in aluminum rings [142]. The effect is related to the fact that, if the phase coherence length of the electrons extends beyond the ring-circumference [143], a magnetic flux through the ring is perceived by the electrons as a non-gaugeable Aharonov-Bohm phase [144]. This is the case at zero temperature. For small rings, the effect persists at sufficiently low finite temperature and with weak static disorder.

Beyond condensed matter realizations, ring-shaped setups have also attracted the attention of the cold atom community. Gases of dipolar atoms can be confined and rotated through the quadrupole magnetic field of circular current carrying wires [145, 146]. In an alternative setup, Bose-Einstein condensates are confined in a toroidal geometry through an optical potential of Gaussian laser-beams [147, 148]. In such experiments, a persistent flow of the BEC for more than 40 seconds was reported. In addition, the latter experiment demonstrated the possibility of creating a tunable weak link which can control the current in a similar fashion to superconducting quantum interference devices (SQUIDs) and suggested the emergence of vortex-anti-vortex pairs at a critical velocity. In recent years, the setup was further advanced by introducing rotating weak links to induce super-currents through stirring [149, 150] or through artificial gauge fields (see Sec. 2.5). The decay behavior was studied with two-component gases [151], and the quantization in the current-phase relation was reported [152]. Theoretical studies have addressed the influence of interactions [153, 154].

The earlier results in one-dimensional setups relate to massive, non-relativistic particles. Our realization of Weyl fermions, on the contrary, requires a linear dispersion, which can be modeled using a lattice discretization. In two dimensions, effective massless particles (or excitations) occur in form of Dirac cones [155] at the Fermi level of graphene, and can be imitated in artificial honeycomb lattices [156]. In cold atoms, advances in this direction have been made by the realization of triangular and hexagonal lattices [157, 158], the controlled creation, movement and merging of Dirac points in Fermi gases with a tunable

honeycomb lattice [38] and the experimental realization of the topological Haldane model [159]. In one dimension, ring-shaped optical lattices can be obtained using spatial light modulators (SLM) [160] or co-propagating Laguerre-Gauss beams, i.e. light beams carrying angular momentum [161].

Our particular interest in fermions with linear dispersion stems from their unique electromagnetic properties. For graphene-like structures, a large diamagnetic response was predicted at half-filling [162–164] and zero-response elsewhere. Interactions which are commonly associated with a suppression of a diamagnetic response lead to interesting features such as a paramagnetic response in doped samples, and hence the concept of *many-body orbital paramagnets* [165, 166]. Different suggestions for the observed behavior have related it to the breaking of Galilean invariance [166], lattice and pseudo-spin effects [167, 168], topological features [169, 170] and to quantum metric tensor [171]. The recently discovered Weyl semi-metals and Fermi arc states [172–175] represent a three-dimensional analog of graphene and further motivate the investigation of Weyl fermions in different dimensions.

Here, we study a ring-shaped lattice model that displays the linear dispersion of Weyl fermions. The model is a particular fixed-parameter version of a Creutz ladder and therefore similar to the one in the previous section. In this chapter, however, we do not study topological properties, but we are interested in the so-called *Drude weight* [143] which characterizes the dc-conductivity of the system. We assume different types of interactions (of Hubbard on-site and nearest-neighbor type) and make extensive calculations of the conductivity for different particle densities and therefore employ both analytical techniques (perturbation theory) and tensor network calculations. For exclusive on-site interactions, we show that the Drude weight of the interacting Weyl fermions displays a similar behavior as known from other setups, in particular the Hubbard model: The diamagnetic response of the current is suppressed with growing interactions. This situation is completely altered when allowing for nearest-neighbor interactions which are asymmetric in the sense that they are different for the different internal states (of the pseudo-spin) of the particles. We show that in this case, the diamagnetic current shows an exotic interaction-driven enhancement.

We proceed as follows: We first introduce the circular lattice model which is in the focus of our study (Sec. 4.1). We motivate the model through a derivation from the Dirac Hamiltonian describing relativistic fermions in quantum field theory (QFT) and discuss its relevance from a topological insulator point of view. We then turn to the response of a ring to a magnetic flux (Sec. 4.2). We discuss the relation between flux and current and show a derivation of current-current responses and electrical conductivity using linear response theory. In particular, we introduce and contextualize the so-called Drude weight. In Sec. 4.3 we explain the physics of the non-interacting system. We then demonstrate how the effect of weak interactions can be tackled through a perturbation theory approach (Sec. 4.4). In Sec. 4.5, we present our numerical results for different combinations of on-site and nearest-neighbor interactions and compare them to the perturbation theory. To further underline the universality of the setup, we briefly discuss the scaling in the continuum and thermodynamic limit (Sec. 4.6).
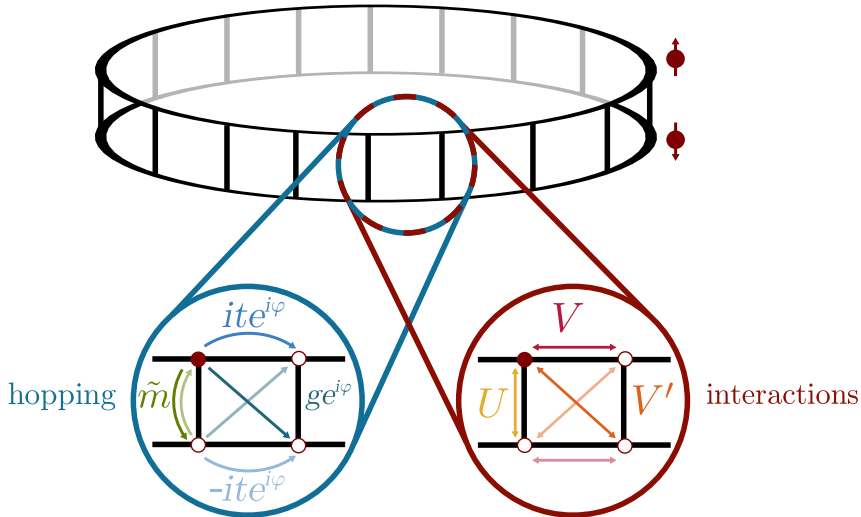
Figure 14: **Weyl fermions on a ring lattice: hopping and interaction terms.** Schematic view of the periodic ladder geometry used to model the dispersion relation of Weyl fermions. The insets show the tunneling terms appearing in the Creutz model (90) and the different types of studied interactions (96).

Due to the periodic boundary conditions needed for the description of the ring, numerical calculations using standard MPS techniques become challenging. We therefore employ binary tree tensor networks, which better account for the geometry. Details on the method are given in App. A.5. Some specifics of possible cold atom implementations are discussed in App. B.2.2. The results presented in this chapter have been published in [24].

4.1 MODEL AND DERIVATION

In this section, we introduce the model under consideration. We first present the Hamiltonian and discuss its features. In Sec. 4.1.1, we take a QFT perspective to explain the origin of the model and demonstrate its discretization. We then discuss the same model from the condensed matter perspective of topological insulators (Sec. 4.1.2). In Sec. 4.1.3, we explain how interactions enter the picture.

The Hamiltonian describing the physics of our system is given as

$$H = H_{\text{kin}} + H_{\text{int}} \tag{89}$$

with a kinetic contribution H_{kin} and an interaction term H_{int}. The first term is similar to the imbalanced Creutz ladder introduced in the previous chapter (36) and given by

$$H_{\text{kin}} = \underbrace{\sum_{j=1}^{L} [c_{j+1}^\dagger (it\sigma_z - g\sigma_x)e^{i\varphi}c_j + \text{h.c.}]}_{H_{\text{kin},\parallel}} + \underbrace{\sum_{j=1}^{L} [\tilde{m}c_j^\dagger \sigma_x c_j + \text{h.c.}]}_{H_{\text{kin},\perp}}, \tag{90}$$

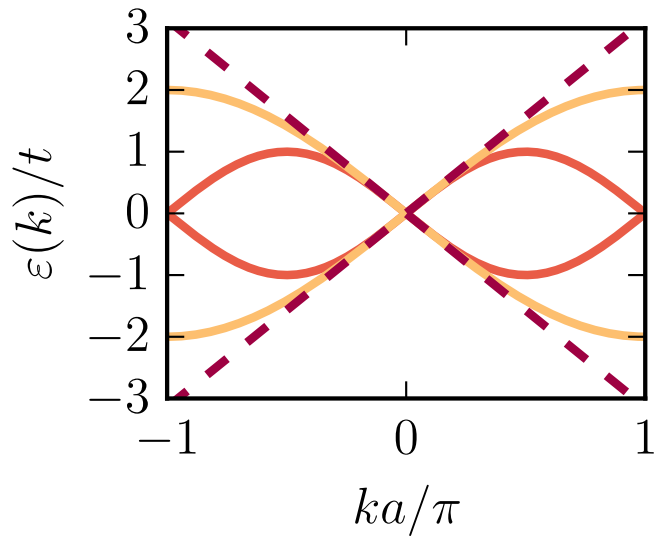Figure 15: **Dispersion relation of a Weyl fermion.** The dashed dark red line shows the linear dispersion of a Weyl fermion, which results from the masslessness of the theory. A naive attempt to mimic this dispersion on a lattice ($m = g = 0$) leads to fermion doubling (light red): Apart from the linear behavior around $k = 0$, another Dirac-point is found at $k = \pm\pi$. By adding additional terms following the Wilson prescription ($t = g = \tilde{m}$), we can get rid of this spurious discretization effect.

where we choose a slightly different notation, and explicitly distinguish the kinetic terms that move a particle along the ring ($H_{\text{kin},\parallel}$) or not ($H_{\text{kin},\perp}$). The fermionic operators are two-component spinors $c_j = (c_{j,\uparrow}, c_{j,\downarrow})^T$ and $\uparrow$ and $\downarrow$ denote the internal states. Particles can hop along the legs of this ladder with hopping parameter t (and thereby pick up a phase $\pm\frac{\pi}{2} \to \exp(\pm i\frac{\pi}{2}) = \pm i$) or hop diagonally changing the site and the internal state simultaneously (inter-chain hopping g). In contrast to the model in the previous chapter, there is no imbalance term but instead hopping along the rungs of the ladder, i.e. a spin-flipping term $\tilde{m}$ (see Fig. 14).

It is crucial to note here that the Hamiltonian possesses periodic boundary conditions ($c_{L+1} = c_1$) and our setup therefore has a ring-shaped geometry. A magnetic flux Φ threading the ring translates into a uniform vector potential along the ring reflected by a Peierls phase $\varphi = (2\pi/L)(\Phi/\Phi_0)$ that particles pick up when hopping from one site to a neighboring one. The constant $\Phi_0 = h/e$ is called the *flux quantum*. Alternatively, in the setup of cold atoms, we can consider the phase as the effect of an artificial gauge field (compare Sec. 2.5).

The Fourier transform of this Hamilton reads

$$H_{\text{kin}} = \sum_k c_k^\dagger \left\{ t\sin(\tilde{k}a)\sigma_z + \left[\tilde{m} - g\cos(\tilde{k}a)\right]\sigma_x \right\} c_k, \tag{91}$$

where $k \in \{-\frac{\pi}{a}\frac{(L-1)}{2L}, \ldots, -\frac{2\pi}{La}, 0, \frac{2\pi}{La}, \ldots, \frac{\pi}{a}\}$ and $\tilde{k} = k + \varphi/a$ incorporates the shift induced in the momenta by the phase φ; a is the lattice spacing. If we choose the parameters $t = \tilde{m} = g$, the dispersion relation reads

$$\varepsilon_\pm(k) = \mp 2t \, \text{sign}(ka) \sin\left(\frac{ka}{2}\right). \tag{92}$$

This dispersion displays a single Dirac-Weyl crossing at $k = 0$ and $\varepsilon(k) \approx \pm \hbar v_F k$ with $v_F = ta/\hbar$ for $k \ll 2\pi/a$ (see Fig. 15). For later use, we note the operators in the eigenbasis, i.e. with $H_{\text{kin}} = \sum_k \varepsilon_s(k) d_{k,s}^\dagger d_{k,s}$,

$$d_{k,s}^\dagger = \sum_\sigma N_{\tilde{k},s}^\sigma c_{k,\sigma}^\dagger, \tag{93}$$

where $s = \pm$ is the index of the valence $(-)$ or the conduction band $(+)$ and the form-factors are given as

$$N_{k,s}^\uparrow = sg_k/[2(1 - sf_k)]^{1/2} \quad \text{and} \quad N_{k,s}^\downarrow = (1 - sf_k)/[2(1 - sf_k)]^{1/2} \tag{94}$$

with $g_k = \text{sign}(ka)\sin(ka/2)$ and $f_k = \text{sign}(ka)\cos(ka/2)$.

We consider interactions between the originally free fermions (90),

$$H_{\text{int}} = \sum_{\sigma,\sigma'} \sum_{i,j} v_{ij}^{\sigma,\sigma'} n_{i,\sigma} n_{j,\sigma'} \tag{95}$$

with

$$v_{ij}^{\sigma,\sigma'} = \frac{1}{2}(U\delta_{i,j}\delta_{\bar{\sigma},\sigma'} + V\delta_{j,i\pm1}\delta_{\sigma,\sigma'} + \tilde{V}\delta_{j,i\pm1}\delta_{\bar{\sigma},\sigma'}), \tag{96}$$

where $\bar{\sigma}$ labels the opposite spin to σ (see again Fig. 14). The first term describes on-site Hubbard interactions acting between fermions with different pseudo-spin. The other two terms describe nearest-neighbor interactions between particles with the same (V) or with different spin (V'). We will see later that the presence of the nearest-neighbor terms significantly alters the physics of the model if they are asymmetric, i.e. $V - V' \neq 0$.

4.1.1 *Relativistic QFT perspective*

We introduced the dispersion relation (92) as that of a Weyl fermion. To motivate this notion, we present now a derivation of the Hamiltonian (91) from the perspective of relativistic quantum field theory.

In QFT, the dynamics of relativistic fermions is described by the Dirac equation, which in Hamiltonian notation reads [176]

$$H_{\text{D}} = \sum_{\mu,\nu} \int_{\Lambda^d} \frac{\mathrm{d}^d k}{(2\pi)^d} \, \Psi_\mu^\dagger(\mathbf{k}) \, [h_D(\mathbf{k})]^{\mu\nu} \, \Psi_\nu(\mathbf{k}). \tag{97}$$

Here $\Psi(\mathbf{k})$ and $\Psi^\dagger(\mathbf{k})$ are the spinor fermionic field operators, which fulfill $\{\Psi_\mu(\mathbf{k}), \Psi_\nu^\dagger(\mathbf{k}')\} = (2\pi)^d \delta_{\mu,\nu}\delta(\mathbf{k} - \mathbf{k}')$ and

$$h_D(\mathbf{k}) = \hbar c \sum_{i=1}^d \alpha_i k_i + mc^2\beta. \tag{98}$$

Furthermore, m is the particle mass, c is the speed of light, and α_i and β are the Dirac matrices. Due to the specifications of the latter, one can determine the dispersion relation as $\varepsilon_{D,\pm}(k) = \pm c\sqrt{\hbar^2\mathbf{k}^2 + m^2c^2}$. In the particular case of particles with $m = 0$, the dispersion becomes linear, $\varepsilon_{D,\pm}(k) = \pm c\hbar\,|\mathbf{k}|$. Such massless fermions are the afore-mentioned *Weyl fermions*.

To discretize the field, we can introduce a Bravais lattice with lattice constant a, $\Lambda = \{\mathrm{r} : r_i/a \in \mathbb{Z} \,\forall\, 1 \le i \le d\}$, and obtain in real space

$$\tilde{H}_{\mathrm{D}} = \sum_{\mathbf{r}\in\Lambda} a^d \left(\frac{i\hbar c}{2a} \sum_{i=1}^{d} \Psi^\dagger(\mathbf{r})\alpha_i\Psi(\mathbf{r} + a\mathbf{u}_i) + \frac{mc^2}{2}\Psi^\dagger(\mathbf{r})\beta\Psi(\mathbf{r}) + \text{h.c.} \right), \quad (99)$$

where $\{\mathbf{u}_i\}$ are the unit vectors of the lattice.

However, when transforming this discretized Hamiltonian back to momentum space one obtains $\tilde{H}_D = \int_{\mathrm{BZ}} \frac{\mathrm{d}^d k}{(2\pi)^d} \Psi^\dagger(\mathbf{k})\tilde{h}_D(k)\Psi(\mathbf{k})$ when integrating over the Brillouin zone $\mathrm{BZ} = (-\pi/a, \pi/a]^d$, and

$$\tilde{h}_D(\mathbf{k}) = \frac{\hbar c}{a}\sum_i \alpha_i \sin(k_i a) + mc^2\beta, \qquad (100)$$

which is obviously different from the original expression (98).

To discuss the ramifications of the discretization, we now focus on the case of a one-dimensional model, $d = 1$. This allows us to simplify the notation and to account for the specifics of our model. If we index the sites of the Bravais lattice and introduce second quantization, $\Psi(x) \to (c_{i,\uparrow}, c_{i,\downarrow})^T/\sqrt{a}$, the lattice-discretized Hamiltonian (99) becomes

$$\tilde{H}_{\mathrm{D}} = \sum_i \frac{i\hbar ca}{2}c_i^\dagger\alpha_i c_{i+1} + \frac{mc^2}{2}c_i^\dagger\beta c_i + \text{h.c.} \qquad (101)$$

and, after Fourier transformation,

$$\tilde{H}_{\mathrm{D}} = \sum_k c_k^\dagger\tilde{h}_D(k)c_k \qquad \text{with} \qquad \tilde{h}_d(k) = \frac{\hbar c}{a}\alpha_1\sin(ka) + mc^2\beta. \qquad (102)$$

While this expression correctly reproduces the energy for long wavelength $k \ll \pi/a$, it yields a second point in the Brillouin zone, $k = \pi/a$, with a similar linear dispersion (see also Fig. 15). This is problematic as these *fermion doublers* will couple to the Dirac QFT at $k = 0$ as soon as interaction terms are included in the model. Due to the Nielsen-Ninomiya theorem [177, 178], fermion doubling is an inevitable process in discretization if all symmetries of the original setup are to be conserved. However, by giving up the chiral symmetry, we can follow the prescription by Wilson [179] and introduce an additional mass-shift term $\frac{c^2\delta m}{2}c_i^\dagger\beta c_{i+1}$ in the Hamiltonian (101). In the Fourier-transformed model, this results in

$$\tilde{H}_{\mathrm{D}} = \frac{\hbar c}{a}\alpha_1\sin(ka) + (m + \delta m\cos(ka))c^2\beta. \qquad (103)$$

In particular, to have a single *massless* fermion at $k = 0$, we can set $\delta m = -m$. We can then shift the mass of the particle at $k = \pi/a$ to a very high energy on the order of the cut-off by setting $2mc^2 = \hbar c/a \Rightarrow m = \hbar/2ac$.

By identifying the Dirac matrices in terms of Pauli matrices as $\alpha_1 = \sigma_z$ and $\beta = \sigma_x$, one can identify the terms in our model (91) (without a field, $\varphi = 0$) with their field-theoretic counterpart. The hopping along the legs of the ladder $\pm it$ corresponds to the kinetic energy, the vertical hopping identifies the mass term as $\tilde{m} = mc^2$, and the diagonal hopping corresponds to the mass-shift ($g = \delta m\, c^2$). By then setting $\tilde{m} = g$, we make the theory massless at $k = 0$ and the additional condition $t = \tilde{m} = g$ moves the mass of the particle at $k = \pi/a$ to high energies. Our parameters relate to the continuum model as $t = \tilde{m} = g = \hbar c/a$.

To complete the derivation of our lattice model from QFT, we note that the effect of a an electromagnetic potential would enter as a momentum-shift $\mathbf{k} \to \mathbf{k} + \frac{e}{c}\mathbf{A}$ in the Dirac Hamiltonian (98) and propagate through the derivation to the lattice discretization (103). The effect is therefore in one-to-one agreement with the one that we have incorporated into our lattice model through the Peierls substitution (compare Eq. (91)).

4.1.2   *Topological insulator perspective*

From a condensed matter perspective, one can also appreciate the necessity of avoiding fermion doubling. We note once again the similarity between the Creutz Hamiltonians in this (91) and in the previous chapter (40). Similar to the earlier model, we can identify parameter regimes in our model which are associated with different winding numbers (compare Eq. 42). Namely, we can identify a phase with $t = g < |\tilde{m}|$ which corresponds to a topological insulator, and a phase with $t = g > |\tilde{m}|$, which is topologically trivial. The parameter choice $t = g = \tilde{m}$, which is in the focus of our attention, therefore indicates the critical point between these two gapped phases. Notably, such a critical phase occurs at the surface of two-dimensional topological insulators [180].

If we had followed the derivation from the continuum without taking care of the fermion doubling, we would have wound up with the Hamiltonian (100), which is equivalent to the choice $g = 0$ in our model. In that case, the winding number (or the Zak phase) evaluates to zero for both $t > \tilde{m}$ and $t < \tilde{m}$, indicating two topologically trivial insulators, and the lattice model would have failed to reproduce the topological invariant of a single massive QFT. This is due to the fact that the fermion doubling yields two Dirac points at $k = 0$ and $k = \pi/a$ that yield contributions with opposite signs that cancel. The Wilson prescription gets rid of this spurious effect.

4.1.3   *Interactions*

The on-site interactions in Eq. (95) can be derived from contact interactions between the Weyl fermions in the field-perspective,

$$H_{\text{int,on}} = \int \mathrm{d}x \int \mathrm{d}x' \sum_{\mu,\nu} \psi_\mu^\dagger(x)\psi_\nu^\dagger(x') \left[\frac{u}{2}\delta(x - x')\delta_{\mu,\bar\nu}\right] \psi_\nu(x')\psi_\mu(x). \quad (104)$$

Discretization of the lattice casts these into

$$H_{\text{int,on}} = \frac{u}{a} \sum_j c_{j,\uparrow}^\dagger c_{j,\uparrow} c_{j,\downarrow}^\dagger c_{j,\downarrow} = \frac{u}{a} \sum_j n_{j,\downarrow} n_{j,\uparrow}, \tag{105}$$

where again, we associated the spinor components of the relativistic particles with the internal degree of freedom on our lattice, $\Psi(x = ja) \to (c_{j,\uparrow}, c_{j,\downarrow})^T / \sqrt{a}$ and substituted $\int_0^{La} \to a \sum_{j=1}^L$. We see that we can associate the contact interaction in the continuum model with the Hubbard interactions of our lattice, if we require $U = \frac{u}{a}$.

A field-theoretic motivation of the nearest-neighbor interactions is more intricate. Let us assume that

$$H_{\text{int,nn}} = \int dx \int dx' \sum_{\mu,\nu} \left[\frac{v}{2} \delta_{\mu,\nu} + \frac{v'}{2} \delta_{\mu,\bar{\nu}} \right] \delta'(x - x') \psi_\mu^\dagger(x) \rho_\nu(x') \psi_\mu(x). \tag{106}$$

For convenience, we introduced a density operator $\rho_\sigma(x) = \psi_\sigma^\dagger(x) \psi_\sigma(x)$. We can now use the identity $f(x)\delta'(x) = f'(x)\delta(x)$ and again discretize:

$$H_{\text{int,nn}} = \int dx \sum_{\mu,\nu} \left[\frac{v}{2} \delta_{\mu,\nu} + \frac{v'}{2} \delta_{\mu,\bar{\nu}} \right] \psi_\mu^\dagger(x) \rho_\nu'(x) \psi_\mu(x) \tag{107}$$

$$= \lim_{a \to 0} a \sum_j \sum_{\mu,\nu} \left[\frac{v}{2} \delta_{\mu,\nu} + \frac{v'}{2} \delta_{\mu,\nu'} \right]$$
$$\psi_\mu^\dagger(ja) \left(\lim_{b \to 0} \frac{\rho_\nu(ja + b) - \rho_\nu(ja)}{b} \right) \psi_\mu(ja). \tag{108}$$

If, in particular, we choose $a = b$ in the discretized model, we obtain

$$H_{\text{int,nn}} = \sum_j \sum_{\mu,\nu} \left[\frac{v}{2a^2} \delta_{\mu,\nu} + \frac{v'}{2a^2} \delta_{\mu,\nu'} \right] \left(n_{j,\mu} n_{j+1,\nu} - n_{j,\mu} n_{j,\nu} \right). \tag{109}$$

A comparison with our lattice Hamiltonian (95) shows that we can associate $V = \frac{v}{a^2}$ and $V' = \frac{v'}{a^2}$. Additionally, the above expression renormalizes the onsite interactions such that effectively $U = \frac{1}{a}\left(u - \frac{v'}{a}\right)$.

4.2   PERSISTENT CURRENTS AND DRUDE WEIGHT

In the previous section, we have introduced a fermionic lattice model that captures the physics of relativistic, massless fermions. Due to the ring-shaped geometry of our setup, a magnetic flux piercing the ring leads to an Aharonov-Bohm effect: Independent of whether the magnetic field extends to the ring, the corresponding gauge field has a physical effect on the fermions on the ring (compare Sec. 2.5). This is reflected by a (Peierls) phase in the tunnelings in the lattice Hamiltonian.

Here, we want to develop an understanding of how this gauge field can be interpreted physically and how it affects the dynamics of the particles on the ring. We therefore study the linear response to the gauge potential. We will see that this response manifests as a current flowing in the ring. This is interesting,

as the system does not exhibit a potential difference that drives the current, and leads to the notion of *persistent currents* (compare Sec. 2.6). We can then conceive two scenarios: One possibility is that the current counter-acts the external magnetic field. Due to the fact that the circular flow of a current is equivalent to an *orbital magnet*, it is called *diamagnetic*. Alternatively, the current can enhance the external field, and is then named *paramagnetic*. The Drude weight D quantifies this finding.

To have a pedagogical approach to the matter, we first introduce the basic concepts of linear response theory (LRT) in Sec. 4.2.1. We then apply the LRT to the model at hand and show how the Drude weight quantifies the current response to a (time-independent) gauge field (Sec. 4.2.2). We also demonstrate that the Drude weight can be directly linked to the flux-dependence of the ground state energy, which will be of high relevance for the later perturbative and numerical study.

4.2.1   *Basics of linear response theory*

Consider a system in the Heisenberg picture with Hamiltonian H_0 and a perturbation caused by some external parameter $\phi(t)$ coupling to an operator B of the system. The perturbation $H_{\text{source}} = \phi(t)B(t)$ is turned on at some point t_0 in time, i.e. $\phi(t) = 0$ for $t < t_0$. The full Hamiltonian then reads

$$H = H_0 + H_{\text{source}}. \tag{110}$$

The influence on some observable A of a slight perturbation (i.e. in first order) can be written as $\langle A(t) \rangle = \langle A(t) \rangle_{\text{unpert}} + \langle \delta A(t) \rangle$. We are interested in the proportionality factor χ between the linear perturbation and the perturbing parameter ϕ, $\langle \delta A(t) \rangle = \int \mathrm{d}t' \; \chi_{AB}(t, t')\phi(t')$. χ is called the susceptibility. $\langle \delta A(t) \rangle$ can be determined through the so-called *Kubo formula* [181]

$$\begin{aligned} \langle \delta A(t) \rangle &= -\frac{i}{\hbar} \int_{-\infty}^{t} \mathrm{d}t' \; \langle [A(t), B(t')] \rangle \, \phi(t') \\ &= -\frac{i}{\hbar} \int_{-\infty}^{\infty} \mathrm{d}t' \; \theta(t - t') \langle [A(t), B(t')] \rangle \, \phi(t'). \end{aligned} \tag{111}$$

We can therefrom extract the susceptibility as

$$\chi_{AB}(\tau) = -\frac{i}{\hbar} \langle [A(\tau), B(0)] \rangle \, \theta(\tau), \tag{112}$$

where $\tau = t - t'$ and θ is the Heaviside step-function. We note that the result can be Fourier-transformed to obtain the susceptibility in spectral form as

$$\langle \delta A(\omega) \rangle = \chi_{AB}(\omega)\phi(\omega) \quad \text{with} \quad \chi_{AB}(\omega) = \lim_{\epsilon \to 0} \int_{-\infty}^{+\infty} \mathrm{d}t \; e^{i(\omega + i\epsilon)t} \chi_{AB}(t) \tag{113}$$

and observe that it is "local" in ω: A system reacts to a perturbation with a given frequency with a response at the same frequency. At $T = 0$, the susceptibility can be decomposed in the *exact eigenstates decomposition*

$$\chi_{AB}(\omega) = \frac{1}{\hbar} \lim_{\epsilon \to 0} \sum_{n \neq 0} \langle 0|A|n \rangle \langle n|B|0 \rangle \left[\frac{1}{\omega + \Delta\epsilon_n + i\epsilon} - \frac{1}{\omega - \Delta\epsilon_n + i\epsilon} \right] \tag{114}$$

where $\Delta\epsilon_n = (E_n - E_0)/\hbar$ and E_n are the eigenenergies of the unperturbed system. The infinitesimal ϵ guarantees the convergence for $t > 0$.

Without going into detail, we note that any response χ can be split into a real component χ' and an imaginary component χ'' such that $\chi = \chi' + i\chi''$. The imaginary part is called the *dissipative* (or absorptive) part as it identifies the capacity of a system to absorb energy at a given frequency. The real part is named the *reactive* part. For later use, we note

$$\chi'_{AB}(\omega) = \frac{1}{\hbar} \sum_{n \neq 0} \langle 0|A|n\rangle \langle n|B|0\rangle \, \mathcal{P}\left(\frac{2\Delta\epsilon_n}{\omega^2 - \Delta\epsilon_n^2}\right) \tag{115}$$

where we use the Dirac relation [182]

$$\lim_{\eta^+ \to 0} \frac{1}{x - a + i\eta} = \mathcal{P}\left(\frac{1}{x - a}\right) - i\pi\delta(x - a), \tag{116}$$

with the Cauchy principal value $\mathcal{P}$.

4.2.2 *Linear response theory and Drude weight*

Let us now turn back to the problem at hand: a ring pierced by a magnetic flux. In the kinetic part of our lattice Hamiltonian (90), we included the magnetic flux through the Peierls phase . Let us assume for a moment a more general gauge field $\mathbf{A}(t) = A(t)\mathbf{e}_\varphi$ and therefore

$$H_{\text{kin},\parallel} = \sum_{i=1}^{L} [c_{i+1}^\dagger (it\sigma_z - g\sigma_x)e^{i\varphi(t)} c_i + \text{h.c.}] \tag{117}$$

with $\varphi(t) = \frac{ea}{\hbar} A(t) = \frac{2\pi}{L} \frac{\Phi(t)}{\Phi_0}$. Such a gauge field corresponds to an electric field $E = \dot{A}(t)$ that drives a current. We want to determine the optical conductivity σ which establishes the relation between this electric field and the current, and which in its most general form is defined as [134]

$$I_\alpha(\mathbf{r}, t) = \int d^3r' \int_{-\infty}^{t} dt' \, \sigma_{\alpha\beta}(\mathbf{r} - \mathbf{r}', t - t') E_\beta(\mathbf{r}', t'). \tag{118}$$

Here, we consider only one-dimensional systems and the conductivity tensor σ becomes a scalar. If, in addition, we drop the spatial dependence (homogeneous field) and Fourier-transform the conductivity to frequency space, we obtain

$$I(\omega) = \sigma(\omega)E(\omega). \tag{119}$$

For small fields, we can expand the Hamiltonian as

$$H(\varphi(t)) = H(\varphi = 0) - \underbrace{\varphi(t)}_{= \frac{ea}{\hbar} A(t)} \left[\frac{\hbar L}{e} \hat{I}_p\right] - \frac{\varphi^2(t)}{2} H_{\text{kin},\parallel}(\varphi = 0) + \mathcal{O}(\varphi(t)^3) \tag{120}$$

with the paramagnetic current operator defined in terms of the general current operator $\hat{I}$ (19) as $\hat{I}_p \equiv \hat{I}(\varphi = 0)$. We established earlier that the (physical)

current is defined as the negative derivative of the energy with respect to the field, and therefore

$$\hat{I}(\varphi) = \hat{I}_p + \frac{e\varphi}{\hbar L} H_{\text{kin},\parallel} + \mathcal{O}(\varphi^2) \tag{121}$$

$$= \hat{I}_p + \frac{e^2 a}{\hbar^2 L} A H_{\text{kin},\parallel} + \mathcal{O}(\varphi^2). \tag{122}$$

This current has two contributions: a paramagnetic term and a stress tensor that in the one-dimensional case is just presented by the kinetic energy of the hopping along the ring. Using $A(\omega) = \frac{E(\omega)}{i\omega}$, we can re-express the current as

$$\hat{I} = \hat{I}_p + \frac{1}{i\omega} \left(\frac{e^2 a}{\hbar^2 L} H_{\text{kin},\parallel} \right) E. \tag{123}$$

Let us first consider the paramagnetic component coupling to the external magnetic field. This expression corresponds to H_{source} in Eq. (110). Using Eq. (114), we can therefore calculate a (paramagnetic) current-current response

$$I_p(\omega) = a L \chi_{II}(\omega) A(\omega) \tag{124}$$

where

$$\chi_{II}(\omega) = \lim_{\epsilon \to 0} \frac{1}{\hbar} \sum_{n \neq 0} \left| \langle 0 | \hat{I}_p | n \rangle \right|^2 \left(\frac{1}{\omega + \Delta\epsilon_n + i\epsilon} - \frac{1}{\omega - \Delta\epsilon_n + i\epsilon} \right) \tag{125}$$

with a real contribution (compare Eq. (115))

$$\chi'_{II}(\omega) = \frac{2}{\hbar} \sum_{n \neq 0} \left| \langle 0 | \hat{I}_p | n \rangle \right|^2 \mathcal{P} \left(\frac{\Delta\epsilon}{\omega^2 - \Delta\epsilon_n^2} \right). \tag{126}$$

If we insert the expression for the paramagnetic current in Eq. (123) and compare it to the definition of the conductivity (119), we find

$$\sigma(\omega) = \frac{1}{i\omega} \left[a L \chi_{II}(\omega) + \left(\frac{e^2 a}{\hbar^2 L} H_{\text{kin},\parallel} \right) \right]. \tag{127}$$

The imaginary component of the conductivity can be written as

$$\sigma''(\omega) = \frac{2 e^2 a}{L \hbar^2 \omega} \left[\frac{1}{2} \langle -H_{\text{kin},\parallel} \rangle - \frac{\hbar}{e^2} \mathcal{P} \sum_{n \neq 0} \left| \langle 0 | L \hat{I}_p | n \rangle \right|^2 \frac{\Delta\epsilon_n}{\Delta\epsilon_n^2 - \omega^2} \right]. \tag{128}$$

The real part of this optical conductivity can be split into two contributions as [183–185]

$$\sigma'(\omega) = D\delta(\omega) + \sigma_{\text{reg}}(\omega) \tag{129}$$

where the Drude weight (or charge-stiffness) D is given as

$$D = \frac{1}{2} [\omega \sigma''(\omega)]_{\omega \to 0} = \frac{1}{L} \left(\frac{e^2 a}{\hbar^2} \right) \left(\frac{1}{2} \langle -H_{\text{kin},\parallel} \rangle - \left(\frac{\hbar^2}{e^2} \right) \sum_{n \neq 0} \frac{\left| \langle 0 | L \hat{I}_p | n \rangle \right|^2}{E_n - E_0} \right). \tag{130}$$

In the optical conductivity (129), the Drude weight appears as the pre-factor of a delta peak at $\omega = 0$. It therefore expresses the infinite response to a constant (non-oscillating) (dc-)field [183]. This fact explicitly relates the Drude weight to a persistent current and is different from the response to an oscillating (ac-)field (Lenz law).

The derivative of the ground state energy with respect to the flux Φ can be written as

$$\frac{\partial^2 E}{\partial \Phi^2} \overset{H.F.}{=} \frac{\partial}{\partial \Phi} \left(\left\langle \psi(\Phi) \left| \frac{\partial H}{\partial \Phi} \right| \psi(\Phi) \right\rangle \right)$$
$$= \left\langle \psi(\Phi) \left| \frac{\partial^2 H}{\partial \Phi^2} \right| \psi(\Phi) \right\rangle + ((\partial_\Phi \langle \psi(\Phi)|) H |\psi(\Phi)\rangle + \langle \psi(\Phi)| H (\partial_\Phi |\psi(\Phi)\rangle)).$$

(131)

If we plug in the expansion of the Hamiltonian in Eq. (120) and apply first-order perturbation theory,

$$\left. \frac{\partial |\phi(\Phi)\rangle}{\partial \Phi} \right|_{\Phi=0} = \underbrace{\frac{2\pi\hbar}{e\Phi_0}}_{=1} \sum_{n \neq 0} \frac{\langle n|\hat{I}_p|0\rangle}{E_0 - E_n} |n\rangle,$$

(132)

we obtain

$$\left. \frac{\partial^2 E}{\partial \Phi^2} \right|_{\Phi=0} = \frac{e^2}{\hbar^2} \left[\frac{1}{L^2} \langle -H_{\text{kin},\parallel} \rangle - \frac{2\hbar^2}{e^2} \sum_{n \neq 0} \frac{\left| \langle n|\hat{I}_p|0\rangle \right|^2}{E_n - E_0} \right].$$

(133)

Comparison with the Drude weight (130) then establishes the relation [143]

$$D = \left. \frac{La}{2\pi} \frac{\partial^2 E}{\partial \Phi^2} \right|_{\Phi=0}.$$

(134)

As anticipated earlier, the Drude weight determines qualitatively and quantitatively the transport properties of a ring: For insulators (which could be either a band or Mott insulator), D vanishes; for ideal conductors, D saturates [185, 186]. The distinction between metal and isolator through the Drude weight can also be appreciated by observing that D is inversely proportional to the effective-mass tensor [187]. Therefore $D \to 0$ corresponds to an infinite mass impeding transport.

Using the current-flux relation (21), we can write

$$D = -\frac{La}{2\pi} \frac{\partial I}{\partial \Phi}.$$

(135)

We see that a positive Drude weight describes a current that counter-acts the magnetic field (diamagnetic), while a negative Drude weight describes a current sustaining the field (paramagnetic). For completeness we note that in the literature, definitions differ depending on whether or not the derivative is written with respect to the flux Φ or the Peierls phase φ, and also on whether a factor of 2π is separated in the definition (129) [185, 188, 189].
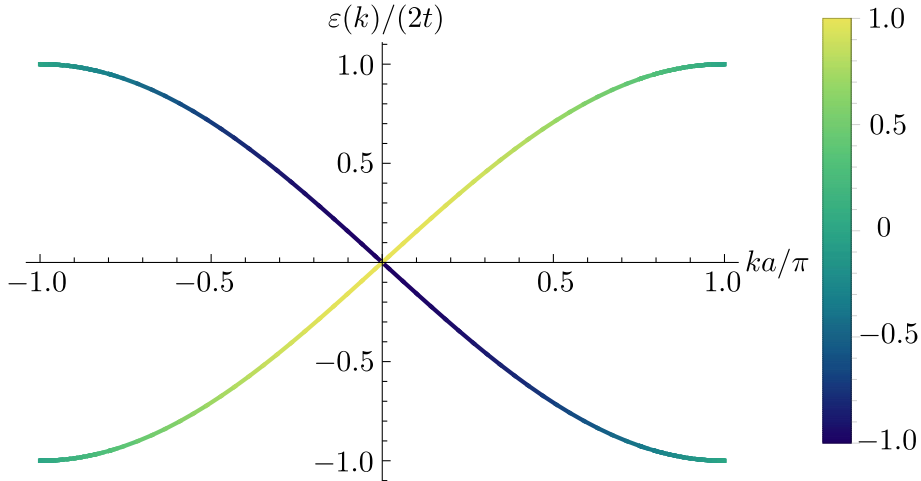
Figure 16: **Dispersion relation of the Creutz-Hubbard model and expectation value of the spin.** We re-address the lattice-dispersion of a single Weyl fermion introduced in Fig. 15. The colors of the bands indicate the contribution of the two species ↑ and ↓ to the different modes or, differently stated, the effective spin $\langle n_{i,\uparrow} - n_{i,\downarrow} \rangle$. Around the Fermi level, a spin-momentum locking occurs: the spin of a mode is definite and determines the travel direction of the particle, which is proportional to the slope of the dispersion.

Note that the Drude weight is closely related to the Meissner fraction of a superfluid. However, the two quantities are distinguishable by the order in which the limit in the frequency $\omega \to 0$ and the (in our derivation due to homogeneity not considered) wavelength $k \to 0$ are taken [190, 191]. The peculiarities of the distinction remain subject to debate [189].

4.3 FREE WEYL FERMIONS

In absence of interactions, we can understand the full dynamics of the Weyl fermions by looking at the dispersion relation (92) and Fig. 16. In Sec. 2.6, we derived the current in a lattice system from a microscopical perspective and therefrom established the macroscopic expression $I = -\partial E / \partial \Phi$ (21). We can understand the macroscopic expression in yet another microscopical image by rephrasing the current as

$$I = -\frac{\partial E}{\partial \Phi} = -\underbrace{\left(\frac{\partial \varphi}{\partial \Phi}\right)}_{=\frac{2\pi}{L\Phi_0}=\frac{e}{\hbar L}} \sum_{\tilde{k}_{\text{occ}}} \frac{\partial \varepsilon_{\tilde{k}}}{\partial \varphi} = -\frac{e}{\hbar L a} \sum_{\tilde{k}_{\text{occ}}} \frac{\partial \varepsilon_{\tilde{k}}}{\partial \tilde{k}} = -\frac{e}{La} \sum_{\tilde{k}_{\text{occ}}} v_{\tilde{k}} \qquad (136)$$

with $v_k = \frac{1}{\hbar} \frac{\varepsilon_k}{k}$, i.e. as the charged sum over the velocity of the occupied modes.

From the field-theoretic perspective, the infinity of modes below the Fermi level (compare Fig. 15) could a-priori be problematic. However, it can be shown that an appropriate regularization of the field theory can fix this problem. The observed current behavior is then exactly the one observed in the lattice [192]. This confirms that only particles close to the Fermi level contribute significantly to the persistent current and justifies the use of a finite lattice.
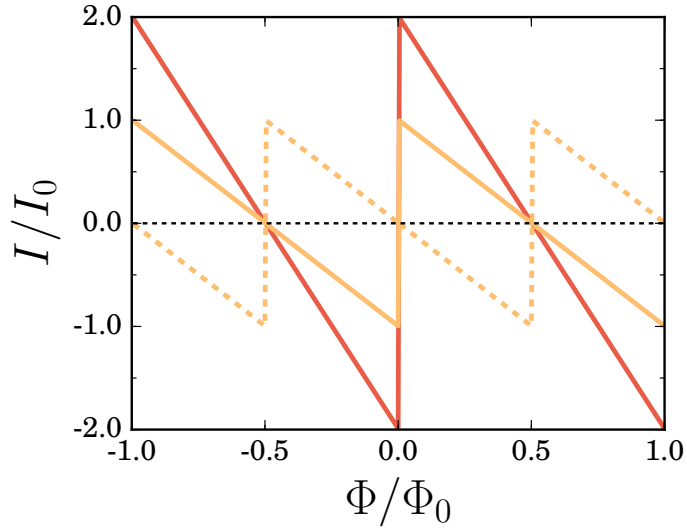
Figure 17: **Currents in the non-interacting system.** In red, the current in the half-filled lattice system with fermion doubling ($m/t = g/t = 0$), in orange the current for the system with a single Dirac-point ($m/t = g/t = 1$). Both systems display a sawtooth-periodicity with $\Phi/\Phi_0 = n$ where $n \in \mathbb{Z}$. The current in the system with two Dirac-cones is twice as large as in the case of a single Dirac point. Both currents were calculated for a system with an even number of sites. Note that an odd number leads to a parity-induced shift of the curves by $\Phi/\Phi_0 = 1/2$ (dashed lines).

Close to the Fermi level, all particles have the same velocity (i.e. slope of the dispersion), but differ in the direction of travel. In fact, the (pseudo-)spin associated with a mode is directly coupled to the particle's velocity. More precisely, the modes with $k \approx 0$ display have a defined spin $\uparrow$ or $\downarrow$, as can be seen from Eq. 93. This spin-momentum coupling or *chirality* is visualized in Fig. 16 and a characteristic property of Weyl fermions.

Let us discuss shortly the observed current behavior (see Fig. 17). The current is periodic with respect to the applied flux. This periodicity is fully analogous to the one observed in a superconductor. Moreover, the current is always such that the total magnetic flux (of the combined system of external field and the current) is a multiple of the flux quantum Φ_0. Microscopically, we observe that for $\Phi = n\Phi_0$ with $n \in \mathbb{Z}$, there is a degeneracy between any allowed left-moving mode k and its right-moving counterpart at $-k$. This degeneracy leads to an undefined current value. For $\Phi \neq n\Phi_0$, the symmetry is broken, and a defined, directed current is observed.

Mathematically, the current shape is obtained by summing over the contributions of all occupied modes; in the particular case of half-filling,

$$I = \frac{2et}{\hbar L} \sum_{\tilde{k}_{\text{occ}}} \frac{\partial}{\partial \varphi} \left| \sin \left(\frac{ka + \varphi}{2} \right) \right| \tag{137}$$

$$= \frac{et}{\hbar L} \left[\text{sign}(\varphi) \left[\cos \left(\frac{\varphi}{2} \right) + \cos \left(\frac{\pi + \varphi}{2} \right) \right] \right. \tag{138}$$

$$\left. + \sum_{0 < \tilde{k}_{\text{occ}} < \frac{\pi}{a}} \underbrace{\left[\cos \left(\frac{ka + \varphi}{2} \right) - \cos \left(\frac{-ka + \varphi}{2} \right) \right]}_{= -2 \sin(ka/2) \sin(\varphi/2)} \right].$$

where we rewrite the sum in pairs of positive and negative momenta and introduce an additional term to avoid over-counting. In the limit of large L, this yields a characteristic sawtooth shape,

$$I \stackrel{L \to \infty}{=} \frac{et}{\hbar L} \left(\text{sign}(\varphi) - \varphi \underbrace{\sum_{\tilde{k} > 0} \sin \left(\frac{ka}{2} \right)}_{= \frac{L}{\pi}} \right) = \frac{et}{\hbar L} \left(\text{sign}(\Phi) - 2 \frac{\Phi}{\Phi_0} \right) \tag{139}$$

$$= 2 I_0 \left(\frac{1}{2} - \frac{\Phi}{\Phi_0} - \left\lfloor \frac{1}{2} - \frac{\Phi}{\Phi_0} \right\rceil \right), \tag{140}$$

where first, we restrain ourselves to $-1 < \frac{\Phi}{\Phi_0} < 1$, and only in the last step we use the periodicity of the flux-dependence to generalize to arbitrary fluxes. The expression is equivalent to the one found in a continuum model [192]. The maximal current corresponds to a single charge traveling with Fermi velocity along the perimeter of the ring,

$$I_0 = \frac{e}{La} \frac{ta}{\hbar} = \frac{e v_F}{La}. \tag{141}$$

For the model with two Dirac points, we observe that the current is twice as large due to the presence of the Fermi doubling (see Fig. 17). Another relevant effect is the so-called *parity shift*: Depending on the parity of the particle number in the system, the current is shifted by $\Phi = \Phi_0/2$.

The most relevant quantity for our study, however, is the Drude weight, which we derived in Eq. (134). To avoid ambiguities due to the parity shift (in particular in the determination of para- and diamagnetic currents [185]), here and in the following, we will use the definition [187, 193, 194]

$$D = \begin{cases} \frac{La}{2\pi} \frac{\partial^2 E}{\partial \Phi^2} \Big|_{\Phi/\Phi_0 = 0} & \text{if } L \text{ odd}, \\ \frac{La}{2\pi} \frac{\partial^2 E}{\partial \Phi^2} \Big|_{\Phi/\Phi_0 = 1/2} & \text{if } L \text{ even}, \end{cases} \tag{142}$$

i.e. we study the current shift around the continuous zero-crossing of the current. The motivation behind this procedure is that D refers to the response of an equilibrium between the charge carriers. It therefore makes sense to calculate it at the value of Φ where the ground state energy has a minimum [187]. If we
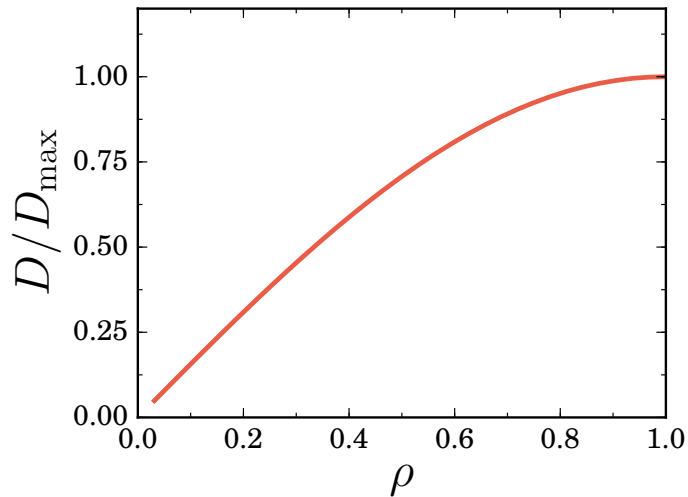
Figure 18: **Drude weight for the non-interacting system.** For different fillings of
the lattice, we plot the Drude weight. For $\rho \ll 1$, the current response in-
creases linearly with the number of particles: every particle is moving in an
almost empty lattice and can react independently to an applied field. For
$\rho \approx 1$, the presence of other particles prevents a linear scaling, the Drude
weight saturates.

allow for different fillings ρ of the dispersion band, a straight forward calculation
yields

$$D_0(\rho) = \underbrace{\left(\frac{v_F e^2}{\pi h}\right)}_{=\frac{2tae^2}{h^2}=D_{\max}} \frac{\pi}{2L} \cos\left(\frac{\pi}{2}(1-\rho)\right) \cot\left(\frac{\pi}{2L}\right). \tag{143}$$

Here, $\rho = 1$ corresponds to a density of one particle per lattice site j (often called
half-filling due to the possibility to occupy two internal states). The Drude weight
for different particle densities is shown in Fig. 18.

4.4 PERTURBATION THEORY

Our following study of the Drude weight of the interacting Weyl fermions will
rely on numerical, essentially exact calculations. Nevertheless, the results can be
substantiated with those from a many-body diagrammatic perturbation theory
that we introduce shortly in this section and will compare to when presenting
our numerical results. We acknowledge that this derivation was originally done
by M. Bischoff, a co-author of Ref. [24].

We have shown in Sec. 4.2 that the Drude weight can be understood as a
property of the ground state, namely the second derivative of the ground state
energy with respect to an applied flux (134). We also presented the Drude weight
for the free fermions in Eq. (143). In the presence of weak interactions, we
can study the perturbative change to the flux-dependent energies. This shift
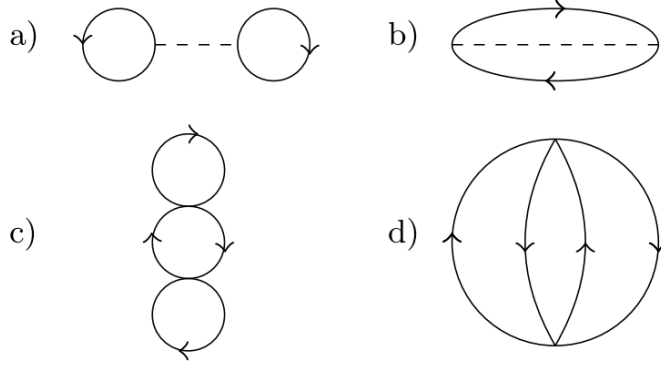translates into a correction of the free-fermionic Drude weight.

Figure 19: **Diagrams of the perturbation theory.** (a) The Hartree diagram and (b) the Fock diagram represent the processes contributing in first order perturbation theory to the ground state energy in Eq. (146). The second-order processes (150)+(151) are represented by the Hugenholtz diagrams in (c) and (d). The continuous lines correspond to propagators, the dashed lines identify inter-particle interactions.

As the perturbation contributions can be understood as scattering events, for convenience, we start by expressing the interaction term of the Hamiltonian in momentum basis,

$$H_{\text{int}} = \frac{1}{L} \sum_{s,s';r,r'} \sum_{k,k',q} W_{kk'q}^{srr's'} d_{k+q,s}^{\dagger} d_{k'-q,r}^{\dagger} d_{k',r'} d_{k,s'}, \tag{144}$$

where s, s', r, r' label the energy bands, on which the respective operators act, and $W_{kk'q}^{srr's'} = \sum_{\sigma,\sigma'} v_q^{\sigma,\sigma'} N_{k+q,s}^{\sigma} N_{k'-q,r}^{\sigma'} N_{k',r'}^{\sigma'} N_{k,s'}^{\sigma}$. The Fourier transformation of the interaction coefficients (96) yields

$$v_q^{\sigma,\sigma'} = [U \delta_{\bar{\sigma},\sigma'}/2 + V \cos(q) \delta_{\sigma,\sigma'} + \tilde{V} \cos(q) \delta_{\bar{\sigma},\sigma'}]. \tag{145}$$

We now expand the energy perturbatively with respect to the two-particle interactions. In the above language, the first order perturbation term can be expressed as

$$E_1(\Phi) = \frac{1}{L} \sum_{\sigma,k,k'} (W_{k,k',0}^{----}(\Phi) - W_{k,k',k-k'}^{----}(\Phi)), \tag{146}$$

where $W_{k,k',0}^{----}$ and $W_{k,k',k-k'}^{----}$ are the Hartree and the Fock term, respectively. This yields for the Drude weight

$$D_1 = \frac{\pi}{2L^2} \sum_{k,k'} (g_k g_{k'} - f_k f_{k'}) \left(v_{k-k'}^{\sigma,\bar{\sigma}} - v_{k-k'}^{\sigma,\sigma} + v_0^{\sigma,\sigma} - v_0^{\sigma,\bar{\sigma}} \right) \tag{147}$$

$$= \frac{\pi}{L^2} (V - \tilde{V}) \frac{\csc^2(\pi/(2L)) \sin^2(\pi\rho/2)}{1 + 2\cos(\pi/L)} \\ \times \cos(\pi/L)[\cos(\pi/L) - \cos(\pi\rho)], \tag{148}$$

and in the thermodynamic limit

$$\lim_{L \to \infty} D_1 = \frac{4}{\pi} (V - V') \sin^4(\pi\rho/2). \tag{149}$$

As the original free fermionic theory is gapless, the second-order processes in the perturbation theory have to be treated carefully. The strategy here is to first determine the contributions in the finite system and then study the scaling for $L \to \infty$. Two possible processes contribute to the energy $E_2 = E_2^{(1)} + E_2^{(2)}$, which are represented by Hugenholtz diagrams in Fig. 19 and given as

$$E_2^{(1)} = \frac{1}{L^2} \sum_{k,k',q} \frac{1}{\varepsilon_-(\tilde{k}') - \varepsilon_+(\tilde{k}')} [(k_-, k'_+|v|k_-, k'_-) - (k_-, k'_+|v|k'_-, k_-)] \\ \times [(k'_-, q_-|v|k'_+, q_-) - (k'_-, q_-|v|q_-, k'_+)] \tag{150}$$

and

$$E_2^{(2)} = -\frac{1}{4L^2} \sum_{k,k',q} \frac{(k_-, k'_-|v|\bar{k}_+, \bar{k}'_+) - (k_-, k'_-|v|\bar{k}'_+, \bar{k}_+)}{\varepsilon_-(\tilde{k}) - \varepsilon_+(\tilde{k}) + \varepsilon_-(\tilde{k}') - \varepsilon_+(\bar{k}' + 2\varphi)} \\ \times [(\bar{k}_+, \bar{k}'_+|v|k_-, k'_-) - (\bar{k}_+, \bar{k}'_+|v|k'_-, k_-)]. \tag{151}$$

In these expressions, the bracketed terms evaluate to

$$(k_s, k'_{s'}|v|q_r, q'_{r'}) = \frac{U}{2} \sum_\sigma N_{\tilde{k},s}^\sigma N_{\tilde{k}'s'}^{\bar{\sigma}} N_{\tilde{q},r}^\sigma N_{\tilde{q}'r'}^{\bar{\sigma}} \tag{152}$$

for on-site interactions U and

$$(k_s, k'_{s'}|v|q_r, q'_{r'}) = \sum_\sigma [V \cos(k - q) N_{\tilde{k},s}^\sigma N_{\tilde{k}'s'}^\sigma N_{\tilde{q},r}^\sigma N_{\tilde{q}'r'}^\sigma \\ + \tilde{V} \cos(k - q) N_{\tilde{k},s}^\sigma N_{\tilde{k}'s'}^{\bar{\sigma}} N_{\tilde{q},r}^\sigma N_{\tilde{q}'r'}^{\bar{\sigma}}] \tag{153}$$

for the nearest-neighbor interactions V and V'. Through algebraic manipulations we find that $E_2^{(2)}$ always evaluates to zero. Therefore

$$E_2 = E_2^{(1)} = -\frac{1}{32L^2 t} \sum_{k'} \frac{1}{g_{\tilde{k}'}} \left\{ U^2 \left[\sum_k \sin\left(\frac{k - k'}{2}\right) \right]^2 \right. \\ \left. + 2 \left[\sum_k \sin\left(\frac{k - k'}{2}\right) [(\tilde{V} + V)\cos(k - k') + (\tilde{V} - V)(\cos\tilde{k} - \cos\tilde{k}' + 1)] \right]^2 \right\}. \tag{154}$$

Now, for the U-dependent term we can evaluate the Drude weight contribution by taking the derivative with respect to Φ and obtain

$$D_2^U = -\frac{U^2}{32L^2 t} \frac{2\pi}{L} \sum_{k'} \left(\frac{2\dot{g}_{k'} - g_{k'}\ddot{g}_{k'}}{g_{k'}^3} \right) \left\{ \sin\left(\frac{k - k'}{2}\right) \right\}^2. \tag{155}$$

In the limit $L \to \infty$, the energy can be expressed as the integral

$$\lim_{L \to \infty} D_2^U = -\frac{U^2}{8\pi^2} \sin^4\left(\frac{\pi\rho}{4}\right) \int_{k'_{\text{occ}}} \frac{2 - \sin^2(k'/2)}{\sin(k'/2)} \text{sgn}(k') dk'. \tag{156}$$

The limit of the V-dependent contribution is less evident. We spare it here and note that we evaluated the term numerically, checking the convergence for $L \to \infty$.

(a)
(b)
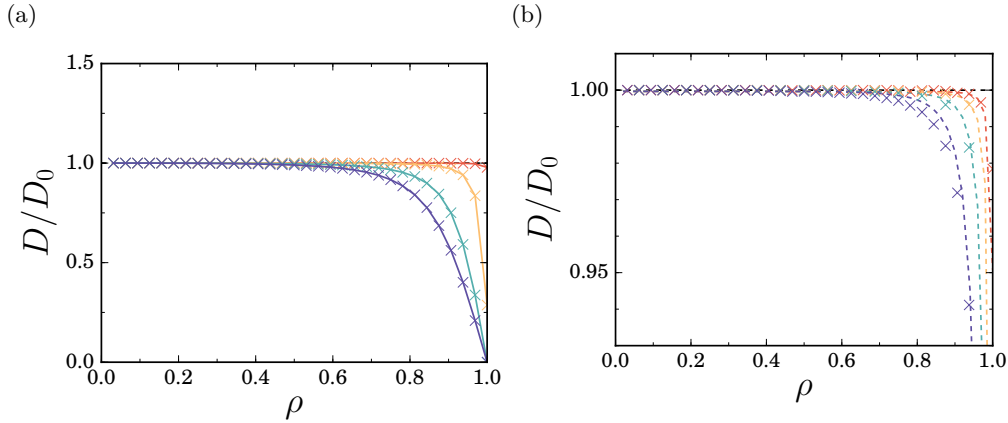
Figure 20: **Drude weight suppression for on-site interactions.** (a) The Drude weight D (in units of the non-interacting Drude weight D_0) for the model with exclusive on-site interactions ($V = V' = 0$) is reduced with respect to the non-interacting system. Red: $V/t = 0.0625$, orange: $V/t = 0.5$, blue: $V/t = 2.0$, violet: $V/t = 4.0$. (b) Comparison of the results from DMRG (crosses) and second-order perturbation theory for small U (dashed lines), showing a good agreement. Red: $U/t = 0.0625$, orange: $U/t = 0.125$, blue: $U/t = 0.25$, violet: $U/t = 0.5$. The numerical results were determined in a system with $L = 32$ lattice sites.

4.5 CURRENT RESPONSE FOR DIFFERENT TYPES OF INTERACTIONS

We have developed an understanding of the current response in a system of free Weyl fermions and explored the limit of weak interactions. We now turn to arbitrary interaction strengths and present the results of our numerical studies. Along the way, we also discuss the predictions from perturbation theory and compare the results. For technical details of the simulations, we refer the reader to App. A.5.

4.5.1 *On-site interactions*

If the particles are interacting only through on-site interactions U (i.e. $V = V' = 0$), we observe a suppression of the Drude weight, $D < D_0$. This is shown in Fig. 20a.

Indeed, the first order correction to the Drude weight (149) evaluates to zero, $D_1 = 0$. The second-order contribution D_2 (156) can only be negative, i.e. leading to a suppression with respect to D_0. The agreement of the second-order perturbation theory with the exact results is presented in Fig. 20b. Note that for the free Weyl fermions, the Drude weight scaling is reminiscent of the one found in the Hubbard model [185].

(a)

(b)
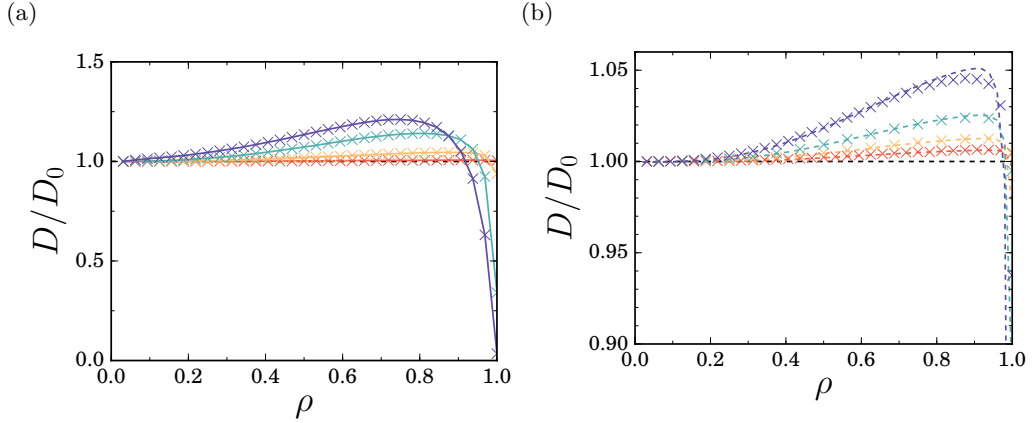
Figure 21: **Drude weight enhancement for inhomogeneous nearest-neighbor interactions with $V > V'$.** (a) The (numerically determined) relative Drude weight D/D_0 for fixed $V = 2V'$ is plotted against the filling ρ: The current response shows an interaction-dependent enhancement. Red: $V/t = 0.0625$, orange: $V/t = 0.5$, blue: $V/t = 2.0$, violet: $V/t = 4.0$. (b) For weak interactions, the numerical result (crosses) are shown together with the second-order perturbation theory calculations (dashed lines): they show good agreement. Red: $V/t = 0.0625$, orange: $V/t = 0.125$, blue: $V/t = 0.25$, violet: $V/t = 0.5$. Both plots show results for systems with $L = 64$ sites.

Figure 22: **Drude weights for combined on-site and nearest-neighbor interactions.** The relative Drude weight is shown for fixed $V/t = 2V'/t = 4.0$ and different on-site interactions: At intermediate fillings the Drude weight enhancement is stable for comparably large on-site interactions. Only for $U \gg V$, the Drude weight is suppressed. Red: $U = 0$, orange: $U = V$, blue: $U = 3V$, violet: $U = 10V$.
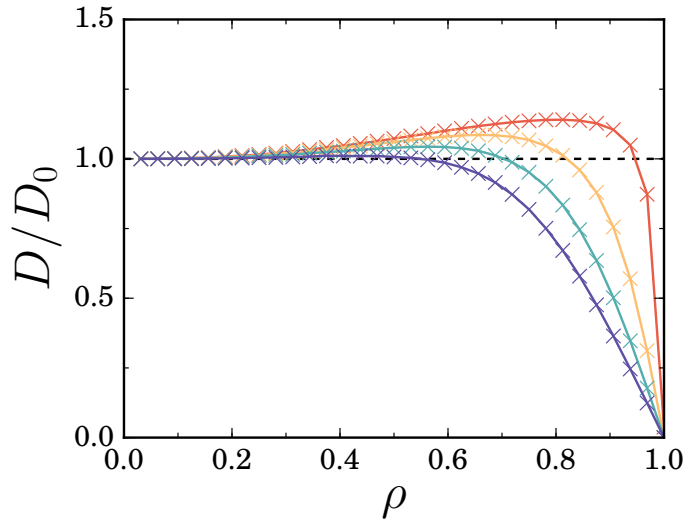
(a)

(b)
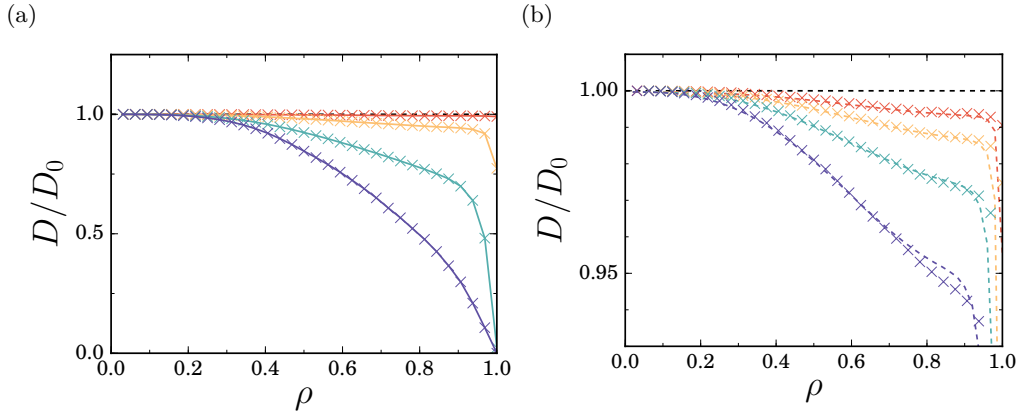
Figure 23: **Drude weight suppression for inhomogeneous nearest-neighbor interactions with $V < V'$.** (a) The relative Drude weight D/D_0 for fixed $V' = 2V$ is plotted against the filling ρ: The current response shows an interaction-dependent suppression. Red: $V'/t = 0.0625$, orange: $V'/t = 0.5$, blue: $V'/t = 2.0$, violet: $V'/t = 4.0$. (b) The same quantity for weak interactions: Tensor network results (crosses) are compared to the perturbation theory prediction. Red: $V'/t = 0.0625$, orange: $V'/t = 0.125$, blue: $V'/t = 0.25$, violet: $V'/t = 0.5$; here $L = 32$.

4.5.2 *Nearest-neighbor interactions*

For nearest-neighbor interactions we find a quite different behavior. As our perturbation theory results show, the effect on the Drude weight depends on the difference of the inter- and the intra-species interactions $(V - V')$ (149). We can therefore distinguish different cases.

If the interaction is *equal* for the fermions with same and different pseudo-spin, the first order term of the perturbation theory is suppressed, $D_1 = 0$. Indeed, the numerical analysis shows that $D = D_0$ for all fillings (with small corrections for $\rho = 1$).

On the other hand, if the interaction between particles of the same pseudo-spin dominates the one with opposite spin, we expect an enhancement of the Drude weight, $D_1 > 0$. In the following, we fix $V = 2V'$ and present the results of our numerical study in Fig. 21. In particular, we observe that for intermediate fillings, the effect leads to an amplification of the current response to up to 25 %. The agreement for small interactions with the perturbation theory is shown in Fig. 21b. Notably, the effect does not only exist on a perturbative scale, but subsists for comparably large interactions $V, V' \gg t$. For physical setups, nearest-neighbor interactions often occur with on-site interactions of the same order. We therefore also study the competition of the interactions. The results are shown in Fig. 22: The enhancement of the Drude weight is stable for a large range of on-site interactions. Only comparably strong on-site interactions (here $U \approx 10V$) lead to a suppression of the Drude weight for all the fillings.

For completeness, we also present results for the case $V < V'$, in particular $V' = 2V$ (Fig. 23). The observed Drude weight suppression further validates the predictions of the perturbation theory.

4.6   CONTINUUM VS. THERMODYNAMIC LIMIT

The results presented in the above section were obtained for discretized lattice rings. The obtained results converge fast in the number of lattice sites and can therefore be seen as a good approximation to the limit $L \to \infty$. We can interpret these results in two ways: One possibility is to keep the parameters of our Hamiltonian and the lattice constant fixed and to increase the number of sites on the lattice. This would physically correspond to an increase in the circumference of the ring and yields a scaling towards a thermodynamic limit. Alternatively, we can consider a ring of a given finite length and decrease the lattice spacing in consequent numerical simulations. In this scenario, the parameters of the lattice Hamiltonian are chosen such as to represent a discretization of the continuum problem (compare Sec. 4.1.1). We discuss the equivalence of the two perspectives in the following.

Thermodynamic limit perspective. To consider the thermodynamic limit, we assume a lattice ring encircling a solenoid with flux Φ. The lattice constant a and all the coefficients of the model (89) are kept constant when increasing the number of lattice sites L. In the case of free fermions, we can see from Eq. (141) that the maximal current scales like $I \propto 1/L$ with increasing number of lattice sites. This decrease is quite intuitive: With growing number of lattice sites, the diameter of the ring extends and the constant circulation caused by the flux entails a weaker current in larger distance. The Drude weight (143), however, converges to a constant. If we include interactions, we observe the changes of the Drude weight as discussed in the previous section.

Continuum perspective. In the continuum problem, we consider Weyl fermions moving around a flux Φ on a ring with fixed physical length $La \equiv \tilde{L}$ and velocity $c = v_F$. To account for these properties, the coefficients of the lattice model have to be adapted as $t = \hbar v_F / a$, $U = u/a$ and $V = v/a^2$ (compare Secs. 4.1.1 and 4.1.3). In the example of the free fermions, we see that neither the current (141) nor the Drude weight (143) is affected by such a scaling, i.e. (by construction) they are convergent with $L \to \infty$. In the study of the Drude weight, the continuum and the thermodynamic limit of the lattice model can therefore be treated equivalently.

If we include interactions and want to derive definitive statements about the continuum model from the lattice model with fixed t, U, V and V', these coefficients should scale proportionally when increasing the number of lattice sites. This is indeed the case for the hopping $t \propto 1/a$ and the on-site interactions $U \propto 1/a$. It is, however, not true for the nearest-neighbor interactions $v \propto 1/a^2$ and $v' \propto 1/a^2$. Nonetheless, we can draw conclusions valid for the continuum model from our results. In particular, if we take a continuum configuration with some fixed v_F, u, and require $v, v' \propto ua$, the results of the discretization with lattice constant a fully apply.

INTERACTING SU(N)-FERMIONS IN A HARMONIC TRAP

In the previous sections, we first studied an intrinsic lattice system. We then looked at a hybrid of a continuum and a lattice system, i.e. a field theory which can be discretized and also plays an important role for lattice systems that are realizable with optical lattices. We now turn to an inherently continuous system of fermions with different internal states confined in a harmonic potential and interacting through a $SU(N)$-invariant contact potential. Thereby, we explore still another aspect of the interplay of interactions, geometry and symmetry in one-dimensional systems. Interestingly, we will see how the symmetry of the interactions between the particles can lead again to an organized system, which - despite the continuity of the underlying problem - can be understood as an effective lattice system in the limit of strong interactions.

The organization of particles with different internal states within a one-dimensional confinement is closely linked to the question of magnetic ordering. Quantum magnetism is usually understood as a lattice phenomenon, but it does also occur in continuous systems [195]. Conceptually, the phenomenon can be understood by mapping the internal degrees of freedom of strongly interacting multi-component particles in continuous systems to a $SU(N)$-spin chain. We will see that this leads to a so-called *Sutherland Hamiltonian* [196, 197] (compare Eq. (185)). Such continuous magnetic systems can be considered attractive alternatives to lattice systems where the accessible coupling-parameter range is limited [198]. Due to the advances in the control of ultracold gases, the setup has recently stirred a great experimental interest [199, 200] and a renewed theoretical attention [201–204]. Apart from the magnetism aspect, the understanding of fermionic systems with a larger $SU(N)$-symmetry is also of interest for other fields: In particle physics, e.g., SU(3)-symmetries occur in quantum chromodynamics; in nuclear physics, an SU(6)-symmetry might unify the description of baryons and mesons [195, 205].

Our investigation here is driven by the question of how to explore emergent magnetic structures with simple experimental techniques. To this end, we develop an intuitive understanding of how the particle numbers in the mixture constrain the eigenstates to particular representations of the $SU(N)$-symmetry. In order to identify the different magnetic structures in the physical system, it is important to understand how their symmetry connects to experimentally accessible features. We therefore analyze density and momentum distributions of the particles and discuss in particular a signature which occurs in the momentum distributions of contact-interacting particles, the so-called *Tan contact*. By exploiting the Lieb-Mattis theorem on the energetic ordering of $SU(N)$-symmetric states [206], we establish a connection between the symmetry of the states and their Tan contacts. The latter, due to their accessibility in time-of-flight measurements, permit an identification of the magnetic structure/symmetry.

We proceed as follows: We first introduce the model of interest and the corresponding Hamiltonian (Sec. 5.1). We then study the symmetry of the setup in Sec. 5.2: Starting from a two-particle example, we introduce the notion of Young diagrams and how they can be used to characterize the symmetry under commutation of particles. We generalize to systems of N particles and see that Young diagrams correspond to the irreducible representation of the S_N-symmetry group which classifies the permutations of N particles. This group is closely related to the SU(κ)-symmetry of particles with κ internal states, and therefore relevant for our understanding of the system. In Sec. 5.3, we present experimentally accessible observables. We then combine the acquired knowledge of symmetries and observables to explore different interaction regimes: After a short discussion of free fermions (Sec. 5.4), we turn to the opposite regime of strong interactions in Sec. 5.5, for which we derive an effective description in terms of a spin-lattice model. We characterize the states by their symmetry and establish a connection to the measured Tan contacts. This analysis is extended to the intermediate regime in Sec. 5.6. Due to the inaccessibility via analytical calculations, we explore it by means of MPS calculations and a scaling approach that allows us to transfer the results to larger particle numbers. In Sec. 5.7, we open the model to mixtures of both fermions and bosons and discuss how the previous results generalize. Details of how to address this continuous problem with MPS are presented in App. A.4. Specifications of an (existing) experimental setup to realize the presented model can be found in App. B.2.3.

The findings of this section have been partially published in Refs. [25] and [26].

5.1 MODEL AND HAMILTONIAN

We consider a κ-component Fermi gas, consisting of $N = \sum_{\nu=1}^{\kappa} N_\nu$ particles of mass m, which are trapped in a one-dimensional confinement and interact through a contact potential. This setup is described by a Hamiltonian

$$H = H_0 + H_{\text{int}}, \tag{157}$$

where we collect the kinetic energy and the external potential in H_0 and the interactions in H_{int}.

If we approximate the trapping potential with a one-dimensional harmonic trap of frequency ω (and characteristic length $a_{\text{ho}} = \sqrt{\hbar/m\omega}$), the free Hamiltonian reads

$$H_0 = \sum_{\nu=1}^{\kappa} \sum_{j=1}^{N_\nu} \left(-\frac{\hbar^2}{2m} \frac{\partial^2}{\partial x_{j,\nu}^2} + \frac{1}{2} m\omega^2 x_{j,\nu}^2 \right). \tag{158}$$

The two-body interaction potential H_{int} arises due to scattering of particles and is described by $v(x - x') = g_{1D}\, \delta(x - x')$, where $g_{1D} = -2\hbar^2/ma_{1D}$ and a_{1D} is the 1D effective scattering length [207]. If the scattering length is independent

of the internal state of the particles, the interaction becomes $\mathrm{SU}(\kappa)$-symmetric. In this scenario, the interaction part of the Hamiltonian reads

$$H_{\mathrm{int}} = g_{1\mathrm{D}} \sum_{\nu<\nu'}^{\kappa} H_{\mathrm{int},(\nu,\nu')} \equiv g_{1\mathrm{D}} \sum_{\nu<\nu'}^{\kappa} \sum_{j=1}^{N_\nu} \sum_{j'=1}^{N_{\nu'}} \delta(x_{j,\nu} - x_{j',\nu'}) \tag{159}$$

$$\left(= g_{1\mathrm{D}} \sum_{1\leq i<j\leq N} \delta(x_i - x_j) \right). \tag{160}$$

The definition (159) explicitly excludes the interaction between fermions of the same species, as no s-wave scattering can occur between them. Without changing the physics, we can include such terms (160), knowing that they will never yield a contribution due to the anti-symmetry of the wave functions.

The effect of the interactions can be reformulated in terms of a *cusp-condition* for each pair of coordinates which belong to different species, $x = x_{j,\nu} - x_{j',\nu'}$,

$$\frac{1}{g_{1\mathrm{D}}} \left[\partial_x \Psi(x = 0^+) - \partial_x \Psi(x = 0^-) \right] = \frac{2m}{\hbar^2} \Psi(x = 0), \tag{161}$$

with the many-body wave function $\Psi = \Psi(X) = \Psi(x_1, \dots x_N)$ and the coordinate vector $X = (x_1, \dots, x_N) = (x_{1,1}, \dots x_{N_1,1}, x_{1,2}, \dots x_{N_2,2}, \dots, x_{1,\kappa} \dots x_{N_\kappa,\kappa})$.

For later use, we note that we can make the problem dimensionless by writing the energy in terms of the harmonic oscillator frequency ω and the distances in terms of the harmonic oscillator length, $\tilde{x} = x/a_{\mathrm{ho}}$:

$$H = \hbar\omega \left[\sum_{\nu=1}^{\kappa} \sum_{j=1}^{N_\nu} \left(-\frac{1}{2} \frac{\partial^2}{\partial \tilde{x}_{j,\nu}^2} + \frac{1}{2} \tilde{x}_{j,\nu}^2 \right) + \alpha \sum_{1\leq i<j\leq N} \delta(\tilde{x}_i - \tilde{x}_j) \right] \tag{162}$$

The dimensionless effective interaction parameter $\alpha = a_{\mathrm{ho}} m g_{1\mathrm{D}}/\hbar^2 = 2a_{\mathrm{ho}}/a_{1\mathrm{D}}$ then relates the effective scattering length $a_{1\mathrm{D}}$ to the harmonic oscillator length a_{ho}.

5.2 SYMMETRY OF THE SYSTEM

Our target in this chapter is to establish a link between the symmetry of the eigenstates of the Hamiltonian (157) and experimentally accessible properties. For systems of electrons with spin, a close relation between the symmetry of a state and its magnetic structure was shown [206]. Namely, it was proven that ground states of electrons in an arbitrary symmetric potentials with different total spins $S < S'$ will be ordered energetically as $E(S) < E(S')$. This means that the many-body system realizes an unmagnetized ground state if the total spin is not fixed a priori. In the same paper, it was demonstrated that a similar ordering relation also holds for system with more than two species ($\kappa > 2$), and therefore a higher symmetry $\mathrm{SU}(\kappa)$. This motivates the identification of the irreducible representations of the symmetry in the states of our system, which we then can link to experimentally accessible quantities.

In this section, we therefore develop an intuition of the $\mathrm{SU}(\kappa)$ group and the related S_N group of permutations of N objects. As a warm-up, we review
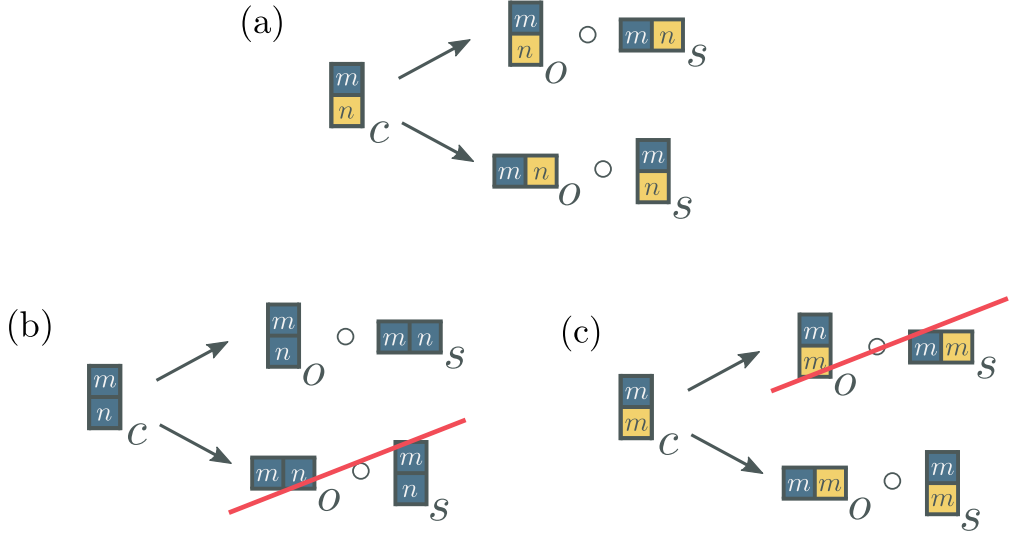
Figure 24: **Symmetries of two-particle states and Young diagrams.** (a) Two fermions in orbitals m and n and internal states σ (blue) and τ (yellow) display an anti-symmetric commutation relation (163), indicated by two vertically stacked boxes. The overall wave function (with index c) can be split into an orbital and a spin component. If the wave function is symmetric in the orbital part (horizontally stacked boxes), it has to be anti-symmetric under spin-exchange (164) and vice versa (165). (b) If both particles have the same spin, $\sigma = \tau$, they are necessarily symmetric under spin-exchange and the orbital exchange is anti-symmetric. (c) Likewise, if two particles share the same orbital label, $n = m$, the orbital exchange is symmetric, and the spin-exchange anti-symmetric.

the symmetry and notation for states of two (identical) particles (Sec. 5.2.1). Based on general considerations on the symmetric and anti-symmetric exchange of particles, we introduce Young diagrams, which a diagrammatic labeling of the irreducible representations of the S_N-symmetry, and discuss the connection to the SU(κ) group (Sec. 5.2.2). We then show how to construct the permissible diagrams for a given mixture of fermions and explain the *pouring principle*, which establishes an energy ordering between the ground states of different symmetry sectors (Sec. 5.2.3).

5.2.1 *Symmetry of states - part I*

Assume that a single fermion in an eigenstate of some potential is fully characterized by its *orbital n* (energy level) and its internal state $\sigma \in \{1, \ldots, \kappa\}$, for which we use the terms *spin* or *species* interchangeably. The single-particle wave function can then be written as $|m, \sigma\rangle = |m\rangle \otimes |\sigma\rangle$. If there are two particles in the system, one could imagine a state $|m, \sigma\rangle \otimes |n, \tau\rangle$, where the first two entries (m, σ) label one particle and the other two entries (n, τ) the other particle. We know, however, that for fermions the many-body wave function is anti-symmetric, and the above notation fails to deliver this property. If we de-

note a valid many-body state as $|m, \sigma; n, \tau\rangle_a$, the exchange of the labels of the two particles - the first takes (n, τ), the second takes (m, σ) - leads to a change of the sign of the wave function:

$$|n, \tau; m, \sigma\rangle_a = -|m, \sigma; n, \tau\rangle_a . \tag{163}$$

The state can then be read as: One of the particles has labels (m, σ), the other particle has labels (n, τ) - but due to the indistinguishability of the two particles, we cannot tell which particle has which label.

The exchange of only the spin-label $\tau \leftrightarrow \sigma$ can have either an anti-symmetric or a symmetric effect (see Fig. 24). The first case corresponds to $|m, \sigma; n, \tau\rangle_a = -|m, \tau; n, \sigma\rangle_a$. If we want to express this state in the basis of the labeled, individual particles, we have to choose signs such that the above condition and the overall constraint (163) are fulfilled. We then obtain

$$
\begin{aligned}
|m, \sigma; n, \tau\rangle_a =& \frac{1}{2} \left(|m, \sigma\rangle \otimes |n, \tau\rangle - |m, \tau\rangle \otimes |n, \sigma\rangle \right. \\
& \left. + |n, \sigma\rangle \otimes |m, \tau\rangle - |n, \tau\rangle \otimes |m, \sigma\rangle \right) \\
=& \frac{1}{2} \underbrace{\left(|m, n\rangle + |n, m\rangle \right)}_{|m;n\rangle_s} \underbrace{\left(|\sigma, \tau\rangle - |\tau, \sigma\rangle \right)}_{|\tau;\sigma\rangle_a}
\end{aligned}
\tag{164}
$$

where in the last step, we have permuted the dimensions such that the orbital degrees of freedom appear first and the spins second. We observe that, as a consequence of the anti-symmetric spin, the orbital is then symmetric. On the other hand, if the spin-exchange is symmetric, $|m, \sigma; n, \tau\rangle_a = |m, \tau; n, \sigma\rangle_a$, it follows

$$
\begin{aligned}
|m, \sigma; n, \tau\rangle_a =& \frac{1}{2} \left(|m, \sigma\rangle \otimes |n, \tau\rangle + |m, \tau\rangle \otimes |n, \sigma\rangle \right. \\
& \left. - |n, \sigma\rangle \otimes |m, \tau\rangle - |n, \tau\rangle \otimes |m, \sigma\rangle \right) \\
=& \frac{1}{2} \underbrace{\left(|m, n\rangle - |n, m\rangle \right)}_{|m;n\rangle_a} \underbrace{\left(|\sigma, \tau\rangle + |\tau, \sigma\rangle \right)}_{|\tau;\sigma\rangle_s}
\end{aligned}
\tag{165}
$$

and we find an anti-symmetric exchange for the orbitals.

We can now write the orbital part of the wave function in position basis, $|n\rangle = \int_{x=-\infty}^{\infty} \phi_n(x) |x\rangle$ where $\phi_n(x) = \langle x|n\rangle$. For an anti-symmetric orbital function $|m; n\rangle_a = -|n; m\rangle_a$, the exchange of coordinates (positions) is equivalent to the exchange of orbital labels in the sense that the earlier also inverts the sign:

$$
\begin{aligned}
\langle x_1, x_2 | m; n\rangle_a &= \frac{1}{2} \left(\langle x_1, x_2 | m, n\rangle - \langle x_1, x_2 | n, m\rangle \right) \\
&= \frac{1}{2} \left(\langle x_1|m\rangle \langle x_2|n\rangle - \langle x_1|n\rangle \langle x_2|m\rangle \right) \\
&= \frac{1}{2} \left(\phi_m(x_1)\phi_n(x_2) - \phi_n(x_1)\phi_m(x_2) \right) \\
&= -\frac{1}{2} \left(\phi_m(x_2)\phi_n(x_1) - \phi_m(x_1)\phi_n(x_2) \right) = -\langle x_2, x_1 | m; n\rangle_a .
\end{aligned}
\tag{166}
$$

We therefore use the terms *orbital* and *spatial* symmetry interchangeably in the following, in particular when the labels m and n do no longer correspond to the energy eigenlevels of the harmonic oscillator.

The above is basic knowledge. Often, however, the distinction between orbital and spin degree of freedom is blurred through unclear notation, and the duality between the two is therefore unclear. We have refreshed it here to make more advanced statements about the symmetries of the many-body states of more than two particles in the following.

5.2.2 S_N-symmetry, $SU(\kappa)$-symmetry and Young tableaux

Consider a function of N variables, e.g. the orbital part of our wave function $|m_1, \sigma_1; \ldots; m_N, \sigma_N\rangle$ in position basis, $\psi(x_1, x_2, \ldots, x_N)$. Alternatively, we could look at the spin component of the wave function, and then had the spin labels for the N particles as arguments. Let us assume that $\psi(x_1, x_2, \ldots, x_N)$ is an eigenfunction of the Hamiltonian. Due to the invariance of the Hamiltonian under any permutation P of particles, the wave function $\psi(x_{P(1)}, \ldots, x_{P(N)})$ is also an eigenfunction belonging to the same value. Then, in particular, any permutation of two particles can entail a sign +1 (symmetric) or -1 (anti-symmetric orbital exchange).

S_N-SYMMETRY.   We can characterize these permutations by their effect on the wave function as e.g. "Any exchange of two particles is anti-symmetric", "Any exchange is symmetric", "$N-1$ particles behave anti-symmetric under exchange, but symmetric with respect to the last", etc. This classification corresponds to so-called cycles, and leads to the irreducible representations (irreps) of the symmetry group S_N. These irreps can be visualized through so-called *Young diagrams* (see Fig. 25a): N boxes are aligned such that the number of boxes in every consecutive column and row does not increase. If all boxes are aligned in a row, this means that the wave function is fully symmetric under any exchange of two particles. For a Young diagram with all boxes aligned in a column, any exchange of two particles is anti-symmetric. All other Young diagrams describe mixed symmetries, i.e. states that are symmetric to certain permutations and anti-symmetric with respect to others.

$SU(\kappa)$-SYMMETRY.   We can now associate each of the particles with a fermionic species $\nu \in \{1, \ldots, \kappa\}$ and fill the diagrams with these labels. Graphically, we indicate this by painting the boxes in different colors. Due to the overall anti-symmetry of the fermionic wave function, the spatial exchange of two particles of the same species is necessarily anti-symmetric (compare Fig. 24). As a consequence, only boxes in the same column can share the same color. On the other hand, for two particles in different species, the order of the species (the color ordering) does not matter (Fig. 25b). We can therefore avoid overcounting by demanding that the index of the species (or the associated color) does not decrease in vertical direction and has to increase in horizontal direction. The so-labeled Young diagrams are called *Young tableaux*. We observe that
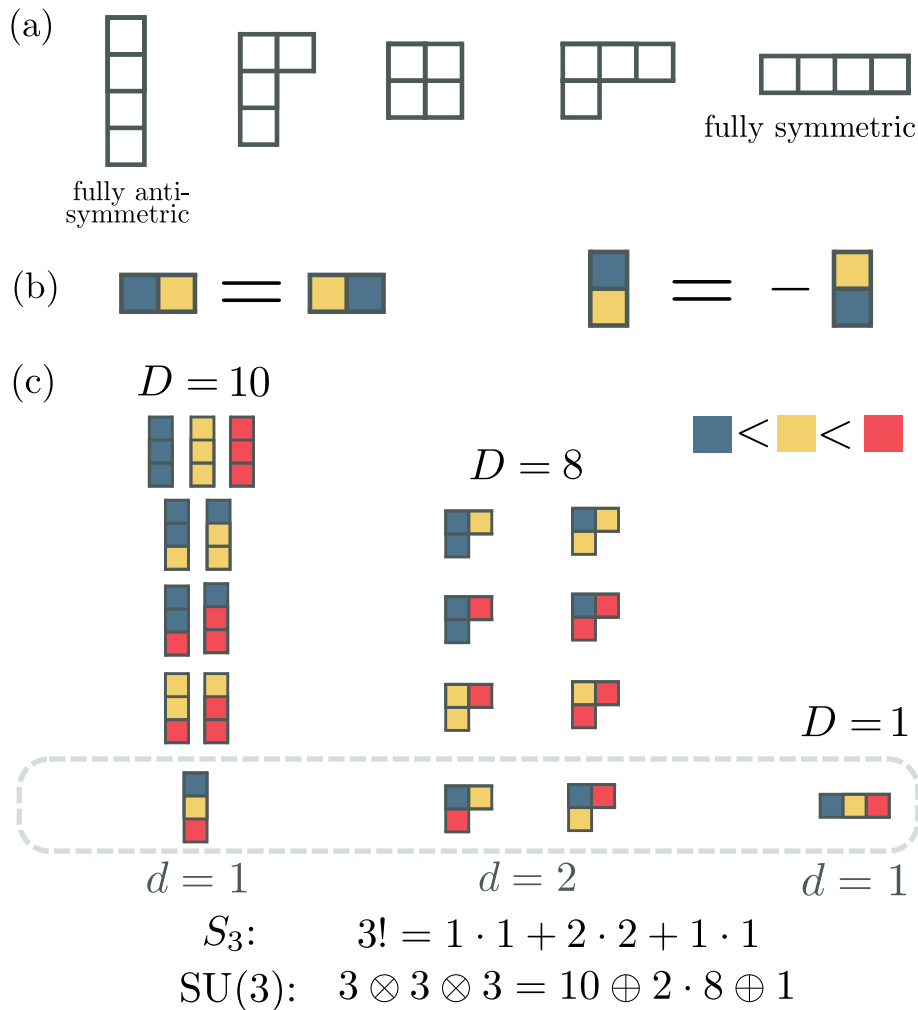
Figure 25: **Simple examples of Young diagrams and tableaux.** (a) All possible Young diagrams with $N = 4$ particles. (b) The commutation rules for a symmetric (left) and an anti-symmetric exchange (right) in diagrammatic notation. (c) For N distinguishable particles (here: $N = 3$ and $\kappa = 3$, blue, yellow and red), $N!$ permutations are possible which fall into irreducible subspaces of the symmetric group S_N. These irreducible subspaces are given by the possible Young diagrams with three boxes. To obtain the degeneracy d of these representations, one can count the so-called *standard Young tableaux* which are built by filling the boxes such that the colors increase in their ordering along rows and columns (dashed box). At the same time, d represents the multiplicity of the same tableaux (tableaux that are equivalent under the rule in (b)); therefore here: $N! = 3! = 1 \cdot 1 + 2 \cdot 2 + 1 \cdot 1$. Alternatively, one can fill the Young diagrams with all possible combinations of species for which the ordering is strictly increasing in every row and non-decreasing in each column. Counting these then yields the multiplicities D of the respective irreps of the SU(κ)-group (decouplet, octet, singlet). The degeneracy d of these irreps is equivalent to the multiplicity of the standard Young tableaux. Therefore we find for the $3 \otimes 3 \otimes 3$ representation of SU(3): $3^3 = 1 \cdot 10 + 2 \cdot 8 + 1 \cdot 1$.
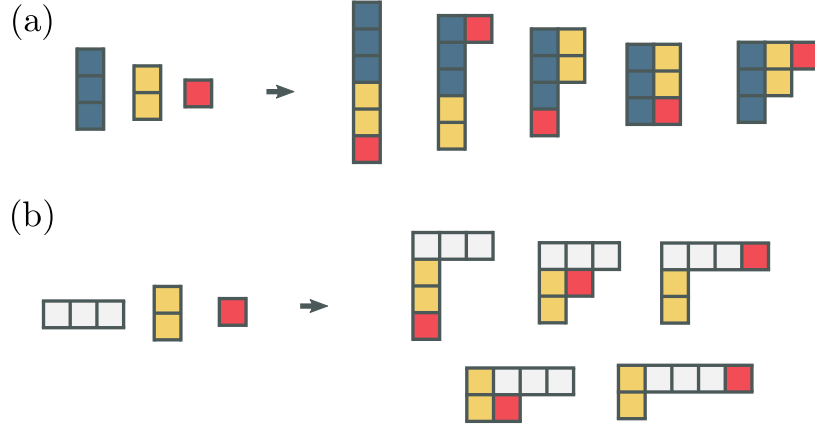
Figure 26: **Permissible Young diagrams for the spatial/orbital wave function of given particle configurations.** (a) For the example of $N = 6$ particles with $\kappa = 3$ species distributed as $N_1 = 3$ (blue), $N_2 = 2$ (red) and $N_3 = 1$ (yellow), we show the permitted symmetries of the orbital wave function. The dual spin symmetry is obtained by transposing the diagrams. (b) For later use, we also present the possible symmetries of a similar mixture where the first species is bosonic and the spatial exchange of same-species particles is symmetric.

these Young tableaux generate a basis of the $\kappa \otimes \ldots \otimes \kappa$-representation of SU($\kappa$) (see Fig. 25c). Physically, the SU(κ)-symmetry expresses the invariance under a "rotation" in the κ-dimensional label space. A state is energetically degenerate to another if its commutation relations are not altered - independently of the particular labeling of the particles. This is captured by the multiplicity obtained by counting the tableaux created following the above instructions and known as the *Wigner-Eckart theorem* for the SU(2)-group.

For further details on the relation between the SU(κ) and the S_N-symmetry, we refer the reader to the standard literature [208]. Here, we summarize that the above construction rules allow us to efficiently describe the symmetry of a state. In the following, we show how to construct the allowed Young diagrams for a given fermionic mixture.

5.2.3 *Symmetry of states - part II*

Whenever two particles in the wave function pairwise exchange their spin label in symmetric fashion, the permutation of the orbital label must be anti-symmetric and vice-versa in order to preserve the overall anti-symmetry of the wave function. As an example, assume some state $|\Psi\rangle = |m_1, \tau_1; m_2, \tau_2; m_3, \ldots, m_N, \tau_N\rangle$, where $\{m_1, \ldots, m_N\}$ labels the orbital quantum number and $\{\tau_1, \ldots, \tau_N\}$ represents the spin states of the particles.

If all particles in the systems are fermions, any exchange of two particles has to be anti-symmetric, $|\ldots; m_x, \tau_x; \ldots; m_y, \tau_y; \ldots\rangle = -|\ldots; m_y, \tau_y; \ldots; m_x, \tau_x; \ldots\rangle$. For particles of the same species, $\tau_x = \tau_y$, the exchange of spin labels is necessarily symmetric and as a consequence the orbital wave function is anti-symmetric
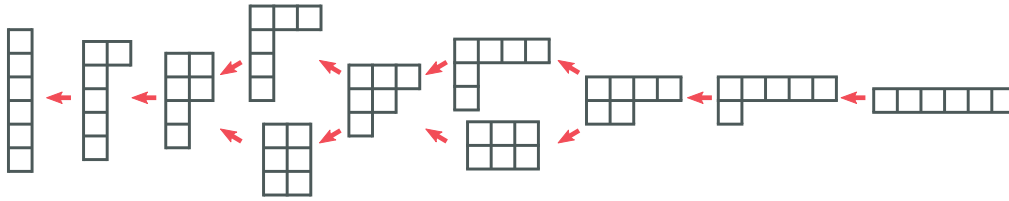
Figure 27: **Young diagrams for a system of six particles.** For a system of six particles, we show all the (in principal) possible Young diagrams: to the very left, the completely anti-symmetric configuration, to the very right the Young tableau of a fully symmetric state; in between intermediate symmetries which are symmetric with respect to particle exchange within columns, anti-symmetric with respect to rows. The red arrows indicate the pouring principle for the orbital symmetry: The further left a diagram, the higher the associated ground state energy with that symmetry configuration.

under any exchange within the same species. For the exchange of particles of different species (with different spin), the exchange of spin-labels is not constrained and can be either symmetric or anti-symmetric. In the first case, the orbital wave function is then anti-symmetric under this exchange and vice-versa. For a given mixture, this allows a construction of all the allowed orbital symmetries of the overall wave function as exemplified in Fig. 26. The corresponding Young diagram for the exchange of spin labels then quite intuitively corresponds to the transposed diagram [208, 209]. If not otherwise stated, in the following, we assume that Young diagrams reflect the spatial symmetry of a system.

POURING PRINCIPLE.   For very general setups of particles interacting via a symmetric potential, it has been shown that a deep connection exists between the symmetry and the energy of a state [206], which is called the *pouring principle* due to its visual nature in terms of Young diagrams. Namely, if a diagram A can be obtained from a diagram B by moving a box (or several) to the down left (it is "poured"), then the ground state energy in this symmetry sector has a higher energy then the latter, $E(A) > E(B)$ ($E(A) \geq E(B)$ for pathological systems). We refer to this finding in the following as the *generalized Lieb-Mattis theorem* and give an example in Fig. 27.

5.3   QUANTITIES OF INTEREST

In this section, we introduce measurable quantities that we later want to link to the previously introduced symmetries of the many-body wave function. We focus on density and momentum distributions, which are experimentally well accessible. We then present a particular property of the momentum distributions of contact-interacting particles, the so-called *Tan contact*, and contextualize it. For the different interaction regimes, the quantities will then be explicitly studied in Secs. 5.4-5.6.

If we write the orbital wave function in position basis, $\Psi(x_1,\ldots,x_N)$, we obtain the one-body density matrix for any component $\nu \in \{1\ldots N\}$ by integrating out all but one degree of freedom,

$$\rho_\nu(x,x') = N_\nu \int \mathrm{d}x_2\ldots\mathrm{d}x_N \Psi(X)\Psi(X') \tag{167}$$

where $X = (x, x_2\ldots, x_N)$ and $X' = (x', x_2\ldots, x_N)$ and the coordinates were reordered such that x and x' belong to the same species ν. Physically, the one-body density matrix measures first-order spatial coherence between two particles of species ν in positions x and x'. We will see that in the limit of free fermions or in the opposing limit of infinite interactions, ρ_ν can be obtained from an exact solution of the many-body wave function. In the case of finite interactions, we obtain the one-body density matrix from DMRG calculations in the lattice-discretized problem (details in App. A.4).

DENSITY DISTRIBUTIONS.   The probably most intuitive property of a state is its density distribution, i.e. the probability to find a particle of a chosen species in a particular region of space. We are particularly interested in this feature, as the probabilities of finding particles of different species in different regions of the trap can reflect some ordering with respect to the different species and might reveal a magnetic ordering of the system. The density distribution is obtained as the "diagonal" of the one-body density matrix (167),

$$n_\nu(x) = \int \mathrm{d}x' \rho_\nu(x,x')\delta(x-x') = \rho_\nu(x,x) \tag{168}$$

and fulfills the normalization condition $\int n_\nu(x)\mathrm{d}x = N_\nu$.

MOMENTUM DISTRIBUTIONS.   The momentum distribution is defined as the Fourier transform of the one-body density matrix :

$$n_\nu(k) = \frac{1}{2\pi} \int\int \mathrm{d}x\mathrm{d}x' \rho_\nu(x,x') e^{-ik(x-x')}. \tag{169}$$

It is of particular interest as it is experimentally accessible through spin-selective time-of-flight techniques (see also App. B.2.3).

TAN CONTACTS.   For eigenstates in the interacting system, the most striking feature of the momentum distribution is a power-law decay for large momenta. The weight of the momentum distribution tails is fixed by the so-called *Tan contact*:

$$\mathcal{C}_\nu \equiv \lim_{k\to\infty} n_\nu(k)k^4. \tag{170}$$

This feature is common to systems of particles interacting through contact potentials, independent of the statistics and the dimension of the gas [210–212]. The decay behavior $n_\nu(k) \propto k^{-4}$ is robust and solely relies on the delta-shape of the interaction. The value of the Tan contact, on the contrary, depends on the particle type, the interaction strengths and the type of confinement. Interestingly, the

Tan contacts can be linked to other physical properties of the system. In particular, as a two-body quantity it is linked to the interaction energy through [213]

$$
\mathcal{C}_\nu = \frac{g_{1D}m^2}{2\pi\hbar^4} \langle H_{\text{int},\nu} \rangle = \frac{g_{1D}m^2}{2\pi\hbar^4} \sum_{\nu \neq \nu'} \langle H_{\text{int},(\nu,\nu')} \rangle . \tag{171}
$$

This connection between the measurable momentum distribution and the internal (symmetry-dependent) interaction energies will become important later on. The total momentum distribution is obtained by summing over the different species, $n(k) \equiv \sum_\nu n_\nu(k)$. As a consequence, the scaling behavior passes down and we obtain a total Tan contact

$$
\mathcal{C} = \frac{g_{1D}m^2}{\pi\hbar^4} \langle H_{\text{int}} \rangle . \tag{172}
$$

Note the different prefactors, which are due to the over-counting $\sum_\nu \langle H_{\text{int},\nu} \rangle = 2 \langle H_{\text{int}} \rangle$.

5.4 FREE FERMIONS

The energy eigenstates of a free particle in a harmonic trap are well-known as

$$
\phi_n(x) = \frac{1}{\sqrt{2^n n!}} \left(\frac{m\omega}{\pi\hbar} \right)^{1/4} H_n \left(\sqrt{\frac{m\omega}{\hbar}} x \right) e^{-\frac{m\omega x^2}{2\hbar}} \tag{173}
$$

where $H_n(z)$ is the n-th Hermite polynomial $H_n(z) = (-1)^n e^{z^2} \frac{\partial^n}{\partial z^n} (e^{-z^2})$ and $n \in \mathbb{N}_0$. The n-th level has an energy of $E_n = \hbar\omega(n + \frac{1}{2})$.

Due to their fermionic nature, particles of the same species ν cannot have the same orbital quantum number and therefore, in the ground state they occupy the N_ν lowest levels. Particles of different components, on the contrary, are not subdued to the Pauli exclusion principle. As a consequence, any component ν of the mixture will occupy the lowest N_ν levels independently, yielding density distributions

$$
n_\nu(x) = \sum_{n=0}^{N_\nu - 1} |\phi_n(x)|^2 . \tag{174}
$$

Examples thereof are given in Fig. 28a.

Without interactions, the wave functions of the particles display the same form in momentum as in real space,

$$
\phi_n(k) = \frac{1}{\sqrt{2^n n!}} \left(\frac{1}{\pi\hbar m\omega} \right)^{1/4} H_n \left(\sqrt{\frac{\hbar}{m\omega}} k \right) e^{-\hbar k^2/(2m\omega)}, \tag{175}
$$

and as a consequence also the density and the momentum distributions share the same shape, compare Figs. 28b(top) and 30a. The number of peaks in the two distributions is equal to the number of fermions in the respective component. The amplitude of these oscillations decays inversely with the particle number.
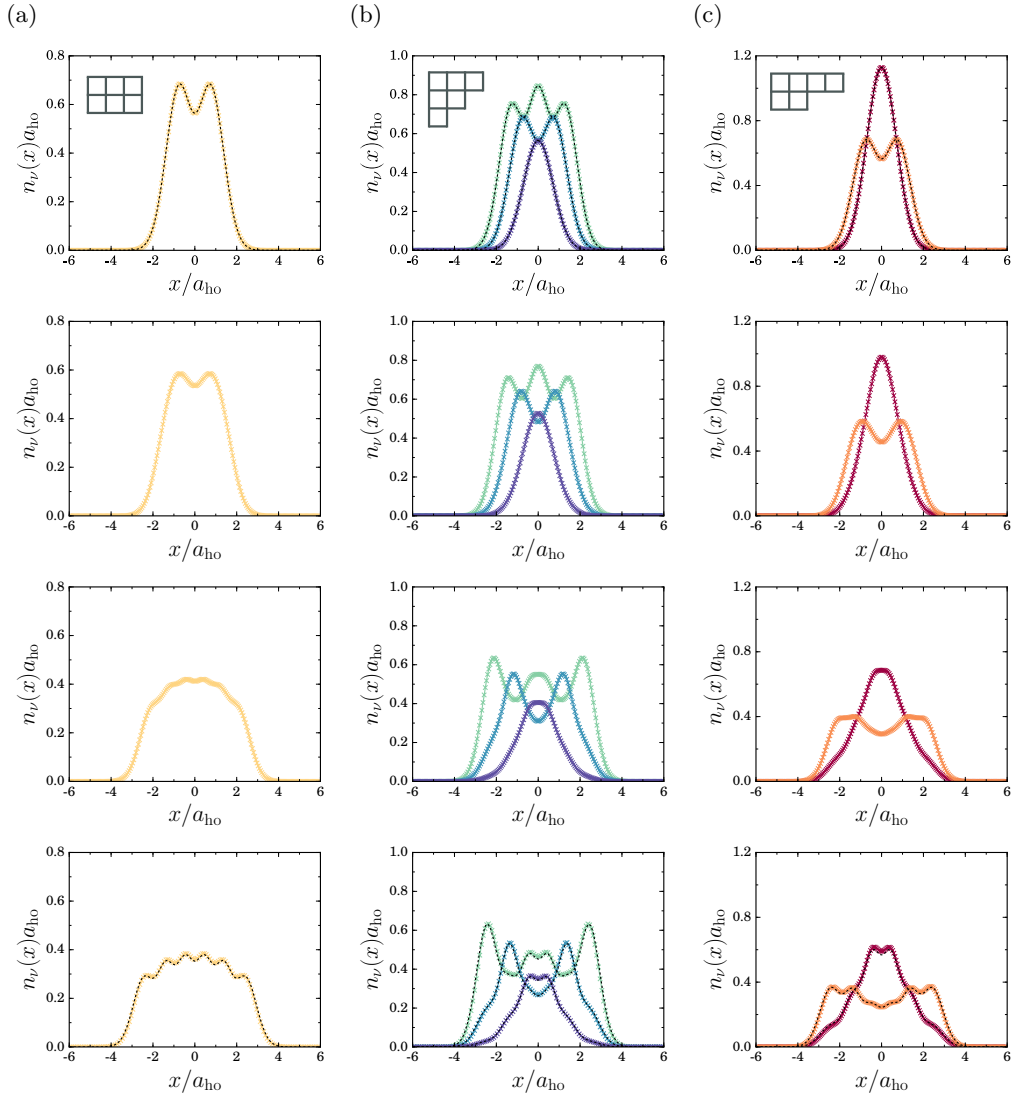
Figure 28: **Density profiles for different fermionic (and bosonic) mixtures and interaction strengths.** The plots show density distribution of $N = 6$ particles distributed onto three species as (a) $2_F + 2_F + 2_F$, (b) $3_F + 2_F + 1_F$, (c) $2_B + 2_F + 2_F$. The top row corresponds to free fermions ($\alpha = 0.0$), followed by $\alpha = 1.0$, $\alpha = 10.0$ and $\alpha = 100.0$. In the bottom row, dashed lines indicate the analytical results of the strong-coupling limit.

5.5   STRONG-COUPLING LIMIT

We now turn to the opposite regime of $1/\alpha \to 0$. In this limit, we find a highly degenerate ground state, which becomes non-degenerate for finite interactions. The physics of the ground state manifold can be cast into an effective Hamiltonian that takes the form of a spin lattice-model. We present the derivation in Sec. 5.5.1. Using solutions of this spin model, we can then construct the continuum density and momentum distributions and measure the Tan contacts of

all states of the manifold. We show the procedure and discuss the results in Sec. 5.5.2.

5.5.1 *Effective model*

In the limit of strong interactions, particles "mimic" the Pauli exclusion principle in the sense that the wave function is always suppressed whenever two particles coincide in space, $\Psi(x_i = x_j) = 0$. This so-called *fermionization* is a consequence of the cusp-condition (161) for $1/\alpha \to 0$. The inverse is not true: From the fact that the wave function is zero for some $x_i = x_j$, we cannot deduce that it is anti-symmetric under the exchange of particles.

The fermionization has even further consequences: Assume that the orbital quantum numbers of the free problem (and the corresponding wave functions (173)) were still valid solutions in the limit of strong interactions. If two particles in different species then had the same orbital quantum numbers, their orbital wave function would be necessarily symmetric and $\Psi(x_i - x_j) = 0$ could not be fulfilled. On the contrary, if all particles occupy different orbitals, we can construct a wave function that is fully anti-symmetric by writing the Slater determinant

$$\Psi_A(x_1, \ldots, x_N) = \frac{1}{\sqrt{N!}} \det[\phi_{i-1}(x_j)]_{i,j=1,\ldots,N}. \tag{176}$$

It is easy to check that this function fulfills the cusp-condition (also for any finite interaction) and has an energy $E_0^\infty = \hbar\omega \sum_{\nu=0}^{N-1} \nu$.

For $\alpha \to \infty$, solutions of the cusp-condition do not need to be differentiable in $x_i = x_j$, and we can imagine further solutions of the form [214, 215]

$$\Psi(x_1, \ldots, x_N) = \sum_{S_N} a_P \chi_P(x_1, \ldots, x_N) \Psi_A(x_1, \ldots, x_N), \tag{177}$$

where the sum runs over all elements of the symmetric group S_N, and

$$\chi_P(x_1, \ldots, x_N) = \begin{cases} 1 & \text{if} \quad x_{P(1)} < \ldots < x_{P(N)}, \\ 0 & \text{otherwise.} \end{cases} \tag{178}$$

For example, a general solution for two particles is

$$\Psi(x_1, x_2) = \frac{1}{\sqrt{2}} \left[a_{12} \Psi_A(x_1, x_2) \theta(x_2 - x_1) + a_{21} \Psi_A(x_1, x_2) \theta(x_1 - x_2) \right], \tag{179}$$

where θ is the Heaviside step-function. By choosing $a_{12} = a_{21} = 1$, we obtain a solution which is anti-symmetric under exchange of positions, while for $a_{12} = -a_{21} = 1$ the solution is symmetric.

For a system with more particles, similar considerations on the anti-symmetry allow us to deduce that all coefficients corresponding to permutations of positions of particles of the same species are equal. Therefore, the number of independent coefficients is reduced to the multinomial coefficient $D_{\{N_\kappa\}} = \frac{N!}{N_1! N_2! \cdots N_\kappa!}$. Linearly independent solutions of the type (177) span the ground state manifold with energy E_0^∞, which therefore is $D_{\{N_\kappa\}}$ degenerate.

For finite, but large interactions, we can make a perturbative approach in $1/g_{1D}$ and therefore define the energy-slope with respect to the inverse interaction strength

$$K \equiv -\frac{\partial E}{\partial g_{1D}^{-1}} = \frac{\partial \langle H \rangle}{\partial g_{1D}^{-1}} = -\left\langle \frac{\partial H}{\partial g_{1D}^{-1}} \right\rangle = g_{1D} \langle H_{\text{int}} \rangle, \tag{180}$$

where we have used the Hellmann-Feynman theorem in the third step. By plugging in our wave function ansatz (177) and using the cusp-condition (161) for a substitution, we obtain

$$K = \frac{\hbar^4}{m^2} \sum_{P,Q \in S_N} (a_P - a_Q)^2 \alpha_{P,Q} \tag{181}$$

with

$$\alpha_{P,Q} = \alpha_k = \int dx_1 \dots dx_N \ \chi(x_1 \le x_2 \le \dots \le x_N)\delta(x_k - x_{k+1}) \left[\frac{\partial \Psi_A}{\partial x_k}\right]^2, \tag{182}$$

where P and Q are equal up to a transposition of two consecutive coordinates at positions k and $k+1$, and 0 otherwise. Note that α_k does not explicitly depend on P and Q, but only on the sites between which the permutation takes place. The spatial symmetry implies $\alpha_k = \alpha_{N-k}$. Finding the ground state then amounts to maximizing K. The problem can be simplified by using the equality of subsets of coefficients in the wave function (177). As mentioned earlier, this linear dependence reduces the dimension of the effective problem to dimension $D_{\{N_\kappa\}}$, and we can define a *snippet basis* $\mathbf{a}_{\text{snip}}$ of linear independent coefficients. In this basis, we can write the Hamiltonian as $H_{\text{eff}} = E_0^\infty + \frac{\hbar^4}{m^2 g_{1D}}V$ with

$$V_{ij} = \begin{cases} \alpha_{i,j} & \text{if} \quad i \ne j, \\ -\sum_{k \ne i} \alpha_{i,k} & \text{if} \quad i = j. \end{cases} \tag{183}$$

The minimal eigenvector of the matrix represents the ground state of the system.

However, we can get a much better physical intuition, and thereby return to the duality between orbital and spin symmetry. We first note that the snippet basis (labeled by the set of $D_{\{N_\kappa\}}$ independent coefficients) corresponds to different orders of a given set of spins in the one-dimensional system. Let us take the example of a three particle state with $\kappa = 2$. The wave function takes the form

$$\Psi(\underbrace{x_1, x_2}_{\text{species 1}=\uparrow}, \underbrace{x_3}_{\text{species 2}=\downarrow}) = \begin{cases} \dots \\ a_{231}\chi(x_2 < x_3 < x_1)\Psi_A(x_1, x_2, x_3) \to |\uparrow\downarrow\uparrow\rangle \\ a_{312}\chi(x_3 < x_1 < x_2)\Psi_A(x_1, x_2, x_3) \to |\downarrow\uparrow\uparrow\rangle \\ a_{321}\chi(x_3 < x_2 < x_1)\Psi_A(x_1, x_2, x_3) \to |\downarrow\uparrow\uparrow\rangle \\ \dots \end{cases} \tag{184}$$

and we see that every coefficient a_{ijk} is associated with an ordering of spins in space. We observe that the commutation of the coordinates of the particles in species 1 leads to the same spatial ordering of the spins and - as discussed previously - results in the same prefactor ($a_{312} = a_{321}$) as a consequence of the necessary anti-symmetry in the orbital wave function. On the other hand, the permutation in the ordering of different spins leads to a different spin configuration, and therefore in general $a_{231} \neq a_{312}$. The discussed reduction of the dimension of the matrix $\alpha_{P,Q}$ can be understood as a projection onto different spatial spin orderings. These orderings can then be taken as good quantum numbers of an emergent S_N-symmetry [216]. Due to the fact that α_j is only non-zero for a transposition of two consecutive coordinates, we can define an exchange operator for site j and $j+1$, $P_{j,j+1}$, and the Hamiltonian takes the form [215]

$$H_{\text{eff}} = E_0^\infty + \sum_{j=1}^{N-1} J_j(P_{j,j+1} - \mathbb{I}), \tag{185}$$

with $J_j = \frac{N!\hbar^4}{m^2 g_{1D}}\alpha_j$. The operator $P_{j,j+1}$ now commutes spins $1, \ldots, \kappa$ on sites j and $j+1$ of the effective spin-lattice model with N sites. To make the spin-model nature more transparent, we choose a set of generators of the SU(κ)-symmetry in the defining representation $\{T^{[k]}\}_{k=1,\ldots,\kappa^2-1}$. For example for $\kappa = 2$, these generators are the Pauli matrices, for $\kappa = 3$ the Gell-Mann matrices (apart from pre-factors). In general, $T^{[k]}$ are traceless, Hermitian $\kappa \times \kappa$-matrices with an identity relation

$$\sum_{\mu=1}^{\kappa^2-1} T^{[\mu]}_{\alpha\beta} T^{[\mu]}_{\gamma\delta} = \frac{1}{2}\left(\delta_{\alpha\delta}\delta_{\beta\gamma} - \frac{1}{\kappa}\delta_{\alpha\beta}\delta_{\gamma\delta}\right). \tag{186}$$

The elements of the permutation operator describing a transition from spins α and γ to β and δ (on sites j and $j+1$ respectively) are given by $[P_{j,j+1}]^{\beta\delta}_{\alpha\gamma} = \delta_{\alpha\delta}\delta_{\beta\gamma}$. The identity-operator that projects a spin-pair onto itself can be written as $[\mathbb{1}_{j,j+1}]^{\beta\delta}_{\alpha\gamma} = \delta_{\alpha\beta}\delta_{\gamma\delta}$. It is easy to check that

$$\sum_\mu \left[T^{[\mu]}_j\right]_{\alpha\beta}\left[T^{[\mu]}_{j+1}\right]_{\gamma\delta} = \frac{1}{2}\left(\delta_{\alpha\delta}\delta_{\beta\gamma} - \frac{1}{\kappa}\delta_{\alpha\beta}\delta_{\gamma\delta}\right) \tag{187}$$

$$= \frac{1}{2}[P_{j,j+1}]^{\beta\delta}_{\alpha\gamma} - \frac{1}{2\kappa}[\mathbb{1}_{j,j+1}]^{\beta\delta}_{\alpha\gamma}. \tag{188}$$

In the spin basis, we can then rewrite H_{eff} in Eq. (185) as

$$H_{\text{eff}} = E_F + \sum_{i=1}^{N-1} J_j\left(2\mathbf{T}_j \cdot \mathbf{T}_{j+1} - \frac{\kappa-1}{\kappa}\mathbb{1}\right). \tag{189}$$

This writing of the effective Hamiltonian makes its SU(κ)-symmetry transparent. Due to the fact that the coupling constants are always positive ($J_j > 0$), the spin state will try to realize the least symmetric - and therefore the least magnetic - *spin* wave function possible for a given mixture. This fact is dual to the fact that the *orbital* wave function will try to achieve the most symmetric configuration. In the special case of $\kappa = 2$, we obtain a site-dependent Heisenberg model [214].

Note that the Hilbert space of the effective model (189) has dimension κ^N, while the earlier snippet basis had dimension $D_{\{N_\kappa\}}$. This is no contradiction as the spin model allows all possible spin configurations of N particles and $\kappa^N = \sum_{\{N_\kappa\}} D_{\{N_\kappa\}}$. By projecting onto a basis of those spin states representing a fixed mixture, one obtains the reduced dimensions.

5.5.2 *Density and momentum distributions, Tan contacts*

DERIVATION.   Eigenvectors of the matrix (183) or equivalently solutions of the effective spin Hamiltonian (189) represent eigenstates of the general Hamiltonian in the limit of strong interactions. We are interested in the spatial and momentum structure of these states. We therefore study the one-body density matrix (167) in this limit.

Every permutation $P \in S_N$ can be labeled as P_{i_k} where i is the position of the first particle and $k \in \{1, \ldots, (N-1)!\}$ denotes the permutation of the remaining $N - 1$ particles. The wave function then takes the form $\Psi(X) = \sum_{i=1}^{N} \sum_{k=1}^{(N-1)!} a_{i_k} \chi_{P_{i_k}}(X) \Psi_A(X)$, where $X = (x_1, \ldots, x_N)$. To determine $\rho(x_1, x_1')$ for two coordinates x_1 and x_1', we can always assume $x_1 < x_1'$ as $\rho(x_1, x_1') = \rho(x_1', x_1)$. We can then write

$$\rho_\nu(x_1, x_1') = N_\nu \sum_{1 \leq i \leq j \leq N} \rho_\nu^{(ij)}(x_1, x_1') \tag{190}$$

with $\rho_\nu^{(ij)}(x_1, x_1')$ being defined in Eq. (167) and the integral limits chosen such that $(i-1)$ coordinates are smaller than x_1 and $(j-1)$ coordinates are smaller than x_1'. Using the fact that $\int dx_2 \ldots dx_N \, \chi_{P_{i_k}}(X) \chi_{P_{i_l}}(X') \cdots \neq 0$ only if $k = l$ and the permutation symmetry of Ψ_A, we can express the latter as a Vandermonde determinant, and obtain

$$\rho_\nu(x_1, x_1') = N_\nu G_N \sum_{1 \leq i \leq j \leq N} C_{ij} \sum_{P,Q \in S_{N-1}} \epsilon(P)\epsilon(Q)$$
$$\prod_{l=2}^{N} \int_{L_{ij}}^{U_{ij}} dz(z - x_1)(z - x_1')\phi_{P(l)-1}(z)\phi_{Q(l)-1}(z), \tag{191}$$

with $G_N = \frac{2^{N-1}}{\sqrt{\pi}N!(N-1)!}$, $C_{ij} = \frac{\sum_{k=1}^{(N-1)!} a_{i_k} a_{j_k}}{(i-1)!(j-i)!(N-j)!}$ and $(L_{ij}, U_{ij}) = (-\infty, x_1)$ if $l \leq i$, $(x_1', +\infty)$ if $l > j$ and (x_1, x_1') otherwise.

Eq. (191) allows us to determine the momentum and density distributions analytically. Moreover, similar to Eq. (180), we have direct access to the species-resolved Tan contacts via

$$C_\nu = \frac{1}{2\pi} \sum_{\substack{\mu=1 \\ \mu \neq \nu}}^{\kappa} \sum_{k=1}^{N-1} \sum_{P \in \sigma_N(\mu, \nu, k)} (a_P - a_{(\tau_k \circ P)})^2 \alpha_k, \tag{192}$$

where $\sigma_N(\mu, \nu, k)$ is the set of all permutations for which the particles on sites k and $k+1$ are in species μ and ν; τ_k is the transposition of these particles. Finally, we can probe the symmetry of the state by checking the sign-change of a given wave function under exchange of two spins. This allows us to directly lay
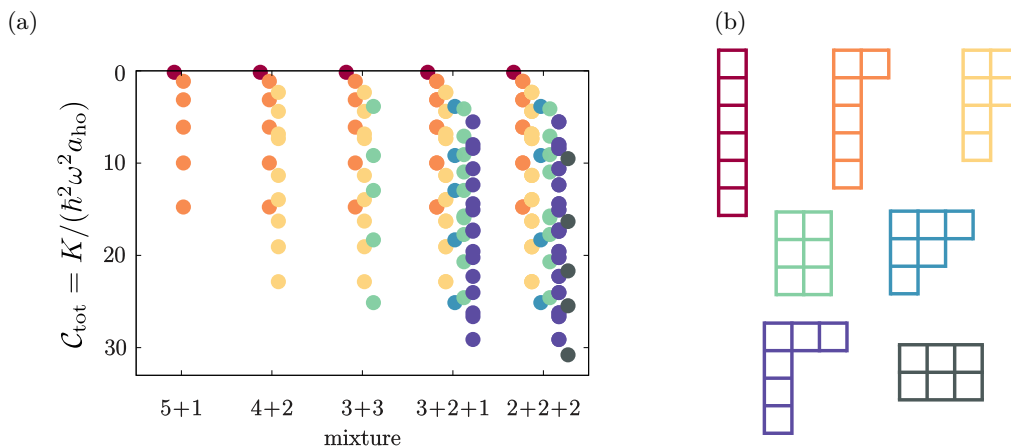
Figure 29: **Tan contacts and Young diagrams for states in the limit of strong interactions.** (a) The (rescaled) interaction energy parameter K (which is proportional to the Tan contact) for all the states in the ground state manifold at $1/\alpha \to 0$ for different mixtures of fermions. The plot shows the energy splitting at finite α. The colors identify the orbital symmetries of the states associated with the Young diagrams given in (b). For the sake of readability, states with different symmetry corresponding to the same mixture are slightly left-right shifted. The ordering of the ground states following the pouring principle is evident (compare Fig. 27).

out the corresponding Young diagrams. Alternatively, we one can make a more formal approach and measure so-called *class-sum operators* [25], which identify the irreducible representation likewise.

APPLICATION.   We now have all the tools at hand to describe the physics in the limit of strong interactions. We observe that the density distribution of a mixture under strong interactions differs significantly from the non-interacting regime (see Fig. 28). This is a combined effect of the interactions and the symmetry constraints that a particular mixture has to fulfill.

In the energy spectrum of the effective Hamiltonian (189), we can identify the irreducible representation (i.e. the Young tableau) for any state (see Fig. 29). Indeed, we observe that for a given mixture, only those diagrams are realized which agree with the construction rules in Sec. 5.2.3 (see in particular Fig. 26). We also observe that within the set of permissible diagrams, a mixture realizes the most symmetric one. Moreover, the ground state energies for different diagrams are ordered with respect to the symmetry. This is in agreement by the pouring principle of the Lieb-Mattis theorem. Indeed, knowledge of the interaction energy (or equivalently the energy slope K) allows a direct identification of the particle mixture - given that the system indeed realizes a ground state. Vice versa, for a given mixture, knowledge of K makes it possible to identify a state and therefore its symmetry. We observe that the spectra for different mixtures are degenerate within a given symmetry sector. This is an important finding:
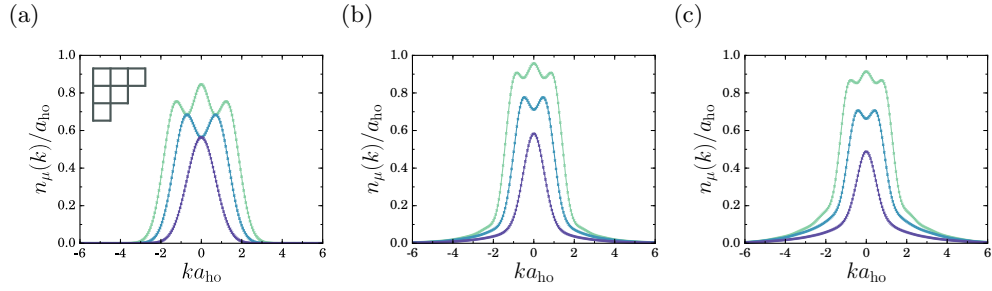
Figure 30: **Momentum distributions for different interaction strengths.** For a system with $\kappa = 3$ species and $N_1 = 3$ (green), $N_2 = 2$ (cyan), $N_3 = 1$ (violet), the momentum distributions of the three species are shown for (a) free fermions ($\alpha = 0$), (b) intermediate interactions ($\alpha = 10$) and (c) strong interactions ($\alpha = 100$).
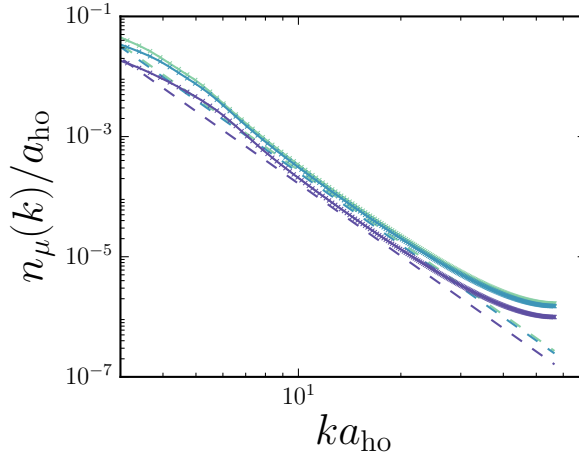
Figure 31: **Momentum distribution tails and Tan contacts.** For the same mixture as in Fig. 30 ($3_F + 2_F + 1_F$), we exemplarily show the relation between momentum distribution tails and Tan contacts: The plot shows the numerically determined momentum distribution tails at interaction strength $\alpha = 10.0$ on a log-log scale. Crosses show the numerical results, the continuous lines are guides to the eye. The dashed lines represent the functions $\mathcal{C}_\nu k^{-4}$ with the Tan contacts C_ν as determined from the interaction energy. As expected, the momentum distribution converge to these lines for large momenta. Deviations from the power-law behavior at very large momenta are due to the discretization in the numerical problem.

The Young tableau fully determines the constraints on an ansatz wave function and therefore the possible energy eigenstates.

The parameter K is linked through the interaction energy to a Tan contact (or a set of Tan contacts for the different species, see Eqs. (171),(172) and (180)). We therefore propose to use spin-dependent time-of-flight measurements to identify K through the slope of the resulting momentum distributions. This yields direct access to the symmetry of the measured state.
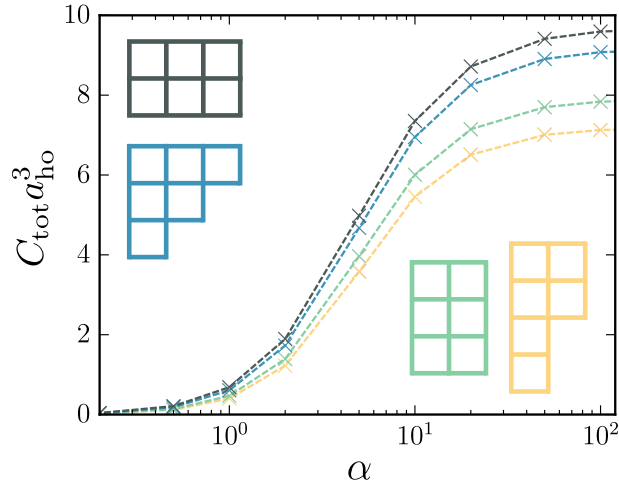
Figure 32: **Scaling of Tan contacts for different mixtures.** For different mixtures (gray: $2_F + 2_F + 2_F$, blue: $3_F + 2_F + 1_F$, yellow: $4_F + 2_F$, green: $3_F + 3_F$), the total Tan contacts are plotted against the interaction strength. The Young diagrams identify the symmetry of the respective state. We observe that the Tan contacts are ordered with respect to their symmetry along the pouring principle for all interaction strengths.

5.6 INTERMEDIATE REGIME

5.6.1 *Numerical results*

In the previous two sections, we have established exact results for the two limits of vanishing and strong interactions. The regime of finite interactions, on the contrary, is not accessible analytically. We therefore perform a MPS/DMRG-study which allows us to determine and measure the ground states for any given mixture in the full parameter regime. Details of the numerical method are given in App. A.4.

In Fig. 28, we show the deformation of the ground state density distribution for different particle mixtures when increasing the interaction strength. We observe a qualitative change in the distributions when correlation effects become important. A comparison of the results at strong, but finite interactions with the exact result for $\alpha \to \infty$ confirms the previous analytical study and allows us to determine a range in the interaction parameter ($\alpha \lesssim 100$) for which the strong-coupling result remains quasi-exact.

Likewise, in the momentum distributions, we can identify the onset of strong correlations by a narrowing of the curves and an enhancement of the high-momentum tails, indicating the fermionization process. An example is given in Fig. 30. The higher probability to find the particles for strong interactions at large momenta is reflected by increasing Tan contacts. We also show an example of how the Tan contacts identify in the momentum distribution tails in Fig. 31. For different mixtures, we present the Tan contacts at finite interactions in Fig. 32.

(a)

(b)
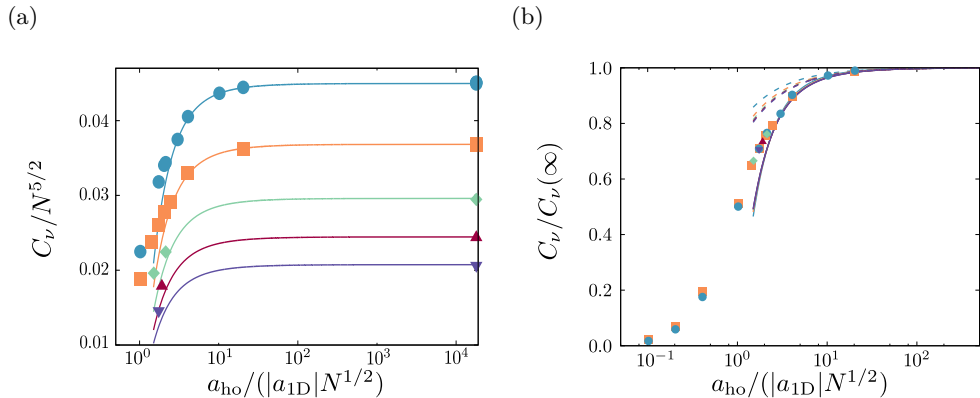
Figure 33: **Scaling of Tan contacts in homogeneous mixtures.** (a) Exact and MPS results for the Tan contacts $\mathcal{C}_\nu$ in balanced mixtures with up to $N = 12$ particles as a function of the parameter $\alpha_0/2 = a_{\text{ho}}/(|a_{1D}| N^{1/2}) \propto g_{1D}$. The rescaling of the Tan contacts with the factor $N^{5/2}$ leads to a collapse of all data with the same κ (but possibly different N) onto a single curve. The results are compared to the perturbative local density approximation (201) in second (dashed lines) and third order (continuous lines). Blue: $\kappa = 2$, yellow: $\kappa = 3$, green: $\kappa = 4$, red: $\kappa = 5$, violet: $\kappa = 6$. (b) Once the limiting value $\mathcal{C}_{g_{1D}\to\infty}$ is factored out, the data collapses completely. This proves the very weak dependence on the number of species κ.

For *strong* interactions we established a link between the symmetry of a state and its Tan contact. In our line of argumentation, we first connected the symmetry to the order of the ground state energies via the Lieb-Mattis theorem. In the limit $\alpha \to \infty$, the energy splitting is directly proportional to the energy slope, which again is proportional to the interaction energy and therefore to the Tan contact. As a consequence, the ground states with different symmetries are ordered with respect to their Tan contacts. For *intermediate* interactions, the ground state energies are a priori not necessarily proportional to their slope and we would be missing a link in the chain of arguments. However, in our numerical observations we observe that the Tan contacts indeed remain ordered (compare Fig. 32). We therefore conjecture that they continue to identify the symmetry of a state.

5.6.2 *Scaling approach and local density approximation*

As demonstrated above, we have the necessary tools at our disposal to determine Tan contacts from interaction energies in the numerics. We could use these results to compare to those measured in an experiment in the tails of momentum distributions. However, our numerical techniques are limited to explore systems with only a few particles ($N \lesssim 12$). In actual experimental setups, on the contrary, the trap might be charged with a much higher number (compare App. B.2.3). We therefore present a scaling approach that - based on very general assumptions - allows us to predict the scaling of the Tan contacts with the

particle number. We then outline how to determine formally exact results within a local density approximation. The results were originally derived by M. Rizzi in our joint publication [25], and are presented here to complement the numerical study.

SCALING APPROACH.   In a harmonic potential, fermions occupy a number of orbitals which scales with the number of particles. This is true both in the limit of free fermions, where the lowest $p_\nu N$ levels for all κ species are occupied independently (with $p_\nu = N_\nu/N$ being the fraction of particles in one species), and for a system with infinitely strong interactions, which shows the same level occupation as a single-species gas due to fermionization. From the Hamiltonian (162) we see that if orbitals up to a level in $O(N)$ are occupied, the non-interacting contribution to the energy scales like $O(N^2)\hbar\omega$. We can write the total energy as

$$E = \hbar\omega N^2 f(\alpha, N, \{p_\nu\}), \tag{193}$$

where f is a function that can only intensively depend on N.

In the thermodynamic limit of $N \to \infty$, the energy per particle $O(N)\hbar\omega$ clearly diverges. Fixing the Fermi energy in the limit $\alpha \to \infty$ to $E_F^{(\infty)} = N\hbar\omega$ then amounts to rescaling the interaction parameter $\alpha_0 = \alpha/\sqrt{N}$. Therefore $E/N = E_F^{(\infty)} f(\alpha_0, \{p_\mu\})$ with $f(0, \{p_\nu\}) = \sum_\nu p_\nu^2/2$ and $f(\alpha_0 \to \infty, \{p_\nu\}) = 1/2$. The scaling of the Tan contact can be derived from Eq. (172) with $g_{1D} = \hbar\omega a_{ho}\alpha_0\sqrt{N}$ to be

$$\mathcal{C}_{tot}(\alpha_0) = \frac{1}{\pi\alpha_{ho}^3}N^{5/2}\alpha_0^2\frac{\partial f(\alpha_0, \{p_\mu\}}{\partial\alpha_0}. \tag{194}$$

This scaling is confirmed in Fig. 33, where the rescaled Tan contacts determined numerically for finite interactions collapse onto a single curve when rescaling the axes. The $N^{5/2}$-scaling of Tan contacts is also observed in Monte Carlo simulations [217].

LOCAL DENSITY APPROXIMATION.   The above result can be further refined and an explicit form of f can be derived. For a homogeneous, periodic system with length L and N particles interacting through a contact potential $\alpha \propto 1/a_{1D}$, the physics of the model is fully determined by a single parameter $\gamma = mg_{1D}/\hbar^2\rho = (1/\rho)/a_{1D}$, relating the average particle distance $1/\rho = L/N$ to the scattering length. This yields a local energy

$$\epsilon[\rho, \gamma] = \frac{\hbar^2}{2m}\rho^3 e(\gamma) \tag{195}$$

where $e(\gamma)$ is a dimensionless equation of state which can be determined via a Bethe-ansatz [218].

For the problem in the harmonic potential, we are encouraged by the above result to find a similar solution which only depends on the parameter α and relates the harmonic oscillator length (instead of the average particle distance) to the scattering length. We therefore assume that the expression for the density-

dependent energy density (195) is locally correct, and write the total energy as a functional of the local density $\rho(x)$,

$$E(\rho) = \int \left(\epsilon[\rho, \gamma] + [V_{\text{ext}}(x) - \mu]\rho(x) \right) \mathrm{d}x \tag{196}$$

where $V_{\text{ext}} = m\omega^2 x^2/2$. The minimization condition $\delta E[\rho]/\delta\rho = 0$ yields

$$\frac{3}{2}\frac{\hbar^2}{m}\rho^2 e(\gamma) - \frac{g_{1\text{D}}}{2}e'(\gamma) = \mu - V_{\text{ext}}(x) \tag{197}$$

with $\int \rho(x)\mathrm{d}x = N$. This fixes the chemical potential. If, in addition, we demand the positivity of the right-hand side of the equation (which yields a compact support with the Thomas-Fermi radius $R = a_{\text{ho}}(2N\mu/E_F^{(\infty)})^{0.5}$), the equation can be solved with respect to ρ. Combining this solution with the Hellmann-Feynman theorem (180) and the Tan relation (172) yields

$$\mathcal{C}_{\text{tot}} = \frac{g_{1\text{D}}m^2}{2\pi\hbar^4} \int \mathrm{d}x \, \rho^2(x)e'\left[\frac{mg_{1\text{D}}}{\hbar^2\rho(x)}\right]. \tag{198}$$

By changing variables $\mu = \tilde{\mu}E_F$, $z = x/R$ and $r(z) = a_{\text{ho}}\rho(x)/\sqrt{N}$ (with normalization condition $\sqrt{2\tilde{\mu}}\int_{-1}^{1} r(z)\mathrm{d}z = 1$), the minimization condition (197) becomes

$$3r(z)^2 e\left[\frac{\alpha_0}{r(z)}\right] - \alpha_0 r(z)e'\left[\frac{\alpha_0}{r(z)}\right] = 2\tilde{\mu}(1 - z^2). \tag{199}$$

This expression only depends on α_0, confirming the earlier claim that the problem is fully described by a single parameter (the rescaled α).

In the particular case of a balanced mixture, the dimensionless equation of state can be expanded for $\alpha_0 \to \infty$ as [218]

$$e(\gamma) = \frac{\pi^2}{3}\left[1 - \frac{4Z_1(\kappa)}{\gamma} + \frac{12Z_1(\kappa)^2}{\gamma^2} - \frac{32}{\gamma^3}\left(Z_1(\kappa)^3 - \frac{Z_3(\kappa)\pi^2}{15}\right) + O\left(\frac{1}{\gamma^4}\right)\right] \tag{200}$$

where $Z_1(\kappa) = -\frac{1}{\kappa}[\Psi(\frac{1}{\kappa}) + C_{\text{Euler}}]$ and $Z_3(\kappa) = [\zeta(3, 1/\kappa) - \zeta(3)]/\kappa^3$ with the digamma-function ψ, the Euler constant C_{Euler} and the Riemann function ζ. By using this to solve Eq. (199) and plugging the result into Eq. (198), we obtain up to second order in $1/\alpha_0$

$$\mathcal{C}_\nu(\alpha_0) = \frac{N^{5/2}}{\pi\kappa a_{\text{ho}}^3}\left[\frac{128\sqrt{2}Z_1(\kappa)}{45\pi^2} + \frac{2(315\pi^2 - 4096)Z_1(\kappa)^2}{81\pi^4\alpha_0} \right.$$
$$\left. - \frac{64\sqrt{2}\left(25(1437\pi^2 - 14336)Z_1(\kappa)^3 + 1728\pi^4 Z_3(\kappa)\right)}{14175\pi^6\alpha_0^2}\right]. \tag{201}$$

Fig. 33 demonstrates that this analytical expression describes correctly the scaling of the Tan contacts for strong interactions.
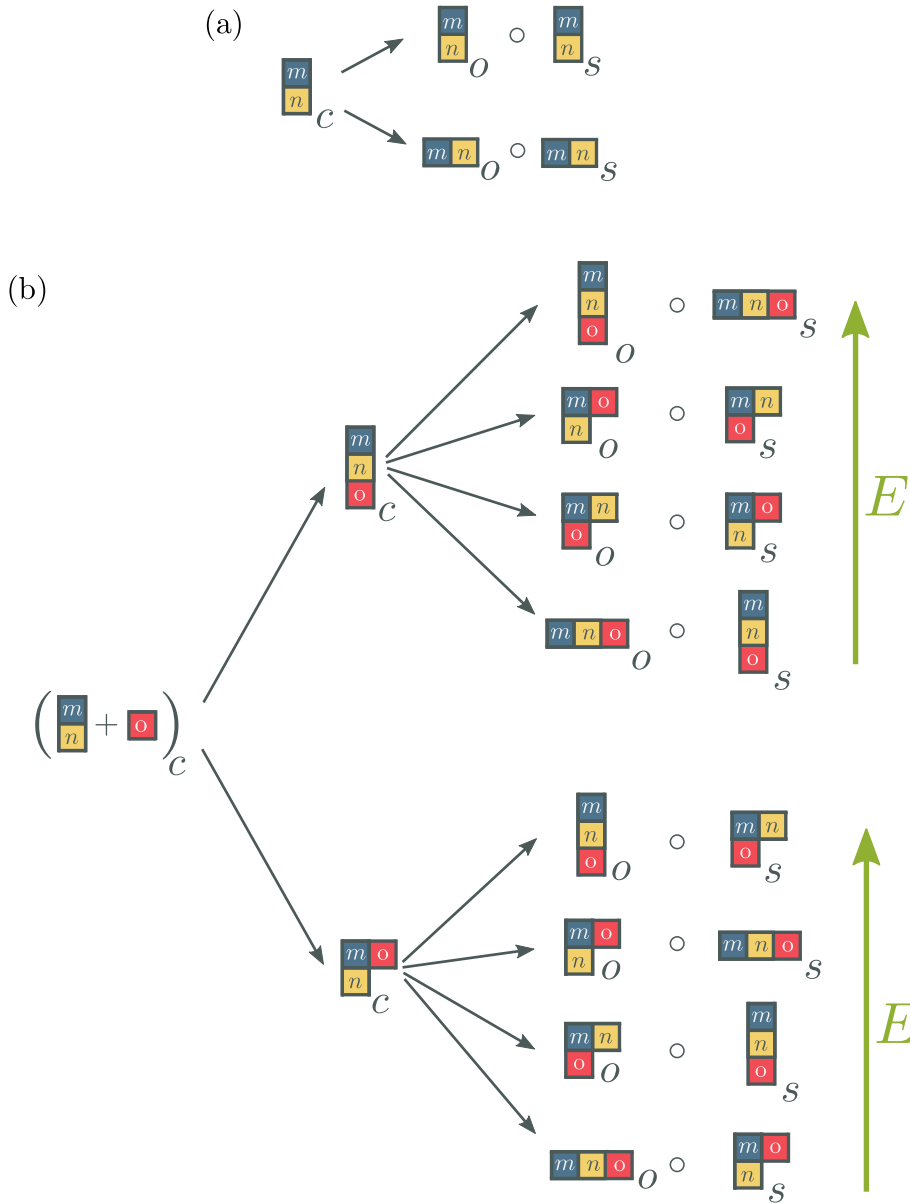
Figure 34: **Symmetries of bosons and fermion-boson mixtures.** (a) Two bosons in orbitals m and n and internal states σ (blue) and τ (yellow) display a symmetric commutation relation. If the wave function is (anti-)symmetric in the orbital part, it also has to be (anti-)symmetric under spin exchange (see Eqs. (202) and (203)). (b) For mixtures of fermions and bosons, the total wave function is only constrained by the commutation rules within the two subsets. The overall wave function can have different symmetries then. Here, we present an example of three particles, two of which are fermions. If the third particle (red) is also a fermion, the overall wave function is anti-symmetric (top). If it is a boson, the total wave function can also be symmetric under exchange of the boson with the fermions (bottom). In this case, the Young diagrams for the orbital and spin degree of freedoms are no longer transposes (as for fermions) or identical (as for bosons). The green arrow indicates the energy-ordering of the ground states according to the pouring principle.

5.7 OUTLOOK: BOSON-FERMION MIXTURES

The above results were obtained for fermionic setups which are in the main focus of this thesis. They can, however, be quite easily generalized to setups that contain mixtures of fermions and bosons. Here, we outline the generalization shortly and discuss the resulting differences.

SYMMETRIES. The principal difference to purely fermionic mixtures is the fact that the overall wave function does no longer obey the anti-symmetry condition (163).

Bosons. If we consider the exchange of two bosons, the many-body wave function does not change its sign, $|m, \sigma; n, \tau\rangle = |n, \tau; m, \sigma\rangle$. Possible solutions therefore have the form

$$
\begin{aligned}
|m, \sigma; n, \tau\rangle &= \frac{1}{2} \left(|m, \sigma\rangle \otimes |n, \tau\rangle + |m, \tau\rangle \otimes |n, \sigma\rangle \right. \\
&\quad \left. + |n, \sigma\rangle \otimes |m, \tau\rangle + |n, \tau\rangle \otimes |m, \sigma\rangle \right) \\
&= \frac{1}{2} \underbrace{\left(|m, n\rangle + |n, m\rangle \right)}_{|n;m\rangle_s} \underbrace{\left(|\sigma, \tau\rangle + |\tau, \sigma\rangle \right)}_{|\tau;\sigma\rangle_s}
\end{aligned}
\tag{202}
$$

where we have again permuted the dimensions to order orbital and spin degrees of freedom. Alternatively,

$$
\begin{aligned}
|m, \sigma; n, \tau\rangle &= \frac{1}{2} \left(|m, \sigma\rangle \otimes |n, \tau\rangle - |m, \tau\rangle \otimes |n, \sigma\rangle \right. \\
&\quad \left. - |n, \sigma\rangle \otimes |m, \tau\rangle + |n, \tau\rangle \otimes |m, \sigma\rangle \right) \\
&= \frac{1}{2} \underbrace{\left(|m, n\rangle - |n, m\rangle \right)}_{|m;n\rangle_a} \underbrace{\left(|\sigma, \tau\rangle - |\tau, \sigma\rangle \right)}_{|\tau;\sigma\rangle_a}.
\end{aligned}
\tag{203}
$$

We observe that the bosonic solution can be either symmetric or anti-symmetric in both orbital and spin. More generally, for a bosonic many-body system, we observe that in order to fulfill the symmetry criterion, the Young diagrams describing the orbital and the spin exchange have to be identical (see Fig. 34a).

Fermions and bosons. For a mixture of fermions and bosons, the symmetry of the overall wave function can have any symmetry which is permissible and respects the symmetry under exchange of bosons and the anti-symmetry under exchange of fermions. We demonstrate this in Fig. 34b.

ORDERING OF STATES. As a consequence of the different symmetry decompositions for fermions and bosons, the Young diagrams representing the orbital and the spin symmetry are no longer dual (i.e. identical or transposed, compare Fig. 34b). A pouring principle describing the ordering of states with respect the orbital symmetry therefore does not translate into a similar rule for the spin symmetry.

For *free particles* with a given mixture, the ground state is obtained by occupying the lowest orbitals for every species separately. As bosons are not subdued

to the Pauli principle, they will all occupy the lowest orbital, and the orbital wave function is completely symmetric under exchange of any two bosons. By building the according Young tableau (and those of possible excited states), it is easy to verify that the pouring principle for the orbital wave function still applies. The difference to the case of a totally anti-symmetry or totally symmetric wave function consists in the fact that states with different spin symmetry can realize the same orbital symmetry. As the orbital symmetry determines the energy of a ground state without interactions completely, we conclude that ground states with a given orbital symmetry can be degenerate (see again Fig. 34).

In the *strongly interacting* limit, we can proceed as follows: We observe that coefficients in the wave function ansatz (177) are linearly dependent if they correspond to an exchange of identical bosons, and $a_P = -a_Q$ (compare Eq. (179)). We can change the definition of the coefficients in the effective Hamiltonian (182), such that $\alpha_{P,Q} \equiv \alpha_k$ if P and Q are equal up to a transposition of two consecutive particles that are either distinguishable *or indistinguishable bosons* at sites k and $k+1$. In the reduced basis of $D_{N,\kappa}$ linearly independent coefficients $\mathbf{a}_{\mathrm{snip}}$, the eigenstates are now found by solving the diagonalizing the matrix V with

$$V_{ij} = \begin{cases} \alpha_{i,j} & \text{if} \quad i \neq j \\ -\sum_{\mathrm{d},k\neq i} \alpha_{i,k} - 2\sum_{\mathrm{b},k\neq i} \alpha_{i,k} & \text{if} \quad i = j, \end{cases} \tag{204}$$

where the index d indicates elements between the snippets that transpose distinguishable particles, while b labels elements between sectors which correspond to a transposition of identical bosons.

The set of coefficients $\mathbf{a}_{\mathrm{snip}}$ identifies the orbital wave function (177) uniquely. In particular, we find that independent of the chosen mixture, the states obey the Lieb-Mattis theorem in the orbital part of the wave function.

For a general boson-fermion mixture, the different exchange relations make it difficult to derive an effective spin model of the kind (189) due to different commutation relations for bosons. Here, we do not attempt to solve the problem, but rather give an intuitive outline of the problem. Consider the two-particle wave function introduced in Eq. (179) and let us assume that the two particles are distinguishable. If the total wave function (orbital and spin) was anti-symmetric, we would call these particles distinguishable fermions. A symmetry of the orbital wave function would then correspond to an anti-symmetry in the spin wave function and vice versa. We discussed for the orbital wave function that a symmetry would yield $a_{12} = -a_{21}$, and we could write the spin projection as $|\psi\rangle_s \propto a_{12} |\uparrow\downarrow\rangle + a_{21} |\downarrow\uparrow\rangle = a_{12}(|\uparrow\downarrow\rangle - |\downarrow\uparrow\rangle)$. It would therefore correctly describe the symmetry of the spin problem as anti-symmetric.

Without further adaptations, we would then get a false result for a system of distinguishable *bosons*. This needs to be taken into account when writing an effective spin model in the spirit of Eq. (185). For systems which are purely fermionic or bosonic, the problem has been addressed in Ref. [215]. In particular, in the effective spin description of a purely bosonic system, the signs of all α_j in the spin Hamiltonian (185) change sign. To obtain the effective spin model for a mixture of bosons and fermions, one has to first determine the global symmetry of the mixture (compare Fig. 34) which fixes the overall exchange statistics for

(a)

(b)

(c)
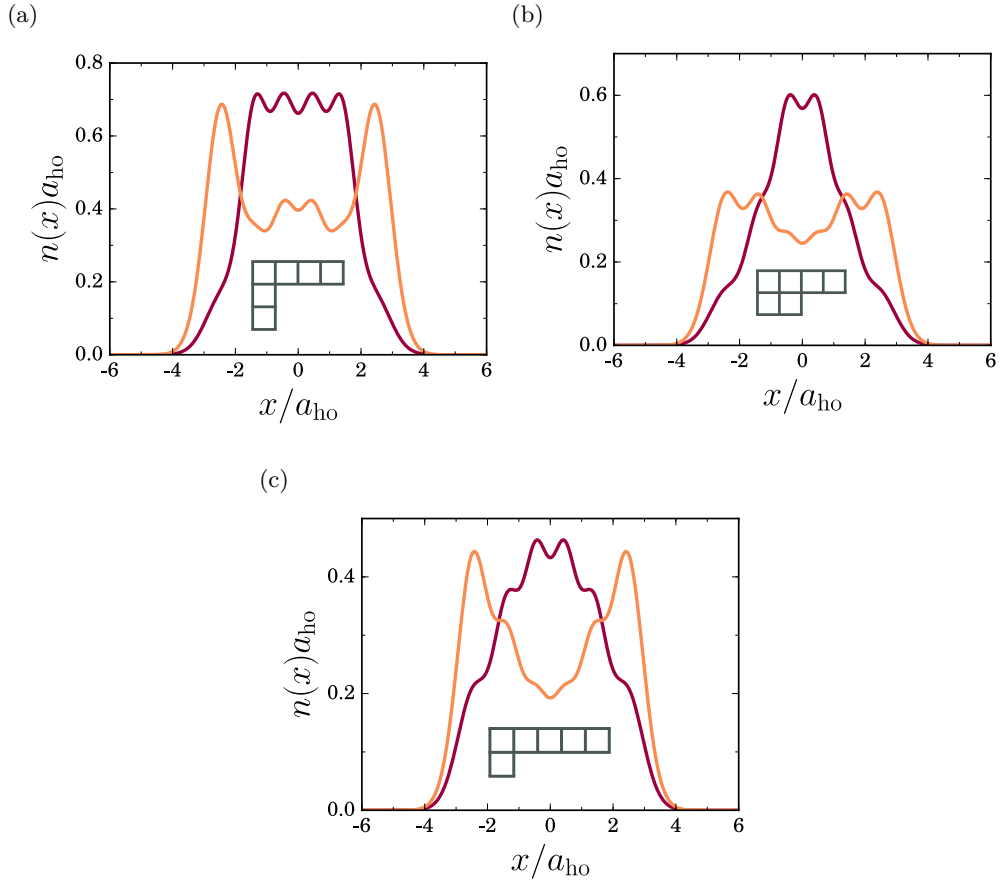
Figure 35: **Ground state density distributions for different boson-fermion mixtures at strong interactions**. The plots present exact results for the density distribution in the limit $1/\alpha \to 0$. (a) A mixture of one fermionic (orange) and one bosonic (red) species with three particles each, $3_F + 3_B$, (b) two fermionic and one bosonic species with two particles each, $2_F + 2_F + 2_B$, (c) one fermionic and two bosonic species with two particles each, $2_F + 2_B + 2_B$. The Young diagrams indicate the orbital symmetry of the states.

any pair of particles. This knowledge permits a statement on whether a (anti-)symmetric commutation in the orbital wave function induces a symmetric or anti-symmetric exchange in the spin wave function.

DENSITY AND MOMENTUM DISTRIBUTIONS, TAN CONTACTS.   Let us now discuss the observable quantities for boson-fermion mixtures and put them into a wider context.

From a mean-field level, a spatial separation between the different species is expected for increasing interactions [219]. However, such considerations become invalid in the regime of strong interactions due to the increasing importance of quantum fluctuations. Nevertheless, for two-species mixtures a spatial separation was also predicted using Luttinger liquid [195] and local density approximation approaches [220, 221]. Exact results for small systems [222] confirm the pre-

diction. Here, we present (numerically) exact density distributions for different binary and ternary mixtures at all interaction strengths: In Fig. 28c, we exemplarily show the deformation of such distributions under increasing interactions. Fig. 35 displays the density distributions for different binary and ternary mixtures in the limit of strong interactions. Our results confirm the spatial separation, which can also be understood through the symmetry considerations for the strongly interacting regime: In order to minimize the costly anti-symmetric exchanges (compare Eq. (204)), fermions orientate towards the edges. For ternary mixtures, we find that density distributions do not only depend on interaction strength but also on the type of the mixture. This shows that the separation is not exclusively an interaction effect, but depends on the underlying symmetry (compare Figs. 35b and 35c). The study at finite interactions shows that the interplay of symmetry and interactions determines the distribution also for a wide range in the intermediate regime.

The momentum distributions of boson-fermion mixtures show the same qualitative changes as the fermionic systems when increasing the interaction strength. However, for balanced mixtures, the Tan contacts differ for fermionic and bosonic species. We observe that the Tan contact of purely fermionic systems (171) then generalizes to

$$
\mathcal{C}_\nu = \frac{g_{1\mathrm{D}} m^2}{2\pi\hbar^4} (1 + \delta_{\nu\nu'}) \langle H_{\mathrm{int},(\nu,\nu')} \rangle \tag{205}
$$

which is still consistent with the definition of the total Tan contact $\mathcal{C}_{\mathrm{tot}} = \sum_{\nu=1}^{\kappa} \mathcal{C}_\kappa$ (172). The latter is then linked to different energy slopes K and again, experimental measurements with spin-resolved time-of-flight measurements could be used to identify the nature of a mixture or - for a given mixture - its symmetry.

CONCLUSIONS

6

In this thesis, we have taken a very broad perspective on the exciting field of designed physical systems that can be realized in cold atom experiments. The highly tunable setup offers a new paradigm in our understanding of quantum many-body systems. Beyond the mere simulation of the physics occurring in existing materials, cold atoms allow the unprecedented possibility of creating *synthetic quantum matter* (i) by exploring parameter regimes of theoretical models that are unattainable in currently known materials and (ii) by combining interesting properties that lead to new, emergent features. In this context, we focused on (quasi-)one-dimensional systems which - as we demonstrated - offer very rich physics. In future research, the models and results presented here can be understood as building blocks in a bottom-up approach to even more intricate higher-dimensional designs.

As a first step, we gave an overview of aspects that we considered interesting to investigate in the above framework. Starting from general aspects of cold atomic setups (an appendix was dedicated to experimental details), we identified and reviewed components that are individually relevant and implementable. One aspect that we considered were features that concern the *geometry* of the lattice and therefore influence how the fermions can move through the system. In particular, if closed paths exist, they allow the creation of artificial gauge fields that play a role for both quasi-one-dimensional and ring-shaped systems. Such artificial gauge fields can drive currents in the system and are also highly-relevant for *topological* features. We also commented on *symmetries* as a ubiquitous feature in physical systems and on their particular role with respect to the previous aspects. We motivated our interest in interactions and the resulting strongly correlated physics, which can no longer be addressed with simple analytical means. As interactions are a recurring ingredient in all our models, we made heavy use of numerical calculations in the form of tensor networks. To offer a self-contained image of such tensor networks and their importance beyond numerics, we presented them in a comprehensive appendix.

We then turned to concrete physical setups that combine two or more of the above ingredients:

- In the *imbalanced Creutz-Hubbard ladder*, we investigated the competition between topological features and interaction effects. We made use of a variety of analytical methods (mapping to effective models, perturbation theory, etc.) and presented extensive numerical results to explore features of the model. The techniques employed could be relevant for other strongly correlated topological insulators; our predictions can be tested in state-of-the-art cold atomic experiments. We laid out the full phase diagram of

the model and showed that an originally topological phase of the AIII-class can be driven to two different non-topological phases by adding only on-site repulsive interactions. We established the nature of the transitions and found that the critical line corresponds to a Dirac CFT at weak interactions, but splits into two critical lines with Majorana CFT for strong interactions. We substantiated this numerical finding in the entanglement entropy scaling with effective theories in limiting cases of the model, and identified experimentally accessible signatures of the different phases.

Follow-up research on the same setup could investigate the nature and the effective quantum field theory of the tri-critical point at which the critical line with an integer central charge splits into two critical lines with half-integer charge. Future research could also focus on different fillings of the model. In this scenario, new features such as fractional effects might emerge which could be interpreted in analogy to the fractional quantum Hall effect in two-dimensional systems. In the same context, topological phases could occur that are entirely interaction-driven and disappear at zero interactions. Another target for follow-up studies could be the exploration of similar lattices with a higher number of sites in the synthetic lattice direction. Such designs could be employed to advance the understanding of bulk-edge behavior from a microscopic perspective and eventually allow an extrapolation to the true two-dimensional regime.

- With *Weyl fermions in one-dimensional ring traps* we studied the effect of repulsive interactions on the current response of particles with an exotic linear dispersion on a circular lattice. For the investigation, we combined a perturbative approach with numerical results obtained with the recently developed method of binary tree tensor networks. We motivated our interest in Weyl fermions through their relevance for both quantum field theory and topological insulator research. We found that a new exotic enhancement of the diamagnetic response occurs for certain configurations of nearest-neighbor interactions and demonstrated that the effect persists over a large interaction range. Moreover, we put forward ideas to realize the setup with ultracold atoms. Nevertheless, the tunability of the Drude weight of interacting Weyl fermions can be considered a more general phenomenon with relevance also for other setups.

  Future investigations could target the origin of the discovered phenomenon and therefore address currents flowing in the Creutz ladder on a microscopical level. It would also be interesting to have a deeper understanding of the influence of lattice effects. In this respect, alternative implementations of linearly-dispersive particles could be envisioned. Finally, in addition to the ring-implementation proposed here, the theory could also be tested on other platforms, for example through transport experiments in cold atom wires.

- In the setup of *harmonically trapped fermions with SU(N)-invariant interactions*, we studied the interplay of symmetry and strong correlations in a continuous one-dimensional system. Therefore, we combined exact results

in the limiting cases with numerical results for the regime of intermediate interactions. Our MPS calculations proved the relevance of tensor network calculations for (discretized) continuum problems, where it is a priori unclear if the underlying assumption on entanglement scaling is fulfilled. For the SU(N)-symmetric fermions, we provided an intuitive understanding of the symmetry and its reflection in the commutation relations of the orbital and spin components of the many-body wave function. We pedagogically reviewed the steps leading to an effective spin model for strong interactions and established a strong link between the resulting magnetization of a state and measurable signatures in its momentum distribution. Using a combination of numerical calculations and a local-density ansatz, we generalized our results to higher particle numbers and intermediate interactions. Finally, by looking at mixtures of both fermions and bosons, we further substantiated the importance of symmetry on the observed physics and confirmed earlier results on boson-fermion separation.

For future investigations, one could anticipate the implementation of the SU(N)-symmetry in tensor networks. This would expand the reach of the numerical simulations to considerably higher particle numbers. It would also be exciting to fully understand the energy ordering of states with respect to their symmetry (including the cases not covered by the Lieb-Mattis theorem). More ambitiously, both theoretical and analytical research could try to integrate the ideas of other physical communities for which high symmetries are important.

As this summary shows, we addressed diverse timely subjects in cold atomic matter which encourage further investigation. From a broader perspective, the scope and the versatility of ultracold atoms and synthetic quantum matter will further expand. Interdisciplinary approaches will allow other fields of physics to benefit from the results obtained through quantum simulations. At the same time, backed through international research initiatives, quantum phenomena are receiving a wider attention and quantum technologies are even beginning to raise the interest of private businesses. It is hard to predict what exactly the future will bring, but it surely will be exciting.

A

NUMERICAL METHOD: VARIATIONAL OPTIMIZATION WITH TENSOR NETWORKS

In the main body of this thesis, we focus on physical properties of the studied one-dimensional fermionic systems and their interpretation. Nonetheless, a considerable time of the investigation period was devoted to understanding, writing, improving and applying tensor network methods. Actually, besides the intrinsically numerical results, much of the theoretical and analytical understanding presented in this thesis was stimulated by earlier numerical investigation. Conversely, the analytical findings then encouraged further numerical studies. It is therefore just to give some credit to this powerful method. The section at hand is not intended to give a comprehensive picture, but rather to present those aspects that were particularly relevant for our work. For a more complete introduction, the reader is referred to our publication in Ref. [223].

Why tensor networks? In the study of quantum many-body systems, advanced numerical tools are an essential means of exploring regimes unaccessible to analytic calculations. Naive brute-force approaches would be too costly due to the exponential growth of the Hilbert space with the number of constituents. A plethora of such techniques exists, and each of them has its advantages and disadvantages: Bosonization is powerful in predicting the universal behavior, but fails to explain microscopic features. Monte Carlo methods struggle with the so-called *sign problem* and mean-field methods like DMFT are limited to higher dimensions due to the strong quantum fluctuations in one-dimensional systems.

If the temperature of a system is small compared to its inherent energy scales, tensor networks present a powerful alternative to these schemes. They rely on the fact that in many realistic systems, the exponentially large Hilbert space is only populated in a small, physically relevant subspace. This is related to the fact that under certain conditions, the ground state entanglement in a bipartition of a system does not scale with the volume of a subsystem, but instead with its surface. In particular for gapped lattice systems, this is the case if the interactions are of finite range or decay sufficiently fast with the distance. This finding has been rigorously proven for a multitude of systems in the so-called *area laws* [20].

Originally developed as *matrix product states* (MPS) to understand the working of the *density matrix renormalization group* (DMRG) [224–227], tensor networks have evolved to a research field of its own. Today, they are not only used for one-dimensional systems, but also for higher dimensions (e.g. in two dimensions as *projected entangled pair states* (PEPS) [228]) and even outside their original condensed matter perimeter, e.g. to simulate lattice gauge theories [229]. Moreover, while first only used as a numerical tool, tensors can now be understood as "quantum informational building blocks", the composition of which can explain e.g. topological behavior [16, 94, 95].

With respect to numerical simulations, a tensor network can be understood as an ansatz which is then optimized to represent a low-energy many-body state (most often the ground state) of a system. This ansatz is minimally biased in the sense that the only constraint is the assumption of a certain (limited) entanglement in the system, and this assumption can be loosened during optimization when necessary. Once calculated, tensor networks can be efficiently stored and subsequently any kind of expectation value (local observables, correlations and global quantities) can be determined.

A certain class of tensor networks is particularly apt for variational ground state search in the spirit of DMRG: So called *loop-free tensor networks* do not contain cycles in the graph which represents the linkage of the tensors. The above-mentioned matrix product states are one instance of this class, but we will see that the generalization of MPS also allows for other geometries which may better reflect certain system properties like gaplessness or periodic boundary conditions.

In the following section (Sec. A.1), we first define loop-free tensor networks and show how operators can be written in the tensor framework. We shortly discuss how to install gauges in tensor networks and give an introduction on how to implement (Abelian) symmetries in the tensors. In Sec. A.2 we outline a generic DMRG method to find the ground state of a system, and explain how the stability of this method is affected by the loop-freedom of the network. Sec. A.3 discusses shortly the technical aspect of treating fermionic systems with the help of Jordan-Wigner transformations. The rest of the chapter is then devoted to the description of instances of the particular tensor networks, which we used in the study of the physical systems: In Sec. A.4, we define MPS and then give details of their application on the different models. In Sec. A.5, we proceed likewise for so-called *binary tree tensor networks* (bTTN).

A.1   TENSOR NETWORKS

A.1.1   *Tensor networks in general*

What is a tensor? In a narrow definition, we consider a tensor a multidimensional array of numbers. The *rank* of a tensor determines this dimensionality. Elements of the array are labeled by a corresponding number of indices. A tensor of rank 0 is a scalar, a rank-1 tensor is a vector (a_i), a rank-2 tensor is a matrix (A_{ij}), etc. We will see later on how to generalize the definition in the presence of symmetries. Graphically, we can represent tensors by boxes (or circles) with a number of links equal to the rank of the tensor (Fig. 36a). Two tensors A and B, which have a dimension for which the corresponding indices α_m and β_n can take the same values in $\{1, \dots, D\}$, can be contracted. A contraction is defined as

$$C_{\alpha_1,\dots,\alpha_{m-1},\alpha_{m+1},\dots,\alpha_M,\beta_1,\dots,\beta_{n-1},v_{n+1},\dots,\beta_N} = \sum_{\alpha_m,\beta_n=1}^{D} A_{\alpha_1,\dots,\alpha_M} B_{\beta_1,\dots,\beta_N} \delta_{\alpha_m,\beta_n}.$$

(206)
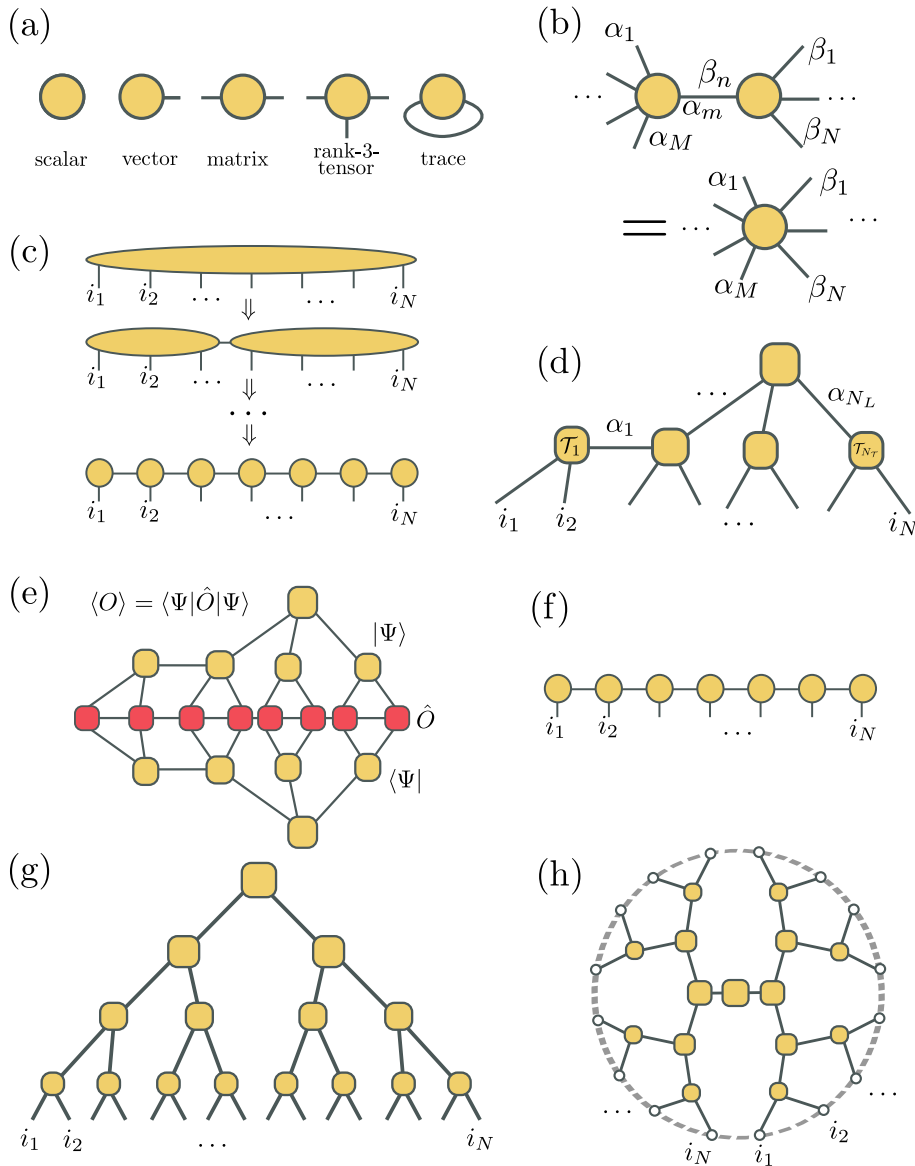
Figure 36: **Basic ingredients for tensor network methods.** (a) A convenient graphical representation of tensors, where each leg represents an index of the mathematical object: this allows for an intuitive pictorial sketch of tensor networks. (b) Contraction of two tensors over a common index $\alpha_m = \beta_n$. (c) Schmidt decomposition of the tensor containing the coefficients of a Hilbert space wave function into two smaller tensors corresponding to subsystems: The vertical legs correspond to the physical degrees of freedom, while the horizontal legs (virtual links) carry information about the entanglement between the two subsystems. The process can be iterated to obtain a tensor network with smaller tensors. (d) A generic loop-free tensor network. (e) Pictorial representation of the expectation value of a multi-site observable, represented by a matrix product operator (MPO). (f) A matrix product state (MPS). (g)-(h) Besides the (linear) decomposition into MPS, other tensor network architectures can be employed for the description of one-dimensional systems. Here, we show binary tree tensor networks (bTTN). The representation in (g) hints at the hierarchical renormalization of entanglement in bTTN, the representation in (h) focuses on their aptness for setups with periodic boundary conditions.

In terms of diagrams, the process is represented by a connection of the corresponding links (see Fig. 36b).

What is a tensor network? A tensor network constitutes a collection of tensors which are linked, i.e. there exists a rule of how to contract the tensors in the set. An example of a generic tensor network is given in Fig. 36(d).

How do tensor networks represent physical states? The wave function of a many-body system of L constituents with physical dimension d living in some Hilbert space H is given as

$$|\Psi\rangle = \sum_{i_1,\ldots,i_L=1}^{d} c_{i_1,\ldots,i_L} |i_1,\ldots,i_L\rangle, \qquad (207)$$

i.e. the number of coefficients needed in this description scales exponentially in L, and $\dim(H) = d^L$. In the notation introduced above, we can understand $c_{i_1,\ldots,i_L}$ as the elements of a rank-L tensor. We can now introduce a bipartition at some physical site of the system such that we obtain two subsystems of constituents with $\mathcal{L} = (i_1,\ldots,i_x)$ and $\mathcal{R} = (i_{x+1},\ldots,i_L)$. For these, we can define Hilbert spaces $H_\mathcal{L}$ and $H_\mathcal{R}$ with $\dim(H_\mathcal{L}) = d^x$ and $\dim(H_\mathcal{R}) = d^{L-x}$, respectively. It is then always possible to write any state of the full Hilbert space in terms of a so-called *Schmidt decomposition*,

$$|\Psi\rangle = \sum_{j=1}^{\kappa} \lambda_j |\varphi_{\mathcal{L},j}\rangle \otimes |\varphi_{\mathcal{R},j}\rangle, \qquad (208)$$

where $\{|\varphi_{\mathcal{L},j}\rangle\}$ and $\{|\varphi_{\mathcal{R},j}\rangle\}$ are sets of pairwise orthogonal states in $H_\mathcal{L}$ and $H_\mathcal{R}$, respectively, and $\kappa = \min\{\dim(H_\mathcal{L}), \dim(H_\mathcal{R})\}$.

The descendingly ordered set of Schmidt coefficients $\{\lambda_j\}$ (often also in the form $\{-\log(\lambda_j)\}$) is called the *entanglement spectrum* of the bipartition and for normed states $\sum_j \lambda_j^2 = 1$, i.e. the values express probabilities of encountering a subsystem state in the overall wave function. The quantity $S = -\sum_j \lambda_j^2 \log(\lambda_j^2)$ is called the *entanglement entropy* and represents the quantum version of the von Neumann entropy. For a pure state, i.e. $\lambda_1 = 1$ and $\lambda_j = 0$ for $j > 1$, the system is unentangled ($S = 0$). On the contrary, for a maximally entangled state $\lambda_j = 1/\sqrt{\kappa}$ and $S = \log\kappa$. To understand the scaling of the entanglement between a growing system $\mathcal{L}$ and a large environment $\mathcal{R}$, we can assume $x \ll L$. For a system with local dimension d, the maximally possible entanglement then scales like $S = x\log d$, i.e. linear in the size of the system.

However, for a great variety of (gapped) systems with local interactions, the entanglement entropy over a bipartition of the ground state does not scale with the size of the bipartition, but instead with its surface. This is called *area law*. For a one-dimensional system, the entanglement entropy therefore saturates with growing length of a subsystem. This behavior is reflected by the scaling of the values λ_j: either $\lambda_j = 0$ for $j > k$ and some given k, or $\lambda_j \propto e^{-cj}$ with some constant c. In the first case, it is easy to see that the number of states needed in the description (208) is drastically reduced. In the second case, we can impose an upper limit D to the number of states to keep, discard all others, and then renormalize the retained, $\lambda_j^2 \to \lambda_j^2/(\sum_{i=1}^{D} \lambda_i^2)$ for $\lambda_j \leq D$. This is at the heart of the density-matrix renormalization group (DMRG). The connection to its

traditional form becomes more transparent when explicitly writing the density matrix of subsystem $\mathcal{L}$ by tracing out all degrees of freedom of subsystem $\mathcal{R}$: $\rho_{\mathcal{L}} = \text{Tr}_{\mathcal{R}} |\Psi\rangle \langle \Psi| = \sum_j \lambda_j^2 |\varphi_{\mathcal{L},j}\rangle \langle \varphi_{\mathcal{L},j}|$.

Diagrammatically, we can understand the splitting of a tensor with higher rank (207) into two tensors of smaller rank (208) as shown in Fig. 36c. If for the blocks in the subsystems further Schmidt decompositions are performed, we obtain a tensor network. Indeed, following this prescription, we always end up with a loop-free tensor network. For completeness, we note that tensor networks can be designed such that they contain loops by construction. This is e.g. the case for PEPS or the *multi-scale entanglement renormalization ansatz* (MERA) [230]. For a given quantum many-body state with L constituents $|\Psi\rangle$, a general tensor network is then given by a set of tensors $\mathcal{T}^{[j]}$, the contraction of which would lead to a tensor $\mathcal{T}_{i_1,\ldots,i_L}$ equal or similar to the coefficient tensor in Eq. (207); namely,

$$
\begin{aligned}
|\Psi\rangle &\approx \sum_{i_1,\ldots,i_L} \mathcal{T}_{i_1,\ldots,i_L} |i_1,\ldots,i_L\rangle \\
&= \sum_{i_1,\ldots,i_L} \sum_{\alpha_1,\ldots,\alpha_L} \mathcal{T}^{[1]}_{\{i\}_1,\{\alpha\}_1} \mathcal{T}^{[2]}_{\{i\}_2,\{\alpha\}_2} \cdots \mathcal{T}^{[N_{\mathcal{T}}]}_{\{i\}_{N_{\mathcal{T}}},\{\alpha\}_{N_{\mathcal{T}}}} |i_1,\ldots,i_L\rangle,
\end{aligned}
\tag{209}
$$

where $N_{\mathcal{T}}$ is the number of tensors in the network and N_α is the number of virtual (i.e. non-physical) links; $\{i\}_x$ and $\{\alpha\}_x$ label the sets of physical and virtual links connected to some tensor $\mathcal{T}^{[x]}$ in the network (compare Fig. 36d).

A.1.2 *Operators and observables, MPOs*

Any operator acting on a single site j with local dimension d can be written as a matrix of the same dimension. In the graphical notation, its action is then obtained by contracting the matrix to the according physical link. Operators that act on two or more sites (e.g. correlators), but have local representations in terms of matrices, can be applied similarly. The expectation value is then obtained by contracting the object with the tensor network representing the conjugate transpose of the wave function (commonly represented by horizontally mirroring the original tensor network, compare Fig. 36e).

Often, one encounters operators which consist of the sum of a large number of locally acting operators. Treating such terms in the tensor network formalism can be tedious as one needs to keep track of the different terms and their network representation. It can then be favorable to use so-called *matrix product operators* (MPOs) [231, 232]. These take the form (compare Fig. 36e):

$$
\hat{O} = \sum_{\{i_j\},\{i'_j\}} \sum_{\{\alpha_j\}} M^{[1],\alpha_1}_{i_1,i'_1} M^{[2],\alpha_1,\alpha_2}_{i_2,i'_2} \cdots M^{[L],\alpha_{L-1}}_{i_L,i'_L} |i_1\rangle \langle i'_1| \otimes |i_2\rangle \langle i'_2| \otimes \ldots \otimes |i_L\rangle \langle i'_L|.
\tag{210}
$$

The additional links $\{\alpha_j\}$ between the locally acting operators make it possible to include all the terms appearing in an operator. A given instance of the set $\{\alpha_j\}$ then uniquely identifies a summand. If the terms in the operator (e.g. in a Hamiltonian) are site-independent, the same tensor $M \equiv M^{[j]}$ can be used on all

sites and a smart assignment between local operators and index-pairs can lead to to an efficient scaling of the virtual dimension $\dim(\alpha)$ even with long-range terms [233].

A.1.3 *Loop-free tensor networks and gauges*

The tensor network description of a state has *gauge freedoms*. For example, matrices X and Y with the property $X \cdot Y = \mathbb{1}$ can be introduced on any virtual link and then absorbed into the respective adjacent tensor without changing the physical content of the description. For loop-free tensor networks, i.e. networks without cycles in their graph, the whole gauge freedom is determined by such *link-local* operations. By fixing a particular gauge, we can give the tensors a particular shape which can reduce the number of explicit contractions necessary in certain computations. Therefore, the prescription can lead to great advantages in the numerical calculations.

We concentrate here on the so-called *unitary gauge*. For a chosen tensor $\mathcal{T}^{[i]}$ (*center*), this gauge can be installed by performing the following procedure: First, label all the tensors in the tensor network according to their graph-distance with respect to the center. Starting from the most distant tensor, then perform the following steps and iterate until the center is reached:

- QR-decompose the tensor at hand $\mathcal{T}^{[j]}$ such that

$$\mathcal{T}^{[j]}_{\{\rho\},\eta} = \sum_{\xi=1}^{d_\xi} \mathcal{Q}_{\{\rho\},\xi} \mathcal{R}_{\xi,\eta}, \qquad (211)$$

  where the index $\{\rho\}$ collects all the links of the tensor pointing away from the center, and η labels the link towards it. The dimension d_ξ might be reduced with respect to the dimension of the original link $\dim(\eta)$ as $d_\xi = \min(\prod \dim(\{\rho\}), \dim(\eta))$. The tensor $\mathcal{Q}$ has the property of being isometric. This means that the contraction of the tensor with its conjugate over the links $\{\rho\}$ yields an identity,

$$\sum_{\{\rho\}} \mathcal{Q}_{\{\rho\},\xi} \mathcal{Q}_{\{\rho\},\xi'} = \delta_{\xi,\xi'}. \qquad (212)$$

- Update the tensor $\mathcal{T}^{[j]} \to \tilde{\mathcal{T}}^{[j]} = \mathcal{Q}^{[j]}$.

- Contract the matrix $\mathcal{R}^{[j]}$ to the adjacent tensor in the graph towards the center $\mathcal{T}^{[i]}$.

The isometry property of the network is shown and applied in Fig. 38a. Once the gauge is installed, changing the center of the gauge from some tensor $\mathcal{T}^{[i]}$ to some other tensor $\mathcal{T}^{[j]}$ is simple, as only those tensors of the network are affected which lie on a direct path between the two. It is then sufficient to apply the above method on this subset (compare Fig. 38c).

Note that the above prescription yields a unique tensor network only due to its property of *loop freedom*. We will see in Sec. A.2 how the absence of loops also allows for stable optimization schemes.
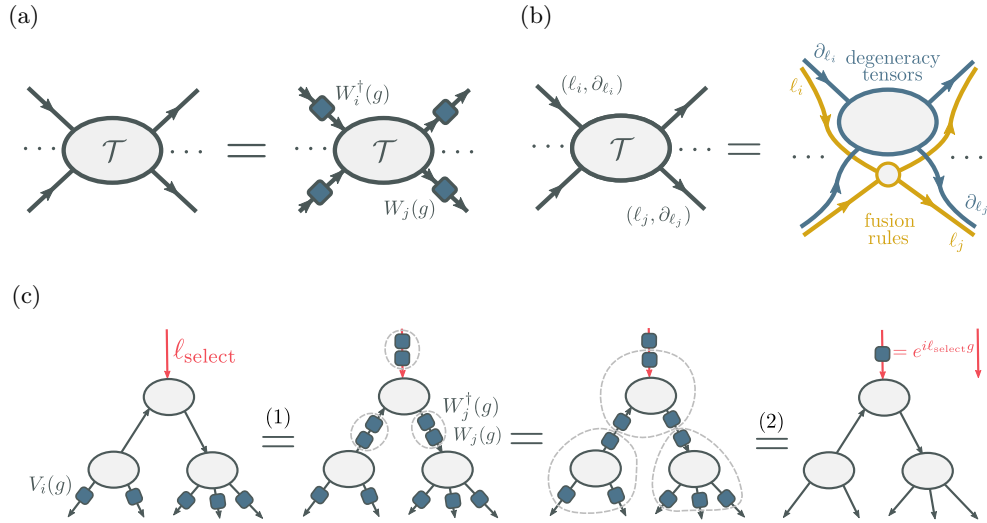
Figure 37: **Symmetric tensors and tensor networks.** (a) The defining feature of a symmetric tensor is its invariance under the application of representations of the symmetry. By definition, representations of the kind $W_j(g)$ $(W_j^\dagger(g))$ act on outgoing (ingoing) links. (b) The internal structure of a symmetric tensor is such that for a set of quantum numbers $\{l_i, l_j, \ldots\}$ on the links, a degeneracy tensor (of dimension $\partial_{l_i} \cdot \partial_{l_j} \cdot \ldots$) can only exist if the fusion rule for this set holds. (c) A point-wise global symmetry acts on the physical legs of some tensor network, which is equipped with a selector-link only containing a single non-degenerate sector with some quantum number of the symmetry ℓ_{select}. (1) Representations of the symmetry can be installed on the virtual links such that (2) we can exploit the properties of symmetric tensors, see (a). The overall action of the symmetry is then the multiplication with a phase $e^{i\ell_{\text{select}}g}$. ℓ_{select} therefore controls the quantum number of the physical state.

A.1.4 *Symmetries in tensor networks*

Symmetries that occur in physical problems usually go along with conserved quantities. More precisely, a system is considered to have a symmetry described by a group $\mathcal{G}$, if for any element $g \in \mathcal{G}$ a unitary representation $U(g)$ can be found such that $[U(g), H] = 0$. In this case, there is an operator commuting with the Hamiltonian and the Hamiltonian becomes block-diagonal when written in the basis of that operator. As a consequence, the eigenvalues (and the corresponding states) of the Hamiltonian can be found by diagonalizing these blocks. Numerically, this can lead to a substantial speed-up with respect to the original problem.

An eigenstate of a symmetric Hamiltonian $|\psi_{\ell,m,\partial}\rangle$, i.e. a state with the property $H |\psi_{\ell,m,\partial}\rangle = E_{\ell,\partial} |\psi_{\ell,m,\partial}\rangle$, can be labeled by the quantum number ℓ, possible higher quantum numbers m, and an additional label ∂, which distinguishes states that cannot be further distinguished by the symmetry. The action of the symme-

try is then $U(g) |\psi_{\ell,m,\partial}\rangle = \sum_{m'} W^{[\ell]}_{m,m'}(g) |\Psi_{\ell,m',\partial}\rangle$ where $W^{[\ell]}(g)$ is the ℓ-sector matrix associated with the group element g.

In particular, Abelian symmetries are characterized by their commutative property $[U(g), U(g')] = 0 \ \forall g, g'$ and have one-dimensional unitary irreducible representations $W^{[l]}(g) = e^{ilg}$. Typical examples for Abelian symmetries are the U(1)-symmetry, which reflects e.g. particle number conservation, or the $\mathbb{Z}_2$-symmetry representing a parity. Let us concentrate on the earlier to better understand the terminology: The U(1)-symmetry group is also called the *continuous planar rotation group*. The group element parameter g can take values of an angle, i.e. from $[0, 2\pi)$, and the group operation is $g \circ g' = (g + g') \mod 2\pi$. The irreducible representations are labeled by integers $\ell \in \mathbb{Z}$. The fusion rule when joining two objects is $\ell \otimes \ell' = \ell + \ell'$.

The fact that the Clebsch-Gordan coefficients are therefore just Kronecker-deltas is similarly true for other Abelian symmetries. This fact allows for an easy implementation of Abelian symmetries in tensor networks: We upgrade any link in the network to be symmetric by associating a quantum number to each index-value $\alpha \in \{1, \ldots, \dim(\alpha)\}$ of a link. As several index values can share the same quantum number, we introduce an additional label ∂_ℓ running over the degenerate subspace: $\alpha \equiv (l, \partial_\ell)$. The action of a symmetry applied to this link-sector with label ℓ is then $e^{i\ell g}$ and $[W(g)]_{jk} = e^{i\ell g}\delta_{jk} \ \forall g \in \mathcal{G}$.

A tensor is then only called *invariant* under the action of a symmetry, if it fulfills $\sum_j \ell_{\text{in},j} = \sum_j \ell_{\text{out},j}$ (see Fig. 37a). Here, those links which are acted on with $W_j^\dagger$ (and therefore with the inverse irreducible representation $\ell^\dagger = -\ell$) are represented with an ingoing arrow (and vice versa). The tensor architecture used in our simulations is fully based on such invariant tensors. Technically, this already leads to a severe reduction of coefficients in a tensor. Take as an example a (traditional) N-leg tensor with indices $i_1, \ldots, i_N$ and associated dimensions $d_1, \ldots, d_N$. Such a tensor stores a number of coefficients $\prod d_j$. In our invariant symmetric tensors, only those coefficients will be stored which are allowed by the fusion rules of the symmetry: $\sum \delta_{\sum l_{j,\text{in}}, \sum l_{j,\text{out}}} \prod \dim(\partial_{l_j})$. The original number-tensor is thereby split into a number of smaller blocks (*degeneracy tensors*). Conceptually, the internal scheme of a symmetric tensor is shown in Fig. 37b.

The numerical routines for all tensor operations then explicitly perform only operations that respect the symmetry constraints. For example, in a contraction of two symmetric tensors, the routine keeps track of all involved quantum numbers, and performs the contraction only for those degeneracy tensors which are compatible by the fusion-rules. This yields a significant speed-up. For a quantitative discussion of the gain, see Ref. [223].

Two types of symmetries are particularly apt to be implemented in tensor networks: *global point-wise symmetries* and *lattice gauge symmetries*. We focus on the first kind here. Global point-wise symmetries are such symmetries that have a group representation which can be written as a direct product of local terms, $U(g) = \otimes_j V_j(g)$. To control the quantum number N of a state, we attach an additional link (*selector link*) to one of the tensors which has dimension 1 and is labeled by this quantum number: $\ell_{\text{select}} = N$ (see Fig. 37c). If we act with the global point-wise symmetry on the physical legs of the network and expand
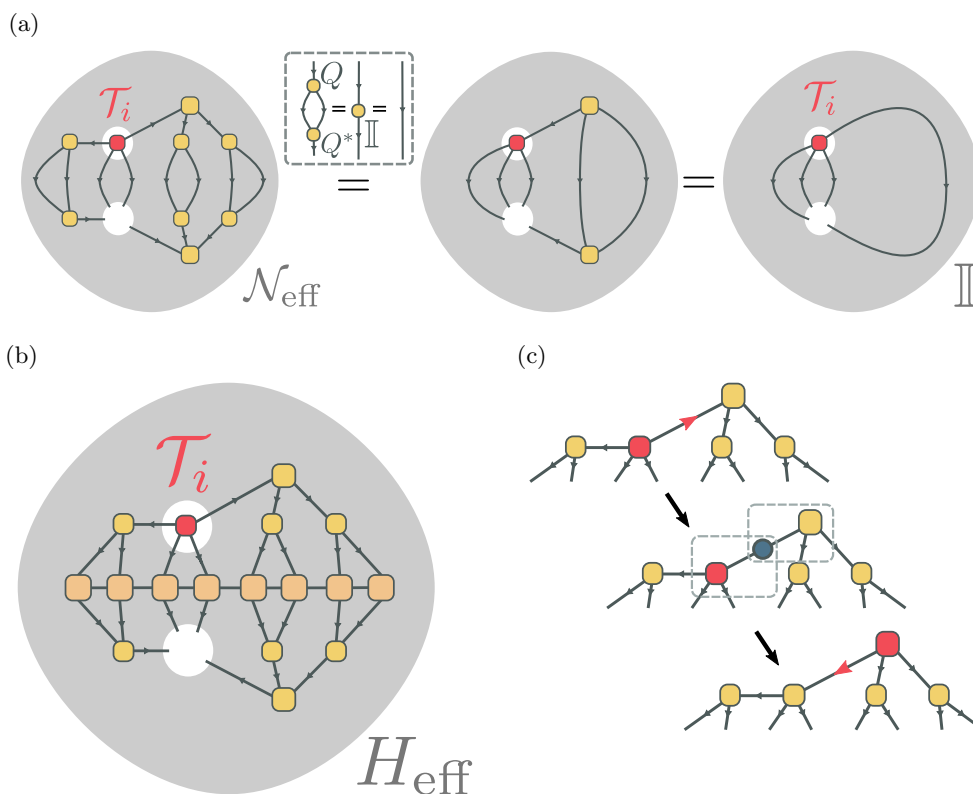
Figure 38: **Variational optimization and gauges.** (a)-(b) Effective norm $\mathcal{N}_{\text{eff}}$ and effective Hamiltonian H_{eff} (grey shaded) with respect to a chosen tensor (red) of a tensor network (yellow) and a Hamiltonian MPO (beige). The installed gauge (arrows, compare Eq. (212)) permits to contract the effective norm to the identity. (c) Having optimized a tensor, the next tensor is addressed. The gauge-center is therefore moved.

identities on the virtual links as $\mathbb{1} = W_j^\dagger(g)W_j(g)$, we can use the invariance of the tensors to absorb the operators on the physical legs and transport the action towards the selector link tensor. We then see that the application of the global symmetry operator has the same effect as the multiplication with a phase e^{igN}. The representation at the selector link therefore determines the sector of the physical state.

We note that symmetries which are not of such a point-wise form (e.g. translational invariance) also play an important role in condensed and cold atomic physics (compare Sec. 2.8). While there are ways to address such symmetries with particular tensor network architectures [234–236], to the present they cannot be treated in a general fashion.

A.2 VARIATIONAL GROUND STATE FINDING

The conceptual idea of DMRG in the language of tensor networks is to consider the tensor network as a variational ansatz, the coefficients of which are adapted

in order to optimally approximate the ground state of the system. Therefore the coefficients in the ansatz are optimized such that a *local* energy expression is minimized. In a *single-site optimization*, this local energy term is obtained by selecting a single tensor of the network and treating all other sites of the system as an environment, which when contracted with the Hamiltonian yields another, *effective* Hamiltonian. The ground state thereof is taken to update the coefficients in the considered tensor. This is done iteratively over all tensors in the network and then repeated until some convergence criterion is matched. To be more precise, the core idea of the variational algorithm consists of the following steps:

Initialization. First, the tensor network is initialized: This includes fixing the network geometry, i.e. the tensors and their linkage, and determining the bond dimension D of the virtual links. If the tensors contain symmetries, the sectors for each link and their degeneracies have to be chosen, which can be done using different approaches [223].

Optimization. The target of the algorithm is to minimize the energy for a given Hamiltonian, $\min \frac{\langle \psi | H | \psi \rangle}{\langle \psi | \psi \rangle}$, and to find the corresponding state $|\psi\rangle$. We can reformulate the problem by considering the conservation of the norm as a constraint which can be treated using Lagrange multipliers. We then target $\min(\langle \psi | H | \psi \rangle - \lambda \langle \psi | \psi \rangle)$. Let us assume that we do not want to access all the coefficients of the system simultaneously, but only those in some tensor $\mathcal{T}_j$; we therefore reduce the problem to finding $\min(\mathcal{T}_j^\dagger H_{\text{eff}} \mathcal{T}_j - \lambda \mathcal{T}_j^\dagger \mathcal{N}_{\text{eff}} \mathcal{T}_j)$, where H_{eff} and $\mathcal{N}_{\text{eff}}$ are effective expressions obtained from contracting the Hamiltonian and (or) the remaining tensors of the network (see Figs. 38a and 38b). If we understand the tensor $\mathcal{T}_j$ as a vector, we can write the minimum condition as

$$\nabla_{\mathcal{T}_j} \left(\mathcal{T}_j^\dagger H_{\text{eff}} \mathcal{T}_j - \lambda \mathcal{T}_j^\dagger \mathcal{N}_{\text{eff}} \mathcal{T}_j \right) = 0 \Rightarrow H_{\text{eff}} \mathcal{T}_j = \lambda \mathcal{N}_{\text{eff}} \mathcal{T}_j . \tag{213}$$

This is a generalized eigenvalue problem, and algorithms to solve the problem suffer from numerical instabilities. However, the absence of loops in the tensor network permits to always gauge the network such that $\mathcal{N}_{\text{eff}} = \mathbb{1}$ (see again Fig. 38a). The problem then reduces to finding the minimal eigenvalue of H_{eff}, which can be performed numerically by standard methods like the Arnoldi algorithm [237].

Sweeping. Subsequently, we address a neighboring tensor, change the gauge to have this tensor as the center (see Fig. 38c) and repeat the optimization step. We proceed this way until we have visited all the tensors in the network. This is called a *sweep*. The order of addressing the tensors is determined beforehand. We continue to sweep through the network until we observe that the energy of the variational ground state converges. To check if the tensor network is a sufficiently good approximation to the actual ground state of the system, the DMRG-process can be repeated with an increased virtual bond dimension $\tilde{D}$ to test the convergence in this parameter.

Two-site optimization. With the above method, in each step the coefficients of a single tensor are optimized. This scheme can easily get stuck in local minima of the energy [227]. For symmetric tensor networks, single-site optimization fails due to the fact that it only allows the optimization of the contents of the degeneracy sectors within a tensor, but does not permit to re-negotiate the dimensions

of the sectors themselves. From a physical perspective (here a system with fixed particle numbers), this prevents particles from being moved through the lattice, i.e. the initial particle distribution of the system cannot be changed. We therefore introduce a so-called *two-site optimization*. The algorithm follows the same steps as described above. However, in the optimization, the coefficients of two neighboring tensors $\mathcal{T}^{[i]}$ and $\mathcal{T}^{[j]}$ are addressed simultaneously. This is computationally more expensive, but yields a significant advantage: The optimized tensor $\tilde{\mathcal{T}}^{[i,j]}$ has the same form (link and degeneracy sectors) as the contraction of $\mathcal{T}^{[i]}$ and $\mathcal{T}^{[j]}$. The reverse operation of splitting $\tilde{\mathcal{T}}^{[i,j]}$ into two new tensors $\tilde{\mathcal{T}}^{[i]}$ and $\tilde{\mathcal{T}}^{[j]}$ permits to open sectors (and degeneracy tensors) in the single tensors which are compatible with the fusion rules, but might not have existed before the optimization. Technically, the splitting is performed using a *singular value decomposition* (SVD):

$$\tilde{\mathcal{T}}^{[i,j]}_{(i_1...i_r)(i_{r+1}...i_n)} = \sum_{k=1}^{d_k} \tilde{T}^{[i]}_{(i_1...i_r)k} \lambda_k \tilde{T}^{[j]}_{k(i_{r+1}...i_n)}. \tag{214}$$

The link between the two new tensors has a total dimension $d_k = \min(\prod_{j=1}^{r} \dim(i_j), \prod_{j=r+1}^{n} \dim(i_j))$. As the coefficients λ_k quantify the entanglement as discussed in Sec. A.1.1, this yields an efficient control of the precision of the ansatz. Either, only a fixed number of states D is kept in each step, or a threshold is defined that controls the minimum probability of an entangled state to be kept. The diagonal matrix $\lambda = \mathrm{diag}(\{\lambda_k\})$ is then contracted into one of the neighboring tensors.

Recently, a so-called *single-site method with subspace expansion* [238, 239] has been presented as a more advanced method that combines the computational efficiency of single-site optimization with the advantages of symmetric tensors.

A.3   MAPPING OF FERMIONIC PROBLEMS

In Sec. 2.9, we introduced Jordan-Wigner transformations as a means of mapping fermionic systems to spin systems. As pointed out earlier, this can be interesting to understand the equivalence of certain physical phenomena. As a consequence, also the language for fermionic and spin problems can be used interchangeably. We demonstrated this in several examples (e.g. when rewriting the Creutz ladder in terms of coupled spin chains in Sec. 3). However, there is still another aspect to Jordan-Wigner transformations which makes them equally relevant for the implementation of physical systems with tensor network states. In this section, we will discuss some aspects of this.

Due to their quantum-informational justification through area laws, tensor network descriptions rely heavily on the locality of the terms occurring in a Hamiltonian. On the contrary, fermions display statistics that are non-local in the sense that an exchange of any two particles, independent of their location, has to be considered by a phase-factor -1 (anti-symmetry of the wave function). The Jordan-Wigner formalism mediates between these seemingly opposing concepts. Namely, it allows us to express a fermionic operator of the type $c_i^\dagger$ by a series of spin operators $\prod_{i<j} \sigma_i^z \sigma_j^+$, a so-called *Jordan-Wigner string*. The crucial point
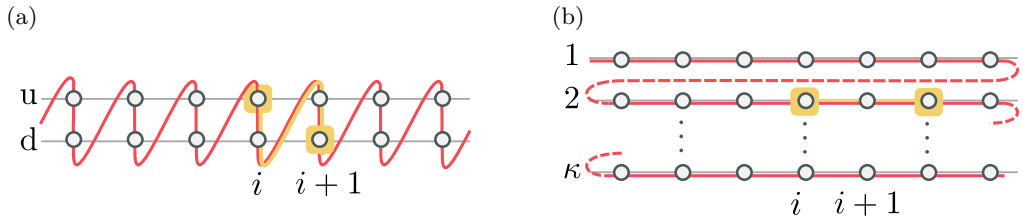
Figure 39: **Assignment of a Jordan-Wigner string to different setups.** (a) In the ladder geometry of the Creutz-Hubbard model, we choose a sawtooth-like ordering. Hopping terms in the underlying model therefore lead to operators which are maximally third-nearest neighbors in the spin description (marked in yellow). (b) In the quasi-one-dimensional lattice discretization of the SU(N)-fermions, no processes involving hopping between different species occur. We therefore apply a snake-like ordering. All terms in the Hamiltonian and in observables involve only Jordan-Wigner strings within a single species.

is that this Jordan-Wigner string consists of a set of local operators which can be efficiently contracted in the tensor network formalism and allow for an easy implementation with matrix product operators.

So far, we have not given a meaning to the notation $i < j$ in the above expression. For quasi-one-dimensional systems, there is no a-priori ordering, and we can assign a such to our liking. It can therefore be advantageous to take the geometry and the symmetries of a system explicitly into consideration. To illustrate this idea, we pick up two of the models studied in the main-text.

In the Creutz-Hubbard model (Sec. 3), we considered a two-species fermionic lattice with inter-leg hopping. Any correlation (or hopping) $c_{i,\sigma}^\dagger c_{j,\sigma'}$ is represented as an operator $\sigma_{i,\sigma}^+ \prod(-\sigma^z)\sigma_{j,\sigma'}^-$, where the product runs over all sites that appear in the chosen ordering between (i,σ) and (j,σ'). It can be instructive to keep this Jordan-Wigner string short to avoid confusion in the mapping and to guarantee an efficient representation as MPO. In this example, this can be realized by choosing a saw-tooth like ordering (see Fig. 39a).

On the contrary, for the SU(N)-fermions in the harmonic trap (Sec. 5), we considered a model in which the number of particles in each species is conserved explicitly. In the discretized model (compare Sec. A.4), hoppings (or correlations) of the kind $c_{i,\sigma}^\dagger c_{j,\sigma'}$ therefore only occur with $\sigma = \sigma'$. As a consequence, a saw-tooth like ordering as in the previous example would only lead to unnecessarily long Jordan-Wigner strings. If instead we choose a snake-like ordering (see Fig. 39b), we avoid such spurious strings. We emphasize that the ordering assigned here does not necessarily need to reflect the distance of the sites in the tensor network description.

A.4   MATRIX PRODUCT STATES

A.4.1   *General*

Matrix product states (MPS) represent the most known and used tensor networks for the description of one-dimensional systems. They are characterized by the fact that every physical site of the system is assigned one tensor and there are no "meta"-levels of tensors involved, i.e. the description (209) simplifies to

$$|\Psi\rangle \approx \sum_{i_1,\dots,i_N} \sum_{\alpha_1,\dots,\alpha_L} \mathcal{T}^{[1]}_{i_1,\alpha_1} \mathcal{T}^{[2]}_{\alpha_1,i_2,\alpha_2} \dots \mathcal{T}^{[N_\mathcal{T}]}_{\alpha_{N-1},i_N} |i_1,\dots,i_N\rangle . \qquad (215)$$

Pictorially, this tensor network is shown in Fig. 36f. Historically, the variational scheme of DMRG [224, 225] existed prior to the notion of tensor networks. MPS emerged later as a very convenient representation of the variational space [240] which lead to a very intuitive quantum-informational interpretation [241]. The technical details of MPS have been described and discussed in great detail, e.g. in Ref. [227].

A.4.2   *Application in present work*

In the present work, matrix product states were used to study all those setups with open boundary conditions. While conceptually displaying the structure (215), our tensors were equipped with one or more symmetries as introduced in Sec. A.1.4. To this end, the Abelian Symmetric Tensor Networks Library developed together with Prof. Montangero and coworkers in Ulm was employed.

The code makes explicit use of the MPO formalism (compare Sec. A.1.2) both for the Hamiltonian in the variational optimization and for the operators in the later measurement of observables. The variational optimization uses a two-site scheme and calls an Arnoldi algorithm (ARPACK [242]) to solve the eigenproblem. The precision of the eigensolver can either be fixed or dynamically adapted during a sweep by setting it to a defined fraction of the difference between the energies reached for the previous two tensors in the optimization. This accounts for the fact that at the beginning of the DMRG algorithm, the randomly initialized tensor network is not yet a good approximation to the ground state and therefore a very precise optimization with respect to the still "wrong" environment is superfluous. With convergence towards a final energy, the precision is then automatically increased.

SU(N)-FERMIONS IN A HARMONIC TRAP.   In order to determine the density and momentum distributions and the contacts in the finitely interacting model, we used a code with the above specifications which in particular implements multiple Abelian symmetries (particle number conservation for each fermionic species). We reproduce here the technical details presented in Ref. [25].

To be able to do MPS calculations on a discretized lattice, we transfer the original, continuous Hamiltonian into its discretized equivalent. We therefore choose a region of the trap which is sufficiently large to contain the full ground

state (ζa_{ho}) and cover it with a grid (in dimensionless units, the region $\tilde{x} \in [-\zeta/2, +\zeta/2]$). The lattice contains L sites, i.e. we set $\tilde{x}_j = (j - (L+1)/2)\Delta\tilde{x}$ with $\Delta\tilde{x} = \zeta/L$ and $j \in \{1, \ldots, L\}$ labeling the j-th site in the lattice. The discretized equivalent of the model (162) then reads

$$
\hat{H} = -\frac{t}{2} \sum_{j=1}^{L-1} \sum_{\sigma} \left(c_{j,\sigma}^{\dagger} c_{j+1,\sigma} + \text{h.c.} \right) + \sum_{j=1}^{L} \sum_{\sigma} \left(\frac{v}{2} \left(j - \frac{L+1}{2} \right)^2 + t \right) c_{j,\sigma}^{\dagger} c_{j,\sigma}
$$

$$
+ U \sum_{j=1}^{L} \sum_{\sigma \neq \sigma'} n_{j,\sigma} n_{j,\sigma'}, \tag{216}
$$

where the index j labels the lattice site and σ labels the N internal SU(N)-invariant levels (species). The operators $c_{j,\sigma}$ and $c_{j,\sigma}^{\dagger}$ are the creation- and annihilation-operators for a fermion at site j and of species σ, and $n_{j,\sigma}$ measures the occupation of the site, $n_{j,\sigma} = c_{j,\sigma}^{\dagger} c_{j,\sigma}$. The coefficients of this model relate to the ones of the dimensionless continuum model as $t = 1/\Delta\tilde{x}^2$, $v = \Delta\tilde{x}^2$ and $U = \alpha/\Delta\tilde{x}$. Subsequently, the fermionic model is mapped to a spin model.

All calculations were then performed with increasing numbers of sites (i.e. diminishing lattice spacing, $\Delta y \to 0$) and the quantities of interest were finite-size scaled to recover the continuum limit. The maximum number of lattice sites considered was $L = 216$ ($\cong (0.02 - 0.08)a_{\text{ho}}$), and depending on the configuration, the virtual bond dimension of the MPS was chosen $m = 200 - 500$, corresponding to maximally discarded probabilities $\lesssim 10^{-6}$. The CPU time needed for the individual calculations depended strongly on the number of particles, the number of species and the interaction strength; for $L = 216$ and $m \approx 250$, it ranged on a scale $t \approx 1 - 14\,\text{d}$.

The Tan contacts were calculated through measurement of the interaction energy of the ground state. Density distributions were determined through measurement of site-occupation in the discretized model; momentum distributions were obtained by Fourier transformation of measured (fermionic) two-point correlators:

$$
n(k) = \frac{1}{L} \sum_{j,l=1}^{L} e^{i(j-l)k} \langle c_j^{\dagger} c_l \rangle. \tag{217}
$$

In the numerical (spin) implementation, the fermionic two-point correlators are measured as a multi-point observable containing a Jordan-Wigner string.

CREUTZ-HUBBARD MODEL.   For the Creutz-Hubbard model, the U(1)-symmetry of particle number conservation in the model was considered in the numerical calculations to explicitly address the case of half-filling. Simulations were run on lattices with up to $L = 256$ sites and with virtual bond dimensions $m \approx 500$. The CPU time needed for a single simulation ranged in the order $t \approx 2 - 5\,\text{d}$.

A.5 BINARY TREE TENSOR NETWORKS

A.5.1 *General*

As the name suggests, *tree tensor networks* [243] are characterized by the fact that their graph is a tree, the free links of which correspond to the physical degrees of freedom (see Fig. 36g). Unlike for MPS, not every tensor possesses physical links. A physical intuition of the structure can be developed by going from the physical links at the bottom of the graph towards the top. In particular for a *binary* tree, two physical links enter each tensor of the lowest level from below and one virtual link from above. When interpreting the physical legs as input channels and the virtual link as an output channel, the process can be understood as a renormalization step, which maps the physical degrees of freedom to an effective (virtual) degree of freedom. This renormalization is repeated when ascending further in the tree. If the bond dimension of the virtual links is fixed, from a certain level on, this mapping from two legs to a single one is no longer exact (bijective), but takes the form of a projection. Unlike other real space renormalization schemes (e.g. the Kadanoff renormalization [244]), the scheme does not retain the lowest energy levels, but those states that constitute the most relevant contribution in terms of entanglement with the rest of the system. It can be proven that tree tensor networks can reproduce the algebraic correlation decay found in gapless systems [245]. Practically, binary tree tensor networks are particularly apt to simulate systems with periodic boundary conditions [246, 247]. On the one hand, neighboring sites have a maximally graph-distance $\propto \log(L)$, while it would be $\propto L$ for an MPS. This is hinted at in Fig. 36h. On the other hand, due to the absence of loops, binary trees are numerically more feasible than other schemes which might offer a smoother entanglement distribution (in the sense that the graph-distance for neighbors with same physical distance is equal), e.g. MERA [230].

A.5.2 *Application in present work*

PERSISTENT CURRENTS OF WEYL FERMIONS.   In the present work, we use an implementation of a binary tree tensor network for the simulation of the Weyl fermions on a ring. The code exploits the Abelian symmetry of particle number conservation, which allows us to control the filling of the system. The variational optimization can be solved as simple eigenvalue problems due to the implementation of an adaptive gauge [246], which we introduced earlier for the general problem of optimization in loop-free tensor networks. Both two-site optimization and single-site optimization with subspace-expansion were used. The number of lattice sites used were in the range $L = 16 - 128$, the bond dimensions were $m = 100 - 200$. Typical CPU times, e.g. for $L = 64$ and $m = 100$, were $t \approx 2 - 5\,\text{d}$.

The Drude weight (134) is given as the second derivative of the ground state energy with respect to the flux. A naive numerical differentiation of $\partial E^2 / \partial \Phi^2|_{\Phi_0}$ requires to determine the finite difference $(E(\Phi_0 - h) - 2E(\Phi) + E(\Phi_0 + h))/2$

with some $h \to 0$. Instead we use that the first derivative of the ground state energy, i.e. the current, is directly accessible due to the Hellmann-Feynman law: $I = -\partial E / \partial \Phi = - \langle \Psi | \frac{\partial H}{\partial \Phi} | \Psi \rangle$. This observable is a sum over correlations which can be precisely measured for a given state. Due to the symmetry of the problem $(E(\Phi_0 + h) = E(\Phi_0 - h)$ and $I(\Phi_0 + h) = -I(\Phi_0 - h))$, up to an error $O(h^2)$ we can then determine the Drude weight from a single data point: $D(\Phi_0) \approx 2I(\Phi_0 + h/2)/h$.

EXPERIMENTAL IMPLEMENTATION
WITH ULTRACOLD ATOMS

The systems investigated in this thesis share the property of being simulatable in cold atom setups. Comprehensive reviews of the techniques needed to realize such setups have been presented e.g. in Refs. [2, 6, 7]. As the focus of this work is the investigation of properties of the fermionic systems, we revise only shortly the technical ingredients needed for the experimental realization - first for quasi-one-dimensional fermionic systems in general (Sec. B.1), then for the particular setups occurring in this work (Sec. B.2).

B.1 GENERALITIES OF COLD ATOM EXPERIMENTS

TRAPPING AND COOLING OF PARTICLES. To access the quantum properties of most particle systems, temperatures close to absolute zero are required. In modern cold atom experiments, indeed extremely low temperatures $T \sim \mathrm{nK}$ can be obtained [248]. To this end, typically a variation of cooling schemes is applied.

Different *laser cooling* methods exist which can reduce the kinetic energy of particles in a gas [249–251]: The most common method, *Doppler cooling*, relies on the fact that atoms perceive the frequency of an applied laser shifted due to their own relative movement. This property can be exploited by tuning the frequency of a laser slightly below some electronic transition in the atom. Only for atoms moving towards the laser, the laser frequency occurs higher (blue-shifted) and can be absorbed. Due to momentum conservation, this slows down the atom. As the direction of a later photon emission is random, it will not alter the net-momentum when averaged over many absorption-emission events. Further laser-cooling techniques include *Sisyphus cooling*, *resolved sideband cooling* and *Raman sideband cooling.*

Evaporative cooling is based on the idea that when lowering a trapping potential, fast particles can overcome the energy barrier and escape, thereby taking away the high-momentum tail of the Boltzmann distribution of the previous equilibrium distribution. The remaining particles can then find a new thermodynamic equilibrium at a lower temperature as they exchange energy through scattering and thereby thermalize. In bosonic gases, this technique allows e.g. the realization of BECs using Rubidium atoms [30]. For fermions, re-equilibration is hindered by the fact that the Pauli principle prevents an efficient energy exchange through scattering. Here, *sympathetic cooling* [252–254] finds application: In a boson-fermion mixture, the bosons are cooled evaporatively and build a cool bath for the fermions which equilibrate to this environment through scattering with the bosons. This has been demonstrated e.g. for ${}^{6}\mathrm{Li}$ fermions with ${}^{7}\mathrm{Li}$ or

[23]Na bosons [255]. Alternatively, fermions with different nuclear or atomic spin can be used to have distinguishable subsets (e.g. with [40]K atoms [256]).

LATTICES.   Optical lattices are built using counter-propagating laser beam-pairs forming a standing wave $\mathbf{E}(\mathbf{r}, t)$ with the laser wavelength $\lambda_L = 2\pi/k_L$ determining the spatial periodicity. If the laser frequency ω_L is far off-resonant with respect to transitions of the atoms, the electric field induces a dipole moment $\mathbf{d} = \alpha(\omega_L)\mathbf{E}(\mathbf{r}, t)$, where α is the frequency-dependent polarizability tensor. This dipole couples to the field, resulting in a shift of the electronic energies (ac-Stark shift). If the electric field is space-dependent, the atoms feel an optical potential [257]

$$V_{\mathrm{dip}}(\mathbf{r}) = -\frac{1}{2}\langle \mathbf{d}\cdot\mathbf{E}(\mathbf{r})\rangle \propto \frac{\alpha(\omega_L)}{2}\left|\mathbf{E}(\mathbf{r})\right|^2, \tag{218}$$

where here $I \propto |\mathbf{E}(\mathbf{r})|^2$ represents the time-averaged intensity of the field. The averaging is justified because the motion of the atoms is much slower than the time-scale imposed by the oscillation of the field $\propto 1/\omega_L$. By combining orthogonal sets of counter-propagating beam-pairs, one can obtain a periodic three-dimensional potential

$$V_{\mathrm{latt}}(\mathbf{r}) = V_0 \sum_{i=1}^{3} \sin^2(k_L r_i) \tag{219}$$

with a maximal value $V_0 \propto \Gamma/\omega_0^3\Delta$. Here, Γ is the decay rate of the excited state and we assume that the detuning $\Delta = \omega_L - \omega_0$ between the laser frequency and an atomic resonance ω_0 is small compared to the transition frequency itself, $\Delta \ll \omega_0$, to allow for a rotating wave approximation. Moreover, we assume that $|\Delta| \gg \Gamma$ in order to avoid scattering of the photons $\propto (\Gamma/\Delta)^2$.

If the lattice is sufficiently deep, a particle in a potential minimum (i.e. at a site of the lattice) perceives its confinement as almost quadratic. In experiments, the harmonic oscillator frequency $\omega_{\mathrm{pot}} = \sqrt{V_0/m}k_L$ can be on the order $\omega_{\mathrm{pot}} \approx 100\,\mathrm{kHz}$ [2]. Its energy $\hbar\omega_{\mathrm{pot}}$ can be compared to the recoil energy $E_R = \hbar^2 k_L^2/2m$, i.e. the kinetic energy due to the absorption/emission of a quantum of the field (e.g. $E_R/\hbar \approx 1\,\mathrm{kHz}$ for [87]Rb). Reformulating the energy as $\hbar\omega_{\mathrm{pot}} = 2E_R(V_0/E_R)^{1/2}$ reveals that lattice depths can be obtained which are multiples of the typical recoil energies.

The cubic lattice in Eq. (219) can be altered by choosing laser-pairs with different wavelengths. Other geometries (e.g. triangular lattices) can be obtained by arranging laser-pairs non-perpendicularly [38, 156]. Moreover, optical lattices can be made spin-dependent by addressing a shift that depends on the hyperfine sublevels to a resonance [257].

TIGHT-BINDING MODELS.   The wave functions for particles in the periodic potential (219) (or a generalization thereof) are given by Bloch functions, and the corresponding energy spectrum forms bands. If the lattice is deep, $V_0 \gg E_R$, these energy bands are well separated. If in addition, the temperature is sufficiently low ($k_B T \ll \hbar\omega_0$), only the lowest band will be populated. As the

particles are localized around the respective minima of the lattice, it is then justified to expand the Bloch functions in terms of maximally localized *Wannier functions*. By projecting all the field operators involved in the description of the system onto the lowest band and expanding them in the Wannier basis, one obtains a so-called *tight-binding model*. In detail: If a field operator of the system $\hat{\psi}_\sigma(\mathbf{r})$ is expanded in localized Wannier functions $w_j(\mathbf{r})$, $\psi(\mathbf{r}) = \sum_j f_{j,\sigma} w_j(\mathbf{r})$ where $f_{j,\sigma}$ is the annihilation operator for a particle of species σ at site j, the original field Hamiltonian

$$H = \sum_{\sigma \in \{\uparrow,\downarrow\}} \int \mathrm{d}^3 r \; \hat{\psi}_\sigma^\dagger(\mathbf{r}) \left[\frac{-\hbar^2}{2m} \nabla^2 + V_{\text{ext},\sigma}(\mathbf{r}) \right] \hat{\psi}_\sigma(\mathbf{r}) \tag{220}$$

with an external potential V_{ext} comprising the possibly spin-dependent optical lattice V_{latt} (219) and possibly an additional external trapping potential V_{trap}, takes the tight-binding form

$$H = \sum_{\sigma=\uparrow,\downarrow} \left[\sum_{i<j} -t_{ij}^\sigma f_{i,\sigma}^\dagger f_{j,\sigma} + \sum_j \frac{\epsilon_{j,\sigma}}{2} n_{j,\sigma} \right] + \text{h.c.} \tag{221}$$

with $n_{j,\sigma} = f_{j,\sigma}^\dagger f_{j,\sigma}$. The tunneling or hopping coefficient can be evaluated as

$$t_{ij}^\sigma = \int \mathrm{d}^3 r \; w_{i,\sigma}^*(\mathbf{r}) \left[\frac{-\hbar^2}{2m} \nabla^2 + V(\mathbf{r}) \right] w_{j,\sigma}(\mathbf{r}). \tag{222}$$

Due to the similarity of the Wannier functions to harmonic oscillator solutions (compare Eq. (173)), their amplitude decays exponentially with the distance between sites. As a consequence, terms that go beyond nearest neighbors are often neglected. The energy offset

$$\epsilon_{j,\sigma} = \int \mathrm{d}^3 r \; V_{\text{ext},\sigma}(\mathbf{r}) \left| w_{j,\sigma}(\mathbf{r}) \right|^2 \tag{223}$$

contains the effects of all the potentials felt by the particles.

INTERACTIONS.   Usually, the Hamiltonian (220) also contains a pseudo-potential term $\int \mathrm{d}^3 r \; \frac{g_{\sigma,\sigma'}}{2} \hat{\psi}_\sigma^\dagger(\mathbf{r}) \hat{\psi}_{\sigma'}^\dagger(\mathbf{r}) \hat{\psi}_{\sigma'}(\mathbf{r}) \hat{\psi}_\sigma(\mathbf{r})$ due to s-wave scattering between either bosons or fermions of distinguishable species ($\sigma \neq \sigma'$). Here, $g_{\sigma,\sigma'} = 4\pi\hbar^2 a_{\sigma,\sigma'}/m$ and $a_{\sigma,\sigma'}$ is the scattering length. In the tight-binding model, the resulting on-site interaction reads

$$H_{\text{int}} = \sum_j \sum_{\sigma \neq \sigma'} \frac{U_{\sigma,\sigma'}}{2} n_{j,\sigma} n_{j,\sigma'} \tag{224}$$

for fermions with different internal state, or (for simplicity assuming homogeneous interactions $U = U_{\sigma,\sigma'}$)

$$H_{\text{int}} = \sum_j \frac{U}{2} n_j(n_j - 1) \tag{225}$$

for bosons. We use $n_j = \sum_\sigma n_{j,\sigma}$ and $U_{\sigma,\sigma'} = g \int \mathrm{d}^3 r \; \left| w_{j,\sigma}(\mathbf{r}) \right|^2 \left| w_{j,\sigma'}(\mathbf{r}) \right|^2$.

Beyond these naturally occurring interactions, the scattering length can be manipulated through so-called *Feshbach resonances*, so far as to change its sign, i.e. changing from repulsive to attractive interactions [13]. The concept relies on scattering atoms in an ultracold gas coupling to a weakly-bound molecular state if the free and the bound state are energetically close. The resonance can be tuned using either magnetic [258] or optical methods [259]. Feshbach resonances were the major ingredient for tuning the BEC-BCS crossover [33] and for suppressing interactions and observing Anderson localization [35, 36].

ARTIFICIAL GAUGE FIELDS.   In Sec. 2.5, we have discussed how a charged particle acquires a phase when moving along a closed path in a magnetic field (Aharonov-Bohm phase). Neutral atoms as used in cold atom experiments do not carry a charge and therefore cannot couple to a gauge field. However, various ways exist to make neutral particles pick up a geometric phase using *artificial gauge fields* [10].

One possibility consists in *rotating* the atomic gas: The resulting Coriolis force in the rotating frame takes the same form as the Lorentz force which charged particles would experience in a magnetic field. This approach has e.g. been demonstrated through vortex creation in two-dimensional Bose-Einstein condensates [260, 261].

A possible way of introducing a Peierls phase into the describing tight-binding model is to shake a lattice [262, 263]. Therefore, a periodic inertial force is applied. Under time-averaging, this renormalizes the tunneling coefficients of the Hamiltonian (and possibly changes their sign). For particularly clever choices of the driving force, the elements can be made complex [264]. For details, see Sec. B.2.1.

In the special case of quasi-one-dimensional models, yet another approach consists in mapping the smaller physical dimension onto internal degrees of freedom, e.g. hyperfine states (synthetic dimension). A hopping along this dimension is then described by a change of the internal state. Physically, the phase imprinting can be achieved through two-photon Raman transitions [11]. This technique has been successfully used to proof chiral edge states in both bosonic [59] and fermionic systems [60].

B.2   EXPERIMENTAL IMPLEMENTATION OF THE PRESENTED MODELS

B.2.1   *Creutz-Hubbard ladder*

In this section, we demonstrate how to implement the fermionic Creutz-Hubbard ladder (36) experimentally. The ideas put forward are part of our publication [23] and were originally developed by A. Bermudez.

By using a deep optical lattice with a strong confinement along two directions, i.e. $V_{0,y}, V_{0,z} \gg V_{0,x} \gg E_R$ (compare Eq. (219)), we obtain a one-dimensional system of the kind (221)+(224). In particular, when considering a gas with two

hyperfine states that we label $|\uparrow\rangle$ and $|\downarrow\rangle$, the tight-binding Hamiltonian takes the form

$$H = \sum_{j=1}^{N} \sum_{\sigma=\uparrow,\downarrow} \left(-t f_{j+1,\sigma}^{\dagger} f_{j,\sigma} + \frac{\epsilon_{\sigma}}{2} n_{j,\sigma} + \text{h.c.} \right) + \sum_{j} U_{\uparrow\downarrow} n_{j,\uparrow} n_{j,\downarrow}, \tag{226}$$

where t is the nearest-neighbor hopping amplitude, ε_{σ} is the (here site-independent) energy of the electronic levels and $U_{\uparrow\downarrow}$ is the on-site interaction.

In order to implement the complex tunneling (37), we could apply one of the techniques discussed in the above section. As an alternative, we detail here the implementation using a periodic modulation of the lattice with generalized Raman-assisted tunneling [56] in spin-independent optical lattice. A first step consists in introducing a state-independent energy gradient by tilting the optical lattice. This can be achieved through acceleration or through an additional ac-Stark effect and yields

$$H_{\text{tilt}} = \sum_{j,\sigma} \Delta j \, f_{j,\sigma}^{\dagger} f_{j,\sigma} \tag{227}$$

where the tilt $\Delta \ll V_{0,x}$ does not modify inter-site terms of the original Hubbard model. However, it is chosen such that the original intra-leg tunneling is impeded: $t \ll \Delta$. The idea is to re-activate the tunneling against the gradient using a variety of ideas.

To start off, we install the *inter-leg hopping* terms via a *two-photon Raman scheme* [56]. Therefore, three additional laser beams are used. A first pair of lasers with frequencies ω_1 and ω_2 is tuned such that it effectively couples the $\uparrow$-level on site j with the $\downarrow$-level on site $j+1$, i.e. $\omega_1 - \omega_2 = (\varepsilon_{\downarrow} - \varepsilon_{\uparrow}) + \Delta$. The lasers is set such that during the process a recoil momentum $\delta k = (\mathbf{k}_1 - \mathbf{k}_2) \cdot \mathbf{e}_x$ is transferred to the particle as to enable the tunneling. Similarly, the laser pair with frequencies ω_1 and ω_3 enables the transition between the $\downarrow$-level on site j with the $\uparrow$-level on site $j+1$. Therefore, $\omega_1 - \omega_3 = (\varepsilon_{\uparrow} - \varepsilon_{\downarrow}) + \Delta$ and $\delta \tilde{k} = (\mathbf{k}_1 - \mathbf{k}_3) \cdot \mathbf{e}_x$. If we apply a rotating wave approximation, this yields

$$H_{\text{Raman}} = \sum_{j} \frac{1}{2} \left(\Omega f_{j+1,\downarrow}^{\dagger} f_{j,\uparrow} + \tilde{\Omega} f_{j+1,\uparrow}^{\dagger} f_{j,\downarrow} \right) + \text{h.c.} \tag{228}$$

with

$$\Omega = \Omega_{12} e^{-\frac{\pi}{4} \sqrt{\frac{V_{0x}}{E_{\text{R}}}}}, \quad \tilde{\Omega} = \Omega_{13} e^{-\frac{\pi}{4} \sqrt{\frac{V_{0x}}{E_{\text{R}}}}} \tag{229}$$

and Ω_{12}, Ω_{13} being the Rabi frequencies of the two-photon processes. We assume here that the transferred momenta are reciprocal to the wavelength of the original lattice, in the sense that $\delta k \cdot \lambda = 2\pi n$ with $n \in \mathbb{Z}$ (and a similar condition holds for the second beam pair). Another condition that has to be met is $|\Omega_{12}|, |\Omega_{13}| \ll \Delta$, i.e. on-site Raman transitions are highly off-resonant and can be neglected.

In order to establish the complex *intra-leg* tunneling, we introduce an *intensity-modulated optical lattice* that takes the form

$$H_{\text{driving}} = \sum_{i,\sigma} V_{\text{d},\sigma}(t) \sin^2(k_{\text{d}} x_i^0) f_{i,\sigma}^{\dagger} f_{i,\sigma}, \tag{230}$$

and the intensity of this ac-Stark shift for each of the hyperfine states is modulated periodically in time, $V_{\mathrm{d},\sigma}(t) = V_{\mathrm{d},0} \sin(\omega_{\mathrm{d},\sigma} t - \phi_\sigma)$ with frequency $\omega_{\mathrm{d},\sigma}$ and phase ϕ_σ. We assume $V_{d,0} \ll V_{0,x}$ here to avoid a periodic modulation on bare tunnelings of the original Hubbard model and only consider the resulting periodic driving of the on-site energies. In particular, if the wavelength of the intensity-modulated optical lattice is twice the one of the original lattice ($\lambda_d = 2\lambda$), only even sites are subjected to a periodic modulation. Under the resonance condition $n\omega_{\mathrm{d},\sigma} = \Delta$, $n \in \mathbb{Z}$, the nearest-neighbor hopping can be restored by absorbing energy quanta from the periodic driving. Setting $\omega_{\mathrm{d},\sigma} = \Delta/2$ leads to

$$H_{\mathrm{h}} = -t\mathfrak{J}_2\left(\frac{V_{\mathrm{d},0}}{\Delta}\right) \sum_{i,\sigma} e^{-\mathrm{i}2\phi_\sigma} f_{i+1,\sigma}^\dagger f_{i,\sigma} + \mathrm{h.c.}, \tag{231}$$

where $\mathfrak{J}_2(x)$ is the second-order Bessel function of the first kind [58, 265] and the phases of the periodic modulations must fulfill $\phi_\uparrow = -\phi_\downarrow$. As a consequence, also the inter-leg hopping (228) will be off-resonantly modified by driving, altering the expression to

$$H_{\mathrm{d}} = \frac{\Omega}{2}\mathfrak{J}_0\left(\frac{V_{\mathrm{d},0}}{\Delta}\right) \sum_i \left(f_{i+1,\downarrow}^\dagger f_{i,\uparrow} + f_{i+1,\uparrow}^\dagger f_{i,\downarrow}\right) + \mathrm{h.c.} \tag{232}$$

We note that also on-site Raman transitions can be activated due to the intensity-modulated lattice. However, this spurious effect can be suppressed by appropriate tuning of $V_{d,0}$ with respect to Δ.

Last, we establish an imbalance between the two internal states. This can be done by detuning the Raman lasers in Eq. (228) slightly from resonance, which yields (in rotating wave approximation)

$$H_{\mathrm{local}} = \frac{\delta}{2} \sum_i \left(f_{i,\uparrow}^\dagger f_{i,\uparrow} - f_{i,\downarrow}^\dagger f_{i,\downarrow}\right). \tag{233}$$

The parameters of our model (36) can now easily be retrieved by associating the operators $f_{i,\uparrow} \to c_{i,\mathrm{u}}$ and $f_{i,\downarrow} \to c_{i,\mathrm{d}}$ and identifying

$$t_{\mathrm{h}} = +t\mathfrak{J}_2\left(\frac{V_{\mathrm{d},0}}{\Delta}\right), \quad \theta = 2\phi_\uparrow, \quad t_{\mathrm{d}} = -\frac{\Omega}{2}\mathfrak{J}_0\left(\frac{V_{\mathrm{d},0}}{\Delta}\right), \quad \Delta\varepsilon = \delta/2. \tag{234}$$

This completes the derivation.

B.2.2 *Weyl fermions on a ring*

The Creutz ladder considered in Sec. 4, namely Eq. (89), is very similar to the one discussed in the previous section. Similar schemes can therefore be envisioned for its realization. Slight differences in the description also make the model amenable to experiments making use of the 'toolbox' proposed in Ref. [266], where Raman transitions are combined with a bi-chromatic super-lattice and a staggered optical potential.

However, certain particularities have to be considered, namely the circular form of the lattice and the relevance of nearest-neighbor interactions. The first

issue can be addressed by modeling the optical lattice cylindrically using pairs of *Laguerre-Gauss beams* [161]. These beams carry angular momentum and therefore allow the realization of angular or cylindrical lattices. Artificial gauge fields through plaquettes on the cylinder surface can then be realized using additional Laguerre-Gauss lasers for two-photon Raman processes (similar to the prescriptions above); a rotation of the lattice potential around the cylinder axis permits to model a synthetic magnetic flux piercing the cylinder. Another possibility is the creation of circular lattices using *spatial light modulation* [160]. With this technique, the phase of an incoming laser can be modified locally, allowing for designed intensity patterns.

In order to obtain nearest-neighbor interactions, the use of dipolar atoms or molecules can be considered [267–270]. Indeed, recently the observation of long-range spin-exchange interactions [271] and the realization of an extended Hubbard model [272] have been reported for this setup. Alternatively, the naturally occurring interactions could be dressed through lattice-shaking [262] or cavity resonances [273].

B.2.3   *SU(N)-invariant fermions*

The realization of harmonically trapped fermions that interact through SU(N)-invariant interactions has been reported in Ref. [199]. In this experiment, the nuclear spin states of ^{173}Yt atoms with $I = 5/2$ were chosen as internal states, allowing the realization of an SU(N)-symmetry with $N \leq 2I + 1 = 6$ spin components. The invariance of the interaction relies on the fact that the nuclear-spin nature has no influence on the interaction strength. Moreover, no spin-changing collisions occur. The low-temperature regime (here $T/T_F < 0.3$ where T_F is the Fermi temperature) is obtained with the standard methods discussed before. The gas of atoms (with approximately 6000 atoms per species) is then confined in a deep two-dimensional lattice with an effective radial confinement $\omega_\perp = 2\pi \times 25\,\mathrm{kHz}$ (or $V_0/E_R = 40$ where E_R is the recoil energy). Together with a weak axial confinement at $\omega_x \approx 2\pi \times 80\,\mathrm{Hz}$ this leads to ≈ 600 cigar-shaped fermionic wires (with ≈ 20 atoms in the central wire). Due to the high frequency, only the radial ground state is then non-negligibly occupied, so that the setup allows the study of true one-dimensional phenomena. The depth of the radial confinement also efficiently prevents a coupling between the different wires.

The interactions between the particles are described by a dimensionless parameter $\alpha = -2\hbar^2/ma_{1\mathrm{D}}$ (compare Sec. 5.1). The one-dimensional scattering length $a_{1\mathrm{D}}$ is a function of the three-dimensional scattering length a and the radial scattering length $a_\perp = \sqrt{\hbar/m\omega_\perp}$: $a_{1\mathrm{D}} \equiv a_{1\mathrm{D}}(a, a_\perp)$ [207]. As a consequence, the interaction strength is tunable through the frequency of the radial confinement.

To register the momentum distribution of the particles, spin-selective time-of-flight measurements can be performed. The trapping potential is therefore released and the detectable after-flight positions can be mapped back to the in-trap momenta. Density distributions can be measured using in-situ imaging [10].

For alternative implementations of SU(N)-symmetries in cold atom experiments, see Ref. [195].

DETAILED PROOFS AND DERIVATIONS

This section is dedicated to calculations that would impair reading fluency in the main text, but nevertheless constitute important results and deserve their place in this thesis.

Sec. C.1 presents an approach to reveal the identity between the Creutz-Hubbard model and a pair of coupled Ising chains. In Sec. C.2, we discuss analytical solutions in one-dimensional systems with open boundary conditions. In particular we show under which conditions such solutions exist and give examples.

C.1 EQUIVALENCE BETWEEN IMBALANCED CREUTZ LADDER AND A PAIR OF ISING CHAINS

In the following, we present an in-depth derivation of the equivalence of the imbalanced Creutz ladder model (36) and a set of two Ising models (53). While *a posteriori* this equivalence can be easily checked, an a priori identification of the transformation rules is difficult due to their complexity (site-dependence, complex phases and mixing of creation and annihilation operators, compare Eq. (50)). The path is also different from a simple diagonalization of the model which is routinely done through Fourier transformation and consequent diagonalization of the spinor basis. It is therefore presented here in a step-by-step fashion. The conceptual idea is to first find a convenient basis, in which we can visualize the different hopping processes. This is done by changing to a Majorana notation, which then allows us to determine the basis change to "disentangle" the two Ising chains.

We consider the free part $H_{\pi C}$ of the Creutz-Hubbard Hamiltonian (36), which in spinor notation $c_j = (c_{j,\mathrm{u}}, c_{j,\mathrm{d}})^T$ reads

$$H_{\pi C} = \tilde{t} \sum_j c_j^\dagger \left(-\mathrm{i}\sigma_3 - \sigma_1 \right) c_{j+1} + \frac{\Delta\varepsilon}{4} \sum_j c_j^\dagger \sigma_3 c_j + \mathrm{H.c.} \qquad (235)$$

Via the transformation $c_j = (-i\sigma_3)^j \tilde{c}_j$, the phases of the intra-leg hopping is gauged to the inter-leg hopping terms. This allows us to make the hopping along the two legs look more alike at the price of having site-dependent diagonal hopping terms:

$$H_{\pi C} = \tilde{t} \sum_j \tilde{c}_j^\dagger \left(-\mathbb{1} + (-1)^j \sigma_2 \right) \tilde{c}_{j+1} + \frac{\Delta\varepsilon}{4} \sum_j \tilde{c}_j^\dagger \sigma_3 \tilde{c}_j + \mathrm{H.c.} \qquad (236)$$

We now define two sets of Majorana fermions $u_{j,1}$, $u_{j,2}$ and $d_{j,1}$, $d_{j,2}$, with the characteristic properties

$$u_{j,1}^\dagger = u_{j,1} \quad \text{and} \quad \{u_{j,1} u_{l,1}\} = \delta_{j,l}, \qquad (237)$$
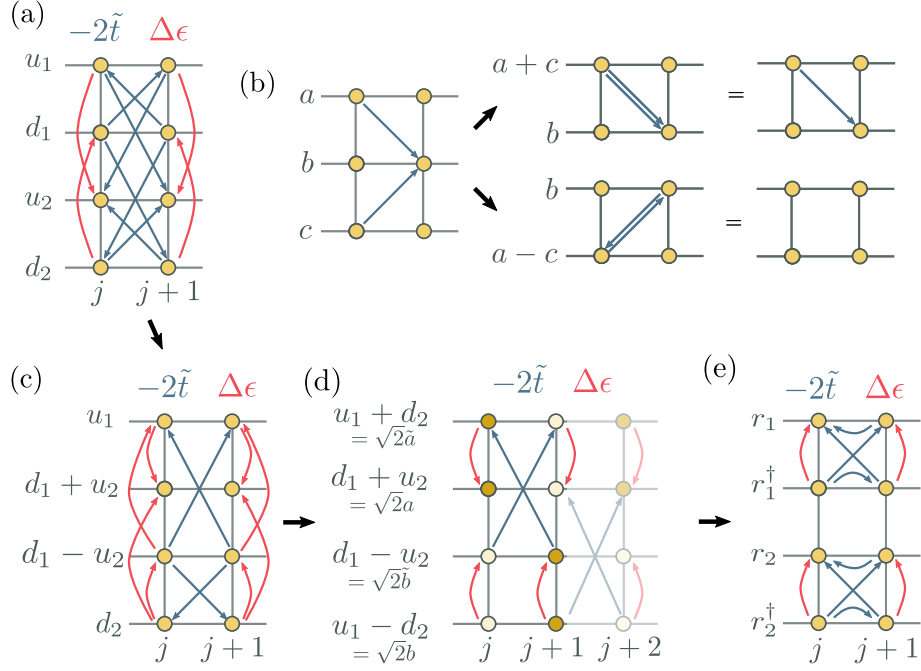
Figure 40: **"Disentangling" the two Ising chains.** (a) The original model written in terms of Majoranas (239). Connected sites correspond to Majorana terms appearing in the Hamiltonian; the arrowheads determine the sign of the coefficient (here for j odd). (b) Simple graphical rules allow us to simplify the description. Namely, whenever two Majoranas point towards a third with arrows of the same color (amplitude), the addition/subtraction leads to a simplification. (c) Application of this rule leads to a stepwise simplification of the description until (d) in a new Majorana basis, the visualization of Eq. (241) reveals two unconnected subsystems, underlined here by different colors of the Majoranas. For better understanding, an additional site is shown here. (e) Returning to standard fermionic operators yields two copies of a Kitaev-Majorana chain (244).

and similar relations for $u_{j,2}$, $d_{j,1}$ and $d_{j,2}$. In particular, we choose

$$\begin{pmatrix} u_{j,1} \\ u_{j,2} \end{pmatrix} = \begin{pmatrix} 1 & 1 \\ i & -i \end{pmatrix} \begin{pmatrix} \tilde{c}_{j,\mathrm{u}}^{\dagger} \\ \tilde{c}_{j,\mathrm{u}} \end{pmatrix}, \quad \begin{pmatrix} d_{j,1} \\ d_{j,2} \end{pmatrix} = \begin{pmatrix} 1 & 1 \\ i & -i \end{pmatrix} \begin{pmatrix} \tilde{c}_{j,\mathrm{d}}^{\dagger} \\ \tilde{c}_{j,\mathrm{d}} \end{pmatrix}. \quad (238)$$

The Hamiltonian can be expressed in the new basis $\mathbf{m}_j = (u_{j,1}, d_{j,1}, u_{j,2}, d_{j,2})^T$ as

$$H_{\pi\mathrm{C}} = \frac{i}{4}\left[\tilde{t}\sum_j \mathbf{m}_j^T \cdot \begin{pmatrix} 2i(-1)^{j+1}\sigma_2 & -2\mathbb{1} \\ 2\mathbb{1} & 2i(-1)^{j+1}\sigma_2 \end{pmatrix} \cdot \mathbf{m}_{j+1} \right.$$
$$\left. + \frac{\Delta\varepsilon}{4}\sum_j \mathbf{m}_j^T \cdot \begin{pmatrix} 0 & 2\sigma_3 \\ -2\sigma_3 & 0 \end{pmatrix} \cdot \mathbf{m}_j \right]. \quad (239)$$

The terms occurring in this Hamiltonian are visualized in Fig. 40a. The diagram helps us to identify a new Majorana basis $\tilde{\mathbf{m}}_j = (a_j, \tilde{a}_j, b_j, \tilde{b}_j)$ with

$$
\begin{aligned}
a_j &= \frac{d_{j,1} + u_{j,2}}{\sqrt{2}}, & \tilde{a}_j &= \frac{u_{j,1} + d_{j,2}}{\sqrt{2}}, \\
b_j &= \frac{u_{j,1} - d_{j,2}}{\sqrt{2}}, & \tilde{b}_j &= \frac{d_{j,1} - u_{j,2}}{\sqrt{2}}.
\end{aligned}
\tag{240}
$$

In this basis, the Hamiltonian reads

$$
\begin{aligned}
H_{\pi C} = \frac{2i}{4} \Bigg[&\tilde{t} \sum_j \tilde{\mathbf{m}}_j^T \begin{pmatrix} 0 & \mathbb{I} + (-1)^j \sigma_3 \\ -(\mathbb{I} + (-1)^j \sigma_3) & 0 \end{pmatrix} \tilde{\mathbf{m}}_{j+1} \\
&+ \frac{\Delta \varepsilon}{4} \sum_j \tilde{\mathbf{m}}_j \begin{pmatrix} -i\sigma_2 & 0 \\ 0 & -i\sigma_2 \end{pmatrix} \tilde{\mathbf{m}}_j \Bigg]
\end{aligned}
\tag{241}
$$

and corresponds to two independent Majorana systems, as can be easily seen in Fig. 40d. We can define new (standard) fermionic operators to better understand the independent chains:

$$
\begin{aligned}
\begin{pmatrix} a_j \\ \tilde{a}_j \\ b_j \\ \tilde{b}_j \end{pmatrix} &= \begin{pmatrix} i & -i & 0 & 0 \\ 1 & 1 & 0 & 0 \\ 0 & 0 & i & -i \\ 0 & 0 & 1 & 1 \end{pmatrix} \begin{pmatrix} p_{j,1} \\ p_{j,1}^\dagger \\ p_{j,2} \\ p_{j,2}^\dagger \end{pmatrix} & \text{for } j \text{ odd,} \\[2em]
\begin{pmatrix} a_j \\ \tilde{a}_j \\ b_j \\ \tilde{b}_j \end{pmatrix} &= \begin{pmatrix} 0 & 0 & i & -i \\ 0 & 0 & 1 & 1 \\ i & -i & 0 & 0 \\ 1 & 1 & 0 & 0 \end{pmatrix} \begin{pmatrix} p_{j,1} \\ p_{j,1}^\dagger \\ p_{j,2} \\ p_{j,2}^\dagger \end{pmatrix} & \text{for } j \text{ even.}
\end{aligned}
\tag{242}
$$

The crucial observation is that the Hamiltonian then consists of two independent parts (Fig. 40e):

$$
\begin{aligned}
H_{\pi C} = \sum_{n=1,2} \Bigg[&\tilde{t} \sum_j (-1)^n \left(i(-1)^j p_{j,n}^\dagger p_{j+1,n} - i p_{j,n}^\dagger p_{j+1,n}^\dagger + \text{H.c.} \right) \\
&+ \frac{\Delta \epsilon}{4} \sum_j \left(2 p_{j,n}^\dagger p_{j,n} - 1 \right) \Bigg].
\end{aligned}
\tag{243}
$$

After an additional (aesthetic) transformation $p_{j,n} = (-1)^n i^{2j+1} r_{j,n}^\dagger$ (if j odd) or $p_{j,n} = r_{j,n}^\dagger$ (if j even), we find the two decoupled systems in the form of Kitaev-Majorana chains:

$$
\begin{aligned}
H_{\pi C} = &-\tilde{t} \sum_j \sum_{n=1,2} \left(r_{j,n}^\dagger r_{j+1,n} + r_{j,n}^\dagger r_{j+1,n}^\dagger + \text{H.c.} \right) + \\
&\frac{\Delta \varepsilon}{4} \sum_j \sum_{n=1,2} \left(2 r_{j,n}^\dagger r_{j,n} - 1 \right).
\end{aligned}
\tag{244}
$$

The full transformation from the original to the new basis $(\tilde{\tilde{p}}_j = (r_{j,1}, r_{j,2}^\dagger)^T)$ can then be written as

$$
\begin{aligned}
r_{j,1} &= \frac{i^j}{\sqrt{2}}\left(i c_{j,\mathrm{u}} + (-1)^j c_{j,\mathrm{d}}^\dagger\right), \\
r_{j,2} &= \frac{i^j}{\sqrt{2}}\left(c_{j,\mathrm{u}} + i(-1)^j c_{j,\mathrm{d}}^\dagger\right).
\end{aligned}
\tag{245}
$$

Finally, the Ising models (53) are revealed through a Jordan-Wigner transformation (52).

C.2   OPEN BOUNDARY CONDITIONS AND EXACT SOLUTIONS FOR ONE-DIMENSIONAL CHAINS

In this section, we address the problem of exact solutions for free particles in finite one-dimensional lattice systems with open boundary conditions. Often such systems are addressed by constructing standing-wave solutions from two counter-propagating waves of the same system with periodic boundary conditions. The resulting solutions are then proportional to $\sin(kx + \varphi)$, where in a system with L sites the phase φ and the wave vector k are chosen such that the wave function has amplitude zero on the (virtual) sites 0 and $L + 1$. Here we show that this strategy is misleading under certain circumstances and prove that standing-wave solutions with a single wavelength are not always possible. We then discuss the exceptional, solvable cases. The notation follows Ref. [274].

MODEL AND TARGET.   We study the very general Hamiltonian

$$
H = h_0 \sum_{j=1}^{L} \left(c_j^\dagger c_j - \frac{1}{2}\right) - t \sum_{j=1}^{L} \left(c_j^\dagger c_{j+1} + \gamma c_j^\dagger c_{j+1}^\dagger + \mathrm{H.c.}\right),
\tag{246}
$$

i.e. a non-interacting fermionic chain with hopping t, pair-creation and -annihilation γt and on-site potential h_0. Via a Jordan-Wigner transformation, this model can be shown to be equivalent to an Ising model for $\gamma = \pm 1$ and to the XY-model for $\gamma = 0$. In spin notation, the potential then takes the role of a paramagnetic term.

Via the mapping $c_j = \frac{1}{2}(a_j + i b_j)$, $c_j^\dagger = \frac{1}{2}(a_j - i b_j)$, we find an alternative description in terms of Majoranas ($a_j^\dagger = a_j$, $b_j^\dagger = b_j$), the *Kitaev-Majorana chain* [96] (compare Sec. 2.7):

$$
H = \frac{i h_0}{2} \sum_{j=1}^{L} a_j b_j - \frac{it}{2} \sum_{j=1}^{L-1} [(1-\gamma) a_j b_{j+1} + (1+\gamma) a_{j+1} b_j].
\tag{247}
$$

We can rewrite the Hamiltonian in compact notation with vectors $\mathbf{a} = (a_1, \ldots, a_L)^T$ and $\mathbf{b} = (b_1, \ldots, b_L)^T$ as

$$
H = \frac{i}{4} \begin{pmatrix} \mathbf{a}^T & \mathbf{b}^T \end{pmatrix} \underbrace{\begin{pmatrix} 0 & B \\ -B^T & 0 \end{pmatrix}}_{=\tilde{B}} \begin{pmatrix} \mathbf{a} \\ \mathbf{b} \end{pmatrix},
\tag{248}
$$

where

$$B = \begin{pmatrix} h_0 & -t(1-\gamma) & 0 & & 0 \\ -t(1+\gamma) & h_0 & -t(1-\gamma) & \dots & 0 \\ 0 & -t(1+\gamma) & h_0 & & 0 \\ & \vdots & & \ddots & \vdots \\ 0 & 0 & 0 & \dots & h_0 \end{pmatrix}. \tag{249}$$

is a real matrix. The target is to find vectors of the kind $v_k^T = (f_k^T, -ig_k^T)$ that diagonalize the block matrix $\tilde{B}$ (i.e. $v_k^\dagger \tilde{B} v_k = \varepsilon_k$) for open boundary conditions. These vectors will correspond to the amplitudes of the Majoranas at the respective site of the chain.

In the following, we first show that the diagonalization of the model with ansatz eigenfunctions with a single frequency k,

$$f_k(j) \propto e^{ikj}, \quad g_k(j) \propto e^{ikj} e^{i\theta_k}, \tag{250}$$

and linear combinations of this eigenvector and its complex conjugate are insufficient to describe a solution if $\gamma \notin \{0, 1, -1\}$. In particular, we show how an imbalance between the number of free parameters in the ansatz functions and boundary conditions prevents such solutions. For (i) cases with a reduced number of boundary constraints, (ii) a case with particular symmetric dispersion relations, we then determine the solutions.

IMPOSSIBILITY OF SOLVING THE GENERAL PROBLEM WITH A SINGLE FREQUENCY EIGENFUNCTION. In order to find eigenvectors of the Hamiltonian, the coefficients in f_k and g_k have to fulfill the conditions

$$Bg_k = \varepsilon_k f_k \quad \text{and} \quad B^T f_k = \varepsilon_k g_k. \tag{251}$$

In the bulk, this yields the equivalent equations

$$\begin{aligned} -t(1+\gamma)g_k(n-1) + h_0 g_k(n) - t(1-\gamma)g_k(n+1) &= \varepsilon_k f_k(n), \\ -t(1-\gamma)f_k(n-1) + h_0 f_k(n) - t(1+\gamma)f_k(n+1) &= \varepsilon_k g_k(n). \end{aligned} \tag{252}$$

With the ansatz (250) we find that the eigenfunctions are associated with an energy ε_k and a phase θ_k that are given by

$$\varepsilon_k = \sqrt{(h_0 - 2t\cos k)^2 + 4\gamma^2 t^2 \sin^2 k}, \tag{253}$$

$$\theta_k = \arg\left(\frac{h_0}{2} - t\cos k - i\gamma t \sin k\right). \tag{254}$$

Due to the symmetry $\varepsilon_{-k} = \varepsilon_k$ and $\theta_{-k} = -\theta_k$, any linear combination of two counter-propagating waves

$$\begin{pmatrix} f_k(j) \\ g_k(j) \end{pmatrix} = a\begin{pmatrix} f_k(j) \\ g_k(j) \end{pmatrix} + b\begin{pmatrix} f_{-k}(j) \\ g_{-k}(j) \end{pmatrix} \tag{255}$$

also solves the bulk equations. It is important here that the symmetry of the dispersion relation only allows superpositions of waves at two (and not more) wave numbers k and $-k$.

In addition to these bulk equations, any valid solution has to also fulfill the boundary equations

$$h_0 g_k(1) - t(1-\gamma)g_k(2) = \varepsilon_k f_k(1), \tag{256}$$
$$h_0 f_k(1) - t(1+\gamma)f_k(2) = \varepsilon_k g_k(1), \tag{257}$$
$$-t(1+\gamma)g_k(L-1) + h_0 g_k(L) = \varepsilon_k f_k(L), \tag{258}$$
$$-t(1-\gamma)f_k(L-1) + h_0 f_k(L) = \varepsilon_k g_k(L). \tag{259}$$

If site 0 was part of the bulk, the ansatz function would fulfill

$$-t(1+\gamma)g_k(0) + h_0 g_k(1) - t(1-\gamma)g_k(2) = \varepsilon_k f_k(1). \tag{260}$$

instead of Eq. (256). To satisfy Eq. (260) with a solution of Eq. (256), the condition $-t(1+\gamma)g_k(0) = 0$ has to be fulfilled. In a similar fashion, the comparison of bulk and boundary conditions for Eqs. (257)-(259) imposes similar constraints. The full set reads

$$-t(1+\gamma)g_k(0) = 0, \tag{261}$$
$$-t(1-\gamma)f_k(0) = 0, \tag{262}$$
$$-t(1-\gamma)g_k(L+1) = 0, \tag{263}$$
$$-t(1+\gamma)f_k(L+1) = 0. \tag{264}$$

In the case $\gamma \neq \pm 1$, the boundary conditions simplify to

$$f(0) = g(0) = f(L+1) = g(L+1) = 0. \tag{265}$$

With the ansatz (255) we then get the following constraints on the coefficients:

$$a + b = 0, \tag{266}$$
$$a \sin\theta_k = 0, \tag{267}$$
$$a \sin(k(L+1)) = 0, \tag{268}$$
$$a \sin(k(L+1) + \theta_k) = 0. \tag{269}$$

For the solution to be non-trivial ($a = -b \neq 0$), we need the following three equations to be fulfilled:

$$\theta_k = n\pi, \tag{270}$$
$$k(L+1) = m\pi, \tag{271}$$
$$k(L+1) + \theta_k = p\pi, \tag{272}$$

where $n, m, p \in \mathbb{Z}$. Using the definition of θ_k (254), Eq. (270) is equivalent to

$$\arg(h_0/2 - t\cos k - i\gamma t \sin k) = n\pi \Leftrightarrow \gamma t \sin k = 0. \tag{273}$$

For $k \neq n\pi$, this is impossible under the condition $\gamma \neq 0$, which concludes our proof. We stress once again that this impossibility is closely related to the symmetry of the dispersion relation. The possible ansatz (255) has an insufficient

number of free parameters to respect all boundary constraints (261)-(264). Below, we discuss the different parameter choices for which solutions do exist. In particular, we show (for $h_0 = 0$) that systems with more symmetric dispersion relations allow to construct solutions that respect all of the above constraints.

SOLVABLE CASES.

The case $\gamma = 0$. From Eq. (254) we obtain $\theta_k = 0$. Then, the allowed momenta fulfill $k(L + 1) = n\pi$ and the resulting functions are

$$f_k(j) = \sin(kj), \quad g_k(j) = \sin(kj). \tag{274}$$

This kind of solution which is exact for the XY-model with magnetic field is often - mistakenly - also given for the generic system.

The case $\gamma = \pm 1$. For $\gamma = 1$, the constraint on $f(0)$ and $g(L + 1)$ is lifted as Eqs. (262) and (263) are always fulfilled, and only the conditions (261) and (264) constrain the coefficients. This allows for solutions with linear combinations of only two counter-propagating waves with wave vectors $\pm k$. As a consequence, the allowed wave vector of the permitted modes have to fulfill $k(L + 1) - \theta_k = n\pi$ and we obtain the known solution for the Ising model [129]:

$$f_k(j) = \sin(kj - \theta_k), \quad g_k(j) = \sin(kj). \tag{275}$$

Interestingly, the constraint on the wave vector allows L real solutions for $h_0 > 1$, but only $L - 1$ real solutions for $h_0 < 1$. The "missing" solution then possesses a complex wavenumber. Consequently, the solution has an amplitude which decays into the bulk (as $\sin(kx) \to \sinh(\kappa x)$ for $k = i\kappa$), and represents the edge modes in the Kitaev chain picture.

In the same fashion, for $\gamma = -1$, the constraints on $g(0)$ and $f(L + 1)$ are lifted. Then Eqs. (262) and (263) allow modes with $k(L + 1) + \theta_k = n\pi$ and

$$f_k(j) = \sin(kj), \quad g_k(j) = \sin(kj + \theta_k). \tag{276}$$

The case $h_0 = 0$. In the absence of a potential/magnetic field, we observe that the dispersion relation $\varepsilon(k)$ has a higher symmetry,

$$\varepsilon(k) = \varepsilon(-k) = \varepsilon(\pi - k) = \varepsilon(-\pi + k), \tag{277}$$
$$\theta(k) = -\theta(-k) = \pi - \theta(\pi - k) = -\pi + \theta(\pi + k). \tag{278}$$

This allows us to make a more elaborate ansatz than in Eq. (255) with four free parameters:

$$f(k_1, k_2)(j) = ae^{ik_1 j} + be^{-ik_1 j} + ce^{ik_2 j} + de^{-ik_2 j}$$
$$= f_k(j) = ae^{ikj} + be^{-ikj} + ce^{i(\pi-k)j} + de^{-i(\pi-k)j}, \tag{279}$$

$$g(k_1, k_2)(j) = ae^{i(k_1 j + \theta_{k_1})} + be^{-i(k_1 j + \theta_{k_1})}$$
$$+ ce^{i(k_2 j + \theta_{k_2})} + de^{-i(k_2 j + \theta_{k_2})}$$
$$= g_k(j) = ae^{i(kj + \theta_k)} + be^{-i(kj + \theta_k)}$$
$$- ce^{i((\pi-k)j - \theta_k)} - de^{-i((\pi-k)j - \theta_k)}. \tag{280}$$

In the non-trivial case ($\gamma \neq \pm 1$), these function have to fulfill the conditions

$$f_k(0) = 0, \quad g_k(0) = 0, \quad f_k(L+1) = 0, \quad g_k(L+1) = 0, \qquad (281)$$

which impose the following constraints on the coefficients:

$$a + d = -(b + c), \qquad (282)$$
$$(a - d)e^{i\theta_k} = -(b - c)e^{-i\theta_k}, \qquad (283)$$
$$(a \pm d)e^{ik(L+1)} = -(b \pm c)e^{-ik(L+1)}, \qquad (284)$$
$$(a \mp d)e^{i(k(L+1)+\theta_k)} = -(b \mp c)e^{-i(k(L+1)+\theta_k)}. \qquad (285)$$

Here, the upper sign corresponds to an odd length of the chain, the lower sign to an even length.

Chains of odd length. Let us first consider a chain of odd length. Combining Eq. (282) with Eq. (284) and Eq. (283) with Eq. (285), we find the conditions

$$\sin(k(L+1))(b+c) = 0, \qquad (286)$$
$$\sin(k(L+1))(b-c) = 0. \qquad (287)$$

These conditions are only fulfilled for $k(L+1) = n\pi$. Otherwise, they yield the trivial solution $a = b = c = d = 0$. In the first case, the coefficients are then not fully determined, and can be chosen as

$$f_k(j) = \begin{cases} (a-d)e^{i\theta_k}\sin(kj - \theta_k) & \text{for } j \text{ odd,} \\ (a+d)\sin(kj) & \text{for } j \text{ even,} \end{cases} \qquad (288)$$

$$g_k(j) = \begin{cases} (a+d)\sin(kj + \theta_k) & \text{for } j \text{ odd,} \\ (a-d)e^{i\theta_k}\sin(kj) & \text{for } j \text{ even.} \end{cases} \qquad (289)$$

In particular, we can find two linearly independent solutions with $a = d$ and $a = -d$. This choice makes the model similar to the even chain presented below.

Chains of even length. For a chain of even length, there are two possible solutions: Combining Eq. (282) with Eq. (285) and Eq. (283) with Eq. (284) yields

$$\sin(k(L+1) + \theta_k)(b+c) = 0, \qquad (290)$$
$$\sin(k(L+1) - \theta_k)(b-c) = 0. \qquad (291)$$

If we choose $b = -c$, we steadily get the discretization $k(L+1) - \theta_k = n\pi$ and coefficients with $a = -be^{-i2\theta_k} = ce^{-i2\theta_k} = -d$, and therefore functions of the form (up to an overall phase and normalization)

$$f_k^1(j) = \sin(kj - \theta_k) + \sin((\pi - k)j + \theta_k) \qquad (292)$$

$$= \begin{cases} 2\sin(kj - \theta_k) & \text{for } j \text{ odd,} \\ 0 & \text{for } j \text{ even,} \end{cases} \qquad (293)$$

$$g_k^1(j) = \sin(kj) - \sin((\pi - k)j) \qquad (294)$$

$$= \begin{cases} 0 & \text{for } j \text{ odd,} \\ 2\sin(kj) & \text{for } j \text{ even.} \end{cases} \qquad (295)$$

The alternative choice $(b = c)$ yields $a = -b = -c = d$ and the discretization $k(L + 1) + \theta_k = n\pi$ with functions

$$f_k^2(j) = \sin(kj) - \sin((\pi - k)j) \tag{296}$$

$$= \begin{cases} 0 & \text{for } j \text{ odd,} \\ 2\sin(kj) & \text{for } j \text{ even,} \end{cases} \tag{297}$$

$$g_k^2(j) = \sin(kj + \theta_k) + \sin((\pi - k)j - \theta_k) \tag{298}$$

$$= \begin{cases} 2\sin(kj + \theta_k) & \text{for } j \text{ odd,} \\ 0 & \text{for } j \text{ even.} \end{cases} \tag{299}$$

Due to the symmetry of the problem, it is sufficient to consider wave numbers $0 < k < \pi/2$, where the cases $k = 0$ and $k = \pi/2$ are excluded as they yield the trivial solution of zero-vectors. Assume for simplification that $0 < k < \pi/2$ and $\gamma > 0$. As a consequence $0 < \theta_k < \pi/2$. The modes k_1 (with index n in discretization condition) and k_2 (with index m) fulfill $k_1 = \pi - k_2$ if $n + m < L + 2$ (for the first quantization condition) and if $n + m < L$ (for the second quantization condition). Due to the symmetry of the problem, the modes k_1 and k_2 can be unambiguously chosen by selecting n from $\{1, \ldots, L/2\}$ or from $\{1, \ldots, L/2 - 1\}$, respectively. This yields $L/2 + L/2 - 1 = L - 1$ solutions. For $|\gamma| < 1$, the additional mode is obtained by solving $\tanh(\kappa(N + 1)) = \pm\gamma \coth(\kappa)$, and then defining $k = \pi/2 \pm i\kappa$. For $|\gamma| > 1$, we can find an additional imaginary solution $i\kappa$ fulfilling $\tanh(\kappa(N + 1)) = \gamma \tanh(\kappa)$ for $\gamma > 0$ and $\tanh(\kappa(N + 1)) = -\gamma \tanh(\kappa)$. $|\gamma| = 1$ then marks the transition point of a gapped regime with edge modes and the gapless XY-regime.

BIBLIOGRAPHY

[1] R. P. Feynman, "Simulating physics with computers," Int. J. Theor. Phys. **21**, 467–488 (1982).

[2] I. Bloch, J. Dalibard, and W. Zwerger, "Many-body physics with ultracold gases," Rev. Mod. Phys. **80**, 885–964 (2008).

[3] J. Cirac and P. Zoller, "Quantum computations with cold trapped ions," Phys. Rev. Lett. **74**, 4091–4094 (1995).

[4] Y. Makhlin, G. Schön, and A. Shnirman, "Quantum-state engineering with Josephson-junction devices," Rev. Mod. Phys. **73**, 357–400 (2001).

[5] A. Aspuru-Guzik and P. Walther, "Photonic quantum simulators," Nat. Phys. **8**, 285–291 (2012).

[6] M. Lewenstein, A. Sanpera, V. Ahufinger, B. Damski, A. Sen, and U. Sen, "Ultracold atomic gases in optical lattices: mimicking condensed matter physics and beyond," Adv. Phys. **56**, 243–379 (2007).

[7] X.-W. Guan, M. T. Batchelor, and C. Lee, "Fermi gases in one dimension: From Bethe ansatz to experiments," Rev. Mod. Phys. **85**, 1633–1691 (2013).

[8] M. A. Cazalilla, R. Citro, T. Giamarchi, E. Orignac, and M. Rigol, "One dimensional bosons: From condensed matter systems to ultracold gases," Rev. Mod. Phys. **83**, 1405–1466 (2011).

[9] M. Aidelsburger, M. Atala, S. Nascimbène, S. Trotzky, Y.-a. Chen, and I. Bloch, "Experimental Realization of Strong Effective Magnetic Fields in an Optical Lattice," Phys. Rev. Lett. **107**, 255301 (2011).

[10] J. Dalibard, F. Gerbier, G. Juzeliunas, and P. Öhberg, "Colloquium: Artificial gauge potentials for neutral atoms," Rev. Mod. Phys. **83**, 1523–1543 (2011).

[11] A. Celi, P. Massignan, J. Ruseckas, N. Goldman, I. B. Spielman, G. Juzeliūnas, and M. Lewenstein, "Synthetic Gauge Fields in Synthetic Dimensions," Phys. Rev. Lett. **112**, 043001 (2014).

[12] V. Galitski and I. B. Spielman, "Spin–orbit coupling in quantum gases," Nature **494**, 49–54 (2013).

[13] C. Chin, R. Grimm, P. Julienne, and E. Tiesinga, "Feshbach resonances in ultracold gases," Rev. Mod. Phys. **82**, 1225–1286 (2010).

[14] X. Chen, Z.-C. Gu, and X.-G. Wen, "Classification of gapped symmetric phases in one-dimensional spin systems," Phys. Rev. B **83**, 035107 (2011).

[15] X. Chen, Z.-C. Gu, and X.-G. Wen, "Complete classification of one-dimensional gapped quantum phases in interacting spin systems," Phys. Rev. B **84**, 235128 (2011).

[16] N. Schuch, D. Pérez-García, and I. Cirac, "Classifying quantum phases using matrix product states and projected entangled pair states," Phys. Rev. B **84**, 165139 (2011).

[17] G. Vidal, J. I. Latorre, E. Rico, and A. Kitaev, "Entanglement in Quantum Critical Phenomena," Phys. Rev. Lett. **90**, 227902 (2003).

[18] P. Calabrese and J. Cardy, "Entanglement entropy and quantum field theory," J. Stat. Mech. Theory Exp., P06002 (2004).

[19] M. B. Plenio, J. Eisert, J. Dreißig, and M. Cramer, "Entropy, Entanglement, and Area: Analytical Results for Harmonic Lattice Systems," Phys. Rev. Lett. **94**, 060503 (2005).

[20] J. Eisert, M. Cramer, and M. B. Plenio, "Colloquium : Area laws for the entanglement entropy," Rev. Mod. Phys. **82**, 277–306 (2010).

[21] J. Eisert, "Entanglement and tensor network states," eprint arXiv:1308.3318 (2013).

[22] R. Orús, "A practical introduction to tensor networks: Matrix product states and projected entangled pair states," Ann. Phys. (N. Y.) **349**, 117–158 (2014).

[23] J. Jünemann, A. Piga, S.-J. Ran, M. Lewenstein, M. Rizzi, and A. Bermudez, "Exploring Interacting Topological Insulators with Ultracold Atoms: The Synthetic Creutz-Hubbard Model," Phys. Rev. X **7**, 031057 (2017).

[24] M. Bischoff, J. Jünemann, M. Polini, and M. Rizzi, "Tuning the Drude weight of Dirac-Weyl fermions in one-dimensional ring traps," Phys. Rev. B **96**, 241112 (2017).

[25] J. Decamp, J. Jünemann, M. Albert, M. Rizzi, A. Minguzzi, and P. Vignolo, "High-momentum tails as magnetic-structure probes for strongly correlated SU(k) fermionic mixtures in one-dimensional traps," Phys. Rev. A **94**, 053614 (2016).

[26] J. Decamp, J. Jünemann, M. Albert, M. Rizzi, A. Minguzzi, and P. Vignolo, "Strongly correlated one-dimensional Bose–Fermi quantum mixtures: symmetry and correlations," New J. Phys. **19**, 125001 (2017).

[27] M. Hartmann, F. Brandão, and M. Plenio, "Quantum many-body phenomena in coupled cavity arrays," Laser Photonics Rev. **2**, 527–556 (2008).

[28] T. Byrnes, N. Y. Kim, K. Kusudo, and Y. Yamamoto, "Quantum simulation of Fermi-Hubbard models in semiconductor quantum-dot arrays," Phys. Rev. B **78**, 075320 (2008).

[29] A. P. Nizovtsev, "A Quantum Computer Based on NV Centers in Diamond: Optically Detected Nutations of Single Electron and Nuclear Spins," Opt. Spectrosc. **99**, 233 (2005).

[30] K. B. Davis, M. O. Mewes, M. R. Andrews, N. J. Van Druten, D. S. Durfee, D. M. Kurn, and W. Ketterle, "Bose-Einstein condensation in a gas of sodium atoms," Phys. Rev. Lett. **75**, 3969–3973 (1995).

[31] M. R. Andrews, C. G. Townsend, H.-J. Miesner, D. S. Durfee, D. M. Kurn, and W. Ketterle, "Observation of Interference Between Two Bose Condensates," Science **275**, 637–641 (1997).

[32] M. Greiner, O. Mandel, T. Esslinger, T. W. Hänsch, and I. Bloch, "Quantum phase transition from a superfluid to a Mott insulator in a gas of ultracold atoms," Nature **415**, 39–44 (2002).

[33] M. Greiner, C. A. Regal, and D. S. Jin, "Emergence of a molecular Bose–Einstein condensate from a Fermi gas," Nature **426**, 537–540 (2003).

[34] S. Nascimbène, N. Navon, K. J. Jiang, F. Chevy, and C. Salomon, "Exploring the thermodynamics of a universal Fermi gas," Nature **463**, 1057–1060 (2010).

[35] G. Roati, C. D'Errico, L. Fallani, M. Fattori, C. Fort, M. Zaccanti, G. Modugno, M. Modugno, and M. Inguscio, "Anderson localization of a non-interacting Bose–Einstein condensate," Nature **453**, 895–898 (2008).

[36] J. Billy, V. Josse, Z. Zuo, A. Bernard, B. Hambrecht, P. Lugan, D. Clément, L. Sanchez-Palencia, P. Bouyer, and A. Aspect, "Direct observation of Anderson localization of matter waves in a controlled disorder," Nature **453**, 891–894 (2008).

[37] M. Schreiber, S. S. Hodgman, P. Bordia, H. P. Luschen, M. H. Fischer, R. Vosk, E. Altman, U. Schneider, and I. Bloch, "Observation of many-body localization of interacting fermions in a quasirandom optical lattice," Science **349**, 842–845 (2015).

[38] L. Tarruell, D. Greif, T. Uehlinger, G. Jotzu, and T. Esslinger, "Creating, moving and merging Dirac points with a Fermi gas in a tunable honeycomb lattice," Nature **483**, 302–305 (2012).

[39] C. Weitenberg, M. Endres, J. F. Sherson, M. Cheneau, P. Schauss, T. Fukuhara, I. Bloch, and S. Kuhr, "Single-spin addressing in an atomic Mott insulator.," Nature **471**, 319–24 (2011).

[40] D. Greif, L. Tarruell, T. Uehlinger, R. Jördens, and T. Esslinger, "Probing Nearest-Neighbor Correlations of Ultracold Fermions in an Optical Lattice," Phys. Rev. Lett. **106**, 145302 (2011).

[41] D. Jaccard, H. Wilhelm, D. Jérome, J. Moser, C. Carcel, and J. M. Fabre, "From spin-Peierls to superconductivity: (TMTTF)2PF6 under high pressure," J. Phys. Condens. Matter **13**, L89–L95 (2001).

[42] S. J. Tans, M. H. Devoret, H. Dai, A. Thess, R. E. Smalley, L. J. Geerligs, and C. Dekker, "Individual single-wall carbon nanotubes as quantum wires," Nature **386**, 474–477 (1997).

[43] R. Saito, G. Dresselhaus, and M. S. Dresselhaus, *Physical properties of carbon nanotubes* (World Scientific Publishing, Singapore, 1998).

[44] T. Giamarchi, *Quantum Physics in One Dimension* (Oxford University Press, Oxford, 2003).

[45] H. Bethe, "Zur Theorie der Metalle," Z. Phys. **71**, 205–226 (1931).

[46] J. Hubbard, "Electron Correlations in Narrow Energy Bands," Proc. R. Soc. A Math. Phys. Eng. Sci. **276**, 238–257 (1963).

[47] U. Schneider, L. Hackermüller, S. Will, T. Best, I. Bloch, T. A. Costi, R. W. Helmes, D. Rasch, and A. Rosch, "Metallic and Insulating Phases of Repulsively Interacting Fermions in a 3D Optical Lattice," Science **322**, 1520–1525 (2008).

[48] R. Jördens, N. Strohmaier, K. Günter, H. Moritz, and T. Esslinger, "A Mott insulator of fermionic atoms in an optical lattice," Nature **455**, 204–207 (2008).

[49] N. W. Ashcroft and N. D. Mermin, *Solid State Physics* (Holt, Rinehart and Winston, New York, NY, 1976).

[50] O. Boada, A. Celi, J. I. Latorre, and M. Lewenstein, "Quantum Simulation of an Extra Dimension," Phys. Rev. Lett. **108**, 133001 (2012).

[51] H. Tasaki, *Ferromagnetism in Itinerant Electron Systems: Rigorous Examples from Flat-Band Hubbard Models* (Springer, Boston, MA, 1994).

[52] J. Vidal, R. Mosseri, and B. Douçot, "Aharonov-Bohm Cages in Two-Dimensional Structures," Phys. Rev. Lett. **81**, 5888–5891 (1998).

[53] B. Douçot and J. Vidal, "Pairing of Cooper Pairs in a Fully Frustrated Josephson-Junction Chain," Phys. Rev. Lett. **88**, 227005 (2002).

[54] Y. Aharonov and D. Bohm, "Significance of Electromagnetic Potentials in the Quantum Theory," Phys. Rev. **115**, 485–491 (1959).

[55] R. Peierls, "Zur Theorie des Diamagnetismus von Leitungselektronen," Z. Phys. **80**, 763–791 (1933).

[56] D. Jaksch and P. Zoller, "Creation of effective magnetic fields in optical lattices: the Hofstadter butterfly for cold neutral atoms," New J. Phys. **5**, 56–56 (2003).

[57]H. Miyake, G. A. Siviloglou, C. J. Kennedy, W. C. Burton, and W. Ketterle, "Realizing the Harper Hamiltonian with Laser-Assisted Tunneling in Optical Lattices," Phys. Rev. Lett. **111**, 185302 (2013).

[58]M. Aidelsburger, M. Atala, M. Lohse, J. T. Barreiro, B. Paredes, and I. Bloch, "Realization of the Hofstadter Hamiltonian with Ultracold Atoms in Optical Lattices," Phys. Rev. Lett. **111**, 185301 (2013).

[59]B. K. Stuhl, H.-I. Lu, L. M. Aycock, D. Genkina, and I. B. Spielman, "Visualizing edge states with an atomic Bose gas in the quantum Hall regime," Science **349**, 1514–1518 (2015).

[60]M. Mancini, G. Pagano, G. Cappellini, L. Livi, M. Rider, J. Catani, C. Sias, P. Zoller, M. Inguscio, M. Dalmonte, and L. Fallani, "Observation of chiral edge states with neutral fermions in synthetic Hall ribbons," Science **349**, 1510–1513 (2015).

[61]J. Vidal, B. Douçot, R. Mosseri, and P. Butaud, "Interaction Induced Delocalization for Two Particles in a Periodic Potential," Phys. Rev. Lett. **85**, 3906–3909 (2000).

[62]M. Creutz and I. Horváth, "Surface states and chiral symmetry on the lattice," Phys. Rev. D **50**, 2297–2308 (1994).

[63]M. Creutz, "End States, Ladder Compounds, and Domain-Wall Fermions," Phys. Rev. Lett. **83**, 2636–2639 (1999).

[64]M. Rizzi, V. Cataudella, and R. Fazio, "Phase diagram of the Bose-Hubbard model with T3 symmetry," Phys. Rev. B **73**, 144511 (2006).

[65]C.-C. Chien and M. Di Ventra, "Controlling transport of ultracold atoms in one-dimensional optical lattices with artificial gauge fields," Phys. Rev. A **87**, 023609 (2013).

[66]C.-C. Chien, S. Peotta, and M. Di Ventra, "Quantum transport in ultracold atoms," Nat. Phys. **11**, 998–1004 (2015).

[67]M. Atala, M. Aidelsburger, M. Lohse, J. T. Barreiro, B. Paredes, and I. Bloch, "Observation of chiral currents with ultracold atoms in bosonic ladders," Nat. Phys. **10**, 588–593 (2014).

[68]M. Piraud, F. Heidrich-Meisner, I. P. McCulloch, S. Greschner, T. Vekua, and U. Schollwöck, "Vortex and Meissner phases of strongly interacting bosons on a two-leg ladder," Phys. Rev. B **91**, 140406 (2015).

[69]S. Greschner, M. Piraud, F. Heidrich-Meisner, I. P. McCulloch, U. Schollwöck, and T. Vekua, "Symmetry-broken states in a system of interacting bosons on a two-leg ladder with a uniform Abelian gauge field," Phys. Rev. A **94**, 063628 (2016).

[70]F. Kolley, M. Piraud, I. P. McCulloch, U. Schollwöck, and F. Heidrich-Meisner, "Strongly interacting bosons on a three-leg ladder in the presence of a homogeneous flux," New J. Phys. **17**, 092001 (2015).

[71]J. M. Kosterlitz and D. J. Thouless, "Long range order and metastability in two dimensional solids and superfluids. (Application of dislocation theory)," J. Phys. C Solid State Phys. **5**, L124–L126 (1972).

[72]J. M. Kosterlitz and D. J. Thouless, "Ordering, metastability and phase transitions in two-dimensional systems," J. Phys. C Solid State Phys. **6**, 1181–1203 (1973).

[73]J. M. Kosterlitz, "The critical properties of the two-dimensional xy model," J. Phys. C **7**, 1046–1060 (1974).

[74]F. Haldane, "Continuum dynamics of the 1-D Heisenberg antiferromagnet: Identification with the O(3) nonlinear sigma model," Phys. Lett. A **93**, 464–468 (1983).

[75] F. D. M. Haldane, "Model for a Quantum Hall Effect without Landau Levels: Condensed Matter Realization of the Parity Anomaly," Phys. Rev. Lett. **61**, 2015–2018 (1988).

[76] X. Chen, Z.-C. Gu, Z.-X. Liu, and X.-G. Wen, "Symmetry protected topological orders and the group cohomology of their symmetry group," Phys. Rev. B **87**, 155114 (2013).

[77] K. V. Klitzing, G. Dorda, and M. Pepper, "New method for high-accuracy determination of the fine-structure constant based on quantized hall resistance," Phys. Rev. Lett. **45**, 494–497 (1980).

[78] D. J. Thouless, M. Kohmoto, M. P. Nightingale, and M. den Nijs, "Quantized Hall Conductance in a Two-Dimensional Periodic Potential," Phys. Rev. Lett. **49**, 405–408 (1982).

[79] B. A. Bernevig and S.-C. Zhang, "Quantum Spin Hall Effect," Phys. Rev. Lett. **96**, 106802 (2006).

[80] M. Konig, S. Wiedmann, C. Brune, A. Roth, H. Buhmann, L. W. Molenkamp, X.-L. Qi, and S.-C. Zhang, "Quantum Spin Hall Insulator State in HgTe Quantum Wells," Science **318**, 766–770 (2007).

[81] R. B. Laughlin, "Quantized Hall conductivity in two dimensions," Phys. Rev. B **23**, 5632–5633 (1981).

[82] H. L. Stormer and D. C. Tsui, "The Quantized Hall Effect," Science **220**, 1241–1246 (1983).

[83] N. Goldman, J. C. Budich, and P. Zoller, "Topological quantum matter with ultracold gases in optical lattices," Nat. Phys. **12**, 639–645 (2016).

[84] N. K. Wilkin and J. M. F. Gunn, "Condensation of "Composite Bosons" in a Rotating BEC," Phys. Rev. Lett. **84**, 6–9 (2000).

[85] N. R. Cooper, N. K. Wilkin, and J. M. F. Gunn, "Quantum Phases of Vortices in Rotating Bose-Einstein Condensates," Phys. Rev. Lett. **87**, 120405 (2001).

[86] M. Hafezi, A. S. Sørensen, E. Demler, and M. D. Lukin, "Fractional quantum Hall effect in optical lattices," Phys. Rev. A **76**, 023613 (2007).

[87] R. N. Palmer, A. Klein, and D. Jaksch, "Optical lattice quantum Hall effect," Phys. Rev. A **78**, 013609 (2008).

[88] E. Kapit and E. Mueller, "Exact Parent Hamiltonian for the Quantum Hall States in a Lattice," Phys. Rev. Lett. **105**, 215303 (2010).

[89] N. Y. Yao, C. R. Laumann, A. V. Gorshkov, S. D. Bennett, E. Demler, P. Zoller, and M. D. Lukin, "Topological Flat Bands from Dipolar Spin Systems," Phys. Rev. Lett. **109**, 266804 (2012).

[90] N. R. Cooper and J. Dalibard, "Reaching Fractional Quantum Hall States with Optical Flux Lattices," Phys. Rev. Lett. **110**, 185301 (2013).

[91] A. E. B. Nielsen, G. Sierra, and J. I. Cirac, "Local models of fractional quantum Hall states in lattices and physical implementation," Nat. Commun. **4**, 2864 (2013).

[92] M. Aidelsburger, M. Lohse, C. Schweizer, M. Atala, J. T. Barreiro, S. Nascimbène, N. R. Cooper, I. Bloch, and N. Goldman, "Measuring the Chern number of Hofstadter bands with ultracold bosonic atoms," Nat. Phys. **11**, 162–166 (2014).

[93] R. Islam, R. Ma, P. M. Preiss, M. Eric Tai, A. Lukin, M. Rispoli, and M. Greiner, "Measuring entanglement entropy in a quantum many-body system," Nature **528**, 77–83 (2015).

[94] F. Pollmann, A. M. Turner, E. Berg, and M. Oshikawa, "Entanglement spectrum of a topological phase in one dimension," Phys. Rev. B **81**, 064439 (2010).

[95] A. M. Turner, F. Pollmann, and E. Berg, "Topological phases of one-dimensional fermions: An entanglement point of view," Phys. Rev. B **83**, 075102 (2011).

[96] A. Y. Kitaev, "Unpaired Majorana fermions in quantum wires," Physics-Uspekhi **44**, 131–136 (2001).

[97] I. Affleck, T. Kennedy, E. H. Lieb, and H. Tasaki, "Rigorous results on valence-bond ground states in antiferromagnets," Phys. Rev. Lett. **59**, 799–802 (1987).

[98] L. Fidkowski and A. Kitaev, "Topological phases of fermions in one dimension," Phys. Rev. B **83**, 075103 (2011).

[99] A. Altland and M. R. Zirnbauer, "Nonstandard symmetry classes in mesoscopic normal-superconducting hybrid structures," Phys. Rev. B **55**, 1142–1161 (1997).

[100] A. V. Gorshkov, M. Hermele, V. Gurarie, C. Xu, P. S. Julienne, J. Ye, P. Zoller, E. Demler, M. D. Lukin, and A. M. Rey, "Two-orbital SU(N) magnetism with ultracold alkaline-earth atoms," Nat. Phys. **6**, 289–295 (2010).

[101] S. Capponi, P. Lecheminant, and K. Totsuka, "Phases of one-dimensional SU(N) cold atomic Fermi gases-From molecular Luttinger liquids to topological phases," Ann. Phys. (N. Y.) **367**, 50–95 (2016).

[102] I. P. McCulloch and M. Gulácsi, "The non-Abelian density matrix renormalization group algorithm," Europhys. Lett. **57**, 852–858 (2002).

[103] A. Weichselbaum, "Non-abelian symmetries in tensor networks: A quantum symmetry space approach," Ann. Phys. (N. Y.) **327**, 2972–3047 (2012).

[104] T. Matsubara and H. Matsuda, "A Lattice Model of Liquid Helium, I," Prog. Theor. Phys. **16**, 569–582 (1956).

[105] P. Jordan and E. Wigner, "Uber das Paulische Äquivalenzverbot," Z. Phys. **47**, 631–651 (1928).

[106] N. P. Landsman, "Spontaneous symmetry breaking in quantum systems: Emergence or reduction?" Stud. Hist. Philos. Sci. Part B - Stud. Hist. Philos. Mod. Phys. **44**, 379–394 (2013).

[107] J. D. Fraser, "Spontaneous Symmetry Breaking in Finite Systems," Philos. Sci. **83**, 585–605 (2016).

[108] B. Zeng and X.-G. Wen, "Gapped quantum liquids and topological order, stochastic local transformations and emergence of unitarity," Phys. Rev. B **91**, 125121 (2015).

[109] S. Chern, "Characteristic Classes of Hermitian Manifolds," Ann. Math. **47**, 85 (1946).

[110] M. V. Berry, "Quantal Phase Factors Accompanying Adiabatic Changes," Proc. R. Soc. A Math. Phys. Eng. Sci. **392**, 45–57 (1984).

[111] M. Hafezi, A. S. Sørensen, M. D. Lukin, and E. Demler, "Characterization of topological states on a lattice with Chern number," Europhys. Lett. **81**, 10005 (2008).

[112] E. Alba, J. K. Pachos, and J. J. García-Ripoll, "Winding number order in the Haldane model with interactions," New J. Phys. **18**, 033022 (2016).

[113] M. Gerster, M. Rizzi, P. Silvi, M. Dalmonte, and S. Montangero, "Fractional quantum Hall effect in the interacting Hofstadter model via tensor networks," eprint arXiv:1705.06515 (2017).

[114] C. N. Varney, K. Sun, M. Rigol, and V. Galitski, "Interaction effects and quantum phase transitions in topological insulators," Phys. Rev. B **82**, 115125 (2010).

[115] K. von Klitzing, "The quantized Hall effect," Rev. Mod. Phys. **58**, 519–531 (1986).

[116] R. B. Laughlin, "Anomalous quantum Hall effect: An incompressible quantum fluid with fractionally charged excitations," Phys. Rev. Lett. **50**, 1395–1398 (1983).

[117] A. Kitaev, "Fault-tolerant quantum computation by anyons," Ann. Phys. (N. Y.) **303**, 2–30 (2003).

[118] C. Nayak, S. H. Simon, A. Stern, M. Freedman, and S. Das Sarma, "Non-Abelian anyons and topological quantum computation," Rev. Mod. Phys. **80**, 1083–1159 (2008).

[119] M. Tovmasyan, E. P. L. van Nieuwenburg, and S. D. Huber, "Geometry-induced pair condensation," Phys. Rev. B **88**, 220510 (2013).

[120] S. Takayoshi, H. Katsura, N. Watanabe, and H. Aoki, "Phase diagram and pair Tomonaga-Luttinger liquid in a Bose-Hubbard model with flat bands," Phys. Rev. A **88**, 063613 (2013).

[121] M. Tovmasyan, S. Peotta, P. Törmä, and S. D. Huber, "Effective theory and emergent SU(2) symmetry in the flat bands of attractive Hubbard models," Phys. Rev. B **94**, 245149 (2016).

[122] D. Sticlet, L. Seabra, F. Pollmann, and J. Cayssol, "Topological superconductivity in the one-dimensional interacting Creutz model," J. Phys. Conf. Ser. **592**, 012133 (2015).

[123] J. Zak, "Berry's phase for energy bands in solids," Phys. Rev. Lett. **62**, 2747–2750 (1989).

[124] J. B. Kogut, "An introduction to lattice gauge theory and spin systems," Rev. Mod. Phys. **51**, 659–713 (1979).

[125] J. Dziarmaga, "Dynamics of a Quantum Phase Transition: Exact Solution of the Quantum Ising Model," Phys. Rev. Lett. **95**, 245701 (2005).

[126] A. Kitaev and C. Laumann, "Topological phases and quantum computation," eprint arXiv:0904.2771 (2009).

[127] J. H. Taylor and G. Müller, "Magnetic field effects in the dynamics of alternating or anisotropic quantum spin chains," Physica A **130**, 1–33 (1985).

[128] T. Kato, *Perturbation Theory for Linear Operators*, Vol. 132, Classics in Mathematics (Springer, Berlin, Heidelberg, 1995).

[129] P. Pfeuty, "The one-dimensional Ising model with a transverse field," Ann. Phys. (N. Y.) **57**, 79–90 (1970).

[130] P. Silvi, T. Calarco, G. Morigi, and S. Montangero, "Ab initio characterization of the quantum linear-zigzag transition using density matrix renormalization group calculations," Phys. Rev. B **89**, 094103 (2014).

[131] P. Di Francesco, P. Mathieu, and D. Sénéchal, *Conformal Field Theory*, Graduate Texts in Contemporary Physics (Springer New York, New York, NY, 1997).

[132] U. Fano, "Effects of configuration interaction on intensities and phase shifts," Phys. Rev. **124**, 1866–1878 (1961).

[133] P. W. Anderson, "Theory of localized magnetic states in metals," J. Appl. Phys. **37**, 1194 (1966).

[134] G. D. Mahan, *Many-Particle Physics* (Springer US, Boston, MA, 2000).

[135] B. S. Deaver and W. M. Fairbank, "Experimental Evidence for Quantized Flux in Superconducting Cylinders," Phys. Rev. Lett. **7**, 43–46 (1961).

[136] N. Byers and C. N. Yang, "Theoretical Considerations Concerning Quantized Magnetic Flux in Superconducting Cylinders," Phys. Rev. Lett. **7**, 46–49 (1961).

[137]L. Onsager, "Magnetic flux through a superconducting ring," Phys. Rev. Lett. **7**, 50 (1961).

[138]M. Büttiker, Y. Imry, and R. Landauer, "Josephson behavior in small normal one-dimensional rings," Phys. Lett. A **96**, 365–367 (1983).

[139]L. P. Lévy, G. Dolan, J. Dunsmuir, and H. Bouchiat, "Magnetization of mesoscopic copper rings: Evidence for persistent currents," Phys. Rev. Lett. **64**, 2074–2077 (1990).

[140]D. Mailly, C. Chapelier, and A. Benoit, "Experimental observation of persistent currents in GaAs-AlGaAs single loop," Phys. Rev. Lett. **70**, 2020–2023 (1993).

[141]H. Bluhm, N. C. Koshnick, J. A. Bert, M. E. Huber, and K. A. Moler, "Persistent Currents in Normal Metal Rings," Phys. Rev. Lett. **102**, 136802 (2009).

[142]A. C. Bleszynski-Jayich, W. E. Shanks, B. Peaudecerf, E. Ginossar, F. von Oppen, L. Glazman, and J. G. E. Harris, "Persistent Currents in Normal Metal Rings," Science **326**, 272–275 (2009).

[143]W. Kohn, "Theory of the insulating state," Phys. Rev. **133**, A171–A181 (1964).

[144]F. Bloch, "Josephson Effect in a Superconducting Ring," Phys. Rev. B **2**, 109–121 (1970).

[145]J. A. Sauer, M. D. Barrett, and M. S. Chapman, "Storage Ring for Neutral Atoms," Phys. Rev. Lett. **87**, 270401 (2001).

[146]S. Gupta, K. W. Murch, K. L. Moore, T. P. Purdy, and D. M. Stamper-Kurn, "Bose-Einstein Condensation in a Circular Waveguide," Phys. Rev. Lett. **95**, 143201 (2005).

[147]C. Ryu, M. Andersen, P. Cladé, V. Natarajan, K. Helmerson, and W. Phillips, "Observation of Persistent Flow of a Bose-Einstein Condensate in a Toroidal Trap," Phys. Rev. Lett. **99**, 260401 (2007).

[148]A. Ramanathan, K. C. Wright, S. R. Muniz, M. Zelan, W. T. Hill, C. J. Lobb, K. Helmerson, W. D. Phillips, and G. K. Campbell, "Superflow in a Toroidal Bose-Einstein Condensate: An Atom Circuit with a Tunable Weak Link," Phys. Rev. Lett. **106**, 130401 (2011).

[149]K. C. Wright, R. B. Blakestad, C. J. Lobb, W. D. Phillips, and G. K. Campbell, "Driving Phase Slips in a Superfluid Atom Circuit with a Rotating Weak Link," Phys. Rev. Lett. **110**, 025302 (2013).

[150]L. Corman, L. Chomaz, T. Bienaimé, R. Desbuquois, C. Weitenberg, S. Nascimbène, J. Dalibard, and J. Beugnon, "Quench-Induced Supercurrents in an Annular Bose Gas," Phys. Rev. Lett. **113**, 135302 (2014).

[151]S. Beattie, S. Moulder, R. J. Fletcher, and Z. Hadzibabic, "Persistent Currents in Spinor Condensates," Phys. Rev. Lett. **110**, 025301 (2013).

[152]S. Eckel, F. Jendrzejewski, A. Kumar, C. J. Lobb, and G. K. Campbell, "Interferometric Measurement of the Current-Phase Relationship of a Superfluid Weak Link," Phys. Rev. X **4**, 031052 (2014).

[153]M. Cominotti, D. Rossini, M. Rizzi, F. Hekking, and A. Minguzzi, "Optimal Persistent Currents for Interacting Bosons on a Ring with a Gauge Field," Phys. Rev. Lett. **113**, 025301 (2014).

[154]D. Aghamalyan, M. Cominotti, M. Rizzi, D. Rossini, F. Hekking, A. Minguzzi, L. C. Kwek, and L. Amico, "Coherent superposition of current flows in an atomtronic quantum interference device," New J. Phys. **17**, 045023 (2015).

[155]A. K. Geim and K. S. Novoselov, "The rise of graphene," Nat. Mater. **6**, 183–191 (2007).

[156] M. Polini, F. Guinea, M. Lewenstein, H. C. Manoharan, and V. Pellegrini, "Artificial honeycomb lattices for electrons, atoms and photons," Nat. Nanotechnol. **8**, 625–633 (2013).

[157] P. Soltan-Panahi, J. Struck, P. Hauke, A. Bick, W. Plenkers, G. Meineke, C. Becker, P. Windpassinger, M. Lewenstein, and K. Sengstock, "Multi-component quantum gases in spin-dependent hexagonal lattices," Nat Phys **7**, 434–440 (2011).

[158] J. Struck, C. Olschlager, R. Le Targat, P. Soltan-Panahi, A. Eckardt, M. Lewenstein, P. Windpassinger, and K. Sengstock, "Quantum Simulation of Frustrated Classical Magnetism in Triangular Optical Lattices," Science **333**, 996–999 (2011).

[159] G. Jotzu, M. Messer, R. Desbuquois, M. Lebrat, T. Uehlinger, D. Greif, and T. Esslinger, "Experimental realization of the topological Haldane model with ultracold fermions," Nature **515**, 237–240 (2014).

[160] L. Amico, D. Aghamalyan, F. Auksztol, H. Crepaz, R. Dumke, and L. C. Kwek, "Superfluid qubit systems with ring shaped optical lattices," Sci. Rep. **4**, 4298 (2015).

[161] M. Łacki, H. Pichler, A. Sterdyniak, A. Lyras, V. E. Lembessis, O. Al-Dossary, J. C. Budich, and P. Zoller, "Quantum Hall physics with cold atoms in cylindrical optical lattices," Phys. Rev. A **93**, 013604 (2016).

[162] J. W. McClure, "Diamagnetism of Graphite," Phys. Rev. **104**, 666–671 (1956).

[163] J. W. McClure, "Theory of diamagnetism of graphite," Phys. Rev. **119**, 606–613 (1960).

[164] M. Sharma, L. Johnson, and J. McClure, "Diamagnetism of graphite," Phys. Lett. A **44**, 445–446 (1973).

[165] A. Principi, M. Polini, G. Vignale, and M. I. Katsnelson, "Many-Body Orbital Paramagnetism in Doped Graphene Sheets," Phys. Rev. Lett. **104**, 225503 (2010).

[166] S. H. Abedinpour, G. Vignale, A. Principi, M. Polini, W.-K. Tse, and A. H. MacDonald, "Drude weight, plasmon dispersion, and ac conductivity in doped graphene sheets," Phys. Rev. B **84**, 045429 (2011).

[167] M. Koshino and T. Ando, "Anomalous orbital magnetism in Dirac-electron systems: Role of pseudospin paramagnetism," Phys. Rev. B **81**, 195431 (2010).

[168] G. Gómez-Santos and T. Stauber, "Measurable Lattice Effects on the Charge and Magnetic Response in Graphene," Phys. Rev. Lett. **106**, 045504 (2011).

[169] A. Raoux, M. Morigi, J.-N. Fuchs, F. Piéchon, and G. Montambaux, "From Dia- to Paramagnetic Orbital Susceptibility of Massless Fermions," Phys. Rev. Lett. **112**, 026402 (2014).

[170] A. Gutiérrez-Rubio, T. Stauber, G. Gómez-Santos, R. Asgari, and F. Guinea, "Orbital magnetic susceptibility of graphene and MoS2," Phys. Rev. B **93**, 085133 (2016).

[171] F. Piéchon, A. Raoux, J.-N. Fuchs, and G. Montambaux, "Geometric orbital susceptibility: Quantum metric without Berry curvature," Phys. Rev. B **94**, 134423 (2016).

[172] X. Wan, A. M. Turner, A. Vishwanath, and S. Y. Savrasov, "Topological semimetal and Fermi-arc surface states in the electronic structure of pyrochlore iridates," Phys. Rev. B **83**, 205101 (2011).

[173] A. A. Burkov and L. Balents, "Weyl Semimetal in a Topological Insulator Multilayer," Phys. Rev. Lett. **107**, 127205 (2011).

[174] M. Z. Hasan, S.-Y. Xu, I. Belopolski, and S.-M. Huang, "Discovery of Weyl Fermion Semimetals and Topological Fermi Arc States," Annu. Rev. Condens. Matter Phys. **8**, 289–309 (2017).

[175]B. Yan and C. Felser, "Topological Materials: Weyl Semimetals," Annu. Rev. Condens. Matter Phys. **8**, 337–354 (2017).

[176]M. E. Peskin, *An Introduction to Quantum Field Theory* (Westview Press, Boulder, CO, 1995).

[177]H. B. Nielsen and M. Ninomiya, "A no-go theorem for regularizing chiral fermions," Phys. Lett. B **105**, 219–223 (1981).

[178]H. Nielsen and M. Ninomiya, "Absence of neutrinos on a lattice," Nucl. Phys. B **185**, 20–40 (1981).

[179]K. Wilson, *Erice lectures notes*, 1975.

[180]M. Z. Hasan and C. L. Kane, "Colloquium: Topological insulators," Rev. Mod. Phys. **82**, 3045–3067 (2010).

[181]R. Kubo, "Statistical-Mechanical Theory of Irreversible Processes. I. General Theory and Simple Applications to Magnetic and Conduction Problems," J. Phys. Soc. Japan **12**, 570–586 (1957).

[182]P. Nozieres and D. Pines, *Theory Of Quantum Liquids* (Westview Press, Boulder, CO, 1999).

[183]B. S. Shastry and B. Sutherland, "Twisted boundary conditions and effective mass in Heisenberg-Ising and Hubbard rings," Phys. Rev. Lett. **65**, 243–246 (1990).

[184]A. J. Millis and S. N. Coppersmith, "Interaction and doping dependence of optical spectral weight of the two-dimensional Hubbard model," Phys. Rev. B **42**, 10807–10810 (1990).

[185]R. M. Fye, M. J. Martins, D. J. Scalapino, J. Wagner, and W. Hanke, "Drude weight, optical conductivity, and flux properties of one-dimensional Hubbard rings," Phys. Rev. B **44**, 6909–6915 (1991).

[186]S. Kirchner, H. Evertz, and W. Hanke, "Transport properties of one-dimensional Hubbard models," Phys. Rev. B **59**, 1825 (1999).

[187]G. Q. Pellegrino, "Persistent current and Drude weight in one-dimensional rings with substitution potentials," J. Phys. Condens. Matter **13**, 8121–8134 (2001).

[188]F. Dias, I. Pimentel, and M. Henkel, "Persistent current and Drude weight in mesoscopic rings," Phys. Rev. B **73**, 075109 (2006).

[189]B. Hetényi, "Drude Weight, Meissner Weight, Rotational Inertia of Bosonic Superfluids: How Are They Distinguished?" J. Phys. Soc. Japan **83**, 034711 (2014).

[190]D. J. Scalapino, S. R. White, and S. Zhang, "Insulator, metal, or superconductor: The criteria," Phys. Rev. B **47**, 7995–8007 (1993).

[191]G. Giuliani and G. Vignale, *Quantum theory of the electron liquid* (Cambridge University Press, Cambridge, 2005).

[192]D. Sticlet, B. Dóra, and J. Cayssol, "Persistent currents in Dirac fermion rings," Phys. Rev. B **88**, 205401 (2013).

[193]G. Bouzerar, D. Poilblanc, and G. Montambaux, "Persistent currents in onedimensional disordered rings of interacting electrons," Phys. Rev. B **49**, 8258–8262 (1994).

[194]T. Giamarchi and B. S. Shastry, "Persistent currents in a one-dimensional ring for a disordered Hubbard model," Phys. Rev. B **51**, 10915–10922 (1995).

[195]M. A. Cazalilla and A. M. Rey, "Ultracold Fermi gases with emergent SU(N) symmetry," Reports Prog. Phys. **77**, 124401 (2014).

[196]B. Sutherland, "Model for a multicomponent quantum system," Phys. Rev. B **12**, 3795–3805 (1975).

[197]M. Takahashi, "Many-Body Problem of Attractive Fermions with Arbitrary Spin in One Dimension," Prog. Theor. Phys. **44**, 899–904 (1970).

[198]S. Murmann, F. Deuretzbacher, G. Zürn, J. Bjerlin, S. M. Reimann, L. Santos, T. Lompe, and S. Jochim, "Antiferromagnetic Heisenberg Spin Chain of a Few Cold Atoms in a One-Dimensional Trap," Phys. Rev. Lett. **115**, 215301 (2015).

[199]G. Pagano, M. Mancini, G. Cappellini, P. Lombardi, F. Schäfer, H. Hu, X.-J. Liu, J. Catani, C. Sias, M. Inguscio, and L. Fallani, "A one-dimensional liquid of fermions with tunable spin," Nat. Phys. **10**, 198–201 (2014).

[200]S. Taie, Y. Takasu, S. Sugawa, R. Yamazaki, T. Tsujimoto, R. Murakami, and Y. Takahashi, "Realization of a SU(2)xSU(6) System of Fermions in a Cold Atomic G," Phys. Rev. Lett. **105**, 190401 (2010).

[201]X. Cui and T.-L. Ho, "Phase Separation in Mixtures of Repulsive Fermi Gases Driven by Mass Difference," Phys. Rev. Lett. **110**, 165302 (2013).

[202]P. Massignan, J. Levinsen, and M. M. Parish, "Magnetism in Strongly Interacting One-Dimensional Quantum Mixtures," Phys. Rev. Lett. **115**, 247202 (2015).

[203]T. Grining, M. Tomza, M. Lesiuk, M. Przybytek, M. Musiał, R. Moszynski, M. Lewenstein, and P. Massignan, "Crossover between few and many fermions in a harmonic trap," Phys. Rev. A **92**, 061601 (2015).

[204]M. E. Beverland, G. Alagic, M. J. Martin, A. P. Koller, A. M. Rey, and A. V. Gorshkov, "Realizing exactly solvable SU(N) magnets with thermal atoms," Phys. Rev. A **93**, 051601 (2016).

[205]F. Gürsey and L. A. Radicati, "Spin and Unitary Spin Independence of Strong Interactions," Phys. Rev. Lett. **13**, 173–175 (1964).

[206]E. Lieb and D. Mattis, "Theory of ferromagnetism and the ordering of electronic energy levels," Phys. Rev. **125**, 164–172 (1962).

[207]M. Olshanii and V. Dunjko, "Short-distance correlation properties of the Lieb-Liniger system and momentum distributions of trapped one-dimensional atomic gases.," Phys. Rev. Lett. **91**, 090401 (2003).

[208]M. Hamermesh, *Group theory and its application to physical problems* (Courier Corporation, North Chelmsford, 2012).

[209]L. Pan, Y. Liu, H. Hu, Y. Zhang, and S. Chen, "Exact ordering of energy levels for one-dimensional interacting Fermi gases with SU(N) symmetry," Phys. Rev. B **96**, 075149 (2017).

[210]S. Tan, "Energetics of a strongly correlated Fermi gas," Ann. Phys. (N. Y.) **323**, 2952–2970 (2008).

[211]S. Tan, "Generalized virial theorem and pressure relation for a strongly correlated Fermi gas," Ann. Phys. (N. Y.) **323**, 2987–2990 (2008).

[212]S. Tan, "Large momentum part of a strongly correlated Fermi gas," Ann. Phys. (N. Y.) **323**, 2971–2986 (2008).

[213]M. Barth and W. Zwerger, "Tan relations in one dimension," Ann. Phys. (N. Y.) **326**, 2544–2565 (2011).

[214]A. G. Volosniev, D. Petrosyan, M. Valiente, D. V. Fedorov, A. S. Jensen, and N. T. Zinner, "Engineering the dynamics of effective spin-chain models for strongly interacting atomic gases," Phys. Rev. A **91**, 023620 (2015).

[215]F. Deuretzbacher, D. Becker, J. Bjerlin, S. M. Reimann, and L. Santos, "Quantum magnetism without lattices in strongly interacting one-dimensional spinor gases," Phys. Rev. A **90**, 013611 (2014).

[216] N. L. Harshman, "One-Dimensional Traps, Two-Body Interactions, Few-Body Symmetries. II. N Particles," Few-Body Syst. **57**, 45–69 (2016).

[217] N. Matveeva and G. E. Astrakharchik, "One-dimensional multicomponent Fermi gas in a trap: quantum Monte Carlo study," New J. Phys. **18**, 065009 (2016).

[218] X.-W. Guan, Z.-Q. Ma, and B. Wilson, "One-dimensional multicomponent fermions with delta-function interaction in strong- and weak-coupling limits: Two-component Fermi gas," Phys. Rev. A **85**, 033632 (2012).

[219] K. K. Das, "Bose-Fermi mixtures in one dimension.," Phys. Rev. Lett. **90**, 170403 (2003).

[220] A. Imambekov and E. Demler, "Exactly solvable case of a one-dimensional Bose–Fermi mixture," Phys. Rev. A **73**, 021602 (2006).

[221] A. Imambekov and E. Demler, "Applications of exact solution for strongly interacting one-dimensional Bose-Fermi mixture: Low-temperature correlation functions, density profiles, and collective modes," Ann. Phys. (N. Y.) **321**, 2390–2437 (2006).

[222] F. Deuretzbacher, D. Becker, J. Bjerlin, S. M. Reimann, and L. Santos, "Spin-chain model for strongly interacting one-dimensional Bose-Fermi mixtures," Phys. Rev. A **95**, 043630 (2017).

[223] P. Silvi, F. Tschirsich, M. Gerster, J. Jünemann, D. Jaschke, M. Rizzi, and S. Montangero, "The Tensor Networks Anthology: Simulation techniques for many-body quantum lattice systems," eprint arXiv:1710.03733 (2017).

[224] S. R. White, "Density matrix formulation for quantum renormalization groups," Phys. Rev. Lett. **69**, 2863–2866 (1992).

[225] S. R. White, "Density-matrix algorithms for quantum renormalization groups," Phys. Rev. B **48**, 10345–10356 (1993).

[226] U. Schollwöck, "The density-matrix renormalization group," Rev. Mod. Phys. **77**, 259–315 (2005).

[227] U. Schollwöck, "The density-matrix renormalization group in the age of matrix product states," Ann. Phys. (N. Y.) **326**, 96–192 (2011).

[228] F. Verstraete and J. I. Cirac, "Renormalization algorithms for Quantum-Many Body Systems in two and higher dimensions," eprint arXiv:cond-mat/0407066 (2004).

[229] L. Tagliacozzo, A. Celi, and M. Lewenstein, "Tensor Networks for Lattice Gauge Theories with Continuous Groups," Phys. Rev. X **4**, 041024 (2014).

[230] G. Vidal, "Entanglement Renormalization," Phys. Rev. Lett. **99**, 220405 (2007).

[231] F. Verstraete, J. J. García-Ripoll, and J. I. Cirac, "Matrix Product Density Operators: Simulation of Finite-Temperature and Dissipative Systems," Phys. Rev. Lett. **93**, 207204 (2004).

[232] I. P. McCulloch, "From density-matrix renormalization group to matrix product states," J. Stat. Mech. Theory Exp. **2007**, P10014–P10014 (2007).

[233] C. Hubig, I. P. McCulloch, and U. Schollwöck, "Generic construction of efficient matrix product operators," Phys. Rev. B **95**, 035129 (2017).

[234] B. Pirvu, J. Haegeman, and F. Verstraete, "Matrix product state based algorithm for determining dispersion relations of quantum spin chains with periodic boundary conditions," Phys. Rev. B **85**, 035130 (2012).

[235] V. Nebendahl and W. Dür, "Improved numerical methods for infinite spin chains with long-range interactions," Phys. Rev. B **87**, 075413 (2013).

[236] A. J. Ferris, "Fourier Transform for Fermionic Systems and the Spectral Tensor Network," Phys. Rev. Lett. **113**, 010401 (2014).

[237] W. E. Arnoldi, "The principle of minimized iterations in the solution of the matrix eigenvalue problem," Q. Appl. Math. **9**, 17–29 (1951).

[238] S. R. White, "Density matrix renormalization group algorithms with a single center site," Phys. Rev. B **72**, 180403 (2005).

[239] C. Hubig, I. P. McCulloch, U. Schollwöck, and F. A. Wolf, "Strictly single-site DMRG algorithm with subspace expansion," Phys. Rev. B **91**, 155115 (2015).

[240] S. Östlund and S. Rommer, "Thermodynamic Limit of Density Matrix Renormalization," Phys. Rev. Lett. **75**, 3537–3540 (1995).

[241] F. Verstraete, V. Murg, and J. Cirac, "Matrix product states, projected entangled pair states, and variational renormalization group methods for quantum spin systems," Adv. Phys. **57**, 143–224 (2008).

[242] R. B. Lehoucq, D. C. Sorensen, and C. Yang, *ARPACK Users' Guide* (Society for Industrial and Applied Mathematics, Philadelphia, PA, 1998).

[243] Y.-Y. Shi, L.-M. Duan, and G. Vidal, "Classical simulation of quantum many-body systems with a tree tensor network," Phys. Rev. A **74**, 022320 (2006).

[244] L. P. Kadanoff, *From Order To Chaos: Essays: Critical, Chaotic and Otherwise* (World Scientific Publishing, Singapore, 1993), pp. 165–174.

[245] P. Silvi, V. Giovannetti, S. Montangero, M. Rizzi, J. I. Cirac, and R. Fazio, "Homogeneous binary trees as ground states of quantum critical Hamiltonians," Phys. Rev. A **81**, 062335 (2010).

[246] M. Gerster, P. Silvi, M. Rizzi, R. Fazio, T. Calarco, and S. Montangero, "Unconstrained tree tensor network: An adaptive gauge picture for enhanced performance," Phys. Rev. B **90**, 125154 (2014).

[247] M. Gerster, M. Rizzi, F. Tschirsich, P. Silvi, R. Fazio, and S. Montangero, "Superfluid density and quasi-long-range order in the one-dimensional disordered Bose-Hubbard model," New J. Phys. **18**, 015015 (2016).

[248] D. C. McKay and B. DeMarco, "Cooling in strongly correlated optical lattices: prospects and challenges," Reports Prog. Phys. **74**, 054401 (2011).

[249] W. D. Phillips, "Nobel Lecture: Laser cooling and trapping of neutral atoms," Rev. Mod. Phys. **70**, 721–741 (1998).

[250] C. N. Cohen-Tannoudji, "Nobel Lecture: Manipulating atoms with photons," Rev. Mod. Phys. **70**, 707–719 (1998).

[251] S. Chu, "Nobel Lecture: The manipulation of neutral particles," Rev. Mod. Phys. **70**, 685–706 (1998).

[252] C. J. Myatt, E. A. Burt, R. W. Ghrist, E. A. Cornell, and C. E. Wieman, "Production of Two Overlapping Bose-Einstein Condensates by Sympathetic Cooling," Phys. Rev. Lett. **78**, 586–589 (1997).

[253] E. Timmermans and R. Côté, "Superfluidity in Sympathetic Cooling with Atomic Bose-Einstein Condensates," Phys. Rev. Lett. **80**, 3419–3423 (1998).

[254] W. Geist, L. You, and T. A. B. Kennedy, "Sympathetic cooling of an atomic Bose-Fermi gas mixture," Phys. Rev. A **59**, 1500–1508 (1999).

[255] A. G. Truscott, "Observation of Fermi Pressure in a Gas of Trapped Atoms," Science **291**, 2570–2572 (2001).

[256] B. DeMarco and D. S. Jin, "Onset of Fermi Degeneracy in a Trapped Atomic Gas," Science **285**, 1703–1706 (1999).

[257] R. Grimm, M. Weidemüller, and Y. Ovchinnikov, "Optical dipole trap for neutral atoms," Adv. At. Mol. Opt. Phys. **42**, 95 (2000).

[258] S. Inouye, M. R. Andrews, J. Stenger, H.-J. Miesner, D. M. Stamper-Kurn, and W. Ketterle, "Observation of Feshbach resonances in a Bose-Einstein condensate," Nature **392**, 151–154 (1998).

[259] P. O. Fedichev, Y. Kagan, G. V. Shlyapnikov, and J. T. M. Walraven, "Influence of nearly resonant light on the scattering length in low-temperature atomic gases," Phys. Rev. Lett. **77**, 12 (1996).

[260] S. Tung, V. Schweikhard, and E. A. Cornell, "Observation of Vortex Pinning in Bose-Einstein Condensates," Phys. Rev. Lett. **97**, 240402 (2006).

[261] R. A. Williams, S. Al-Assam, and C. J. Foot, "Observation of Vortex Nucleation in a Rotating Two-Dimensional Lattice of Bose-Einstein Condensates," Phys. Rev. Lett. **104**, 050404 (2010).

[262] A. Eckardt, "Colloquium: Atomic quantum gases in periodically driven optical lattices," Rev. Mod. Phys. **89**, 011004 (2017).

[263] J. Struck, C. Ölschläger, M. Weinberg, P. Hauke, J. Simonet, A. Eckardt, M. Lewenstein, K. Sengstock, and P. Windpassinger, "Tunable Gauge Potential for Neutral and Spinless Particles in Driven Optical Lattices," Phys. Rev. Lett. **108**, 225304 (2012).

[264] P. Hauke, O. Tieleman, A. Celi, C. Ölschläger, J. Simonet, J. Struck, M. Weinberg, P. Windpassinger, K. Sengstock, M. Lewenstein, and A. Eckardt, "Non-Abelian gauge fields and topological insulators in shaken optical lattices," Phys. Rev. Lett. **109**, 145301 (2012).

[265] F. Großmann and P. Hänggi, "Localization in a Driven Two-Level Dynamics," Europhys. Lett. **18**, 571–576 (1992).

[266] L. Mazza, A. Bermudez, N. Goldman, M. Rizzi, M. A. Martin-Delgado, and M. Lewenstein, "An optical-lattice-based quantum simulator for relativistic field theories and topological insulators," New J. Phys. **14**, 015007 (2012).

[267] L. D. Carr, D. DeMille, R. V. Krems, and J. Ye, "Cold and ultracold molecules: science, technology and applications," New J. Phys. **11**, 055049 (2009).

[268] T. Lahaye, C. Menotti, L. Santos, M. Lewenstein, and T. Pfau, "The physics of dipolar bosonic quantum gases," Reports Prog. Phys. **72**, 126401 (2009).

[269] M. A. Baranov, M. Dalmonte, G. Pupillo, and P. Zoller, "Condensed matter theory of dipolar quantum gases," Chem. Rev. **112**, 5012–5061 (2012).

[270] S. A. Moses, J. P. Covey, M. T. Miecnikowski, D. S. Jin, and J. Ye, "New frontiers for quantum gases of polar molecules," Nat. Phys. **13**, 13–20 (2016).

[271] B. Yan, S. A. Moses, B. Gadway, J. P. Covey, K. R. A. Hazzard, A. M. Rey, D. S. Jin, and J. Ye, "Observation of dipolar spin-exchange interactions with lattice-confined polar molecules," Nature **501**, 521–525 (2013).

[272] S. Baier, M. J. Mark, D. Petter, K. Aikawa, L. Chomaz, Z. Cai, M. Baranov, P. Zoller, and F. Ferlaino, "Extended Bose-Hubbard models with ultracold magnetic atoms," Science **352**, 201–205 (2016).

[273] R. Landig, L. Hruby, N. Dogra, M. Landini, R. Mottl, T. Donner, and T. Esslinger, "Quantum phases from competing short- and long-range interactions in an optical lattice," Nature **532**, 476–479 (2016).

[274]D. G. Olivares and J. J. García-Ripoll, "Exact Diagonalization of 1D Anisotropic XY Model with Open Boundary Conditions," Unpublished (2015).

LIST OF PUBLICATIONS (UPDATED)

The following publications were (in collaboration with others) output of the author's PhD project:

- P. Silvi, F. Tschirsich, M. Gerster, J. Jünemann, D. Jaschke, M. Rizzi, and S. Montangero,
  "The Tensor Networks Anthology: Simulation techniques for many-body quantum lattice systems,"
  arXiv:1710.03733 (2017).

- J. Decamp, J. Jünemann, M. Albert, M. Rizzi, A. Minguzzi and P. Vignolo,
  "Strongly correlated one-dimensional Bose-Fermi quantum mixtures: symmetry and correlations,"
  New J. Phys. 19, 125001 (2017).

- M. Bischoff, J. Jünemann, M. Rizzi, and M. Polini,
  "Tuning the Drude weight of Dirac-Weyl fermions in one-dimensional ring traps,"
  Phys. Rev. B 96, 241112(R) (2017).

- J. Jünemann, A. Piga, S.-J. Ran, M. Lewenstein, M. Rizzi, and A. Bermudez,
  "Exploring Interacting Topological Insulators with Ultracold Atoms: The Synthetic Creutz-Hubbard Model,"
  Phys. Rev. X 7, 031057 (2017).

- J. Decamp, J. Jünemann, M. Albert, M. Rizzi, A. Minguzzi, and P. Vignolo,
  "High-momentum tails as magnetic-structure probes for strongly correlated SU(κ) fermionic mixtures in one-dimensional traps,"
  Phys. Rev. A 94, 053614 (2016).

Where not otherwise stated or referenced, the results presented in this thesis are contributions of the author to the above works.